Characterization of the Process-Induced Fiber Configuration of Long Glass Fiber-Reinforced Thermoplastics

by

Sebastian Goris

A dissertation submitted in partial fulfillment of

the requirements for the degree of

Doctor of Philosophy

(Mechanical Engineering)

at the

University of Wisconsin - Madison

2018

Date of final oral examination: November 28th, 2017

The dissertation is approved by the following members of the final oral committee:

Tim A. Osswald, Professor, Mechanical Engineering

Lih-Sheng (Tom) Turng, Professor, Mechanical Engineering

Natalie Rudolph, Assistant Professor, Mechanical Engineering

Heidi-Lynn Ploeg, Associate Professor, Mechanical Engineering

Pavana Prabhakar, Assistant Professor, Civil and Environmental Engineering

Abstract

Long fiber-reinforced thermoplastics have favorable mechanical properties, low manufacturing costs and superior lightweight characteristics. However, the configuration of the reinforcing fibers changes significantly throughout the entire production process, reflected in mechanisms such as fiber attrition, fiber alignment, and fiber matrix separation. The complexity of the process-microstructure-property relationship limits the use of this material class in a wider range of lightweight applications. This work presents a contribution to gain a better understanding of the underlying physics of fiber motion during molding and to obtain a theoretical link between processing and the fiber microstructure.

As part of this work, novel characterization techniques were developed to overcome the shortcomings of conventional measurement approaches. The measurement concepts comprise methodologies to characterize the fiber orientation, fiber concentration and fiber length by applying sophisticated techniques, which include combining image processing with micro computed-tomography and optical measurement systems. Applying the developed measurement techniques, a range of experimental studies were conducted to investigate the process-induced fiber microstructure. Plate geometries were injection molded at varying nominal fiber concentrations to investigate fiber matrix separation, fiber alignment, and fiber breakage. The experiments revealed substantial variation in the fiber configuration and correlation between the microstructural properties. The substantial fiber matrix separation and fiber breakage found in this work refute the common assumption of uniform fiber concentration and fiber length in molded parts. Additionally, a new experimental setup based on a Couette rheometer was developed to study fiber length reduction under highly controlled conditions, which isolated the impact of processing conditions on fiber attrition. Finally, the generated experimental data are applied to evaluate models predicting the process-microstructure relationship. All models fail to provide acceptable results and the application of these models as truly predictive tools is limited. It was shown that a holistic approach is necessary to capture the process-induced change in fiber configuration, which necessarily includes the interdependencies of the microstructural properties.

Acknowledgments

First, I would like to express my sincere gratitude to my advisor, mentor, and friend Prof. Tim A. Osswald for his continuous patience, motivation, enthusiasm, and immense knowledge. Without his guidance and mentorship, I would have not been able to successfully finish this journey.

I also would like to express my great appreciation to Prof. Natalie Rudolph, Prof. Lih-Sheng (Tom) Turng, Prof. Heidi-Lynn Ploeg, and Prof. Pavana Prabhakar for serving on my dissertation committee and for their encouragement, insightful comments, and continuous advice.

I want to express my appreciation to all the visiting scholars and undergraduate students that I mentored throughout my research work and who assisted with various aspects of this project, including Teresa Back, Riley Bruce, Eliot Busta, Edward Chen, Matthew Drexler, Catherine Fontana, Tobias Heckner, Stephanie Jäger, Andrew Knoeppel, Billy Kucinski, Camila Montoya, Ron Luft, David Pratt, Michael Rademacher, Allen Roman, Jan Teuwsen, Steven Theis, Matthew Thornton, Seth Valenziano, and Siegfried Werner. In addition, I would like to thank my fellow graduate students in the "Fibers Group" who I worked closely with and who helped with critical feedback, discussions of ideas and collaborations in the field of fiber-reinforced composites: Abrahan Bechara, Camilo Perez, Daniel Ramirez, Sara Simon, and Ian Walter.

I would like to thank all current and former members of the Polymer Engineering Center that made my time as a graduate student an unforgettable experience. Only your friendship, support and encouragement made it possible to endure the many challenges, long nights, and tedious laboratory work. In particular, I want to thank Neil Doll, Christoph Kuhn, Thomas Laduch, Roberto Monroy, John Puentes and Christian Schäfer.

I would like to acknowledge the financial support that I received from the Mechanical Engineer-

ing Department through the K.K. Wang Fellowship in 2015 and the scholarships that I received from the Society of Plastics Engineers (SPE), including: the SPE Foundation Injection Molding Scholarship in 2016, the ACCE Graduate Student Scholarship in 2015, the Dr. Jackie Rehkopf Scholarship in 2016 from the SPE Composites and Automotive Divisions, and the Scholarship from the Failure Analysis and Prevention Special Interest Group in 2017.

Most importantly, I would like to thank my family, who continuously and unconditionally supported me during this challenging endeavor. They alone provided the foundation of my development by being invaluable role models and inspiration. My success is a sole projection of the high standards and work ethic by which they have lived their entire lives.

I save my most heartfelt appreciation for Hilary. Besides her outstanding editing skills, I would never have come this far without her love, joy, patience, and caring. She made the time in Madison most enjoyable and fun. In fact, it was her and her family that made me quickly feel at home in the US and I hope for many more years to come.

Table of Contents

List of Figures

List of Tables

List of Abbreviations

3D	Three-Dimensional
ANOVA	Analysis of Variance
CAE	Computer-Aided Engineering
CF	Carbon Fiber
Cross-WLF	Cross-William-Landel-Ferry Model
DPI	Dots per Inch
DOE	Design of Experiments
EATC	European Alliance for Thermoplastic Composites
FRC	Fiber-Reinforced Composites
FVM	Finite Volume Method
GF	Glass Fiber
ISO	International Organization for Standardization
IBOF	Invariant Based Optimal Fitting
LFT	Long Fiber-Reinforced Thermoplastics
MATLAB	MATrix LABoratory; Software for Numerical Computing
MoE	Method of Ellipsis
µCT	Micro Computed-Tomography
NDT	Non-Destructive Testing
PA	Polyamide
PA6	Polyamide 6
PA66	Polyamide 66
PBT	Polybutylene Terephthalate
PLS	Particle Level Simulation
PNNL	Pacific Northwest National Laboratory
PP	Polypropylene

PPGF	Glass Fiber-Reinforced Polypropylene
PPGF05	5%wt Glass Fiber-Reinforced Polypropylene
PPGF10	10%wt Glass Fiber-Reinforced Polypropylene
PPGF20	20%wt Glass Fiber-Reinforced Polypropylene
PPGF30	30%wt Glass Fiber-Reinforced Polypropylene
PPGF40	40%wt Glass Fiber-Reinforced Polypropylene
PPGF50	50%wt Glass Fiber-Reinforced Polypropylene
PPGF60	60%wt Glass Fiber-Reinforced Polypropylene
pvT	Pressure-Volume-Temperature
UV	Ultraviolet
RSC	Reduced Strain Closure
ROI	Region of Interest
RPM	Revolutions per Minute
SEM	Scanning Electron Microscopy
SFT	Short Fiber-Reinforced Thermoplastics
SM	Slit Method
SMC	Sheet Molding Compound

List of Symbols

Symbol	Unit	Meaning
α	–	Number of Dimensions
$\dot{\gamma}$	s^{-1}	Shear Rate
$\dot{\gamma}_c$	s^{-1}	Critical Shear Rate
δ	–	Core Layer Width
ϵ	–	Strain
$\dot{\epsilon}$	s^{-1}	Strain Rate
ζ	–	Dimensionless Drag Coefficient
η	$\mathrm{Pa}\cdot\mathrm{s}$	Viscosity
η_m	$\mathrm{Pa}\cdot\mathrm{s}$	Matrix Viscosity
η_p	$\mathrm{Pa}\cdot\mathrm{s}$	Zero-Shear Viscosity
θ	$^\circ$	Orientation of Fiber
$\theta\left(L_i\right)$	–	Measured Frequency of Fibers
κ	–	Reduced Strain Closure Model Fitting Parameter
λ	–	Attrition Number
$\overline{\lambda}$	–	Average Attrition Number
μ_{eff}	m^{-1}	Effective Linear Attenuation Coefficient
ρ	$\mathrm{kg\,m}^{-3}$	Density
σ	–	Coordinate of the Project Plane
$\boldsymbol{\sigma}$	–	Total Stress Tensor
$\sum_p$	Pa	Particle Stress Tensor
σ_u	Pa	Ultimate Strength of the Fiber
σ_{max}	Pa	Maximum Stress
τ	–	Coordinate of the Project Plane

ϕ	$^\circ$	Orientation of Fiber
ϕ	%wt	Particle Weight Fraction
ϕ_f	%vol	Fiber Volume Fraction
$\overline{\phi_f}$	%vol	Average Fiber Concentration
$\phi_f^n(z)$	–	Normalized Fiber Concentration Distribution
ϕ_f^{max}	–	Maximum Normalized Fiber Volume Concentration
ϕ_{max}	%vol	Maximum Volume Fraction
ϕ_S	$^\circ$	Slit Angle
Ψ	–	Probability Density Function of Fiber Orientation
$\dot{\boldsymbol{\gamma}}_{ij}$	–	Rate of Strain Tensor
λ_s	–	Particle Shape Factor
$\boldsymbol{\omega}_{ij}$	–	Vorticity Tensor
Ω	RPM	Rational Speed
a	mm	Particle Radius
a_e	mm	Effective Particle Radius
a_{ij}	–	Second-Order Fiber Orientation Tensor
a_{ijkl}	–	Fourth-Order Orientation Tensor
a_k	–	Scale Factor
a_r	–	Fiber Aspect Ratio
B_i	–	Dimensionless Variable
C	–	Travel Path of X-Ray
C_B	–	Fiber Breakage Rate Coefficient
C_I	–	Fiber-Fiber Interaction Coefficient
C_p	$\mathrm{J\,K^{-1}}$	Specific Heat
D	mm	Diameter
d_f	mm	Fiber Diameter
E	$\mathrm{N\,mm^{-2}}$	Elastic Modulus
E_f	Pa	Elastic Modulus of the Fiber
F	N	Force
F_{Sphere}	N	Stokes's Drag on a Sphere
$f(\phi)$	–	Sedimentation Function
$f(x,y)$	–	Pixel Intensity of Grayscale Image

g	–	Projection Plane
$\boldsymbol{g}$	$\mathrm{m\,s^{-2}}$	Gravitation Field
$G\left(\phi_S\right)$	–	Intensity Field
$g(x, y)$	–	Pixel Value of Binary Image
h	mm	Characteristic Distance
I	–	X-Ray Intensity
$\boldsymbol{I}$	–	Identity Tensor
$\boldsymbol{j}_\perp$	$\mathrm{n\ m^{-1}\,s^{-1}}$	Particle Flux
k	$\mathrm{W\,m^{-1}\,K^{-1}}$	Thermal Conductivity
k_f	$\mathrm{s^{-1}}$	Fiber Breakage Rate Constant
l	mm	Length
L_0	mm	Starting Fiber Length
L_∞	mm	Unbreakable Length
l_{max}	mm	Maximum Fiber Length of a Fiber Population
L_N	mm	Number-Average Fiber Length
$L_{N_{50}}$	mm	Median of the Number-Average Fiber Length Distribution
l_f	mm	Representative Fiber Length
l_i	mm	Length of a Fiber
$\mathrm{L}_{\mathrm{Initial}}$	mm	Initial Fiber Length
L_S	–	Slit Length
L_{ub}	mm	Unbreakable Length
$L_{W_{50}}$	mm	Median of the Weight-Average Fiber Length Distribution
L_W	mm	Weight-Average Fiber Length
$\mathfrak{L}$	mm	Total Fiber Length of a Fiber Length Distribution
n	–	Index of Particle Friction
N	–	Total Number of Fibers in a Fiber Population
n_i	–	Number of Fibers of a Defined Length
$N\left(\phi\right)$	–	Normalized Fiber Orientation Distribution
$n\left(\phi\right)$	–	Fiber Orientation Distribution
$N \times M$	–	Digital Image Size
$N\left(L_i\right)$	–	Corrected Frequency of Fibers
N_{PDF}	–	Normal Probability Density Function

$\mathfrak{n}$	–	Number-Average Fiber Length Distribution
$\mathfrak{N}$	–	Cumulative Number-Average Fiber Length Distribution
p	Pa	Pressure
$\boldsymbol{p}$	–	Unit Vector Describing Single Fiber Orientation
P_i	–	Fiber Breakage Rate Rate
$p\left(x_i, y_j\right)$	–	Picture Element (Pixel)
S	–	Distribution Shape Factor
t	s	Time
T	°C	Temperature
$\mathbf{T}$	N m	Torque
T_k	–	Global Relative Theshold
T_{Melt}	°C	Melt Temperature
t_{R}	s	Residence Time
r	mm	Radius
R_{ik}	–	Fiber Child Generation Rate
u	$\mathrm{m\,s^{-1}}$	Velocity
$\boldsymbol{u}$	$\mathrm{m\,s^{-1}}$	Velocity Vector
U_0	$\mathrm{m\,s^{-1}}$	Fluid Speed
U_p	$\mathrm{m\,s^{-1}}$	Average Velocity of the Particulate Phase
w	$\mathrm{N\,m^{-1}}$	Distributed Load
$\mathfrak{w}$	–	Weight-Average Fiber Length Distribution
$\mathfrak{W}$	–	Cumulative Weight-Average Fiber Length Distribution
x	–	x-Coordinate
y	–	y-Coordinate
z	–	z-Coordinate

1. Introduction and Motivation

Fiber-reinforced composites (FRC) are a distinctive class of materials defined by the combination of at least two constituents: the matrix material and the reinforcing fibers. By merging the separate phases, the composite has enhanced properties that exceed the performance and capabilities of the individual constituents [1, 2]. In the transportation industries, discontinuous fiber-reinforced polymers have gained importance due to their outstanding material properties, lower manufacturing costs and superior lightweight characteristics [3–5]. Fiber-reinforced materials are more commonly applied as a substitute for metal to achieve a reduction of the overall weight of parts, especially in the automobile industry [6, 7].

Discontinuous fibers are characterized by the fact that the fibers are chopped and change their configuration as a direct response to the deformation experienced by the material during processing. The final state of the fibers determines the local and global properties of the molded part [8]. The configuration of the fibers significantly changes during mold filling of discontinuous fiber-reinforced materials, reflected in the mechanisms referred to as fiber attrition, fiber alignment, and fiber matrix separation [1, 5, 9]. The process-induced change of the fiber microstructure introduces a substantial heterogeneity to the final part, where the concentration of fibers, the length of the fibers, as well as the alignment of fibers can vary within the molded part.

The development of anisotropy is one of the major factors that determines the mechanical properties and the dimensional stability of a molded part [8]. The anisotropic properties of the molded part are a consequence of the fact that fibers show a preferential alignment based on the flow conditions during mold filling [10, 11]. Another important aspect is the reduction of the length of the fibers during processing, referred to as fiber attrition or fiber breakage. In injection molding, the material is injected and forced through a gate at high pressure. As the material is forced to flow, the fibers are subjected to extensive stresses that cause them to deform, buckle, bend and break, resulting in fiber breakage that significantly reduces their

reinforcing effect [12]. Lastly, the fiber concentration can vary within the molded part due to process-induced fiber migration, referred to as fiber matrix separation. Processing discontinuous fiber-reinforced composites can cause a local variation of the fiber concentration, which may lead to a change along the flow path of the material as well as through the thickness of the molded part.

1.1. Processes and Materials

Discontinuous fiber-reinforced composites commonly consist of a thermoset or thermoplastic matrix material. Sheet molding compound (SMC) is the most prominent type of discontinuous fiber-reinforced thermoset and is processed in compression molding [13, 14]. A variety of thermoplastic matrices and processes are available for discontinuous fiber-reinforced composites [15]. Engineering thermoplastics, such as polyamide (PA) or polypropylene (PP) represent the majority of matrix materials used for FRC due to their superior properties compared to commodity plastics [16]. Glass fibers are frequently used for reinforcement due to their availability, low cost and high strength. Although carbon fibers can offer improved performance, the cost increase often does not justify their use as substitute in FRC at this point [17]. Discontinuous fiber-reinforced composites can be further classified as short fiber-reinforced thermoplastics (SFT) and long fiber-reinforced thermoplastics (LFT) [1]. The distinction between LFT and SFT is made by the average fiber aspect ratio (length to diameter). A fiber-filled material with an average aspect ratio of less than 100 is defined as short fiber-reinforced, while long fiber-reinforced composites have an average aspect ratio of more than 100 [18]. Generally speaking, the performance and cost of LFT materials places them between continuous fiber-reinforced composites used for high performance applications and SFT compounds, because LFT can be processed economically with injection molding while providing superior mechanical properties to SFT [5].

The raw material for SFT or LFT processes are supplied in pellet form, as illustrated in Figure 1.1. LFT pellets are either produced by pultrusion or a coating process. Coated LFT pellets consist of fiber bundles that are surrounded by the thermoplastic material and the fibers are not fully impregnated with the thermoplastic matrix (Figure 1.1, center). Pultruded pellets are manufactured by a continuous pultrusion process and the matrix completely impregnates the fibers within the pellet (Figure 1.1, right). The fibers in LFT pellets are aligned along the

major axis in both types of pellet and have a uniform length ranging from 10 mm to 30 mm [19, 20]. SFT pellets are produced by a compounding process, which results in significantly shorter fibers and a non-uniform length (Figure 1.1, left). Current trends in the field of discontinuous fiber-reinforced composites aim to use composite materials with longer fibers in order to increase the reinforcing characteristic of the fibers [5].

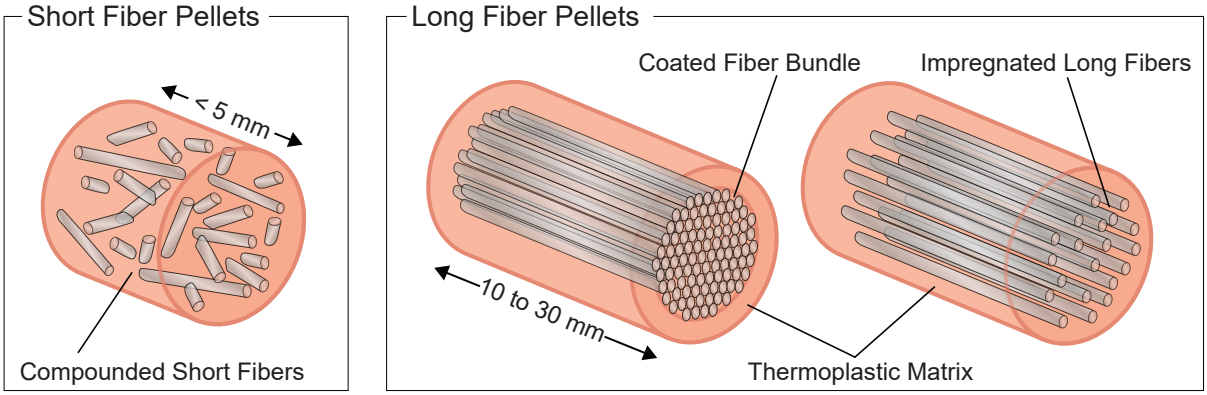

Figure 1.1.: Illustration of short fiber pellets (left) and long fiber pellets: coated fiber bundles (center) and pultruded fibers (right)

LFT materials can be processed with standard processing methods like injection molding or compression without major modifications [19]. However, reducing the process-induced fiber attrition is necessary to exploit the superior reinforcement of the longer fibers. For example, Inoue et al. [21] found that the screw design in the compression zone has a substantial impact on fiber breakages. They found that an optimized screw design (low shear screw with a variable pitch) reduced the fiber breakage compared to a standard screw. Nevertheless, little research has been published discussing optimized machine design and most LFT injection molding is done on conventional injection molding machines and mold designs [15, 22], offering lots of potential for optimization and new developments.

1.2. Motivation

Processing discontinuous fiber-reinforced composites has a profound impact on the arrangement of the fibers in the finished part. Still, the design process of discontinuous fiber-reinforced composites parts does not take into account all aspects of the process-microstructure-property relationship, which consequently results in larger safety factors and limited applications of this material class [23]. Although SFT and LFT have been used for decades, ignorance persists on the underlying physics and phenomena present during processing, including fiber attrition, fiber

matrix separation, and fiber alignment. As a result, the number of defective parts can be a considerable fraction of the total production in some molding processes due to severe reductions in fiber length, the presence of fiber free regions or extensive fiber alignment [5, 24, 25]. This source of inefficiency and uncertainty has been a matter of concern for decades and is only addressed by overdesigning LFT parts or by adding additional reinforcing structures in the part design [13]. Without the ability to control and predict the final properties of the finished part, the full potential of LFT materials for lightweight applications cannot be reached. Understanding and mastering the complexity of the process-microstructure-property relationship in LFT processing is imperative to make the material class available for a wider range of applications. For example, product certification is an important step in developing components with composites. While aerospace and the transportation industries have pushed to drive the component development and part design with composites, the empirical certification processes for composite materials require large time and financial commitments [26]. Although numerical analyses can potentially expedite the certification process, the challenging process-microstructure-property relationship limits the application of numerical tools predicting the microstructural properties and the mechanical performance of discontinuous fiber-reinforced composites. Recently, case studies were published that show the manufacturability and performance for semi-structural components, such as front ends, underbody panels, seats [27–29]. It was shown that the potential of weight reduction by using LFTs can be up to 50% compared to their metallic counterpart, if the process-induced fiber configuration is accounted for appropriately [23].

Computer-aided engineering (CAE) offers a wide range of tools to support all stages of the design process and can be applied to fiber-reinforced composites [13]. In fact, parts made of composites for automotive and aerospace are required to go through a comprehensive numerical analysis and design process before being considered for production [27]. This includes process simulation integrating the process-microstructure analysis as well as the microstructure-property modeling for structural analysis, especially for discontinuous fiber-reinforced thermoplastics [30]. While the process-induced microstructure is influenced by the processing conditions, material selection and part design, the structural analysis can only provide accurate results if the microstructural variables are estimated accurately.

Figure 1.2 illustrates the process-structure-property relationship and highlights the use of predictive tools to estimate the final properties. Overall, it is crucial to choose reasonable modeling and simulation approaches with permissible simplifying assumptions [31]. Hence, all models used in

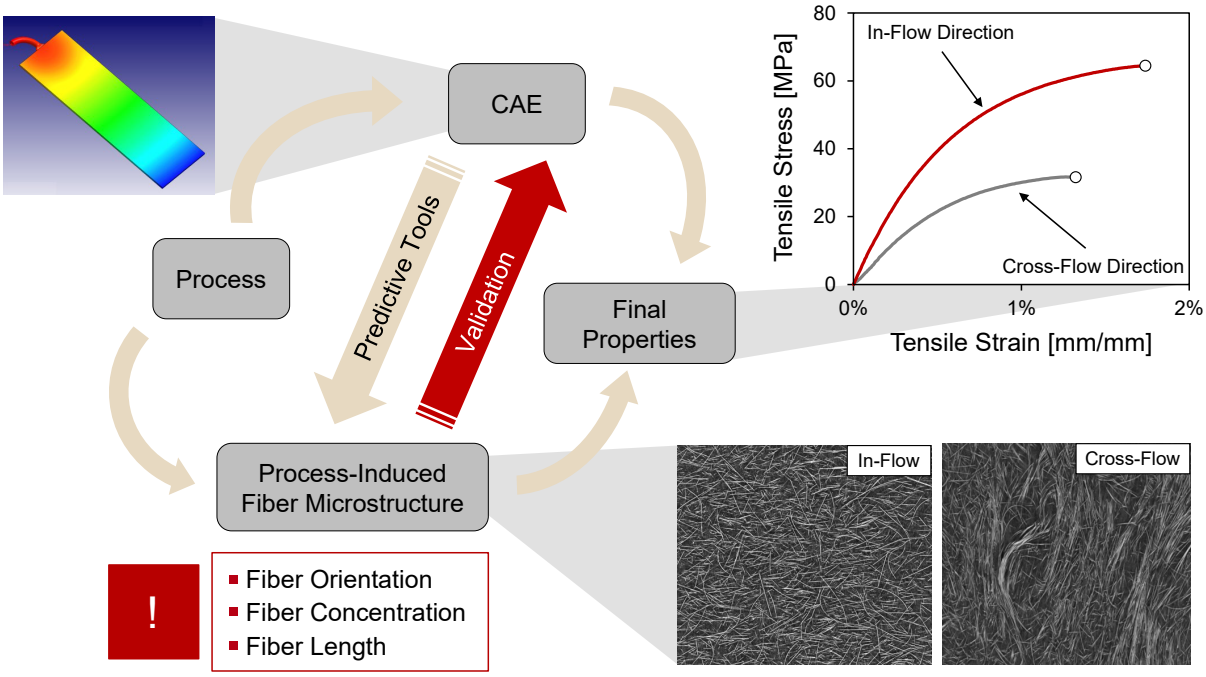

Figure 1.2.: Schematic of the process-structure and structure-property relationship of discontinuous fiber-reinforced composites

the design process require a comprehensive validation by experimental data. In terms of discontinuous fiber-reinforced composites, this means a thorough investigation of the process-induced fiber microstructure and requires a reliable characterization of the state of fibers, including fiber length, fiber orientation and fiber concentration.

The ultimate goal is to establish a fundamental understanding of the process-microstructure relationship in order to ensure that the subsequent structure-property assessment in the structural analysis is adequate. In particular, the interdependencies between length, orientation and concentration of the fibers during processing has not been fully understood yet and an in-depth assessment of the interaction between these properties has yet to be conducted. In order to achieve this goal, progress on the experimental and characterization work, as well as the simulation and modeling side, has to be achieved. Due to limitations of efficient and accurate characterization methods, the interrelationship between the three microstructural variables have not been thoroughly investigated. In particular, there is a lack of experimental data providing a full three-dimensional (3D) characterization of the entire fiber configuration. While there have been several research studies characterizing the process-induced fiber configuration, the measurement procedures vary substantially, calling into question the comparability of reported results. At the same time, all modeling approaches and predictive tools currently available estimate fiber length, density and orientation as if they were decoupled neglecting interaction

between the properties [5, 32, 33]. Only recently, a single particle modeling approach was published that offers a fully coupled simulation of fiber-filled materials at industry relevant fiber concentrations [34].

To fully exploit the potential of LFT materials it is crucial to control and predict the structural qualities of a fiber-reinforced injection molded part, including the configuration of the fibers. Only by adequately incorporating the process-induced fiber microstructure in the design process will it be possible to achieve a reliable prediction of the performance of the molded part.

1.3. Objectives

The research objectives of this dissertation are divided into three parts. First, appropriate measurement techniques to characterize the configuration of the fibers in the finished part are developed and validated. The developed measurement approaches aim to overcome the shortcomings of previously applied characterization methods, particularly in terms of accuracy, repeatability, robustness and time efficiency. The developed measurement techniques will allow accurate characterization of the 3D fiber configuration of sufficiently large samples in a timely manner to obtain statistically meaningful data.

The second objective is to design and conduct a set of experiments providing a comprehensive data set, which can be used to establish the theoretical linkage between processing and fiber microstructure. Pultruded long glass fiber-reinforced polypropylene pellets at varying nominal fiber concentrations are processed for the experimental study. This material combination represents a typical LFT material for industrial applications and, as such, the outcome of this work can be applied to current challenges in the industry. The developed measurement capabilities are used to analyze the process-induced fiber microstructure of manufactured samples. The experimental studies are specifically designed to isolate effects encountered in LFT processing. Injection molding trials of a simple plate geometry were conducted to study the process-induced change in fiber configuration and correlate the microstructural properties. Additionally, a new experimental set-up was developed to study fiber breakage under controlled conditions. The comprehensive experimental results of this work will serve as a reference for the development of new simulation tools, as value input for the mechanical modeling in structural analysis, and improved processing guidelines for LFT materials.

The last part of the dissertation evaluates modeling approaches used to predict the final state

of the fibers during processing by applying the generated experimental data in comparison to simulation results. The fiber breakage experiments in the Couette rheometer are simulated using the Phelps-Tucker model [5] and the model is evaluated by its ability to predict fiber length degradation in LFT processing. Phenomenological models to predict fiber orientation are tested for their ability to capture the full through-thickness orientation pattern for injection molded parts [5, 35]. Despite the lack of published work on modeling fiber-matrix separation in LFT processing, a shear-migration model [33, 36] was currently implemented in commercial software packages for injection molding. This model will be tested on how well it captures the fiber matrix separation observed in the injection molded plates. The overall outcome is an evaluation and validation of current predictive models, as well as recommendations for further work in modeling and simulation of LFT processing. The contributions made by this work will help overcome the limitations of the existing predictive tools for LFT materials.

2. State of the Art

This chapter gives an overview of the present understanding of the process-microstructure-property relationship for fiber reinforced composites, characterization techniques, and simulation approaches for LFT injection molding. The three main microstructural properties (fiber **orientation**, fiber **concentration**, and fiber **length**) are addressed individually in the following sections.

2.1. The Process-Induced Fiber Microstructure

2.1.1. Fiber Alignment

Discontinuous fibers embedded in the molten thermoplastic matrix rotate and translate as a consequence of the deformation of the suspension during processing. The shear and elongation during processing induce a fiber orientation distribution that ultimately causes anisotropic properties in the molded part [35, 37, 38]. The evolution of the fiber orientation in a highly filled material is determined by processing conditions, cavity design and material properties [35, 39]. In general, a distinct orientation pattern through the thickness can be observed in injection molded parts, referred to as the core-shell-skin structure. The core layer in the center of the part consists of fibers that are predominately oriented in cross-flow direction, whereas the fibers in the shell layers are aligned with the flow direction [40]. The skin layer is very thin and usually shows a random fiber orientation [8]. This specific orientation pattern emerges due to the fountain flow effect (see Figure 2.1), which was first studied by Tadmor [41] and describes the reorientation of the polymer molecules (or fibers) at the advancing flow front.

The material at the flow front is forced to move from the center of the cavity outwards onto the mold surfaces. The material freezes upon contact with the cold mold, forming a solidified layer. As additional material enters the cavity, the advancing flow front is continuously stretched and rolls onto the cool wall where it freezes instantly. The high-shear region at the solidified layer

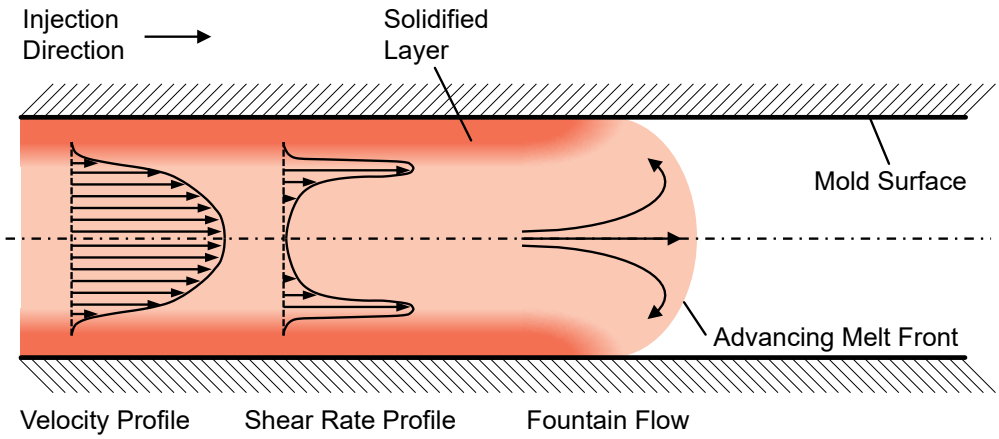

Figure 2.1.: Fountain flow effect: Flow pattern in injection molding at the advancing flow front.

and the advancing molten core cause a strong in-flow fiber alignment in the shell layers [8]. Overall, seven layers can be identified and each layer has its own characteristic fiber orientation, as schematically illustrated in Figure 2.2. The thick core layer consists of fibers predominately oriented in cross-flow direction. Two transition layers with a random fiber orientation surround the core layer. The fibers in the thick shell layers are mainly aligned along the direction of flow. Two thin outer layers (or skin layers) at the mold surfaces show a random fiber orientation.

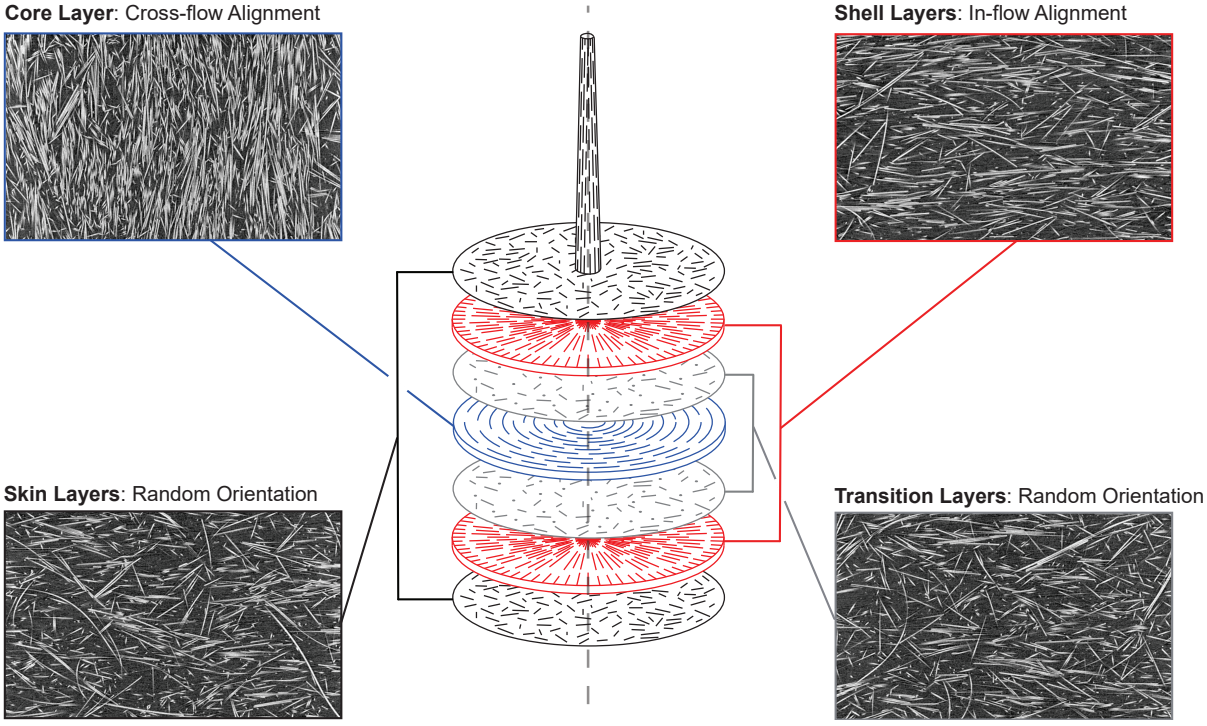

Figure 2.2.: Illustration of the typical fiber orientation distribution through the thickness of an injection molded part, including µCT images of a 40wt% glass fiber-filled PP sample. Center image adapted from [8]

The orientation of a single rigid fiber in 3D space can be described by the angle pair (θ, ϕ), or by the unit vector $\boldsymbol{p}(\phi, \theta)$, directed along the fiber axis by

$$\boldsymbol{p} = \begin{pmatrix} p_1 \\ p_2 \\ p_3 \end{pmatrix} = \begin{pmatrix} cos\,\phi\, sin\,\theta \\ sin\,\phi\, sin\,\theta \\ cos\,\theta \end{pmatrix} \tag{2.1}$$

and as shown in Figure 2.3.

Even in a small volume, adjacent fibers are not aligned in the same direction and instead have a distinct orientation distribution. For a network of fibers in a defined volume, a probability density function $\Psi(\boldsymbol{p})$ offers a complete description of the orientation distribution of the fibers. The probability density function describes the probability of a fiber oriented between the angles θ_i and $(\theta_\mathrm{i} + \mathrm{d}\theta)$, and between ϕ_i and $(\phi_\mathrm{i} + \mathrm{d}\phi)$ [35]. However, calculating the probability density function $\Psi(\boldsymbol{p})$ is too computationally intensive to be implemented in simulation applications. Advani and Tucker [42] proposed a tensorial representation of the fiber orientation, which ultimately emerged as the conventional representation in the field of discontinuous fiber-reinforced composites.

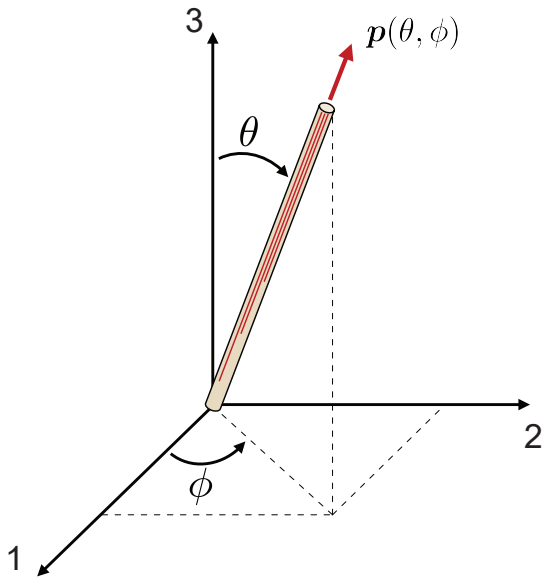

Figure 2.3.: Representation of the orientation of a single rigid fiber by the vector $\boldsymbol{p}(\theta, \phi)$.

The Advani-Tucker orientation tensor a_{ij} considers an average orientation property of all fibers within a discrete volume. The volume is assumed to be large enough to contain a sufficient amount of fiber and still small enough to ensure a uniform orientation distribution of the fibers within the volume.

The components of the symmetric second-order orientation tensor are defined as [42]

$$a_{ij} = \oint \boldsymbol{p}_i \boldsymbol{p}_j \Psi(\boldsymbol{p})\, d\boldsymbol{p} \tag{2.2}$$

where $\boldsymbol{p}_i \boldsymbol{p}_j$ is the dyadic or tensor product of the fiber orientation vector $\boldsymbol{p}$ with itself, and $\oint \Psi(\boldsymbol{p})\, dp$ denotes an integral over all possible fiber orientations. In terms of the orientation distribution and the angle pair (θ, ϕ), the tensor components can be calculated as follows [42]:

$$\begin{aligned}
&a_{11} = \langle\, sin^2\,\phi\, cos^2\,\theta\,\rangle && a_{12} = \langle\, sin^2\,\phi\, cos\,\theta\, sin\,\theta\,\rangle && a_{13} = \langle\, sin\,\phi\, cos\,\phi\, cos\,\theta\,\rangle \\
&a_{21} = a_{12} && a_{22} = \langle\, sin^2\,\phi\, sin^2\,\theta\,\rangle && a_{23} = \langle\, sin\,\phi\, cos\,\phi\, sin\,\theta\,\rangle \\
&a_{31} = a_{13} && a_{32} = a_{23} && a_{33} = \langle\, cos^2\,\phi\,\rangle
\end{aligned} \tag{2.3}$$

where the angle brackets $\langle ... \rangle$ indicate the average of all fibers over a unit volume. Numerical implementations for process simulation and structural analysis typically use the tensorial representation [9, 32]. Experimental data is also conventionally illustrated using the orientation tensor form. The diagonal components of the second order orientation tensor (a_{11}, a_{22}, and a_{33}) describe the degree of orientation with respect to the defined coordinate system. Conventionally, the reference coordinates are defined so that the 1-direction represents the in-flow direction, the 2-direction is the cross-flow direction and the 3-direction is the thickness direction. The off-diagonal components of the orientation tensor show the tilt of the orientation tensor from the coordinate axes. Hence, they are zero only if the coordinate axes align with the principal directions of the orientation tensor [42]. The physical interpretation of the tensor components focuses mainly on the diagonal components of the tensor, illustrated in Figure 2.4. A completely random orientation (left) is described by the diagonal components $a_{11} = a_{22} = a_{33} = \frac{1}{3}$ while perfectly aligned fibers in the 2-direction (right) are described by $a_{11} = 0$, $a_{22} = 1$ and $a_{33} = 0$.

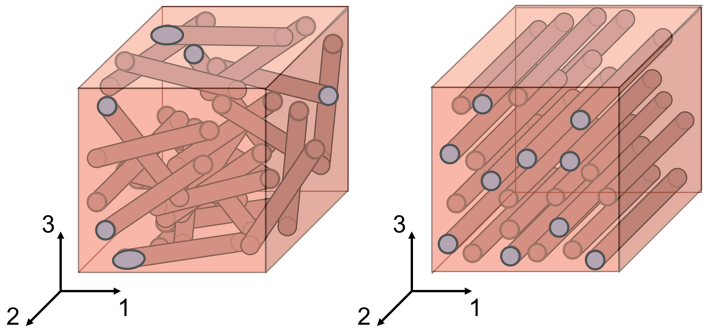

Figure 2.4.: Orientation of a fiber population within a volume: randomly oriented fibers (left) and aligned fibers (right). Adapted from [1]

Process-induced fiber alignment has been a focus of experimental and numerical studies in the field of discontinuous fiber-reinforced composites. Most work focuses on the fiber orientation pattern that emerges due to the fountain flow effect and the characteristics of the shell-core structure. Figure 2.5 shows an example of a measured fiber orientation distribution plotted along the part thickness using the conventional orientation tensor representation.

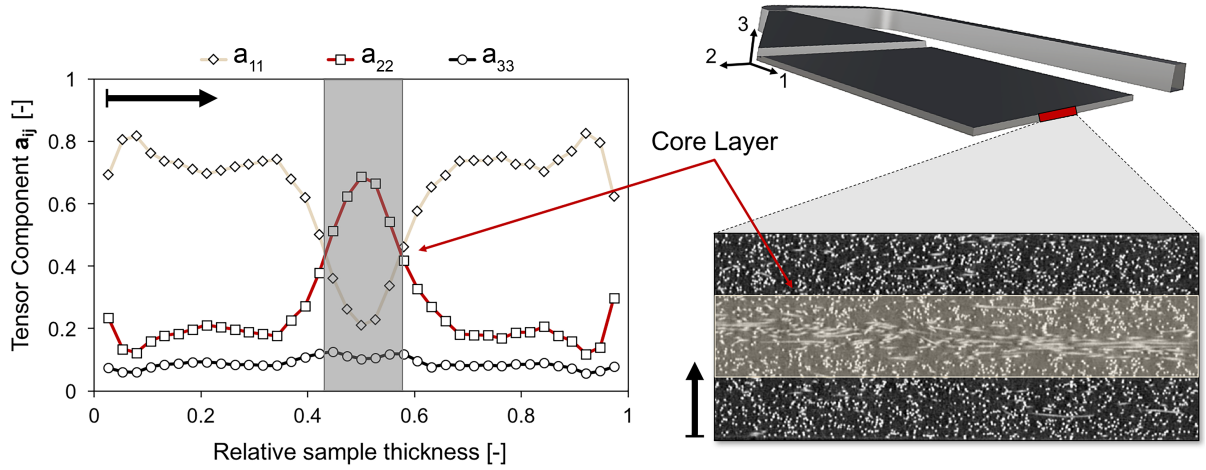

Figure 2.5.: Illustration of the fiber orientation variation along the part thickness of an injection molded sample.

The correlation between processing conditions and fiber orientation was studied by various research groups with a focus on experimental and numerical studies. Bailey and Rzepka [43] published a comprehensive experimental analysis of the fiber orientation in injection molding of 50%wt glass fiber-filled polyamide 6 (PA6). The outcome of their analysis characterized the impact of processing conditions on morphology of the shell-core structure in the molded part. In terms of the degree of fiber alignment, their results show that injection speed and holding pressure are the most influential processing parameters. At low injection molding speeds, the relative core thickness reduced to 58% of the core thickness at standard injection speed. Their overall conclusion is that decreases in the core layer width are caused by any change in mold filling that induces higher stresses. Additionally, Bailey and Rzepka found that the core layer is wider for longer fibers than for shorter fibers. Their hypothesis is that the length of the fibers influences the mobility of fibers to rearrange. Consequently, longer fibers are limited in their aptitude to orient. Toll and Andersson [40] conducted a similar study and came to the same conclusions as Bailey and Rzepka in terms of impact of fiber length and core layer thickness. In addition, Toll and Andersson [40] report a higher in-plane orientation for longer fiber compared to short fiber-filled compounds.

Vincent et al. [44] studied the influence of cavity thickness on the fiber orientation by injection molding simple plates with thicknesses varying from 1.1 to 5.0 mm. Their results suggest a strong correlation of the shell-core structure and the part thickness. The thicker the part, the more distinct the core-shell structure becomes, as shown in Figure 2.6.

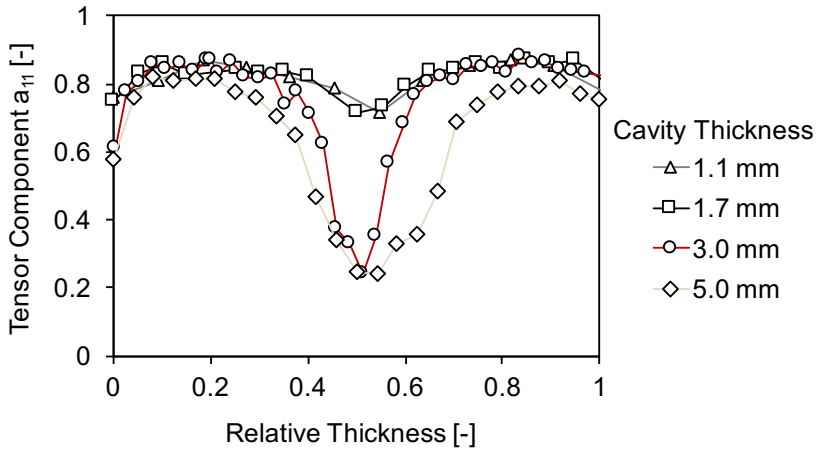

Figure 2.6.: Fiber orientation measured for varying cavity thicknesses. Adapted from [44]

2.1.2. Fiber Matrix Separation

The phenomenon of fiber matrix separation describes the process-induced variation of fiber concentration. The complex flow characteristics present in injection molding during mold filling can cause spatial differences in the fiber concentration within the finished part. Earlier work showed that fiber migration during processing occurs on two scales: variation in the *local fiber concentration through the thickness* of a molded part and *global fiber concentration gradients* along the flow path.

Fiber matrix separation can also be affected by part design and features of the part. The separation effect in rib-filling describes the phenomenon of fibers accumulating in the base of the rib while the tip of the rib remains almost fiber-free and has been studied by a few research groups [25, 45, 46]. While this is an important field of research, the influence of design features on fiber matrix separation is not part of this work and the reader is referred to recently published work on rib-filling by Kuhn et al. [30].

Previous studies have addressed the process-induced concentration gradients throughout molded parts for filled thermoplastics. Toll and Andersson [40] published results showing an increase in fiber concentration from nominal 30%wt in the raw material to 36%wt at the end of the flow path of a film-gated plate for glass fiber-reinforced polyamide 66 (PA66). In a similar study,

O'Regan et al. [47] observed an increase of 3 to 4%vol at the end of the flow path in injection molding of fiber-reinforced PA66. Lafrance et al. [48] showed an increase from 39%wt at the gate to 51%wt at the end of the flow path for a fan-gated plate. Using a spiral mold, Kubat and Szalanczio [49] studied the filler migration effects of a low-density polyethylene filled with glass spheres. Along a total length of 1950 mm, they measured the filler concentration and found substantial migration of the particles towards the end of the flow path. Their results suggest a relative increase of up to 25% filler concentration at the tip of the spiral for glass spheres with diameters between 53 and 105 µm.

Hegler and Menning [50] published work on the filler separation effects during injection molding of glass bead and glass fiber-filled thermoplastics using dumbbell and rectangular box specimens. Their results show that the separation effects were more pronounced with beads than with fibers indicating an influence of the shape and dimensions of the fillers. Furthermore, they conclude that mold geometry and filler concentration are key parameters determining the degree of filler migration in injection molding. Other processing parameters, such as mold temperature, injection speed, matrix material and screw speed did not substantially impact the filler-matrix separation phenomena in their experiments.

Papathanasiou and Ogadhoh [51] studied particle migration during mold filling of glass bead-filled polystyrene with an average bead size varying from 50 to 500 µm. Their results agree with previous studies, showing that the filler matrix separation increases substantially with larger beads with the largest relative increase of 15% more fillers for glass beads with a diameter of 500 µm at the end of the flow. Another major outcome of their work was the observation that particles appear to accumulate at the free surface. For the largest particle sizes used in their study, the concentration of particles near the free surface was almost double than in the feed material. Papathanasiou and Ogadhoh's results strongly indicate that filler migration depends particle size and nominal concentration in the feed material. In 2011, Kovacs published a similar study detailing the segregation effect of glass beads along the flow for injection molded plates and its impact on volumetric shrinkage [52]. His investigation into filler migration again indicated a dependency on particle size and nominal concentration, confirming Papathanasiou and Ogadhoh study [51]. Figure 2.7 shows Kovacs' results of the filler separation along the flow length for glass bead diameters varying from 11 µm to 203 µm (nominal glass bead concentration of 40%wt).

Mondy et al. [53] conducted fiber migration experiments in a wide-gap Couette rheometer for low aspect ratio nylon fibers in glycol. Their measurements show a migration of fibers to the

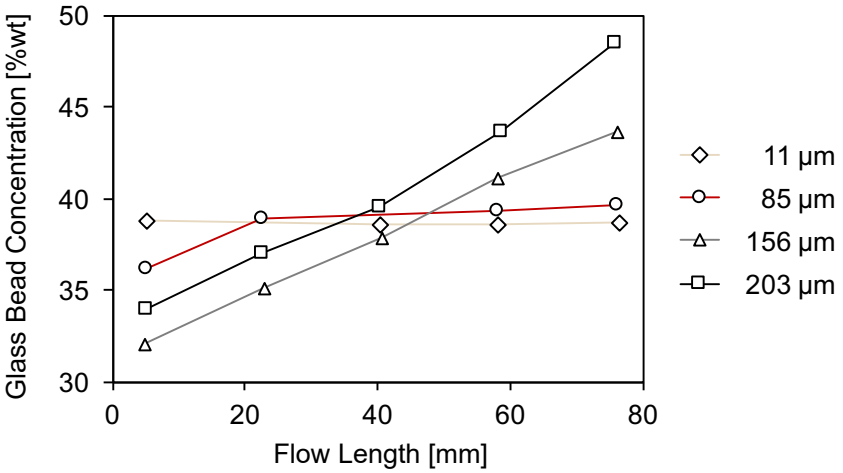

Figure 2.7.: Glass bead migration along the flow path for various glass bead sizes (nominal bead concentration: 40%wt). Adapted from [52].

low-shear regions. While the authors did not find that the aspect ratio impacted the migration, they found an influence of fiber concentration, suggesting that the effect of shear-migration increases at elevated concentrations.

The most recent experimental work on fiber migration was done by Ramzy et al. [54] for hemp and sisal fiber-filled polypropylene. Similar to Kuba and Szalanczio, they used a spiral cavity and measured the concentration variation along the flow path. As reported in previous studies, the results showed an increase in filler concentration along the spiral flow length. The fiber agglomeration at the tip of the spiral showed a relative increase of up to 30%.

All these studies share the conclusion that the fiber concentration increases towards the end of the flow path, suggesting that the last filled location carries an accumulated amount of filler. Furthermore, the processing conditions appear to play a much smaller role than the filler properties when evaluation the degree of fiber matrix separation. The influencing factors are reported to be both the concentration and the shape of the filler. Furthermore, the migration effect is more pronounced in general for longer fibers at higher concentrations than it is for shorter fibers at low concentrations [40].

The through-thickness filler concentration gradient in injection molding has been explored much less frequently. A comprehensive study was conducted by Toll and Andersson [40] for 30%wt glass fiber-reinforced PA66 and a simple plate geometry. They found an agglomeration of fibers in the core layer using a sectioning and microscopic measurement protocol. Their results suggest almost 40% more fibers in the core layer than in the shell for their long fiber PA66 (initial fiber length of 10 mm). For the short fiber grade (initial fiber length of 0.6 mm), the fiber

agglomeration is less pronounced with only 10% more fibers in the core than in the shell region. While other publications also mention the phenomenon of fiber agglomerating in the core of injection molded parts, the observations are mostly side-effects in these studies; no comprehensive analysis exists nor have theories been formulated to explain the underlying mechanism. Velez-Garcia et al. [55] focused on fiber orientation measurements for short fiber-reinforced polybutylene terephthalate (PBT) by applying a newly developed sectioning procedure. From the obtained micrographs, they also reported a fiber concentration gradient through the thickness of the molded center-gated disk. Recently, Sun et al. [56] published an experimental study on using µCT to quantify the fiber orientation of an LFT injection molded instrument panel. While also focusing on orientation measurements, they incidentally analyzed the pixel fraction from µCT scans indicating a strong agglomeration of fibers in the core layer of the molded part.

At this point, no comprehensive explanation of the fiber matrix separation phenomena has been derived and validated. A common hypothesis for the observed phenomena is that shear-induced particle migration causes the variation in fiber concentration. Shear migration describes the irreversible accumulation of particles due to a shear stress gradient [57]. In a simple Poiseuille flow, it was shown that particles tend to migrate from the high shear region at the wall toward the low shear region at the centerline [57, 58]. Similar migration was found in a wide-gap Couette rheometer flow [53]. However, it has not been proven that shear migration also explains the fiber matrix separation in processing fiber-reinforced thermoplastics.

2.1.3. Fiber Attrition

The superior mechanical performance of fiber reinforced composites is achieved by transferring the applied load from the matrix to the reinforcing fibers. Consequently, the interfacial adhesion as well as the length of the fibers embedded in the matrix determine the maximum transferable load. Preserving a fiber length that is sufficiently long to transfer the load while maintaining economical process cycles, is a major research objective in academia and industry [3, 5, 59, 60]. Fiber attrition refers to the fact that fibers break during processing and that the length of the fibers is inevitably reduced from its initial value. While the initial length of the fibers may be uniform and up to 30 mm for LFT materials, fiber attrition results in a distribution of fiber lengths in the finished part ranging from powder-like fibers (<0.1 mm) to a small fraction of fibers retaining their initial length. In general, the degree of fiber attrition is influenced by the type of process, processing parameters, material selection, and mold design [3, 5, 8]. Since

mechanical properties depend on fiber length, it is desired to preserve the length of the fibers as much as possible by using processing conditions that treat the fibers more gently.

Along the entire process line, the fibers are subjected to severe stresses, including hydrodynamic effects, fiber-fiber interaction and fiber-equipment interactions, which can reduce the average fiber length for LFT materials to only 0.5 - 1.0 mm in the finished part [3, 61]. Fiber breakage can be attributed to the following mechanisms [8]:

- Melting effects: This damage mechanism appears at the beginning of polymer processing when the pellets are partially fused and the solid-fiber interaction leads to bending and shear stresses in the fibers, as illustrated in Figure 2.8 (right). This effect is thought to cause a large degree of fiber attrition, which mainly occurs in the melting zone of the screw [21].

- Fiber-fiber interaction: In highly filled material combinations, the fibers collide excessively during processing, which results in length reduction due to fiber bending and friction between fibers, as shown in Figure 2.8 (left).

- Fiber-melt interaction: Fibers are embedded in the thermoplastic matrix, which introduces large stresses to the fibers due to the hydrodynamic forces during the entire process, see Figure 2.8 (left).

- Fiber-wall interaction: Fibers collide and interact with the solid walls of the equipment. Abrasion and friction between the fibers and the walls lead to stress concentration within the fibers, demonstrated by Figure 2.8 (left).

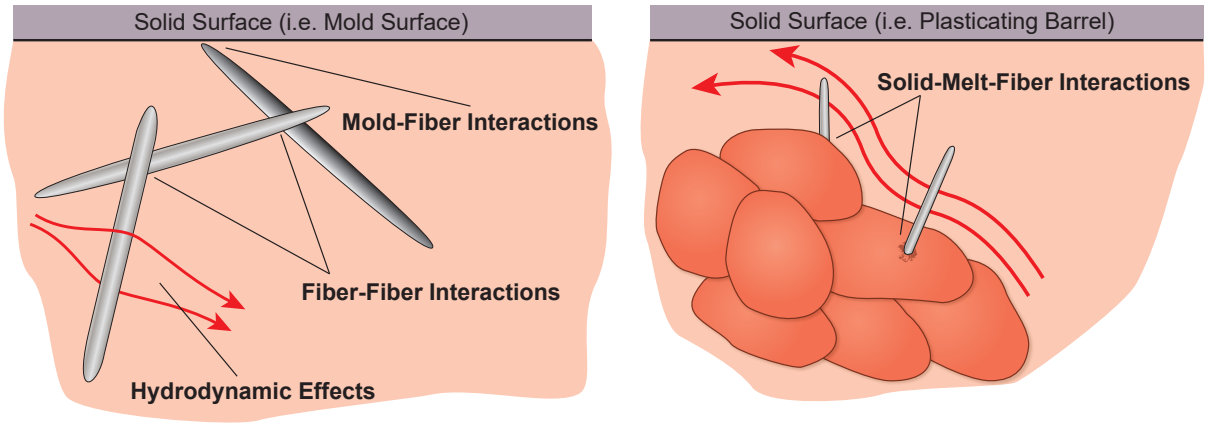

Figure 2.8.: Mechanisms of fiber breakage during processing: Mold-fiber interactions, fiber-fiber interactions, and hydrodynamic effects (left); fiber breakage caused by partially molten pellets, solid-melt-fiber interactions (right), adapted from [8].

An overall sample consists of N total fibers and the length of each fiber may vary from 0 to l_{max}. The entire population can be represented by a histogram with n bins, where each bin has N_i fibers with the length l_i. The total length of the population $\mathfrak{L}$ is defined as

$$\mathfrak{L} = \sum_{i=1}^{n} (N_i \, l_i) \tag{2.4}$$

The obtained distribution is conventionally summarized by calculating representative average values, such as the number-average length and the weight-length average, in order to obtain a concise understanding of the fiber population as a whole.

The number-average fiber length, L_N, is calculated as

$$L_N = \frac{\sum_{i=1}^{n} (N_i \, l_i)}{\sum_{i=1}^{n} (N_i)} \tag{2.5}$$

The weight-average (or length-average) fiber length, L_W, is a second characteristic average of the fiber length distribution, emphasizing the proportion of long fibers in the distribution. This is of particular interest for molded LFT samples since they typically show a length distribution with a distinct peak followed by a long tail decay [62]. It is calculated using

$$L_W = \frac{\sum_{i=1}^{n} (N_i \, l_i^2)}{\sum_{i=1}^{n} (N_i \, l_i)} \tag{2.6}$$

The length distribution can be represented by a discrete probability density function to capture the measured data, which could also be fitted to defined continuous probability density functions, such as the Weibull [63] or Burr distribution functions [64]. The discrete probability density function $\mathfrak{n}$ can be defined as

$$\mathfrak{n}(l_i) = \frac{N_i}{N} \tag{2.7}$$

This distribution function can also be defined in terms of the length-weighted distribution $\mathfrak{w}(l_i)$ using

$$\mathfrak{w}(l_i) = \frac{N_i \, l_i}{\mathfrak{L}} \tag{2.8}$$

By integrating $\mathfrak{n}$ over length, the cumulative length distribution $\mathfrak{N}$ can be obtained, which

describes the fraction of fibers that are smaller than or equal to a given length l_j:

$$\mathfrak{N}(l_j) = Pr(l \leq l_j) = \frac{\sum_{i=1}^{j} (N_i)}{N} \tag{2.9}$$

Similarly, the length-weighted cumulative distribution $\mathfrak{W}$ is calculated using

$$\mathfrak{W}(l_j) = Pr(l \leq l_j) = \frac{\sum_{i=1}^{j} (N_i\, l_i)}{\mathfrak{L}} \tag{2.10}$$

The cumulative distributions $\mathfrak{N}$ and $\mathfrak{W}$ offer a consistent way to graphically compare different data sets without the need of computed average values. Figure 2.9 illustrates $\mathfrak{N}$ (top) and $\mathfrak{W}$ (bottom) for the same data set. The graphs indicate the corresponding average values as well as the median values from the number distribution and length-weighted distribution ($L_{N_{50}}$ and $L_{W_{50}}$).

The majority of fiber breakage is associated with the plasticating phase and different research groups have studied fiber breakage along the different zones of the screw. Turkovich and Erwin [65] found that most fiber length degradation occurs in the melting zone with only minor attrition in the feed or conveying zone. This might be attributed to partially embedded fibers in the solid pellets, which are bent and sheared off during plastication, as previously shown in Figure 2.8. In 2005, Lafranche et al. [48] quantified the fiber length degradation in the plasticating unit for long glass fiber-reinforced Polyamide 6. They measured the fiber length at the different zones of the screw and summarized the results in Figure 2.10. Their results suggest that the remaining fiber length at the nozzle is less than 50% of the initial length (9 mm). Inoue et al. [21] found that the screw design in the compression zone has a substantial impact on fiber breakage. They found that an optimized screw design (low shear screw with a variable pitch) can reduce the fiber breakage compared to a standard screw.

Rohde et al. [3] conducted a comprehensive study on the influence of processing conditions on the residual fiber length in the molded part in LFT injection molding. They designed a full factorial experimental plan and varied the processing parameters, including injection speed, back pressure, holding pressure and screw speed. The outcome of their analysis suggests that back pressure has a strong influence on fiber attrition. A change from 50 to 80 bar back pressure reduced the residual fiber length in the molded part by approximately 30%. Injection speed, holding

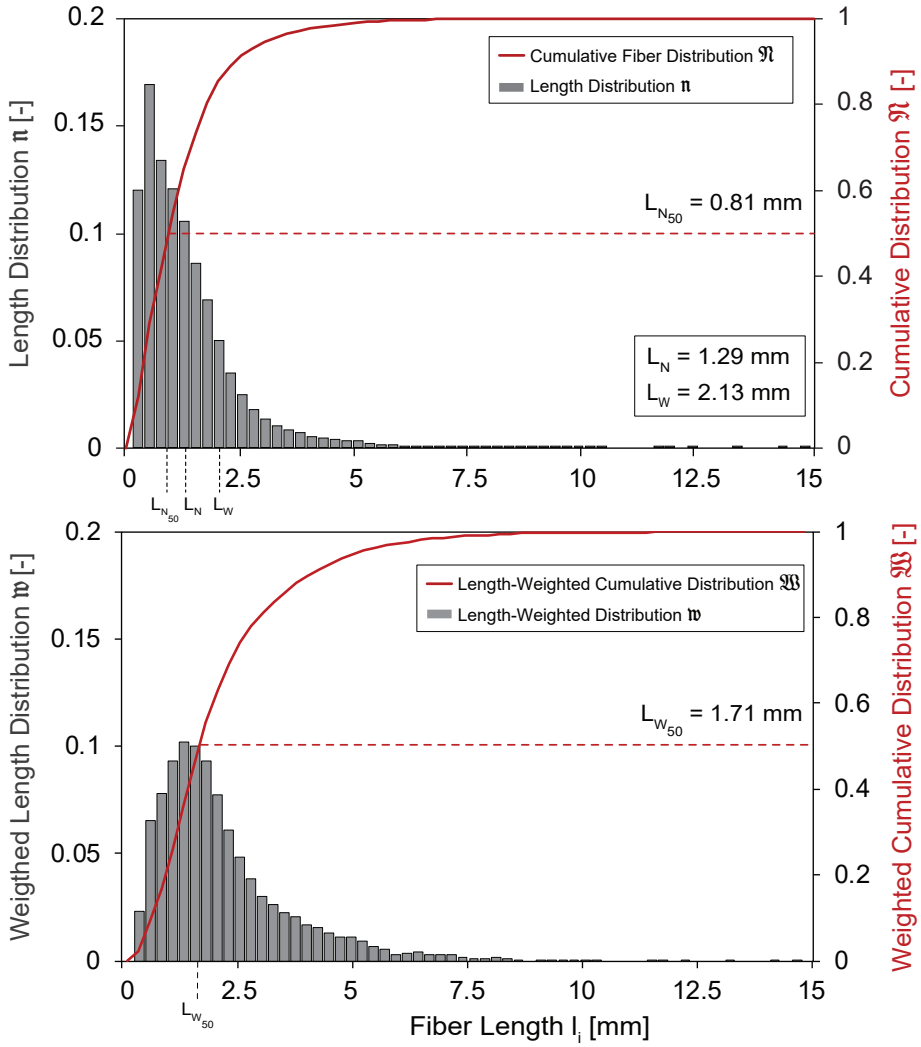

Figure 2.9.: Illustration of the cumulative fiber distribution $\mathfrak{N}$ (top) and the cumulative length-weighted distribution $\mathfrak{W}$ (bottom) representing the same data set.

pressure and screw speed were not found to be significant in their molding trials. Only the combination of increased back pressure and holding pressure were significant in their statistical analysis. Nevertheless, the authors state that it is difficult to isolate the mechanisms that cause fiber attrition due to the complex phase change and shear history that is present in the injection molding process. In contrast, Lafranche et al. [48] conducted a similar experimental study, but reported that the screw speed has a larger impact on fiber breakage than back pressure, and they suggest that the fiber-wall interactions due to screw movement are more important than the fiber-melt interaction caused by the back pressure.

Metten and Cremer [22] found that increased holding pressure decreased the fiber length in the finished part, suggesting that increased holding pressure promotes fiber breakage during LFT injection molding. While their measurements show an average fiber length of 4.8 mm at 200 bar

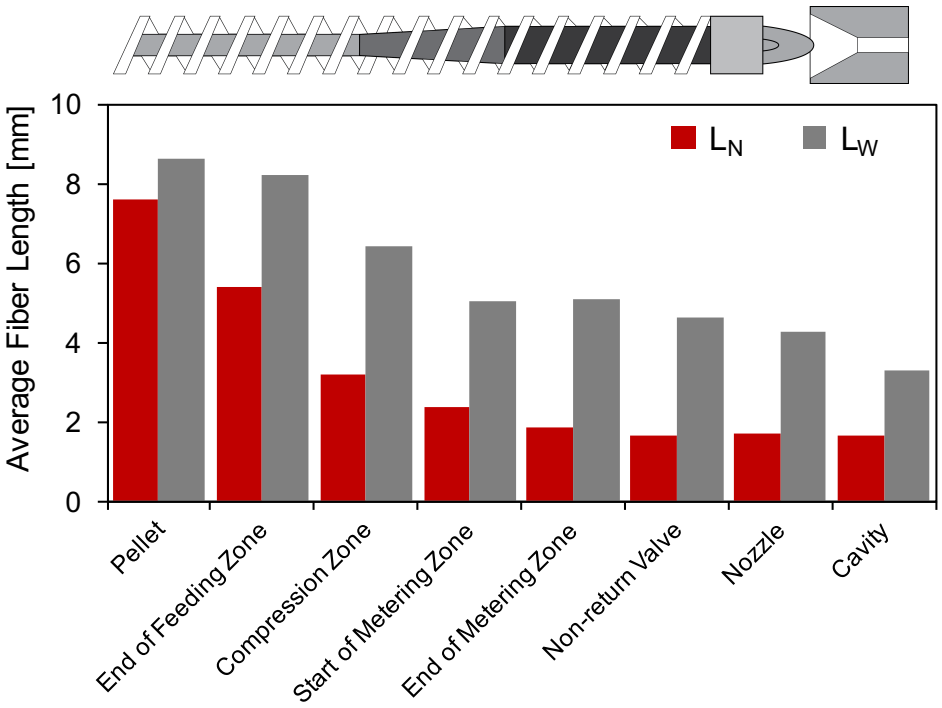

Figure 2.10.: Fiber breakage during the plasticating stage. Adapted from [48].

holding pressure, the fiber length drops below 3 mm at 450 bar holding pressure. This increase in fiber breakage might be caused by the additional motion of the molten core at elevated holding pressure when partially embedded fibers shear off during the packing phase [22].

2.1.4. Microstructure-Property Relationship

As the reinforcing phase in the compound, the state of the fibers determines the mechanical performance of the finished part. For example, the anisotropy which is introduced by the alignment of the fibers has a substantial influence on the mechanical properties. The tensile strength is higher in the direction of fiber alignment and lower in the cross direction. Hence, anisotropy is a key aspect of designing LFT parts since process-induced fiber alignment is inevitable in LFT injection molding. Similarly, the concentration and length distribution of fibers play an important role in the microstructure-property relationship.

Thomason et al. conducted the most comprehensive work to date on the structure-property relationship of discontinuous fiber-reinforced thermoplastics and published several papers from 1996 [66] to 2009 [67]. He and his research group investigated the mechanical properties of glass fiber-reinforced PP with fiber concentrations up to 73%wt and initial fiber lengths varying from 0.1 mm to 50 mm. For all material combinations, specimens were manufactured by either a wet-molding process or injection molding. Comprehensive mechanical testing, including tensile,

flexural and impact tests were conducted at ambient temperature, as well as at -30°C. Also, their work included characterization of the local fiber orientation and fiber length. Ultimately, they were able to draw conclusions about the relationship between the fiber configuration and the mechanical performance of the material. The most important aspects for this work are:

- The authors found a linear increase in tensile strength with fiber concentration for the wet-molded PP samples. The tensile strength was also shown to depend on the average fiber length, up to 3 mm. However, the increase in strength leveled off for all material combinations with fiber length greater than 3 mm, which corresponds to an aspect ratio of 270 (fiber diameter is 11.0 µm). [66]

- The modulus of fiber-reinforced PP increased linearly with the fiber concentration until 40%wt, and the rate of increase was considerably less at higher concentrations. Thomason's results suggest that the modulus of the composite is independent of the fiber length after 0.5 mm (aspect ratio of 45). [68]

- The impact strength increased with increasing fiber concentration and the strength also improved with fiber length, but converged at lengths above 6 mm (aspect ratio of 540). [10]

- For injection molded samples that result in a fiber length distribution, as opposed to a fairly uniform fiber length in the wet-molded samples, the results showed that fiber length had a significant impact. Although the modulus did not show much difference between LFT and SFT, tensile modulus, flexural modulus, and impact resistance all increased with longer fibers. [69, 70]

- For injection molded PP samples, the strength and impact properties showed a maximum value at fiber concentrations of 40 to 50%wt and, at higher concentrations, these properties decreased substantially and reached the values of unreinforced polypropylene at the highest fiber concentration (73%wt). The modulus, however, increased linearly with fiber concentration over the entire range. [60]

- Fiber attrition in the injection molded PP samples showed a linear dependence on fiber concentration. In injection molded PA6 samples, their results also indicated an increase of fiber attrition for fibers with lower diameters. [67]

The main results of Thomason's studies on the relationship between microstructure and mechanical properties for injection molded samples can be summarized in a single graph, as shown

in Figure 2.11. The graph shows the stiffness, strength and impact performance as a function of fiber concentration [60]. The properties are each normalized with respect to the values of the unfilled matrix material. While the modulus increased linearly with fiber concentration, the strength and impact performance show a maximum at 40 to 50%wt. A further increase in fiber concentration resulted in decreased strength and impact properties. At highly filled levels above 60%wt, Thomason's results suggest that these properties even decrease to the same level as unfilled PP.

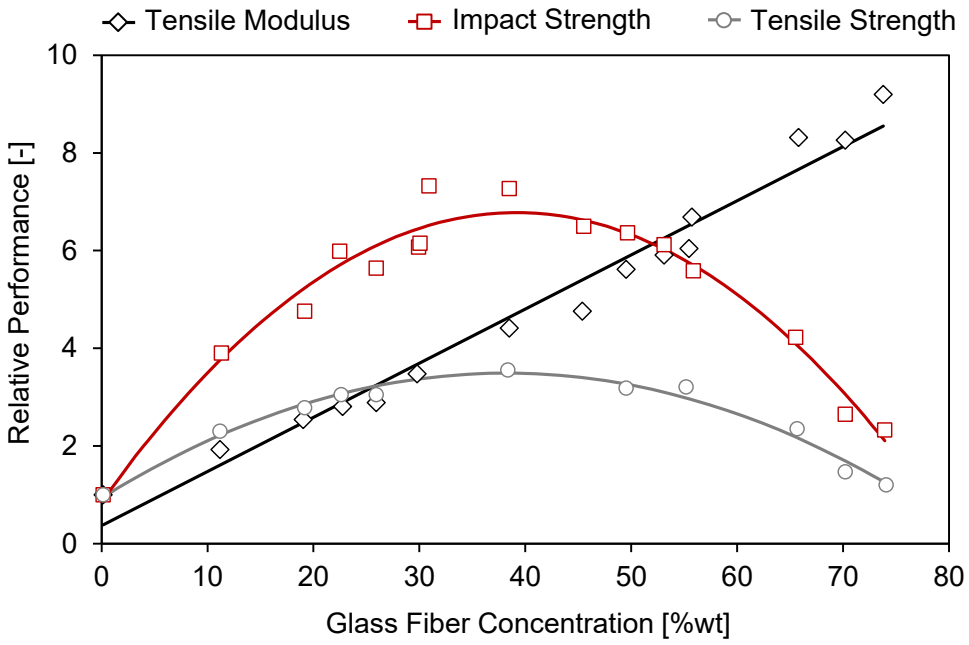

Figure 2.11.: Normalized mechanical properties as function of fiber concentration, obtained experimentally: Tensile modulus, tensile strength and impact strength. Adapted from [60].

The effect of the residual length of the fiber on the mechanical properties of a molded part is illustrated in Figure 2.12. The figure is adapted from Schemme [71] and is based on the experimental work from Thomason et al. [10, 66, 68] discussed in the previous paragraphs. The graph visualizes the effect of the fiber aspect ratio on the tensile modulus, tensile strength, and impact strength. It can be seen that these properties saturate after which point any increase of the fiber length would not further improve the mechanical properties. The figure also qualitatively illustrates the expected range of residual fiber aspect ratios for LFT injection molding, reported in the literature and measured experimentally in this work. This expected range would suggest a strong sensitivity for tensile strength and impact strength for injection molded LFT parts. While Schemme's graph offers a qualitative overview of the relationship between fiber aspect ratio and mechanical properties, the quantitative interpretation of this graph should be done

carefully, because a universal validity has not been proven yet. For example, the underlying experimental data do not account for any variation of fiber orientation or local fiber concentration due to the change in fiber length.

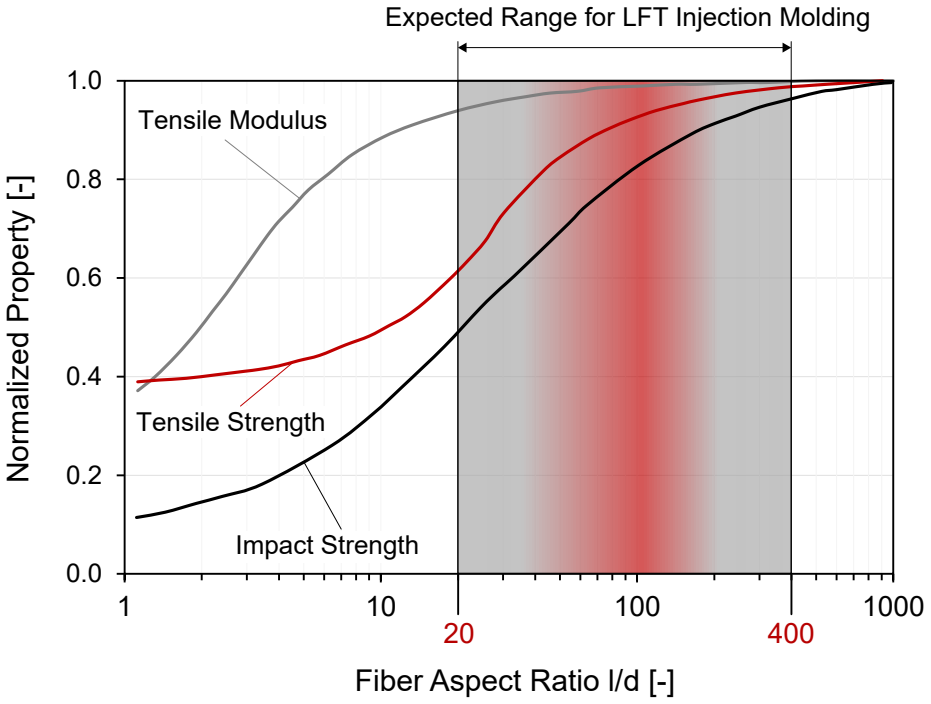

Figure 2.12.: Normalized mechanical properties as function of fiber aspect ratio for tensile modulus, tensile strength, and impact strength. Adapted from [71]. The highlighted range illustrates the qualitative range of fiber aspect ratios expected in LFT injection molding.

2.2. Characterization Techniques

Quantifying the fiber configuration in molded samples is of utmost importance so that the underlying physics of the process-microstructure relationship can be studied experimentally. Furthermore, accurate and reliable experimental data are required to test and develop numerical models and predictive tools. At times, the lack of accurate experimental data limits the progress of validating modeling approaches [5]. Nevertheless, the characterization of fiber configuration is a cumbersome task since even small samples comprise millions of fibers. A wide variety of measurement approaches exist, but no standard has been accepted nor has a uniform procedure been defined. While some measurement concepts share similarities, there are substantial differences in key aspects of the measurement techniques and the execution of the actual measurements.

2.2.1. Measuring Fiber Orientation

For decades, fiber orientation measurements were performed manually by physical sectioning of the sample and inspecting the cross-sections using optical reflection microscopy [38, 72, 73], which is referred to as the method of ellipsis (MoE). The fibers leave elliptical footprints on the polished cross-sections, which are detected and analyzed for individual fibers. The fiber orientation can be quantified by analyzing the shapes of the ellipses, as illustrated in Figure 2.13. An image analysis system imports the captured micrographs and fits ellipses to determine the angles ϕ and θ individually for each fiber [73]. Although newer systems are automated to a degree, this technique still requires a lot of manual work to achieve accurate results. Furthermore, the destructive nature of this method does not allow additional testing of the sample, e.g. fiber length analysis. Moreover, the two-dimensional observation of the ellipses results in ambiguity with respect to the out-of-plane angle θ, because the fiber can be oriented at θ or $\theta + \pi$, as illustrated in Figure 2.13. However, this ambiguity can be resolved by an additional etching after each polishing step, so that a fiber's shadow is visible in the micrograph. By determining the location of the shadow relative to the corresponding fiber, the angle θ can be distinctly defined [55].

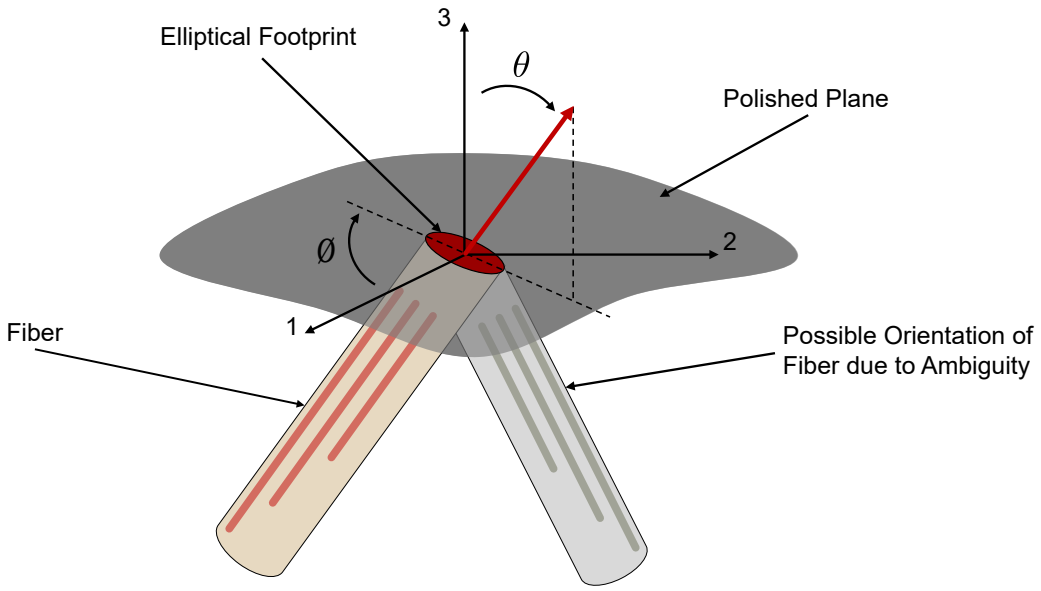

Figure 2.13.: Basic principle of the method of ellipses and illustration of the ambiguity in the out-of-plane angle θ.

A relatively new approach to measure fiber orientation distribution within fiber-reinforced plastic parts is applying the X-ray micro computed-tomography (µCT) technology. This technique is a non-destructive testing (NDT) method, which allows one to obtain the internal material

structure of an object and evaluate its micro-structural properties [74, 75]. The advantage of µCT is that it can achieve high resolution of the full 3D microstructure without destroying the specimen. Originally, µCT was solely used in medical applications, but it has now evolved to be a conventional characterization technique in the material sciences and in industrial applications [74, 76]. A basic schematic of the µCT process is illustrated in Figure 2.14.

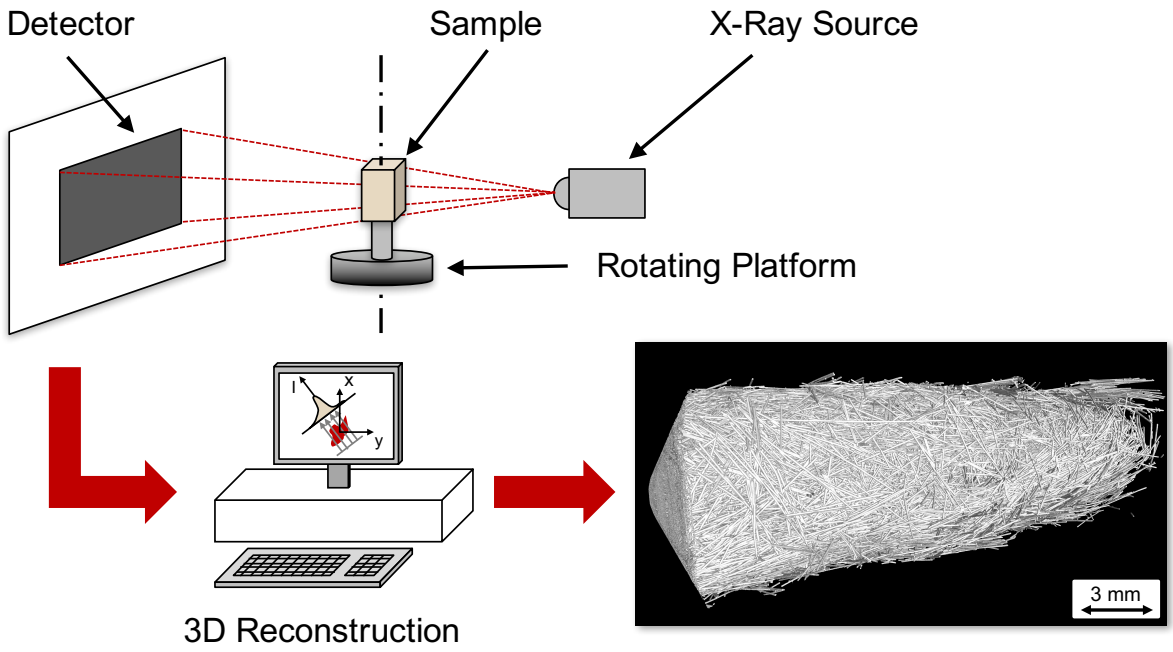

Figure 2.14.: Illustration of X-ray computed-tomography, including a schematic of the µCT setup (top), tomographic reconstruction (bottom left) and a 3D reconstruction (bottom right).

In general, the system consists of an X-ray source, a rotating platform and a detector. The basic principle of µCT is to irradiate a sample with penetrating X-rays, which are attenuated and captured downstream of the object with a detector system creating radiographs. At defined energy levels, the X-ray source irradiates the specimen, which is placed on a rotating platform to achieve a full scan of the sample. The detector records the attenuated X-rays as radiographs at incremental angles during the rotation of the sample. Each captured projection (radiograph) is a two dimensional intensity distribution of the attenuated X-rays. The intensity distribution is directly related to the material's atomic density. A phase of high atomic density within the specimen absorbs more energy than low-density materials.

The X-rays interact with the sample and are attenuated in various ways. For the energy range of the X-rays used in material science, the most relevant mechanisms are Compton scattering and photoelectric effects [74]. Most fundamentally, the attenuation of an X-ray through a sample

can be described by the change in intensity I as

$$dI = -\mu_{eff}(x)I(x)dx \tag{2.11}$$

where μ_{eff} is the effective linear attenuation coefficient and x is the location on the path. Integration of Equation 2.11 along the path C gives

$$-ln\frac{I}{I_0} = \int_C \mu_{eff}(x)dx \tag{2.12}$$

which is also referred to as the Beer-Lambert law. Computing the correct value of μ_{eff} at each position along the path C is the central problem of computed tomography, called tomographic reconstruction. Several approaches and algorithms exist for the reconstruction and the reader is directed to Stock [74] for more detailed information.

After the completion of the 3D reconstruction, the µCT data set can be further processed for qualitative and quantitative analysis of the actual specimen. Different software and algorithms exist to process the µCT images and analyze the fiber orientation distribution. A major challenge in using µCT for fiber orientation analysis is the amount of data that is generated, which has to be post-processed to quantify the orientation. For example, a scan of a 20 x 20 x 3 mm sample at a resolution of 10 µm results into 8 GB of data. There are software packages from the medical field, e.g. Mimics (Materialise NV, Belgium) that can be used for fiber orientation analysis [77]. One of the current market leaders for industrial applications is the software package VG StudioMAX (Volume Graphics GmbH, Heidelberg, Germany), which also has a module for fiber orientation analysis and quantifies the fiber orientation using the structure tensor approach [78]. It was shown that VG StudioMAX provides fast and accurate µCT data analysis currently making it the most commonly used software for fiber orientation measurements [79]. Additionally, research groups frequently develop their own image-processing algorithms to quantify the fiber orientation from µCT scans.

The resolution (voxel size) of the scan is one of the most important parameters that determines the accuracy of the features analysis of scanned samples. However, the trade-off between scan resolution and sample size needs to be considered. In general, finer scan resolutions need samples with smaller dimensions. Although a very fine resolution might be needed for an accurate analysis, a small sample might not fully represent the local orientation, especially for long fiber-filled materials. It has not been established what the minimum resolution might be to perform

an accurate fiber orientation analysis for a specific fiber type. Furthermore, µCT scanning is limited in the case of composite materials with constituents that have similar atomic densities (e.g. carbon fiber-reinforced polyamide) since the contrast of the constituents in the radiograph is low and identifying the fibers can become challenging [80].

Throughout the reported studies, the resolution and sample size used in the microstructure analysis of fiber-reinforced samples vary widely. The sample dimensions range from 3 µm voxel size resolution (sample size: Ø 4 mm disk with a thickness of 4 mm) [81] up to a voxel size of 40 µm (sample size: 40 mm x 40 mm x 30 mm) [82]. Table 2.1 shows an overview of recently published studies focusing on fiber orientation measurements and summarizes the applied imaging technique, sample size and analysis resolution.

Table 2.1.: Overview of fiber orientation measurement techniques applied in recently published studies.

Material	Imaging Technique	Sample Dimensions	Resolution	Reference
PP/GF	µCT	3 x 3 x 3 mm^3	8.0 µm	[83]
PA66/GF	µCT	3 x 3 x 3 mm^3	2.5 µm	[84]
PP/GF	µCT	16 x 16 x 3 mm^3	6.0 µm	[56]
PA6/GF	µCT	4 x 4 x 2 mm^3	1.4 µm	[75]
PA66/GF	µCT	10 x 10 x 2 mm^3	6.5 µm	[85]
PA6/GF	µCT	3.6 x 3.1 x 3.9 mm^3	9.0 µm	[86]
Natural Fibers	µCT	6 x 6 x 3.5 mm^3	7.8 µm	[87]
PP/GF	µCT	n/a	8.1 µm	[88]
PA66/GF	µCT	5 x 20 x (1 to 3) mm^3	6.0 µm	[89]
PP/GF	µCT	Ø 4 mm and 4 mm thickness	3.3 µm	[81]
PA6/GF	µCT	Ø 4 mm and 4 mm thickness	1.8 µm	[90]
PA/GF	µCT	Ø 1.4 mm and 1.4 mm thickness	0.7 µm	[91]
PA6/GF	Cross-sectional polishing and µCT	3.2 x 4 x 15 mm^3	9.0 µm	[80]
PP/GF	Cross-sectional polishing	1.5 x 2 x 1.7 mm^3	0.24 µm	[92]
PP/GF	Cross-sectional polishing	2 x 2 x 0.7 mm^3	n/a	[93]

Bernasconi et al. [80] and Gandhi et al. [77] conducted a comparison between the MoE approach and µCT analysis techniques. Both groups found strong agreement between the two methods. The MoE requires a simpler experimental setup, but is destructive and time-consuming. µCT

offers the great benefit of being nondestructive and providing fast results, but it is a larger capital investment and also requires advanced computing power for post-processing.

2.2.2. Measuring Fiber Concentration

The average fiber concentration of a sample is commonly measured by removing the thermoplastic matrix, either chemically or by pyrolysis, and calculating the weight fraction from the remaining fibers. Due to its simplicity, most authors suggest removing the matrix for glass fiber-reinforced materials by thermal degradation (pyrolysis). Rhode et al. [3] studied the impact of matrix removal by pyrolysis or chemical decomposition on the morphology of single fibers. The results show that performing pyrolysis at 500°C for 2 hours is optimal for a PP sample. Their work indicates that the properties of the glass fibers can change at higher temperatures and the fibers become more brittle. As Rohde et al. pointed out, the increased brittleness can cause additional fiber breakage in handling of the sample. On the other hand, the time needed to completely remove the matrix at lower temperatures is too long to ensure a timely analysis. In other studies, scientists used higher temperatures and different incineration times that ranged from 800°C and 1 h [94] to 530°C and 5 h [48].

The fiber concentration variation in the thickness direction of samples can also be measured by pyrolysis. This approach requires the collection of the material of several layers through the thickness. For each data point along the thickness direction, the sample needs to be prepared by grinding and ashed to determine the fiber density [95]. This measurement procedure is not only cumbersome, but also suffers limitations in terms of sample size, because the part thickness for common injection molded parts ranges between 1 to 4 mm. To obtain sufficient data points (> 10), the ground samples need a thickness between 0.1 and 0.4 mm. On this scale, fiber pull out by the grinding process can cause errors in analysis. Recently, through-thickness analyses were published that used µCT to determine the fiber density [56]. The authors determined the fiber density by calculating the fraction of pixels that represent fibers to the total amount of pixels. The authors found the expected fiber agglomeration in the center of the part, but their values of fiber density (average of 4%vol) are actually off by a factor of two when compared to the expected nominal fiber volume fraction (9%vol).

2.2.3. Measuring Fiber Length

This section reviews the current approaches for characterizing fiber length in SFT and LFT samples. Table 2.2 summarizes the measurement techniques of recently published studies. The majority of the approaches share four main steps. First, a sufficiently large sample is extracted from the part and the matrix material is removed by pyrolysis (matrix removal). Second, a subset of the fibers is selected and prepared to be scanned (down-sampling and fiber dispersion). In the third step, a digital image is created using either a microscope or an optical document scanner (digital imaging). Finally, the digital image is analyzed using image processing software to determine the length of individual fibers (fiber detection). The detection of the fibers is done either manually by clicking on the endpoints of fibers or with the support of (semi-) automated image-processing algorithms.

Table 2.2.: Overview of fiber length measurement techniques used in recently published studies for glass fiber-reinforced (GF) and carbon fiber-reinforced (CF) samples.

Material	Correction for Downsampling	Fiber Dispersion	Fiber Detection	Fibers per Sample	Reference
SFT	No	Diluted suspension	Manual	360±60	[96]
PP/GF	No	Manual dispersion	Manual	100	[97]
PP&PA12/GF	No	Manual dispersion	Manual	300	[98]
PP/GF	No	Manual dispersion	Manual	500	[6]
PP/GF	No	Manual dispersion	Manual	500	[99]
PP/GF	No	Manual dispersion	Manual	500	[70]
PP/GF	No	Manual dispersion	Manual	500	[100]
PP/GF&CF	Yes	Manual dispersion	Manual	2000	[61]
PP/GF&CF	Yes	Manual dispersion	Manual	2000	[101]
PA6/GF	No	Diluted suspension	Manual	400	[94]
PA6/GF	No	Diluted suspension	Manual	400	[102]
PA6/GF	No	Diluted suspension	Manual	1000	[48]
PP/GF	No	Diluted suspension	Manual	1000	[21]
GF	No	Manual dispersion	Semi-automatic	1000	[103]
PP/GF	No	Diluted suspension	Semi-automatic	800	[104]
PP/GF	No	Diluted suspension	Semi-automatic	2000	[105]
PP/GF	No	Diluted suspension	Semi-automatic	2000	[106]
PP/GF	Not needed	Diluted suspension	Semi-automatic	2000	[3]
PP/GF	Not needed	Diluted suspension	Semi-automatic	3000	[107]
PP/GF	No	Manual dispersion	Automatic	1000	[108]

For short fiber-filled materials, the International Organization for Standardization (ISO) defined a standard for fiber length measurements (ISO:22314) [96]. The matrix removal is done by pyrolysis at 625°C for 1.5 h and the fiber dispersion is performed by mixing the fibers in water using ultrasound instead of any mechanical action. After completely drying the suspension,

300±60 randomly picked fibers are measured manually with a microscope or stereoscope. The standard states that this measurement technique is only applicable to short fiber-reinforced materials. Although this standard exists, only one publication was found that specifically analyzed the fiber length according to this standard and cited it [109]. Nevertheless, most measurement procedures in the field are similar to the ISO:22314 standard.

The practice of using a liquid to disentangle and disperse the fibers after pyrolysis is applied by the majority of measurement techniques (Table 2.2). The fibers are placed in a liquid and mixed either manually [107] or using ultrasound [3, 21]. After mixing and dispersing the fibers, a fraction of the suspension is separated and used to generate digital images. Various liquids are sometimes combined with dispersion agents by research groups to improve the dispersion of fibers. Some researchers use untreated water [21], while others add a detergent [110] or glycerine [94] to promote fiber dispersion.

To some degree, the fiber detection step can be supported by image processing software. However, only a few programs can perform a fully automatic recognition of fibers due to intersecting or curved fibers, which is a particular challenge for LFT samples. Semi-automatic image processing algorithms are capable of detecting the length of isolated fibers with no or little curvature [3, 107, 108]. Nevertheless, semi-automatic image processing algorithms still require manual input from the operator to isolate single fibers in clusters. In the majority of the reported studies, the fiber detection is still done completely manually by clicking the endpoints of fibers (see Table 2.2).

Almost all published work on fiber length measurements applies a down-sampling step to decrease the amount of fiber that needs to be measured from more than a million fibers in the original sample to less than 3000 fibers. However, the downsampling step is one of the major factors influencing the accuracy of the obtained results. Kunc and Nguyen [61, 101] described the impact of downsampling on skewing the obtained fiber length distribution and they suggest a defined downsampling concept that ensures statistically representative results for a subset of the fibers. After pyrolysis, an epoxy resin is injected in the center of the dry fibers using a thin needle. The deposited epoxy forms a cylindrically-shaped plug through the entire thickness of the fiber bed. The epoxy is cured and all fibers embedded within the so-called epoxy plug will be measured. The remainder of the fibers that are not bound to the epoxy plug are gently removed by a brush and discarded. A second pyrolysis is necessary to remove the epoxy plug and free the fibers for the dispersion step. It is important to note that any downsampling skews the obtained

results, including the epoxy plug procedure. Nevertheless, this bias in the obtained results can be accounted for if a defined downsampling procedure is used by applying a geometrical correction equation proposed by Kunc and Nguyen [61, 101]. The proposed correction accounts for the fact that relatively more long fibers are selected during downsampling than short fibers due to the small area of the epoxy plug (downsampling area) [61] .

FASEP (Karg Industrietechnik, Krailling, Germany) is a commercially available fiber length measurement system, which can also be used for LFT materials [107]. After pyrolysis, the fibers are mixed in a solution of water and glycerin. The suspension is then placed in an ultrasonic bath to disentangle and disperse the fibers. Subsequently, a set of diluting steps is performed by adding more water and glycerin. Combined with gentle stirring, the fibers are uniformly dispersed in a highly diluted mixture. Finally, small portions of the liquid are extracted randomly with a pipette into a petri dish to create a digital image of the sample. The scanned image is analyzed with a customized module of the image analyzing software Image-Pro Plus (Media Cybernetics, Inc., Rockville, USA), which can detect most fibers semi-automatically. Completely isolated fibers can be detected automatically, but any intersecting fibers or fiber clusters require user input. The supplier recommends measuring at least 2000 fibers by repeating the extraction of additional samples from the diluted suspension.

Although not every publication in Table 2.2 describes the measurement approach in detail, there are significant differences in the fiber dispersion and fiber detection steps. Also, the amount of measured fibers varies from 100 to 3000. The selection of the subsample is mostly done manually by collecting random fibers using tweezers. The fiber dispersion is achieved by either mixing the dry fibers into a suspension, similar to ISO:22314, or by manually spreading the fibers using brushes or tweezers. In the majority of the publications, the detection of the fibers is done by hand and only some report a (semi-) automatic solution using image processing algorithms. Most studies focused on fiber breakage in glass fiber (GF) filled composites, but a few also measured the length distribution in carbon fiber (CF) filled materials [61, 101].

The large variation in important aspects of the measurement techniques calls into question the comparability, repeatability and accuracy of the different studies. Reported results and measured fiber lengths can even differ by a factor of two due to the measurement technique, which was pointed out by the European Alliance for Thermoplastic Composites (EATC) in a call for a new standardized fiber length measurement technique [111]. The fiber length distribution obtained from the collection and downsampling of fibers is necessarily skewed and does not accurately

represent the local fiber population [61]. Additionally, too much manual handling of the fibers with tweezers, spatulas or similar tools will result in the loss of very short fibers and/or the breakage of longer fibers. Lastly, the amount of analyzed fibers can vary by more than an order of magnitude and it is questionable whether a set of 1000 or fewer fibers can be statistically representative of the local fiber length distribution of the sample. Lastly, repeated measurements are rarely performed or reported. Hence, little-to-no information about the measurement variation is available.

2.3. Modeling and Simulation of the Fiber Configuration

Over the last few decades, the ability to predict the process-induced microstructure properties of LFT materials has improved significantly. Particularly, fiber orientation predictions show a robust degree of reliability for simpler geometries and are routinely used in the part or mold design process to account for the process-induced anisotropy. Although modeling approaches exist to predict fiber length and fiber concentration for injection molding, these models are still in development and lack a comprehensive validation for LFT injection molding [112, 113]. The modeling approaches of fiber breakage, fiber alignment and fiber matrix separation are commonly addressed as individual mechanisms and are treated completely isolated.

2.3.1. Rotary Diffusion Model for Fiber Orientation Prediction

Folgar and Tucker [35] proposed a phenomenological model that describes the fiber alignment in concentrated suspensions as a diffusion type mechanism driven by the interactions between fibers. The Folgar-Tucker model is an expansion of Jeffery's model [37], which describes the motion of an ellipsoid in a dilute suspension assuming no interactions. Jeffery's pioneering work provides the basis for modeling the motion of ellipsoidal particles in viscous fluids. In tensor representation [42], Jeffery's equation is

$$\frac{D\boldsymbol{a}_{ij}}{Dt} = -\frac{1}{2}(\boldsymbol{\omega}_{ik}\boldsymbol{a}_{kj} - \boldsymbol{a}_{ik}\boldsymbol{\omega}_{kj}) - \frac{1}{2}\lambda_s(\dot{\boldsymbol{\gamma}}_{ik}\boldsymbol{a}_{kj} - \boldsymbol{a}_{ik}\dot{\boldsymbol{\gamma}}_{kj} - 2\dot{\boldsymbol{\gamma}}_{kl}\boldsymbol{a}_{ijkl}) \tag{2.13}$$

where $\boldsymbol{\omega}_{ij}$ is the vorticity tensor, $\dot{\boldsymbol{\gamma}}_{ij}$ is the rate of strain tensor, $\dot{\gamma}$ the shear rate, and λ_s is the particle shape factor. For large aspect ratio particles, such as fibers, λ computes to 1 [9]. The fourth order orientation tensor is $\boldsymbol{a_{ijkl}}$, which is approximated from the second order orientation tensor $\boldsymbol{a_{ij}}$ using closure approximations [42].

Folgar and Tucker observed that fibers show less alignment in the flow direction than estimated by Jeffery's model. They assumed that the orientation kinetics are still described by the hydrodynamics in Jeffery's equation while the fiber interactions cause a randomizing effect to the fiber orientation. Hence, they added an isotropic rotary diffusion term to Jeffery's model accounting for the orientation kinetics in concentrated suspension and the effect of interactions between the fibers. The governing equation of the Folgar-Tucker model is

$$\begin{aligned} \frac{D\boldsymbol{a}_{ij}}{Dt} &= -\tfrac{1}{2}(\boldsymbol{\omega}_{ik}\boldsymbol{a}_{kj} - \boldsymbol{a}_{ik}\boldsymbol{\omega}_{kj}) - \tfrac{1}{2}\lambda_s(\dot{\boldsymbol{\gamma}}_{ik}\boldsymbol{a}_{kj} - \boldsymbol{a}_{ik}\dot{\boldsymbol{\gamma}}_{kj} - 2\dot{\boldsymbol{\gamma}}_{kl}\boldsymbol{a}_{ijkl}) \\ &\quad +2C_I\dot{\gamma}(\boldsymbol{\delta}_{ij} - 3\boldsymbol{a}_{ij}) \end{aligned} \tag{2.14}$$

The impact of fiber interactions on orientation is governed by a phenomenological interaction coefficient, C_I, and scales linearly with the magnitude of the shear rate $\dot{\gamma}$. The model parameter C_I is assumed to be an intrinsic property of the material (matrix, fiber concentration, fiber length, fiber diameter) [35]. The addition of the isotropic rotary diffusion term to Jeffery's model is strictly phenomenological and not based on the underlying physics. Hence, the value of C_I must be obtained from measurements. Large values of C_I reflect increased interactions in the suspension and will result in a more randomized steady orientation state, whereas a small C_I implies fewer interactions leading to a more preferential orientation. If C_I is zero, Equation 2.14 becomes Jeffery's original equation and the fiber motion is merely driven by hydrodynamics.

Several additions have been made since the original rotary diffusion model was proposed in 1984 to account for experimentally observed mechanisms that the original Folgar-Tucker model cannot account for. Experimental results showed that the fiber orientation develops slower than predicted while the steady state orientation agreed well. To overcome the discrepancies in the transient stage, Wang and Tucker [114] added a second fitting parameter (κ) that slows down the orientation evolution, referred to as the Reduced Strain Closure (RSC) model.

Simulation results for compounds using longer fibers also showed larger deviations from measurements. Phelps and Tucker suggest the longer fibers cause an anisotropic rotary diffusion, as opposed to the isotropic diffusion of the original Folgar-Tucker model. They introduced a new model, the anisotropic rotary diffusion model (ARD), which describes the fiber-fiber interaction coefficient as second order tensor instead of a scalar to account for the anisotropy in the interaction. The ARD model has five fitting parameters that need to be obtained from experimental data and require additional testing for numerical stability or non-physical behavior [9, 32]. Tseng et al. [32] proposed an improved ARD model (iARD) to overcome the complexity in parameter

fitting. They condensed the ARD model to a two parameter model and overcame the numerical instability. The RSC model can be added to both the ARD model and iARD model to slow down the orientation evolution, which adds an additional fitting parameter to the models [9, 32].

2.3.2. Suspension Balance Model for Fiber Migration Prediction

Different theoretical models to describe particle migration in concentrated suspensions have been proposed. For a comprehensive literature review of particle migration in concentrated suspensions, the reader is referred to [33]. Leighton and Acrivos [115] suggested a diffusive flux model, which describes the shear-induced particle migration as a result of irreversible particle collisions. This kinematic modeling approach expresses the migration as gradients of particle concentration and shear rate, but it neglects normal stress differences. Nott and Brady [58] proposed a suspension balance model. This model is a two-phase approach describing the particle phase and suspension separately while incorporating a constitutive model to solve particle and suspension stresses. The particle transport is driven by gradients in these stresses. The basic principle of the modeling approach is illustrated in Figure 2.15. Morris and Boulay [116] expanded the suspension balance model to account for anisotropic migration.

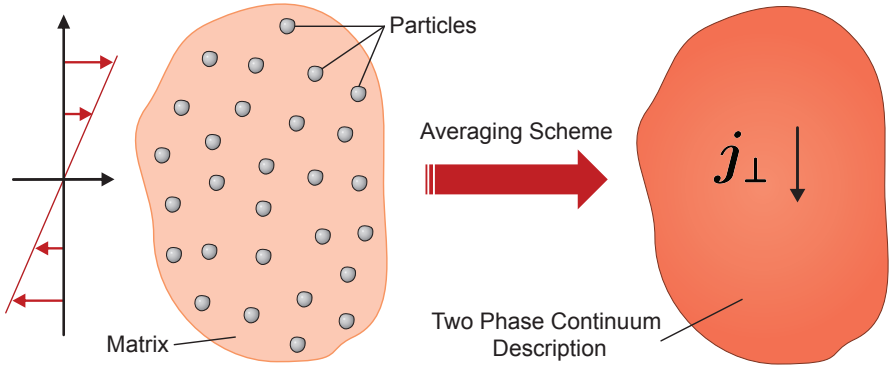

Figure 2.15.: Continuum description of suspension obtained by averaging the discrete phases and the shear-induced particle flux $\boldsymbol{j}_\perp$. Adapted from [57].

The Morris and Boulay suspension model was recently implemented in commercial injection molding simulation software (Moldex3D$^{\text{TM}}$, CoreTech Systems, Taiwan). Using this three-dimensional (3D) finite volume method (FVM) solver, the fiber concentration in an injection molded part can be simulated. The suspension model expresses the conservation of the particle-phase mass balance as

$$\frac{\partial \phi}{\partial t} + \langle \boldsymbol{u} \rangle \cdot \nabla \phi = -\nabla \cdot \boldsymbol{j}_\perp \tag{2.15}$$

$$\boldsymbol{j}_{\perp} = \phi \left(U_p - \langle \boldsymbol{u} \rangle \right) \tag{2.16}$$

where ϕ is the particle mass fraction, $\langle \boldsymbol{u} \rangle$ is the suspension average velocity, $\boldsymbol{j}_{\perp}$ is the particle flux relative to the mean suspension motion, and U_p is the average velocity of the particulate phase. Assuming low Reynolds numbers and a neutrally buoyant condition, the particle flux $\boldsymbol{j}_{\perp}$ can be calculated as

$$\boldsymbol{j}_{\perp} = \frac{2a^2}{9\eta_m} f(\phi) \nabla \cdot \sum_p \tag{2.17}$$

where a is the particle radius, η_m the viscosity of the suspending fluid, $f(\phi)$ is the sedimentation function and $\sum_p$ is the particle stress tensor [116]. According to the original work of Richardson and Zaki [117], the sedimentation function can be estimated by

$$f(\phi) = (1 - \phi/\phi_{max})(1 - \phi)^{n-1} \tag{2.18}$$

The parameter n is the index of particle friction and ϕ_{max} is the maximum volume fraction. The parameter n is assumed to be a material-dependent coefficient and can be obtained from experimental data [36].

Morris and Boulay [116] originally derived the two phase suspension model for spherical particles and tested it for simple flow conditions under isothermal conditions. Recently, Tseng et al. [36] adapted the suspension balance model to be used for simulating fiber matrix separation in injection molding. The adapted model for concentrated fiber suspension includes the calculation of an effective particle radius based on work published by Fan et al. [118]. The effective particle radius, a_e, is calculated by

$$a_e = \frac{d_f}{2} \left(\frac{3\, l_f}{4\, d_f} \right)^{1/3} \tag{2.19}$$

where d_f is the fiber radius and l_f is the length of the fiber.

Tseng et al. [36] simulated the fiber migration for a short fiber-reinforced PBT with the adapted two phase suspension model using Moldex3D$^{\mathrm{TM}}$. Their results suggest that the model can qualitatively predict the tendency of the process-induced fiber concentration in the molded part. However, there are still quantitative discrepancies in the through-thickness prediction of the fiber concentration. Also, their work does not address the relevance of the suspension model's fitting parameters nor how to obtain appropriate values of these parameters for fiber-reinforced thermoplastics.

2.3.3. Modeling Fiber Breakage Prediction

The Phelps-Tucker model [5] is a phenomenological model to predict fiber breakage during processing of discontinuous fiber reinforced composites. The model is currently the only fiber breakage model implemented in commercially available simulation package for injection molding (e.g. Moldex3D^{TM} and Autodesk Moldflow®). The fundamental assumption of the Phelps-Tucker model is that the failure mechanism for fiber breakage during processing is buckling. The total length of all fibers in the domain stays constant and is governed by a basic conservation equation:

$$\frac{dN_i}{dt} = -P_i N_i + \sum_k R_{ik} N_k \tag{2.20}$$

where N_i represents the number of fibers of length l_i. The change of the fiber length distribution is computed by the reduction of fibers in N_i at the breakage rate P_i and the growth of fibers in N_k (child generation) at a rate R_{ik}. Phelps et al. assume that the breakage rate P_i is a function of the material properties and the flow conditions. They define a dimensionless variable B_i that describes the buckling state of the fibers:

$$B_i = \frac{4\,\zeta\,\eta_m\,\dot{\gamma}\,l_i^4}{\pi^3\,E_f\,d_f^4} \tag{2.21}$$

where ζ is a dimensionless drag coefficient, η_m the viscosity of the polymer matrix and $\dot{\gamma}$ is the magnitude of the rate-of-deformation tensor. E_f is the elastic modulus of the fiber and d_f is the diameter of the fiber. Depending on the flow conditions and material properties, a fiber can break due to buckling, described by

$$P_i = \begin{cases} 0 & \text{for } B_i < 1 \\ C_B\dot{\gamma}\,[1 - \exp(1 - B_i)] & \text{for } B_i \geq 1 \end{cases} \tag{2.22}$$

where C_B is the breakage coefficient and fitting parameter for the model. If B_i is less than unity, the flow conditions cannot cause fiber failure.

The child generation rate R_{ik} in Equation 2.20 is computed by

$$R_{ik} = \alpha_k\, N_{PDF}\left(l_i, \frac{l_k}{2}, S\,l_k\right) \tag{2.23}$$

where N_{PDF} is the normal probability density function for the variable l_i with mean $l_k/2$ and

standard deviation $S\,l_k$. The scale factor a_k normalizes R_{ik} to satisfy the conservation equation (Equation 2.20). This probabilistic modeling of the child generation aims to account for inconsistencies of the fibers and the effects of fiber-fiber interactions and allows non-zero probabilities for breakage along the entire fiber.

The model has three empirical model parameters that need to be obtained through experimental data: breakage coefficient (C_B), the hydrodynamic drag coefficient (ζ) and the distribution shape factor (S). At this point, no protocol exits on how the parameters are obtained from experimental data and Phelps et al. [5] merely give a range of values for which the three fitting parameters are physically reasonable: $C_B \ll 1.0$, $\zeta \sim 1$, and $S \sim 1$. This limits the application of the model as a predictive tool and design engineers are often referred to default values (e.g. in Moldex3D$^{\text{TM}}$, the recommended default values are: C_B = 0.002, ζ = 3 and S = 0.25 [119]). However, it is questionable if reasonable results can be obtained for all fiber/matrix combinations by using default model parameters. Phelps et al. state that their model is promising, but requires additional work to completely incorporate the underlying mechanism that causes fiber breakage. In particular, fiber-fiber interactions are not explicitly accounted for in the theoretical framework of the model, but are an important factor for any industrially relevant fiber-filled material.

3. Development and Validation of Characterization Techniques

The characterization and quantification of the process-induced fiber configuration in molded samples is of utmost importance so that accurate experimental data can be obtained and theoretical models can be developed and validated. Although fiber properties have been measured in the past, there is a lack of defined standards and measurement approaches vary between research groups, as discussed in the previous chapter. In this work, new measurement techniques were developed to ensure an accurate, repeatable and efficient characterization of the three main microstructural properties: **fiber length**, **fiber orientation**, and **fiber concentration**. This chapter presents and discusses the developed measurement techniques and shows the outcome of comparative studies with conventional characterization protocols.

3.1. Fiber Orientation Measurement Concept

The key challenge in using µCT for fiber orientation analysis is the image processing of the data required to quantify the orientation of the fibers. Due to the large size of the data sets, there can be computational limitations to the post processing procedure [77]. As part of this work, a novel image processing method that uses basic geometric optics is introduced, rendering this approach an efficient and accurate algorithm. The initial algorithm was proposed by Osswald et al. in 2003 [120] and, here, it is expanded and adapted to analyze the fiber orientation from µCT data.

The algorithm was derived from the single-slit Fraunhofer diffractometer theory, which describes the diffraction of waves through a slit onto a projection at a long distance from the diffracting object. The slit method (SM) algorithm neglects diffraction effects assuming a simple geometric projection of an image through a slit. Figure 3.1 illustrates the basic principle of the SM algorithm. The input image contains two fibers that are projected through a slit onto a virtual

projection plane. The projection of the fibers casts a shadow, where the shape and intensity of the shadow depend on the orientation of the fiber relative to the slit. By rotating the slit, an intensity distribution of the projections as a function of slit orientation can be obtained. This intensity distribution is directly related to the orientation distribution of the fibers in the image.

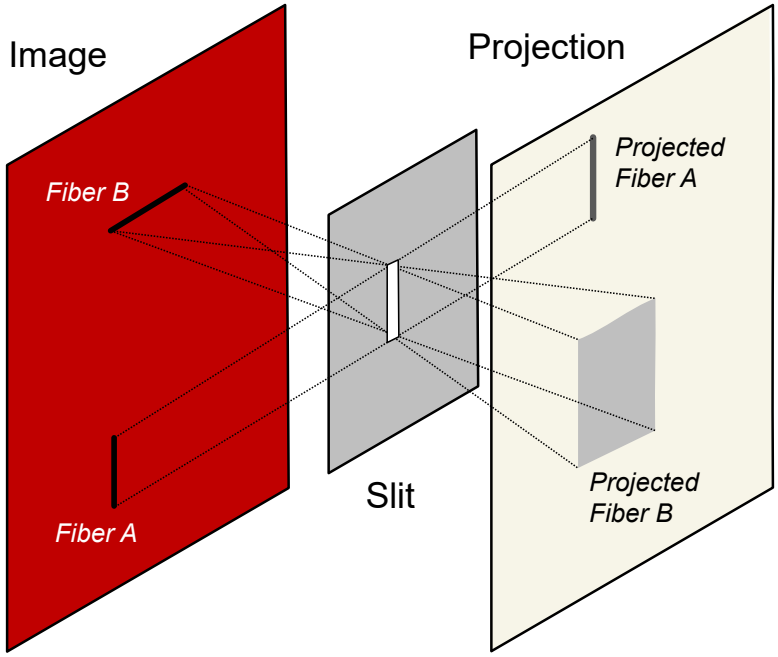

Figure 3.1.: Schematic of the SM algorithm principle: two fibers are projected through a slit. Adapted from [120].

The SM algorithm is implemented in MATLAB^{TM} (The MathWorks Inc., MA, United States) for the numerical slit projection of µCT images to obtain the fiber orientation distribution. The µCT data set is exported to a stack of 2D grayscale images, which are converted to binary images by applying a global threshold. The SM algorithm numerically projects each pixel $p(x_i, y_j)$ with non-zero entries (fiber) through the slit at defined angles ϕ_S. The slit has a defined length L_S and a width of one pixel. The length L_S of the slit varies depending on the resolution and quality of the image. The mapping of a pixel $p\,(x_i, y_j)$ through the slit onto the virtual projection plane g can be defined by

$$p\,(x_i, y_j) \rightarrow g\,(\sigma, \tau) \tag{3.1}$$

where σ and τ are the coordinates of the projections in g. The projections in g are aligned with the slit orientation and comprise all pixels between the end points of the projection defined as $(\sigma_u,\, \tau_u)$ and $(\sigma_l,\, \tau_l)$. The slit projection of $p\,(x_i, y_j) \rightarrow g\,(\sigma, \tau)$ is illustrated in Figure 3.2 (left).

The variables σ_u and τ_u are computed by

$$\begin{cases} \sigma_u = x_i + \frac{1}{2} L_S \cos(\phi_s) \\ \tau_u = y_i + \frac{1}{2} L_S \sin(\phi_s) \end{cases} \tag{3.2}$$

and σ_l and τ_l are calculated as

$$\begin{cases} \sigma_l = x_i - \frac{1}{2} L_S \cos(\phi_s) \\ \tau_l = y_i - \frac{1}{2} L_S \sin(\phi_s) \end{cases} \tag{3.3}$$

The projections of all pixels, $p(x_i, y_j)$ at a defined slit angle ϕ_S are superposed, resulting in an intensity field, $G(\phi_S)$, of the projection through the slit at angle ϕ_S:

$$G(\phi_S) = \sum g(\sigma, \tau) \tag{3.4}$$

$G(\phi_S)$ directly relates to the orientation of the fibers in the input image with respect to the slit orientation. This principle is depicted in Figure 3.2 (right), illustrating projections for a fiber at slit orientations of 0°, 45°, and 90°.

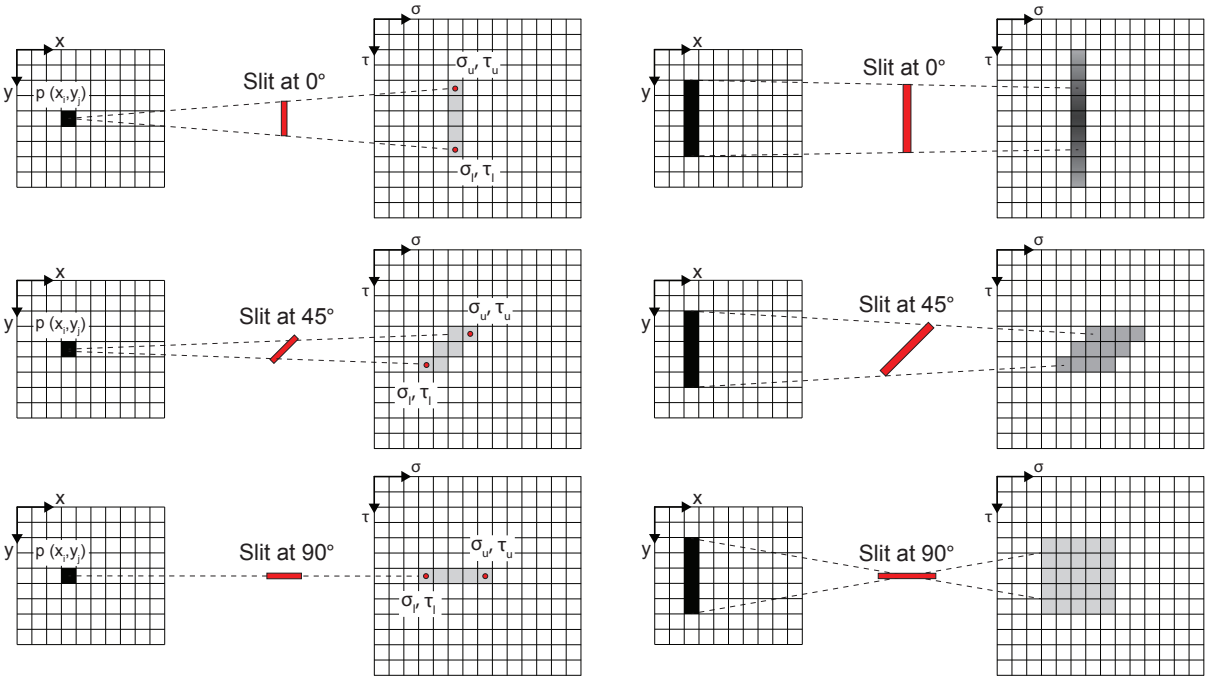

Figure 3.2.: Illustration of the slit projection: Projection of a single pixel (x_i, y_i) (left) and projection of a fiber (right) at 0°, 45° and 90° (inverted gray values for visualization).

The procedure is repeated for all slit angles from 0 to π, generating a spectrum of intensity fields at defined angles. The low intensity entries in $G(\phi_S)$ are removed by applying a global threshold (noise removal), which depends on the resolution of the image and contrast between fiber and matrix of the original µCT data set. Summing the entries of the intensity field $G(\phi_S)$ computes the frequency of fibers oriented at ϕ_S, denoted by

$$n(\phi_S) = \sum_{\sigma=0}^{m} \sum_{\tau=0}^{n} G(\phi_S) \tag{3.5}$$

The final fiber orientation distribution $N(\phi)$ after normalization

$$N(\phi) = \frac{n(\phi_S)}{\sum_{\phi_S=0}^{\pi} n(\phi_S)} \tag{3.6}$$

The developed SM algorithm quantifies the 3D fiber orientation by processing a set of two image stacks from the same µCT data set oriented perpendicularly. From the two image stacks, the orientation distributions for each angle ϕ and θ is obtained as illustrated in Figure 3.3. Subsequently, the orientation density distribution $\Psi(\phi, \theta)$ is generated by mapping the distributions to the defined coordinate system of the µCT data set and the orientation tensor can be calculated as shown in Chapter 2.1.1.

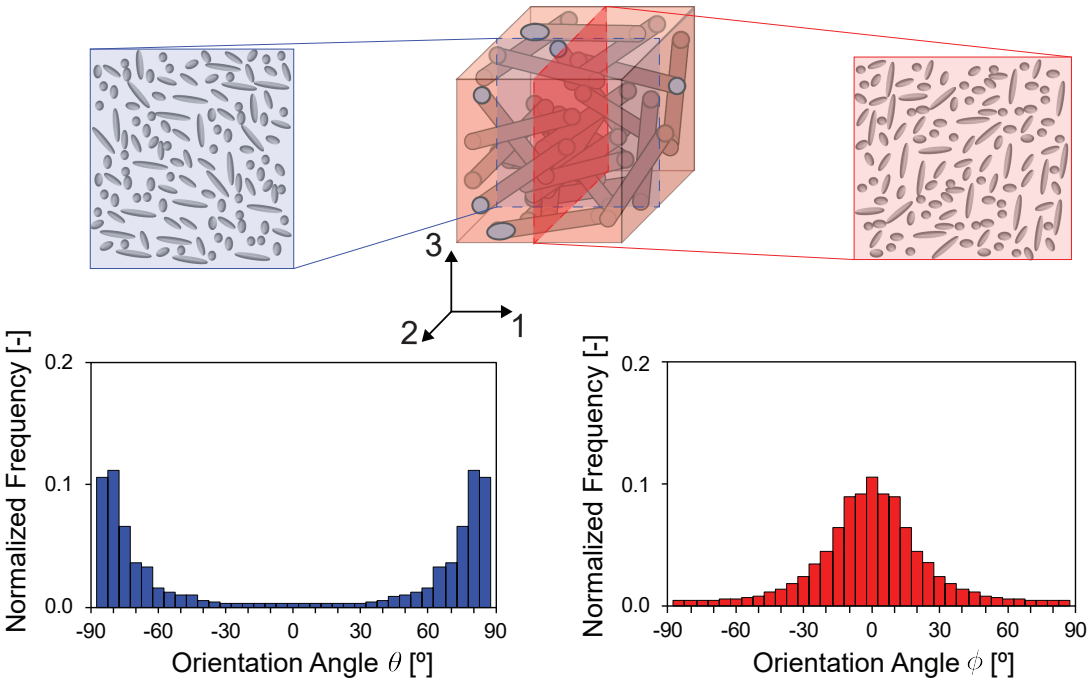

Figure 3.3.: Illustration of the SM algorithm obtaining the 3D fiber orientation by computing the fiber orientation distribution for ϕ and θ from two image stacks oriented perpendicularly.

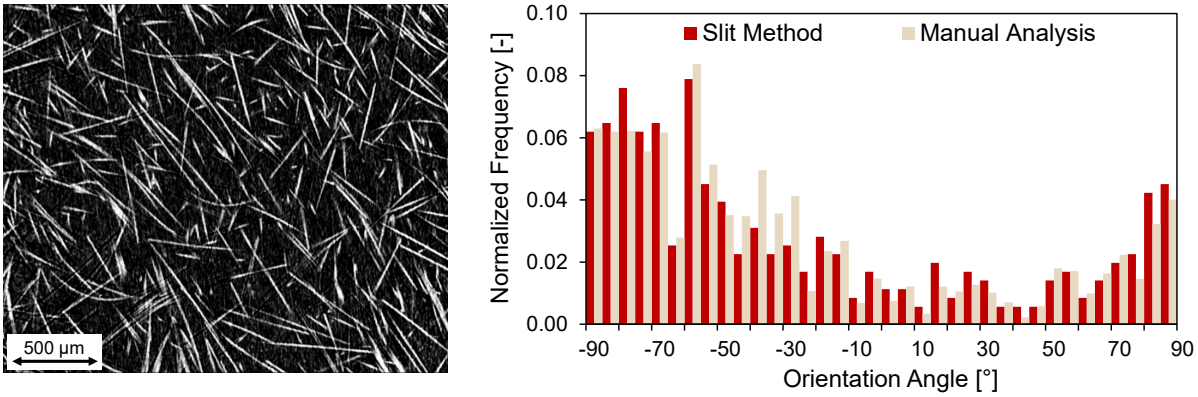

Figure 3.4.: 2D slice from a µCT data set (left) and the measured fiber orientation distribution obtained manually and from the SM algorithm (right).

The SM algorithm was validated by comparing its output to manual fiber orientation measurements of 2D slices from µCT scans. For the manual measurement, each fiber in the digital image was detected by clicking the endpoints using a developed MATLAB tool. The outcome was then compared with the results from the SM algorithm. Figure 3.4 shows the outcome of the comparison for a 2D slice of a 30%wt fiber-reinforced polypropylene sample. The scan has a spatial resolution of 6 µm to avoid any errors due to lack of resolution and to easily identify single fiber filaments. The results show that the SM algorithm accurately determines the fiber orientation distribution with a discrepancy of less than 5% when compared to the manual analysis.

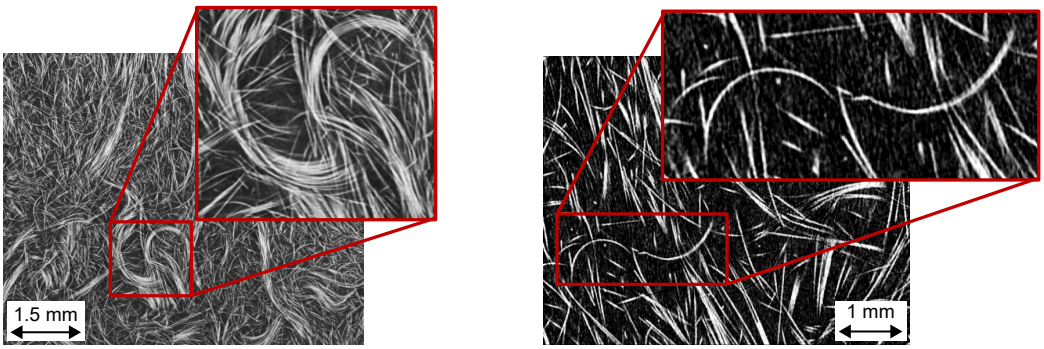

Figure 3.5.: Curvature in LFT parts illustrated in selected µCT images: 40% glass fiber-reinforced PP (left) and 30% glass fiber-reinforced PBT (right).

It is commonly assumed that fibers are perfectly straight [35, 42]. For short fiber compounds, this assumption might be permissible, but the fibers in LFT compounds can have substantial curvature, as shown in Figure 3.5. While the majority of the fibers shown in Figure 3.5 are straight, there are several fibers that show a substantial curvature and waviness. Depending on the material and process, fiber curvature can be very significant [77]. The fiber curvature observed in LFT materials and its implication for the material modeling and structural anal-

ysis was discussed recently by Kunc et al. [121]. However, the impact of fiber curvature on measurement techniques has not yet been addressed.

In order to illustrate the effect of curvature on the obtained fiber orientation distribution using the developed SM algorithm, an arbitrary curved fiber is defined as shown in Figure 3.6 (left). The image is processed with the SM algorithm and compared to a manually measured orientation of the discretized fiber. For the manual measurement, the length of the curved fiber was approximated by discretizing the curvature with straight lines, as illustrated in Figure 3.6 (right).

Figure 3.6.: Arbitrary curved fiber (left) and illustration of the discretized fiber (right).

Figure 3.7 shows the results obtained using the SM method for the curved fiber and the manual measurement of the discretized fiber. The orientation distribution clearly shows five discrete peaks from the discretized approximation. The SM algorithm generates a continuous orientation distribution with peaks at the same orientation as obtained from the manual discretization. Calculating the orientation tensor for the obtained fiber distribution, the discretized measurements result in $a_{11} = 0.78$ and the SM algorithm computes $a_{22} = 0.75$. For a fiber population, the continuous distribution is a more accurate description of the orientation of curved fibers compared to the simplifying assumption of straight fibers in conventional measurement techniques.

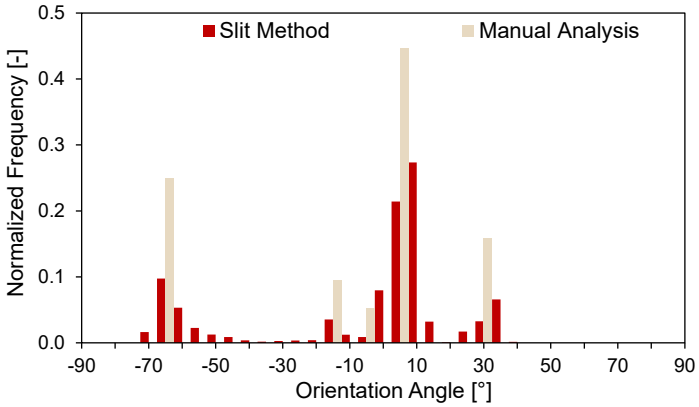

Figure 3.7.: Orientation distribution of arbitrary curved fiber obtained with the SM algorithm and by manually measuring the discretized approximation.

3.1.1. Validation and Comparative Study

A comparative study of fiber orientation measurement techniques was performed comparing the conventional Method of Ellipses (MoE, see Chapter 2.2.1) and µCT analyses. Two injection molded samples (samples A and B) with dimensions of 5 x 5 x 2.85 mm^3 were extracted from the center of an injection molded plate (40%wt glass fiber-reinforced PP). The samples were first scanned at 5 µm and then analyzed using the MoE[1].

Table 3.1.: Overview of fiber orientation measurement techniques for a comparative study.

	MoE	**Mimics**	**VG StudioMAX**	**SM Algorithm**
Imaging Technique	Cross-section polishing and microscopy	µCT	µCT	µCT
Detection	Single fiber (Elliptical cross-section)	Single fiber (Centerline fitting)	Fiber population (Structure tensor [78])	Fiber population (Numerical projections)
Destructive	Yes	No	No	No
Required Resolution	Very fine (0.24 µm)	Less than 1/6 of fiber diameter	Less than fiber diameter	Less than fiber diameter

The µCT data sets were analyzed with three different image processing algorithms. Besides the developed SM algorithm, the commercial software VG StudioMAX 3.0 (see Chapter 2.2.1) and a proprietary analysis tool developed by SABIC and Materialise NV (Leuven, Belgium) were used. The latter is a customized module for the image processing software Mimics Innovation Suite, henceforth referred to as Mimics[2]. The module identifies single fibers in the 3D µCT data set and fits centerlines along the axis of each fiber. From the fitted centerlines, Mimics computes the fiber orientation distribution and the orientation tensor. This approach requires a very fine voxel size since individual fibers in the scan need to be segmented. Although a 5 µm scan resolution provides sufficiently high resolution to separate the fibers, the developer suggests a resolution of less than one sixth of the fiber diameter. The fiber diameter of the scanned sample is 19±1 µm, making the optimal voxel size 3.2 µm or less for use in Mimics. The main characteristics of the four analysis tools are summarized in Table 3.1.

Figure 3.8 shows the obtained fiber orientation results for Sample A (the tensor components a_{11} and a_{22} are shown in two separate graphs for clarity). The results suggest that all measurement

[1]The fiber orientation analysis using the Method of Ellipses was performed by Hongyu Chen and Prof. Donald Baird at the Department of Chemical Engineering, Virginia Polytechnic Institute and State University.

[2]The fiber orientation analysis with Mimics was performed by Chanjuan Liu at SABIC Analytical Technology Department.

techniques show good agreement, particularly in the transition region from the core to the shell layers.

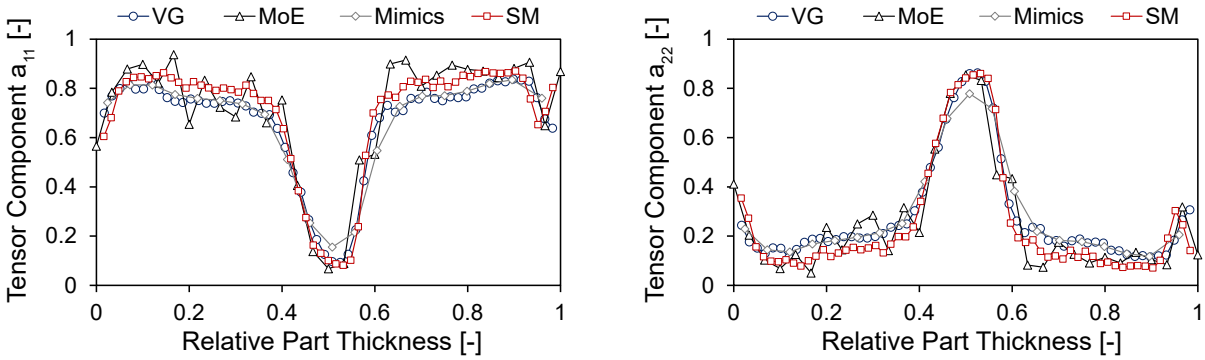

Figure 3.8.: Results of the fiber orientation analyses of Sample A for all four measurement techniques: Tensor components a_{11} (left) and a_{22} (right).

Figure 3.9 shows the fiber orientation results of Sample B. Similar to Sample A, the results suggest the measurement techniques match well. Some discrepancies can be seen in results obtained with the MoE technique in the core layer, indicating some irregularities in the measurements at a relative thickness of 0.45. These irregularities might be attributed to the fact that the increments in polishing and cross-section inspection are performed in coarser steps compared to the µCT analyses. Also, the surface edging required to overcome the ambiguity of the angle detection [55] might not fully work in the fiber-dense core layer.

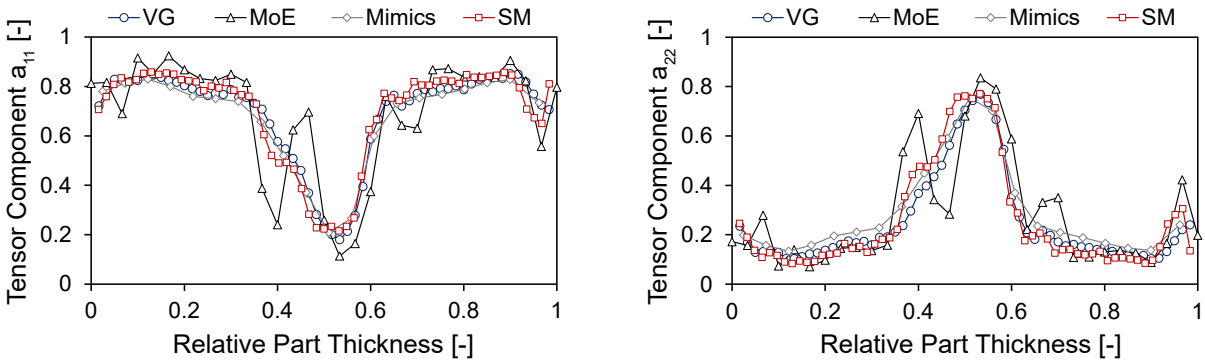

Figure 3.9.: Results of the fiber orientation analyses of Sample B for all four measurement techniques: Tensor component a_{11} (left) and a_{22} (right).

The outcome of the comparative study is that the measurement techniques show strong agreement in the results. In particular, the different analysis tools for µCT scans quantify matching fiber orientation distributions. Although the actual scan resolution for Mimics is larger the recommended value (1/6 of fiber diameter = 3.2 µm), the results agree well with VG StudioMAX 3.0 and the developed SM algorithm. Slight differences in the MoE technique might be caused by the coarser through-thickness resolution. Hence, fewer data points through the thickness are avail-

able due to the more time-consuming steps of polishing, sample edging and image capturing of this technique.

Overall, this comparative study shows the advantages of µCT as a non-destructive and time efficient methodology for fiber orientation analysis. However, the processing of the µCT data is critical and not trivial. While the analysis tools in comparative study agree well, the outcome of the fiber orientation analysis is dependent on the appropriate selection of the image processing algorithm. The developed SM algorithm provides an accurate and time-efficient analysis to quantify the fiber orientation from µCT. Although the SM algorithm has not been optimized in terms of computational efficiency, it already provides a fast analysis with an average 30 min computation time compared to VG StudioMAX 3.0 (15 min) and Mimics (45 min).

3.1.2. Impact of Voxel Size on Fiber Orientation Measurements

In this dissertation, all of the µCT scans are performed on the industrial µCT system Metrotom 800 (Carl Zeiss AG, Oberkochen, Germany). The Metrotom 800 offers a wide range of settings for applications such as metrology, failure detection or microstructure analysis. The resolution (voxel size) of the scan is one of the most important parameters limiting the scale of features that can be analyzed. As described in Chapter 2.2.1, scan resolution and sample size represent an important trade-off for fiber orientation analysis. Although a very fine resolution might be needed for an accurate analysis, a small sample might not fully represent the local orientation, especially for long fiber-filled materials.

A sensitivity analysis of the scan resolution on the results on the fiber orientation analysis

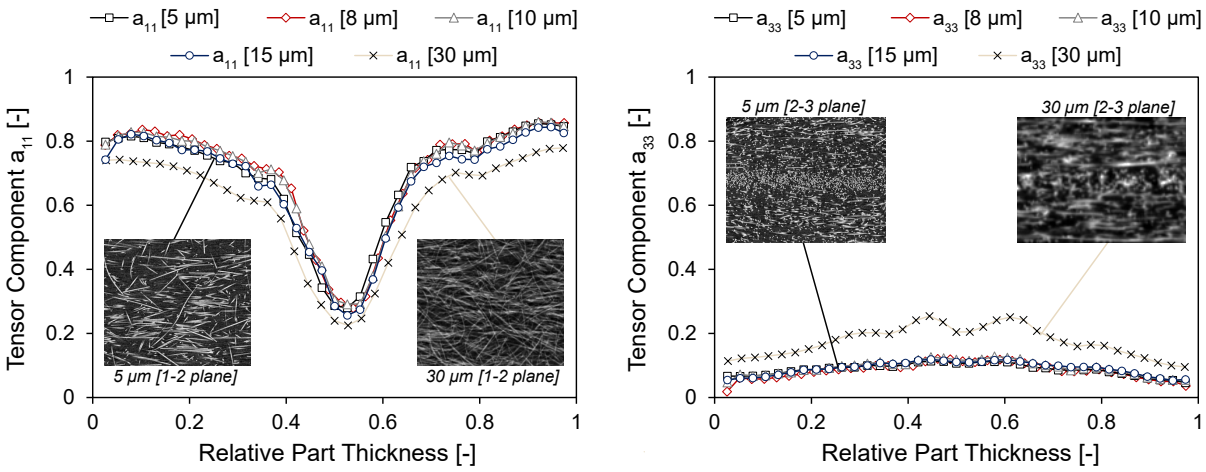

Figure 3.10.: Results of the sensitivity analysis showing the influence of voxel size on the results of the fiber orientation analysis for an identical sample: Tensor components a_{11} (left) and a_{33} right.

was performed. The objective was to determine the largest voxel size and largest sample size without affecting the results of the fiber orientation analysis. An identical sample molded with dimensions of 10 x 10 x 3.2 mm^3 was scanned at resolutions varying from 5 µm to 30 µm and the fiber orientation was analyzed. The injection molded sample comprises a 40% glass fiber-filled PP and fibers with a diameter of 19±1 µm. The results of the sensitivity analysis are illustrated in Figure 3.10.

The outcome of this sensitivity analysis suggests that the same fiber orientation distribution can be obtained for larger voxel sizes up to 15 µm. While the orientation can still be captured qualitatively at 30 µm voxel size, there is a clear error due to the lack of resolution. The fiber orientation analyses for the scans at 5 to 15 µm leads to similar results with discrepancies of less than 1%. The scan at 30 µm shows qualitatively the same through-thickness orientation, but the values are skewed. The value for a_{11} at 30 µm is 0.1 less than the results at smaller voxel sizes and the a_{33} value is on average 0.12 larger.

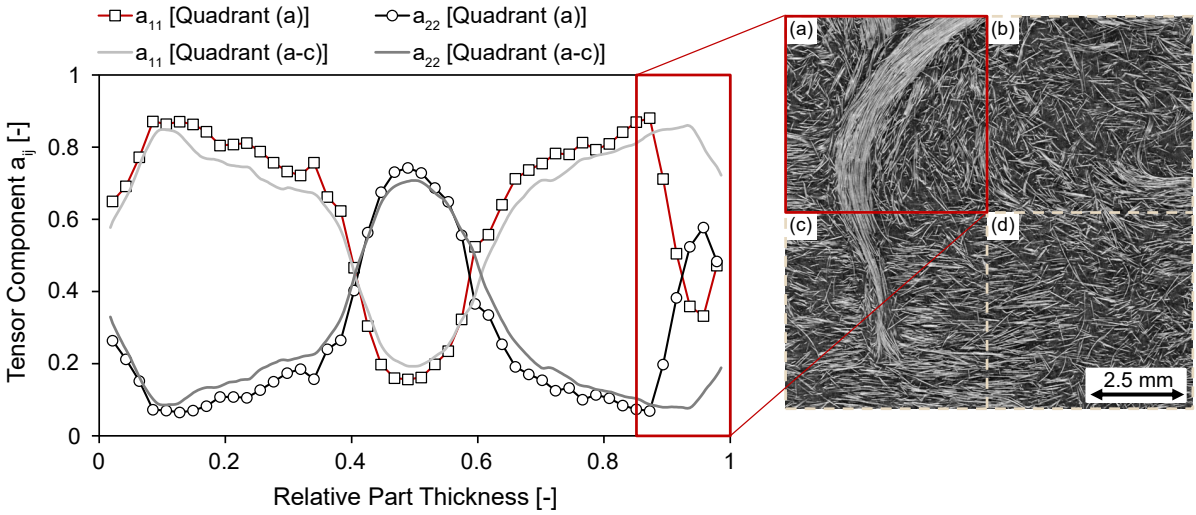

Figure 3.11.: Illustration of the impact of an irregular fiber bundle on the fiber orientation analysis for an injection molding sample (40%wt glass fiber-reinforced PP).

It can be concluded that the voxel size impacts the outcome from fiber orientation analyses. While the sensitivity depends on the material combination of the composite and the fiber size, the results of this study suggest that accurate fiber orientation can be obtained at a voxel size less than the diameter of the fiber (19±1 µm). Smaller voxel sizes do not improve the outcome of the fiber orientation analysis. Hence, it might not be necessary to scan at the smallest possible voxel size to quantify fiber orientation accurately and larger samples would allow a better representation of the local properties. In particular, larger sample sizes can be essential for a robust microstructure analysis, if local irregularities such as voids or non-dispersed fiber

bundles are expected. Figure 3.11 illustrates the impact of a non-dispersed fiber bundle on the orientation analysis. The sample contains a irregularly orientated bundle and was scanned at a voxel size of 10 µm. The fiber orientation for the sample was done separately for the volume that contains the fiber bundle illustrated by quadrant (a) in Figure 3.11 and the remaining volume. The irregularly aligned fiber bundle has a significant impact on the results of fiber orientation analysis. The outcome of the fiber orientation analysis for quadrant (a) shows a largely skewed orientation at the location of the bundle compared the analysis of the remaining volume.

3.2. Fiber Concentration Characterization

As described in Chapter 2.2.2, the most common approach to measure fiber concentration is by determining the weight fraction through pyrolysis. Although this method is destructive, it offers a quick and accurate analysis of the local fiber concentration. However, this approach can only be applied to a limited scale and is mostly used to measure average fiber weight fraction of a sample extracted from a molded part. A new approach is to apply µCT scanning and quantify the through-thickness fiber concentration using image processing. However, no detailed study has been published discussing this approach. This chapter presents a novel measurement protocol using µCT to quantify fiber concentration and the validation of the procedure.

The obtained µCT data sets are processed to determine the change of fiber concentration through the sample thickness by applying an image processing algorithm. The process flow chart of the procedure is illustrated in Figure 3.12. First, the raw µCT data set is aligned and registered using VG StudioMAX 3.0. Subsequently, the data set is exported as an image stack (2D slices) oriented normal to the thickness direction. The 2D slices comprising grayscale images are imported into MATLAB and the fiber volume fraction through the thickness of the sample is calculated using the developed algorithm described in the following paragraphs.

The grayscale images are transformed into binary images by segmentation, which requires selecting a reasonable threshold value to separate each image into black (matrix) and white (fibers) pixels as shown in Figure 3.13 (left). In the grayscale 2D slice, each pixel with the coordinates (x, y) has a distinct grayscale value $f(x, y)$, which depends on the bit depth (e.g. a 16-bit grayscale image has 65,536 tonal levels).

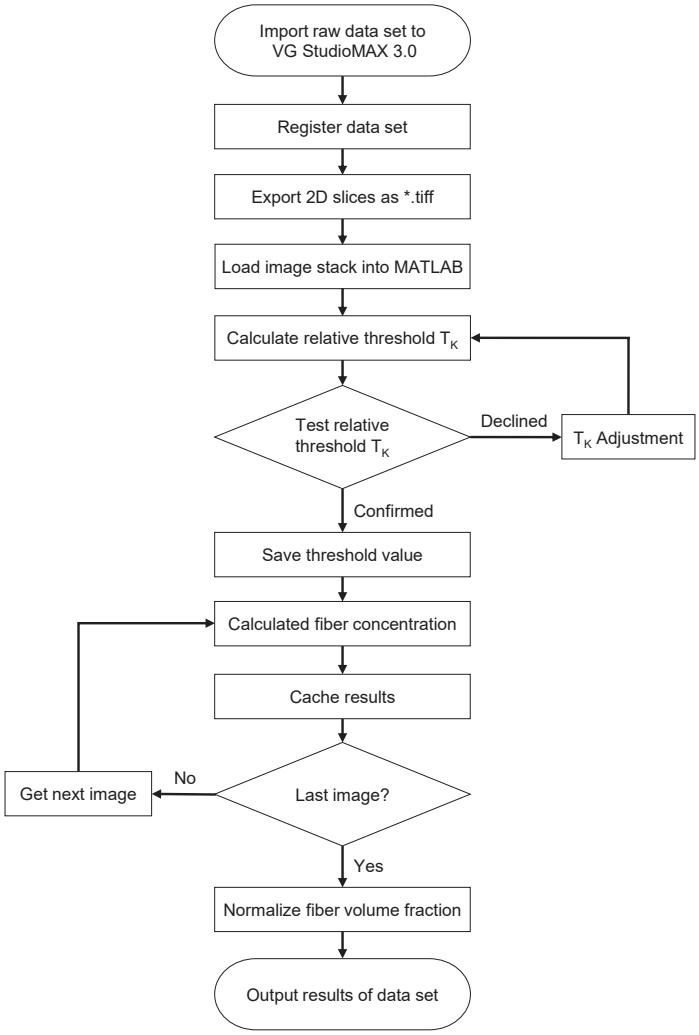

Figure 3.12.: Flow chart of the procedure for the through-thickness concentration analysis.

A basic thresholding approach is used to convert the grayscale image into a binary image by setting a global threshold value. The value for each pixel in the binary image is calculated by

$$g(x,y) = \begin{cases} 1, & \text{if } f(x,y) > T_k \\ 0, & \text{if } f(x,y) \leq T_k \end{cases} \tag{3.7}$$

where T_k is the relative grayscale value for thresholding. For each 2D slice z, the fiber volume fraction $\phi_f(z)$ is calculated by the fraction of white pixels in the entire image $N \times M$:

$$\phi_f(z) = \frac{\sum_{i=1}^{n} \sum_{j=1}^{m} g(x_i, y_j)}{N \times M} \tag{3.8}$$

The true T_k is unknown due to the gradual change in the grayscale value between the two phases as illustrated in Figure 3.13 (left). The choice of the threshold directly determines the size of the

segmented phases and, thus, the fiber volume concentration. Even at very fine resolutions, the true threshold value cannot be detected directly from the µCT data set. A heuristic procedure for the segmentation is proposed by calculating the threshold value as the midpoint between the mean value representing the fibers and the mean value of the background. This selection might not result in the true threshold value, but any uncertainty around the value would merely shift the obtained fiber volume concentration as shown in Figure 3.13 (center). Hence, selecting a single value for T_k and performing a normalization step for the entire image stack (µCT data set) resolves the ambiguity in selecting the true threshold value.

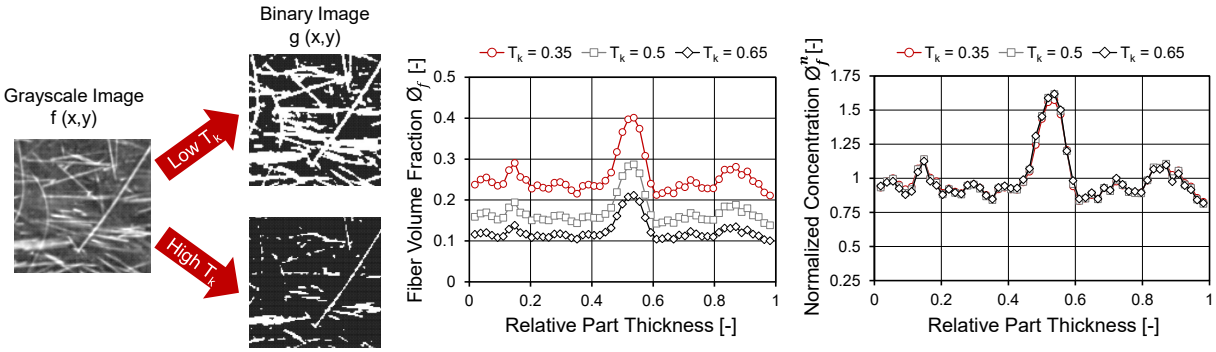

Figure 3.13.: Transforming a grayscale image into a binary image (left), the obtained fiber volume fraction for varying relative threshold values (center), and the normalized fiber concentration distribution (right).

The average fiber concentration of the entire µCT data set $\overline{\phi_f}$ is calculated from the individual fiber volume concentration $\phi_f(z)$ of each slice. The normalized fiber concentration distribution $\phi_f^n(z)$ can be obtained for each image as follows

$$\phi_f^n(z) = \frac{\phi_f(z)}{\overline{\phi_f}} \tag{3.9}$$

For a wide range of values for T_k, the normalized fiber concentration distribution is the same, as shown in Figure 3.13 (right). Only at extreme values, where $T_k < 0.3$ or $T_k > 0.7$, skewed distributions are seen. With this approach, it is possible to accurately obtain the through-thickness fiber concentration from µCT data. If needed, absolute values for the fiber concentration distribution can be calculated by measuring the local fiber concentration of the entire sample through pyrolysis.

The proposed measurement protocol for the through-thickness fiber concentration analysis using µCT was validated by performing a milling and pyrolysis procedure. A simple plate geometry was used to mold samples at 20%wt and 40%wt as shown in Figure 3.14. Samples at the center

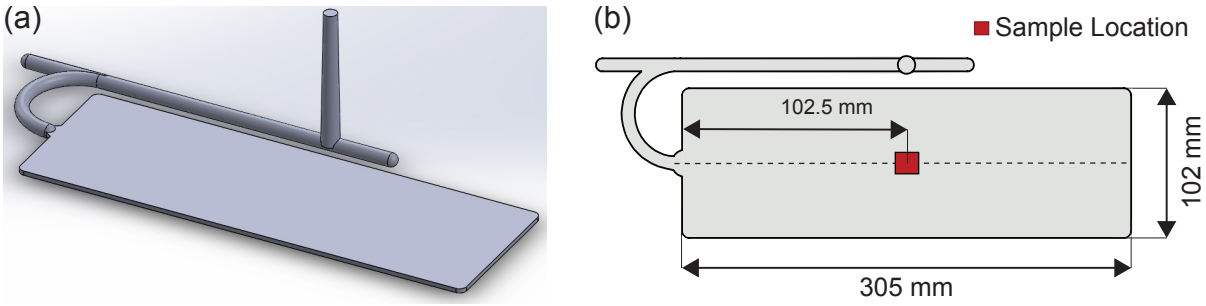

Figure 3.14.: Sketch of the plate geometry (a) and illustration of the sample location for the microstructure analysis (b).

location of the plate were extracted and measured. The procedure was repeated three times for each sample.

After the µCT scan of a sample, the identical sample was milled down in defined increments of 0.2 mm along the thickness. The shavings were carefully collected using a vacuum setup and a 25 µm mesh to ensure capturing all material during milling. The fiber weight concentration for each layer was determined by measuring the sample weight before and after pyrolysis on a high precision scale Explorer (Ohaus, Parsippany, USA) with an accuracy of ±0.01 mg. After converting the obtained measurements to volume fraction, the results from the µCT measurements and from the pyrolysis can be compared.

The fiber diameter of the material is 19 µm and single fiber filaments can be clearly identified in the scans at resolutions below this value. Pre-trial experiments on the impact of resolution on the results showed that finer resolutions do not change the outcome. Table 4.4 summarizes the scan parameters used for all subsequent measurements. The sample size at 5.25 µm is 10 x 15 x 2.85 mm^3.

Table 3.2.: Zeiss Metrotom 800 scan parameters.

Parameter	Value
Voltage [kV]	50
Current [µA]	80
Integration Time [ms]	1000
Gain [-]	8.0
Spot Size [µm]	5.0
Voxel Size [µm]	5.25

The outcome of the comparison is shown in Figure 3.15. The results show strong agreement between the two measurement procedures. Discrepancies between the results from the milling procedure and the µCT analysis are less than 2.5% for each of the six samples. Hence, the

proposed µCT analysis protocol is suitable to accurately and efficiently quantify the fiber concentration through the thickness of the part. Not only is the µCT approach non-destructive, it is a fast analysis of the through-thickness fiber concentration and it also allows additional fiber orientation analyses of the same µCT data set.

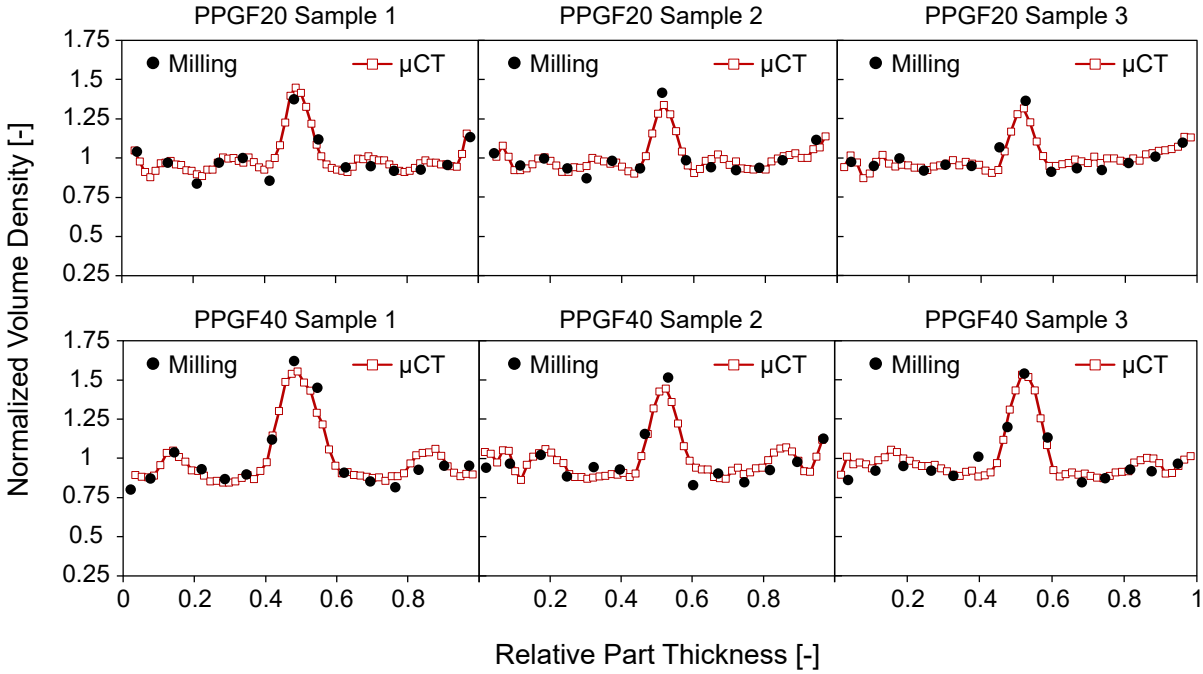

Figure 3.15.: Comparison of the milling procedure and µCT analysis for the through-thickness fiber concentration measurements.

3.3. Fiber Length Measurement Concept

As discussed in Chapter 2.2.3, substantial differences in reported fiber length measurement techniques and the lack of a standard approach raise major concerns about the repeatability and comparability of previously published results. While there have been several research studies characterizing the process-induced fiber length reduction, the measurement procedures vary substantially, calling into question the comparability of reported results. As part of this work, a new measurement technique was developed and compared to other characterization concepts in a comparative study.

The developed measurement technique combines elements from other measurement procedures and aims to minimize the manual input in order to achieve highly reproducible measurements in a timely manner. Figure 3.16 illustrates the main steps of the developed measurement technique. First, a sample with the dimensions of at least twice the initial fiber length is extracted to avoid

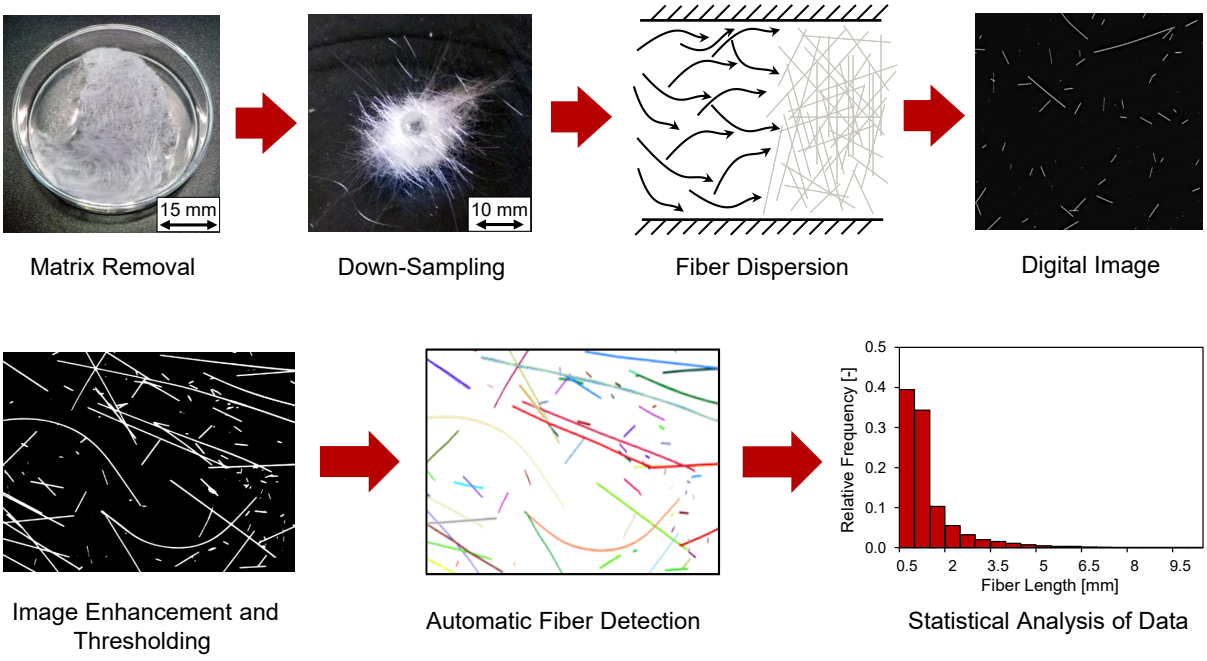

Figure 3.16.: Overview of the steps of the developed fiber length measurement technique.

measuring fibers that crossed the cutting plane during extraction (e.g. an initial fiber length of 15 mm results into extracting round samples with a diameter of 30 mm). Next, the sample is placed in a brass sample holder and constrained by a brass lattice to ensure that the fibers stay in place when the matrix is removed. The pyrolysis is performed in a laboratory furnace at 500°C for 2.0 h. Subsequently, a representative downsampling step is performed, adapted from the epoxy-plug method described by Nguyen and Kunc [61, 101]. All fibers in the defined down-sampling region are collected by injecting an epoxy resin through the thickness of the fiber bed using a hypodermic needle. The down-sampling step using the resin injection is an important step to reduce the overall sample size while collecting a controlled and representative subset of fibers. The outcome of the down-sampling is shown in Figure 3.17 and the overall objectives of this procedure are:

1. Collect a representative population of fibers that statistically resembles the fiber length distribution in the initial sample.

2. Remove all fibers that were cut at the edges of the sample during extraction from the molded part.

3. Obtain a defined amount of fibers for the actual measurement.

In contrast to the epoxy system applied by Nguyen and Kunc, the method presented here uses an ultraviolet (UV) curable epoxy (BONDIC Liquid-glue B0027N07MM, Aurora, Canada). This

UV curable epoxy showed optimal flow behavior for the downsampling step since the viscosity is sufficiently low to be easily injected through a fine hypodermic needle (22-gauge size), but still high enough to form a plug with uniform thickness. Figure 3.17 illustrates the downsampling procedure and shows a µCT scan of the epoxy plug. The UV curable epoxy is a Newtonian fluid and the viscosity at ambient temperature was measured to be 7.33 P·s. Furthermore, the curing time is less than 5 seconds compared to several hours for the mixing-activated epoxy used by Nguyen and Kunc [61, 101].

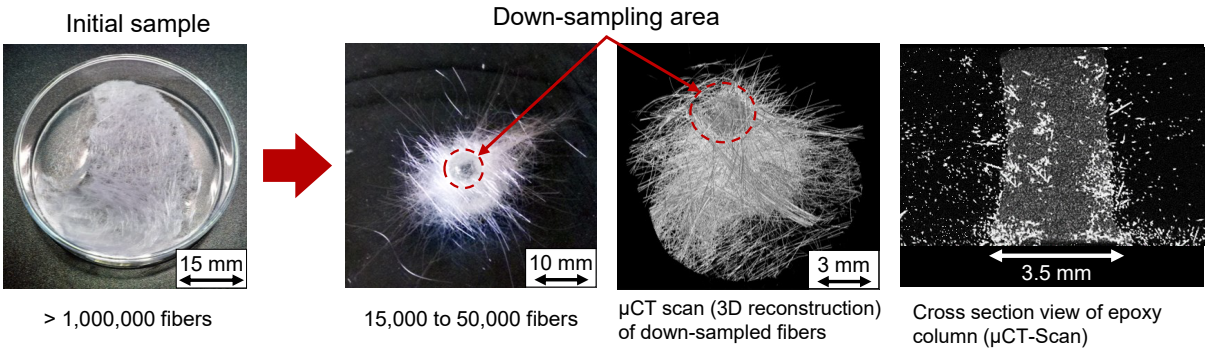

Figure 3.17.: Down-sampling step: Initial sample after pyrolysis (left) and subsample after resin injection (center and right).

Any partial collection of fibers from a larger sample can skew the outcome of the fiber length analysis, as pointed out by Kunc et al. [101, 122]. The cause of this bias comes from the preferential selection of longer fibers. However, the error can be accounted for by applying the Kunc correction, as illustrated in Figure 3.18. A population of three short and three long fibers is down-sampled in a circular region with the diameter d. Although the centroid positions of the long and short fibers are similar, the down-sampling results in the collection of only one short fiber, but all three long fibers. It can be assumed that the fibers are oriented in the 2D plane and the correction can be formulated by applying a geometric correction for the centroid of a fiber L_i passing through the down-sampling area [101]. The corrected frequency $N(L_i)$ of fibers with the length L_i is obtained by:

$$N(L_i) = \theta(L_i)\ (1 + \frac{4\,L_i}{\pi\,d}) \tag{3.10}$$

where $\theta(L_i)$ is the raw frequency of fibers of length L_i obtained after down-sampling and d is the diameter of the down-sampling area.

After the epoxy plug is cured, all surrounding fibers are removed carefully using a brush. The fibers embedded within the epoxy are recovered by a second pyrolysis step at 500°C for 1 h. The

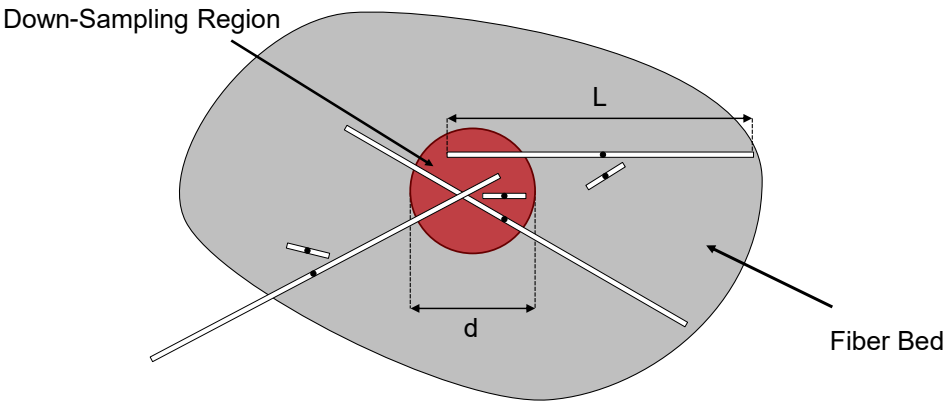

Figure 3.18.: Illustration of the Kunc correction procedure. Adapted from [101].

heat ramp is reduced to 5 K/min to slow down the thermal degradation of the epoxy slightly. This initiates an initial disentanglement of the fibers, which is particularly helpful at higher fiber concentrations.

In the next step, the fibers are dispersed within an enclosed chamber system using bursts of slightly compressed air. The air turbulence causes the fibers to disentangle and disperse uniformly. A few small air bursts (less than 0.5 seconds each) at a pressure of approximately 1 bar are sufficient to disperse the fibers uniformly. It takes less than 15 seconds for all fibers to settle. The fibers fall on a thin glass sheet, which is used to move the sample onto a film scanner. Overall, the fiber dispersion step in an enclosed chamber system using turbulent air flow allows the uniform dispersion of a large amount of fibers in under 30 seconds. A schematic of the current design of the dispersion chamber is shown in Figure 3.19. The enclosed chamber is made of stainless steel and has overall dimensions of 380 mm (height) x 210 mm (width) x 255 mm (depth). The glass sheet is a laboratory-grade float glass and its dimensions are 210 x 260 x 1 mm^3. The inner surface of the dispersion chamber is polished to ensure a smooth surface and coated with a thin layer of dry graphite to prevent fibers from sticking to the surface of the chamber. Pre-trial experiments showed that less than 1% of the glass fibers are lost in the dispersion process.

The dispersed fibers are scanned between 1200 dpi and 2400 dpi to generate a digital image using a flatbed scanner with a transparency unit (Epson Perfection V750 Pro by Seiko Epson Corporation, Suwa, Japan). All fibers in the image are automatically detected by an image processing algorithm developed at the Polymer Engineering Center [82] and based on the work of Wang [123]. Even bent and intersecting fibers are detected by this algorithm (Figure 3.16). This ability is particularly important for accurate results when examining LFT materials because longer fibers can be substantially curved, even after pyrolysis [110]. The current version of the

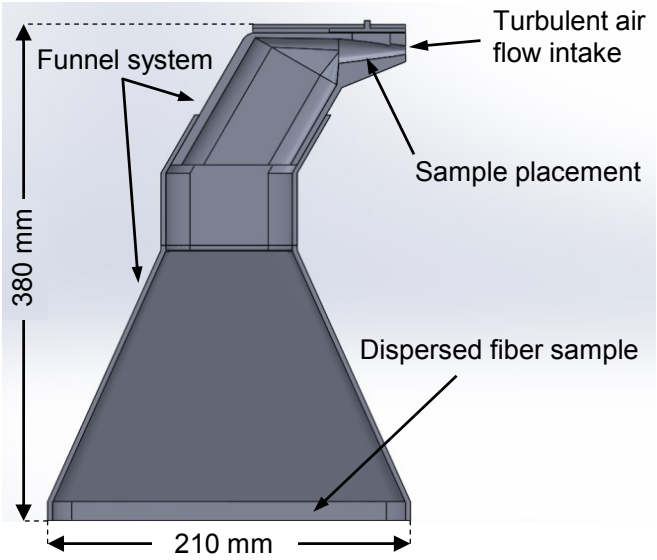

Figure 3.19.: Sketch of the dispersion chamber for the preparation of the fiber sample.

algorithm is coded in MATLAB^{TM} (Version R2016a) and takes between 5 - 10 min to process the images of each sample.

To ensure the measured fiber length distribution is statistically representative, between 15,000 and 50,000 fibers were analyzed for each sample. The measurement time is approximately 60 min per sample, excluding furnace time. All measurements obtained with the present method were repeated five times for each location to ensure accurate results and show the repeatability of the obtained results.

3.3.1. Validation and Comparative Study of Fiber Length Measurement Techniques

The material used in this study is a commercially available glass fiber-reinforced PP with 30%wt (PPGF30) and 40%wt (PPGF40) fiber concentration (SABIC STAMAX^{TM}). The material is supplied as coated pellets with a nominal fiber length of 15 mm. The material was processed on a 320-ton Arburg Allrounder 720S (Arburg GmbH + Co KG, Loßburg, Germany) injection molding machine equipped with a general-purpose screw and diameter of 52 mm. The mold geometry for this study is a simple fan-gated plaque with a thickness of 2 mm as illustrated in Figure 3.20. The processing settings are listed in Table 3.3, which follow the general processing guidelines suggested by the material supplier [124]. Two different molding conditions were defined: *standard* and *gentle*. The standard processing conditions use a higher screw speed (35 RPM) and back pressure (50 bar) than the gentle conditions (27 RPM and 13 bar).

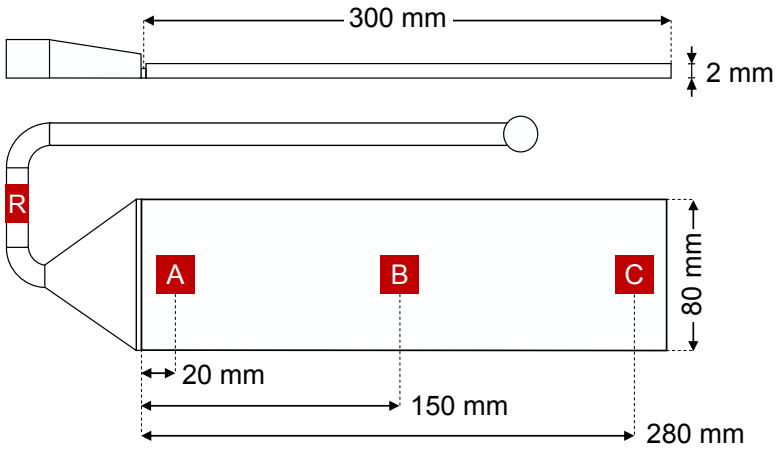

Figure 3.20.: Part dimensions and sample locations for fiber length analysis.

As discussed in Chapter 2.2.3, the majority of current measurement procedures manually select a random subset of fibers from a larger sample after the matrix was removed. These results can be skewed by both the amount of measured fibers and the bias in downsampling, which is also pointed out by Nguyen et al. [61, 101]. In order to generate a baseline for the comparative study of this work, ten identical samples (PPGF40, gentle conditions, position B) were measured according to the reported conventional measurement procedures (see Chapter 2.2.3), referred to as manual measurements. The manual measurement procedure was performed as follows. Samples with the dimensions of 30 x 30 x 2 mm^3 were extracted from the molded part and the matrix was removed by pyrolysis at 500°C for 2.0 h. From each sample, a subset of fibers was carefully removed randomly using plastic tweezers following the procedures described in published studies. The measured amount of fibers varied from 282 to 4612 fibers, which is within the range of the reported studies. The fibers were manually dispersed using fine brushes and a digital image was created. Each fiber in the digital image was manually detected by clicking the endpoints using a developed MATLAB tool. The digital images were generated at

Table 3.3.: Processing conditions for the injection molding trials.

Molding Parameter	Standard Conditions	Gentle Conditions
Melt Temperature [°C]	250	250
Mold Temperature [°C]	50	50
Back Pressure [bar]	50	13
Screw Speed [RPM]	35	27
Injection Time [s]	2.5	2.5

2400 dpi, translated to a binary image and the endpoints of each individual fiber were selected manually. The length of curved fibers was determined by splitting the fiber in segments, fitting circular arcs to any curved segments and adding the length of all segments. This protocol of manual measurements is assumed to reflect the capabilities of the conventional measurement techniques.

The results of this evaluative study are summarized in Figure 3.21, which shows the obtained weight-average length and the number of fibers in each repetition. The manual technique shows a substantial variation in the measured fiber length distributions with the weight-average fiber length varying from 1.03 mm to 3.96 mm (mean of 2.37 mm and standard deviation of 0.95 mm). The large variation in the measurements confirms the claim by EATC that the variation in conventional measurement techniques might differ by a factor of two [111].

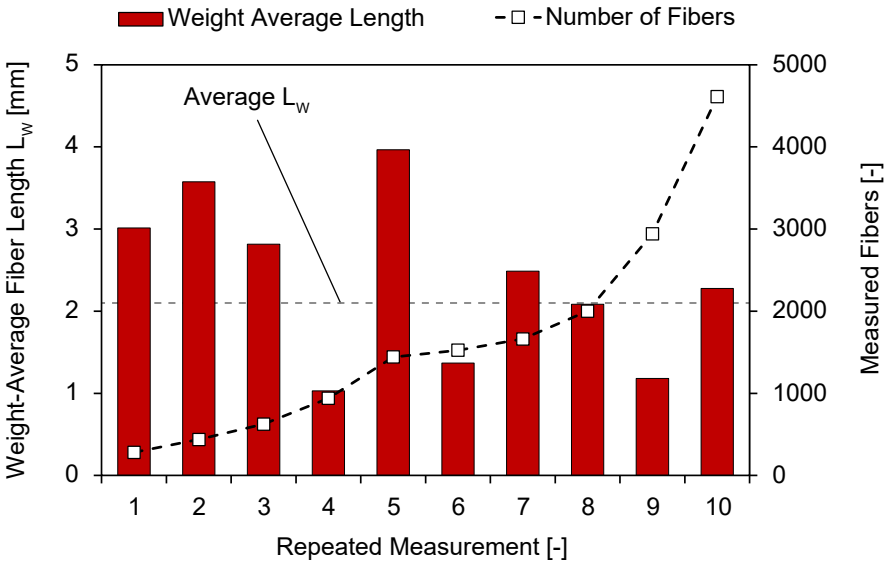

Figure 3.21.: Results obtained from conventional (manual) measurements. Ten individual measurements of sample PPGF40, gentle conditions, location B.

The newly developed measurement technique was compared to the conventional manual approach, the commercially available FASEP measurement system, and a full analysis provided by SABIC (Geleen, The Netherlands). The full analysis is a proprietary measurement system developed by SABIC and based on work by Krasteva [125]. The SABIC procedure analyzes the entire fiber population in a sample and does not perform any downsampling step. The size of the sample is 12 x 12 x 3 mm^3 comprising approximately 350,000 to 750,000 fibers for a single measurement. The sample size was determined as the optimal tradeoff between the amount of fibers that need to measured and the error introduced by cutting fibers when extracting the sample from the molded part [125]. After pyrolysis, all fibers are dispersed manually in subsets

of 40,000 to 50,000 fibers. A digital image of each subset is generated and processed with an automated image processing algorithm. Due to the amount of the overall fibers in a single sample, the manual dispersion is time-consuming. Table 3.4 summarizes the main characteristics of the compared measurement approaches.

Table 3.4.: Overview of measurement techniques for a comparative fiber length analysis study.

	FASEP	**Full Analysis**	**Present Work**
Fiber Dispersion	Diluted suspension	Manual	Turbulent air chamber
Sample Size	Representative (random) fraction	All fibers	Representative down-sampling
Measured Fibers	2000 to 15,0000	350,000 to 750,000	15,000 to 50,0000
Image Processing	Semi-automatically	Fully automatic	Fully automatic
Measurement Duration	2 hours per sample	8 hours per sample	Less than 1 hour per sample

Two different sets of molded samples were defined for the comparative study: PPGF30 (gentle conditions, location B) and PPGF40 (gentle conditions, location B), for sample location see previous Figure 3.20. Measurements were repeated five times at all locations with the present method and the results are shown as average values, with error bars indicating the standard deviations. Two repeated measurements were performed with the FASEP system and one repetition for the full analysis. The results for the PPGF40 (gentle conditions, location B) samples are summarized in Figure 3.22 as average length values and the cumulative length distribution. Figure 3.23 summarizes the obtained average values for the PPGF30 (gentle conditions, location B) samples.

While the FASEP measurements barely show any deviation between the two repeated measurements (±0.1mm), the measurements from the present method show a slightly higher deviation. The full analysis suggests a lower weight average length for the PPGF30, whereas the results for PPGF40 show a discrepancy of less than 2% between FASEP, the full analysis and the present method. However, the results from the manual measurement suggest a 27% higher value for the weight-average fiber length and the standard deviation over the ten repeated samples is 0.95 mm (or 40.0% of the mean).

The fiber length distribution was measured for all process conditions and sample locations using

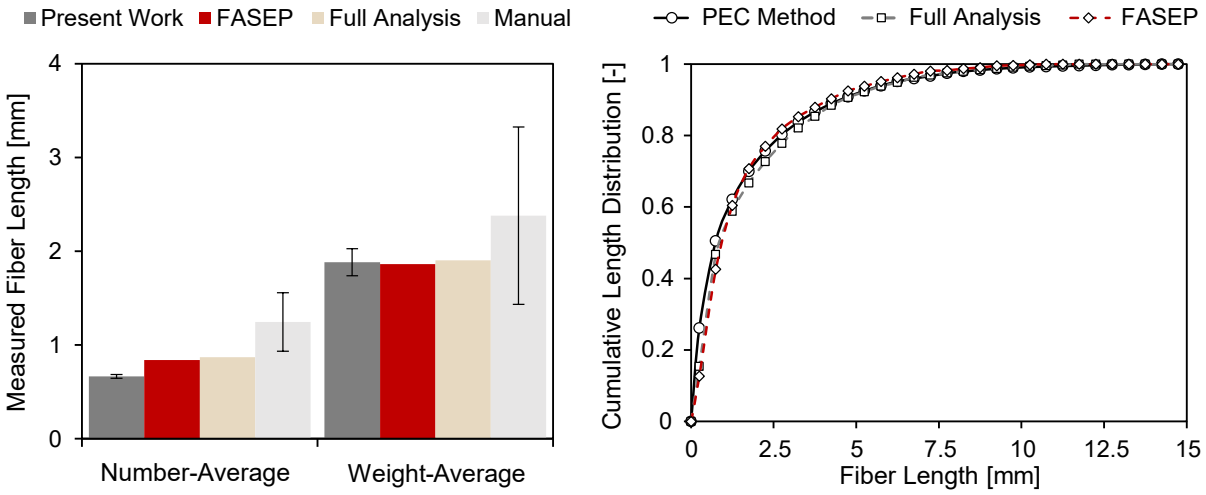

Figure 3.22.: Comparison of the outcome of the fiber length measurements for all measurement protocols (PPGF40, gentle conditions, location B): Average fiber length values, standard deviations indicated by error bars (right) and cumulative fiber length distribution $\mathfrak{W}$ (right).

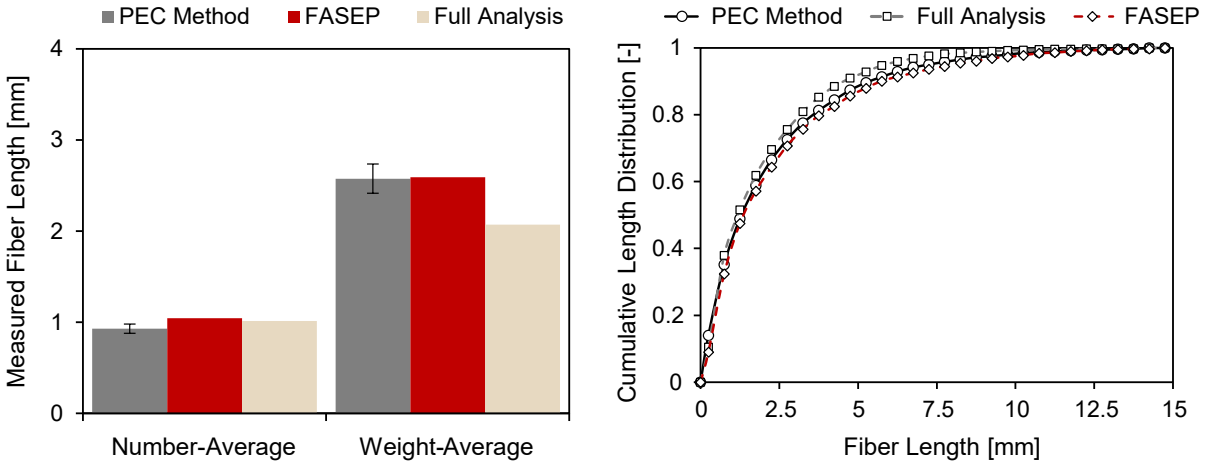

Figure 3.23.: Comparison of the outcome of the fiber length measurements for all measurement protocols (PPGF30, gentle conditions, location B): Average fiber length values, standard deviations indicated by error bars (right) and cumulative fiber length distribution $\mathfrak{W}$ (right).

the present method and the full analysis for a further comparison between the two measurement techniques. Five repetitions for the present method and one repetition for the full analysis were performed for each location. Figure 3.24 shows the weight-average fiber length of the PPGF30 trials, standard conditions (left) and gentle conditions (right). The results from the PPGF40 trials are summarized in Figure 3.25 for the standard conditions (left) and gentle conditions (right). The results show a strong agreement between the measurement techniques. While some samples show a slightly larger discrepancy of around 20% (PPGF40 gentle conditions, location A and PPGF30 gentle conditions, location B), the difference for all other locations is on average less than 5%.

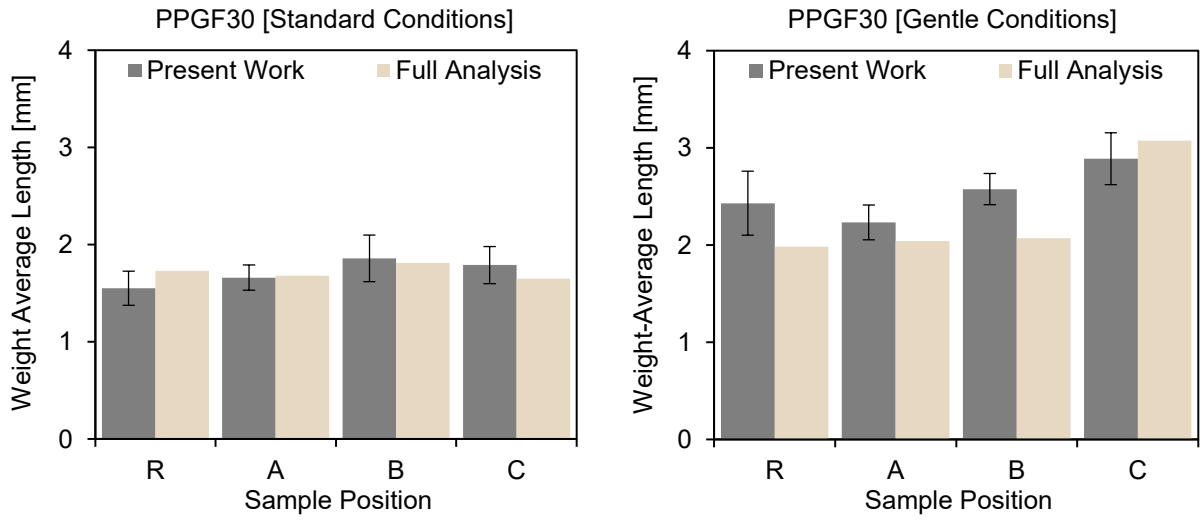

Figure 3.24.: Comparison of full analysis and present method for all locations: PPGF30 at standard conditions (left) and PPGF30 at gentle conditions (right).

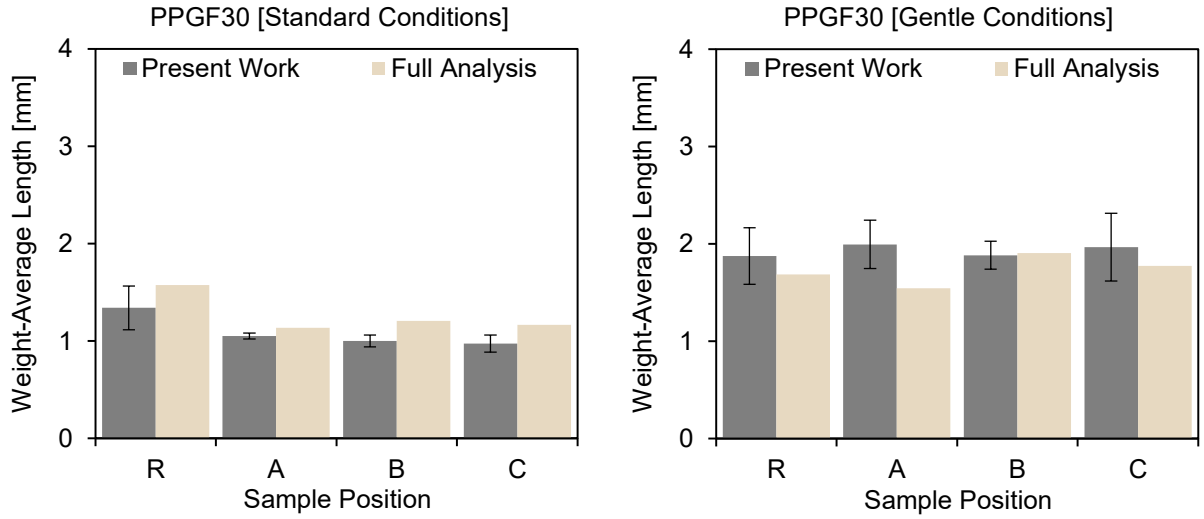

Figure 3.25.: Comparison of full analysis and present method for all locations: PPGF40 at standard conditions (left) and PPGF30 at gentle conditions (right).

The results of the comparative study show the importance of a standardized measurement technique for fiber length analysis. The conventional method of manually selecting a subset of fibers and measuring a small amount of fibers per sample can result in substantial inaccuracies and large variations across repeated measurements. As reported by Nguyen and Kunc [61, 101], there is a bias towards longer fibers from manually collecting and analyzing fiber samples. While measuring a small amount of fibers is certainly less time-consuming regardless of the actual measurement approach, it is questionable if fewer than 1000 fibers can be statistically representative of the local fiber length distribution of the sample. The full analysis approach of a sufficiently large sample might be the ideal procedure since it generates a statistically robust data set and no correction for down-sampling is necessary. However, the time-consuming sample

preparation (fiber dispersion and generation of the digital image) might limit the application of this approach. For example, larger experimental studies on fiber breakage could require repeated measurements, and analyzing 500,000 fibers per sample without automated fiber dispersion is very challenging.

Because it dilutes an entire fiber sample in a liquid, the FASEP system does not require any correction due to down-sampling. However, randomizing the fibers in the suspension and diluting the mixture requires time-consuming manual effort to be performed correctly. Also, a complete randomization of fibers within in a highly-diluted suspension might be difficult to achieve for LFT samples due to the wide range of fibers in the samples. Larger fibers settle faster than smaller ones. Hence, it is challenging to ensure that a truly randomized sample is extracted from the diluted mixture. Nevertheless, the FASEP system uses a measurement protocol with defined steps resulting in repeatable measurements. At the time of this work, it is the only commercially available measurement system for fiber length analysis.

The outcome of the comparative study shows that the present method can be used to generate accurate results with a high level of repeatability, while minimizing the manual effort required to handle, prepare, and analyze a fiber sample. It improves upon the shortcomings of previously proposed characterization methods and the fiber length of large samples to be accurately measured in a timely manner to obtain statistically meaningful data.

The proposed methodology also works for other fiber types. Initial tests with carbon fibers and natural (sisal and hemp) fibers showed that that the same methodology can be applied. Only the matrix removal steps need to be modified accordingly since pyrolysis is not possible for natural fiber reinforced composites and a chemical matrix removal is necessary. Carbon fiber reinforced materials require a nitrogen atmosphere and carefully monitored pyrolysis to prevent oxidation of the fibers. Moreover, the scan resolution needs to be increased to at least 4800 dpi for carbon fibers due to the smaller fiber diameter.

3.4. Discussion and Conclusions of the Developed Characterization Techniques

The analysis of the microstructural properties of discontinuous fiber-reinforced composites is a challenging and cumbersome task, but it is a necessary step to obtain a fundamental understanding of the phenomena present in LFT processing. In this work, novel characterization techniques were developed combining image processing with µCT and optical measurement systems. While accuracy is the most important objective in developing a measurement procedure, the time required to take measurements also plays an important role. The developed characterization tools provide both accuracy and time efficiency, which was highlighted in comparative studies with conventional measurement procedures.

The comparative studies show that the comparability of reported results across different studies using different measurement methodologies is limited due to the influence of the measurement approach causing skewed results. This was particularly evident in the fiber length analysis, where the conventional measurement approach yielded results that were not repeatable. Hence, any comparison of reported results across different studies and research groups has to be done with care due to the discrepancies in measurement techniques. Overall, the outcome highlights the need for a more standardized approach in characterizing the fiber length of molded samples to allow a fair and accurate comparison between experimental studies. As it overcomes the shortcomings of conventional measurement techniques, the developed fiber length measurement technique is a first step to standardization.

Analyzing the through-thickness fiber orientation and fiber concentration distribution was made possible using µCT and it proved to be a mighty tool for the fiber microstructure analysis. A measurement protocol using µCT and image processing was developed and validated for fiber orientation and fiber concentration analyses. While the investment costs of a µCT system limits the application of µCT for microstructure analysis of fiber-reinforced samples, it shows clear advantages over conventional measurement techniques. In fact, µCT allows the analysis of both fiber concentration and fiber orientation from the same data set. Additionally, image processing algorithms for fiber length analysis using µCT are being successfully applied to short fiber-reinforced composites [126]. The non-destructive nature of µCT analysis is particularly useful to connect the process-microstructure relationship with the microstructure-property relationship, because the fiber microstructure of test samples can be characterized before mechanical testing.

Overall, it was shown that the size of the sample and number of repeated measurements are important to reliably obtain the local information of the microstructural property. A single sample can carry local heterogeneities or irregularities, which might skew the outcome of a measurement, if the sample size is small with respect to the heterogeneities. In particular, the longer fibers in LFT materials can result in non-dispersed fiber bundles, as shown in Figure 3.26. Like all material characterization procedures, a robust analysis includes a defined set of repeated measurements [127]. The outcome of this work suggests that at least three repetitions are required to overcome any local irregularity that might occur.

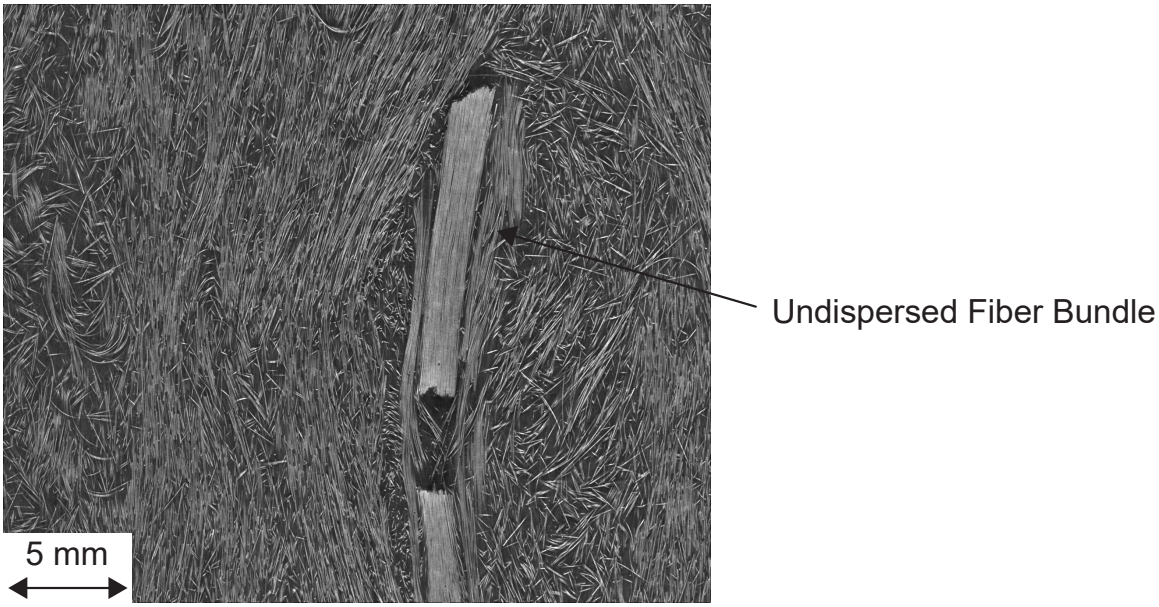

Figure 3.26.: Illustration of an undispersed fiber bundle in an injection molded part (40%wt glass fiber-reinforced PP).

4. Experimental Studies

The experimental work is divided into two main studies. The first study consists of injection molding trials of a simple plate geometry at varying nominal fiber concentration, investigating the process-induced fiber configuration and the correlation between fiber length, fiber orientation, and fiber concentration. Second, an experimental design was developed to study fiber breakage under controlled conditions in simple shear flow, aiming to isolate the effects that drive fiber attrition in LFT processing.

4.1. Injection Molding Experiments

A critical factor in the process-microstructure relationship for discontinuous fiber-reinforced thermoplastics is the nominal fiber concentration. As discussed in Chapter 2.1, the fiber concentration in the feed material substantially affects the phenomena of fiber breakage, fiber alignment, and fiber matrix separation. Consequently, the experimental design of this study was conceptualized around the design factor of nominal fiber concentration, while the processing conditions were kept constant. The material used in this study is a commercially available long glass fiber-reinforced polypropylene (SABIC STAMAX^{TM}). Table 4.1 summarizes the main material properties of the glass fiber-reinforced polypropylene (PPGF).

Table 4.1.: SABIC STAMAX^{TM} LFT material properties according to the material supplier [128].

Material Property	Value
Nominal Fiber Length [mm]	15.0
Fiber Diameter [µm]	19±1
Density of Fibers [g/cm^3]	2.55
Density of PP [g/cm^3]	0.905
Young's Modulus of Single Fibers [GPa]	73
Ultimate Strength of Single Fibers [MPa]	2600

Table 4.2.: Outline of the injection molding trials: Nominal fiber concentration and raw material.

Trial Label	Weight and Concentration	Volume and Concentration	Feed Material
PPGF05	5 %wt	1.8 %vol	25% PPGF20 and 75% neat PP
PPGF10	10 %wt	3.8 %vol	50% PPGF20 and 50% neat PP
PPGF20	20 %wt	8.2 %vol	STAMAX^{TM} 20YM240
PPGF30	30 %wt	13.2 %vol	STAMAX^{TM} 30YM240
PPGF40	40 %wt	19.1 %vol	STAMAX^{TM} 40YM240
PPGF50	50 %wt	26.2 %vol	83% PPGF60 and 17% neat PP
PPGF60	60 %wt	34.7 %vol	STAMAX^{TM} 60YM240

The design-of-experiments (DoE) consists of nominal fiber concentrations varying from 5%wt to 60%wt. Table 4.2 describes the fiber volume and fiber weight concentration, as well as the feed material used to achieve the respective nominal concentrations for each trial. PPGF20, PPGF30, PPGF40 and PPGF60 are provided as compounded pellets by the material supplier (coated long fiber pellets). PPGF05, PPGF10 and PPGF50 were achieved by mixing higher fiber concentrations with neat PP (SABIC^{TM} PP 579S) in a cement mixer before feeding it into the hopper of the injection molding machine. The neat PP is the same as the matrix material of the coated long fiber STAMAX^{TM} pellets.

The parts were molded on a 130-ton Supermac Machinery SM-130 injection molding machine (Supermac Machinery Inc., Gujarat, India). The processing settings followed processing guidelines by SABIC^{TM} [124] and are summarized in Table 4.3. The processing conditions are kept constant unless noted otherwise.

Table 4.3.: Processing conditions for the injection molding trials.

Molding Parameter	Value
Melt Temperature [°C]	250
Mold Temperature [°C]	50
Back Pressure [bar]	5
Injection Time [s]	2
Holding Pressure [bar]	300
Holding Time [s]	22

The part geometry used in this study is a simple plate with dimensions of 102 x 305 x 2.85 mm^3. The cavity is filled through a 20 mm edge-gate with the same thickness as the plate and is fed through a 17 mm full-round runner, as illustrated in Figure 4.1 (a).

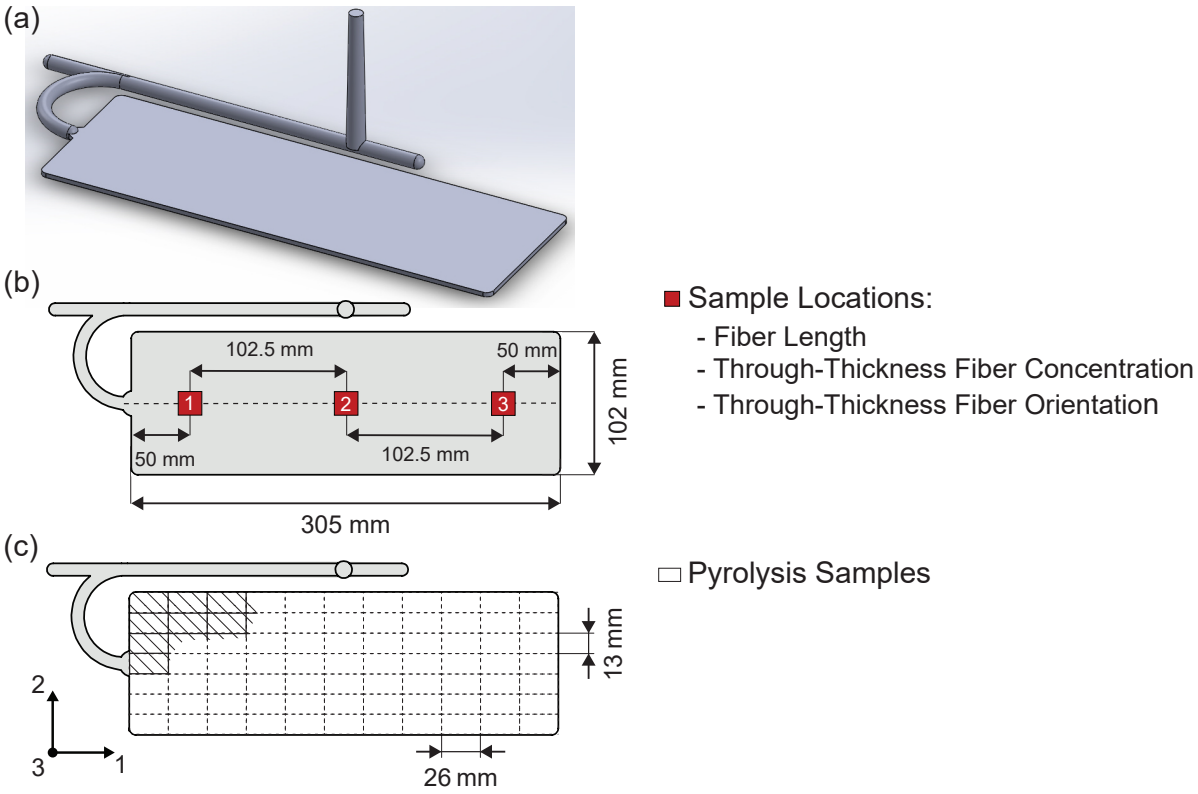

Figure 4.1.: Sketch of the plate geometry and illustration of the sample locations for the microstructure analysis.

The analysis of the microstructural properties is structured as follows. The local fiber length, the through-thickness fiber concentration and the through-thickness fiber orientation are measured at three locations along the centerline of the plate, as shown in Figure 4.1 (b). Location 1 is close to the gate, Location 2 is in the center of the plate, and Location 3 at the of the flow. The global concentration variation throughout the entire part was measured by pyrolysis of 13 x 26 x 2.85 mm^3 samples extracted from the plate, as illustrated in Figure 4.1 (c). Additionally, the fiber length and fiber concentration measurements were performed on purged material samples, which were obtained by air shots from a retracted injection unit at 10% of the injection speed.

The samples were scanned with an industrial µCT system (Metrotom 800, Carl Zeiss AG, Germany). Table 4.4 summarizes the scan parameters used for all measurements. The scan settings are kept constant unless noted otherwise. The scanned sample volume at 5.25 µm resolution is 12.5 x 10 x 2.85 mm^3. The results of this experimental study are presented and discussed in the following sections focusing on the three microstructural properties individually before concluding the outcome of this study and discussing the correlation between fiber length, fiber orientation, and fiber concentration in Chapter 4.1.4.

Table 4.4.: Zeiss Metrotom 800 scan parameters.

Parameter	Value
Voltage [kV]	50
Current [µA]	80
Integration Time [ms]	1000
Number of Projections [-]	2000
Gain [-]	8.0
Spot Size [µm]	5.0
Voxel Size [µm]	5.25

4.1.1. Experimental Analysis of Fiber Alignment

Figure 4.2 summarizes the measured fiber orientation at Locations 1, 2 and 3 for all trials. The plots show the fiber orientation along the direction of flow, a_{11}, and in cross-flow direction a_{22}. The fiber orientation in thickness orientation, a_{33}, is not shown for clarity. Three samples were analyzed for each location and the low standard deviation of the measurement results suggests a high reproducibility in the molded samples.

The trials at higher concentrations (PPGF20 to PPGF60) show the expected core-shell-skin pattern (see Chapter 2.1.1). The core layer consists of fibers predominately aligned along the cross-flow direction while the fibers in the shell layer are oriented along the direction of flow due to the fountain flow effect. The orientation in thickness direction a_{33} is low with average values of less than 0.06 and is uniform through the thickness for all trials.

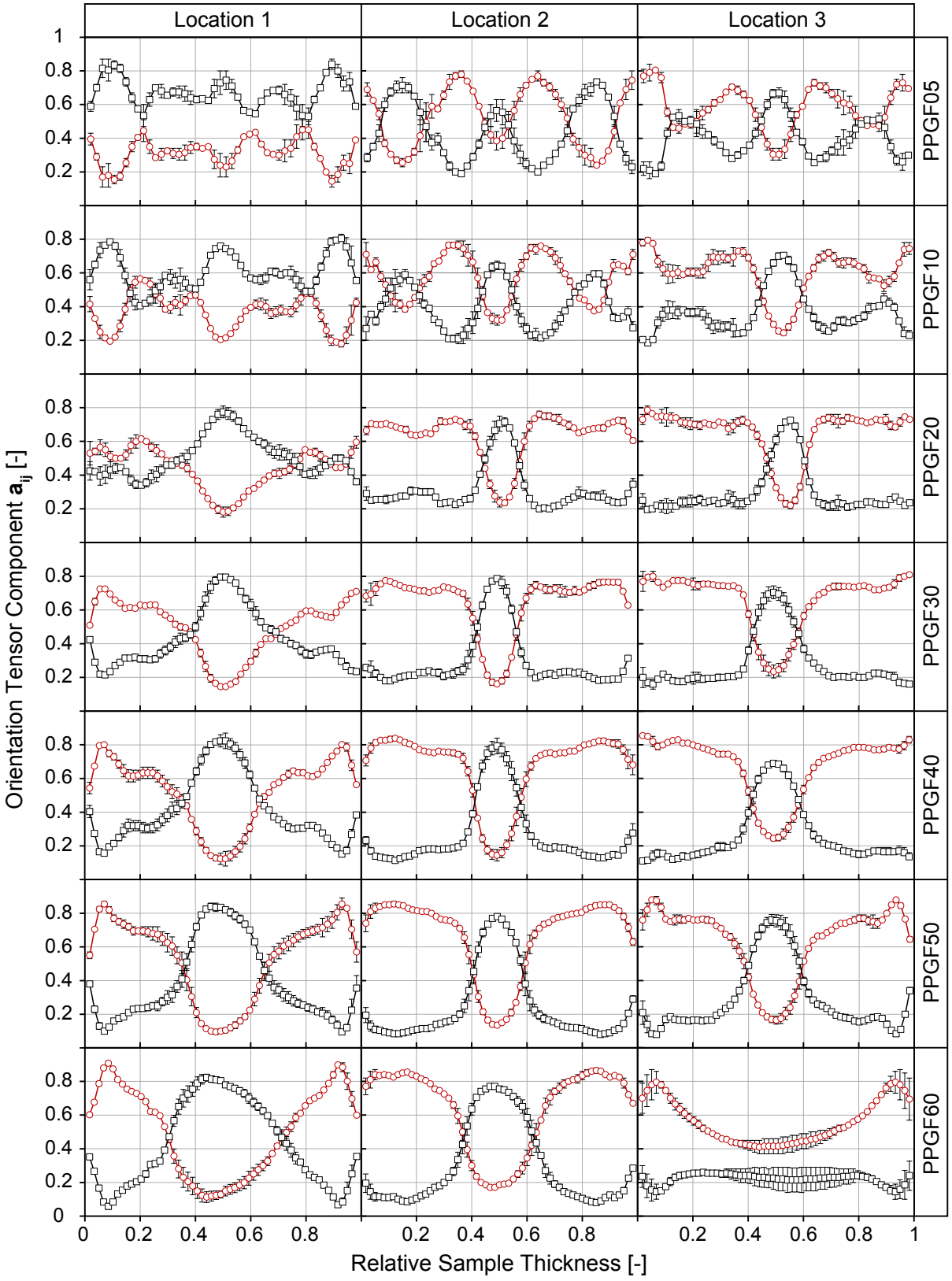

Figure 4.2.: Summary of the measured through-thickness fiber orientation at Locations 1, 2 and 3 for all trials. a_{11}: -○- and a_{22}: -□- (a_{33} is not shown for clarity).

The measurements of the samples with 5%wt and 10%wt nominal fiber concentration indicate an alternating fiber orientation through the thickness of the sample, which is particularly distinctive at Location 2 (see Figure 4.2):

- Core layer: A thin core layer shows a slight preferential fiber alignment in cross-flow direction with an a_{22} value of 0.58 for PPGF05 and 0.63 for PPGF10.
- Layer with fiber orientation along flow direction: After a small transition region, two thick layers with a strong in-flow fiber alignment can be observed at a relative thickness of approximately 0.35 (0.65). The measurements suggest a strong fiber alignment in the direction of flow with average values for a_{11} of 0.78 for both PPGF05 and PPGF10.
- Cross-flow alignment layer: After a second transition region, the measurements indicate a distinctive layer with fibers predominately oriented in the cross-flow direction at a relative layer thickness of approximately 0.15 (0.85). The PPGF05 trial shows a higher degree of orientation in this layer with an average value for a_{22} of 0.71 while the results for PPGF10 suggest a value of 0.59.
- After a third transition region, the thin skin layer close to the surface can be identified with preferential orientation in the direction of flow.

For all trials, the samples close to the gate (Location 1) show a wider core layer than those at Locations 2 and 3, while the degree of orientation in the shell layer is lower. This can be explained with the radial flow field close to the gate due to the edge gate.
The measurements for PPGF60 at Location 3 suggest a large core layer and an overall random fiber orientation, including an overall larger standard deviation for the repeated measurements. This indicates that the high fiber fraction of 60%wt might have caused a non-uniform flow front at the end of flow due to the high suspension viscosity.
The measurements show that the nominal fiber concentration affects the degree of orientation in the core and shell layers as well as the width of the core layer. Figure 4.3 shows the preferential orientation a_{11} in the shell layer (left) and the orientation in cross-flow direction a_{22} in the core along with the core layer width (right) for all trials. In the shell layer, the fiber alignment in the direction of flow (a_{11}) increases with increasing nominal fiber concentration, the strongest alignment occurs with 50%wt, corresponding to a value of 0.85 for a_{11}. The cross-flow fiber orientation in the core also increases with increasing fiber concentration until 40%wt and slightly

reduces for higher concentrations. The maximum value for a_{22} in the core layer is 0.79 for PPGF40. The core width shows a steady increase from 0.09 at PPGF05 to 0.23 at PPGF60.

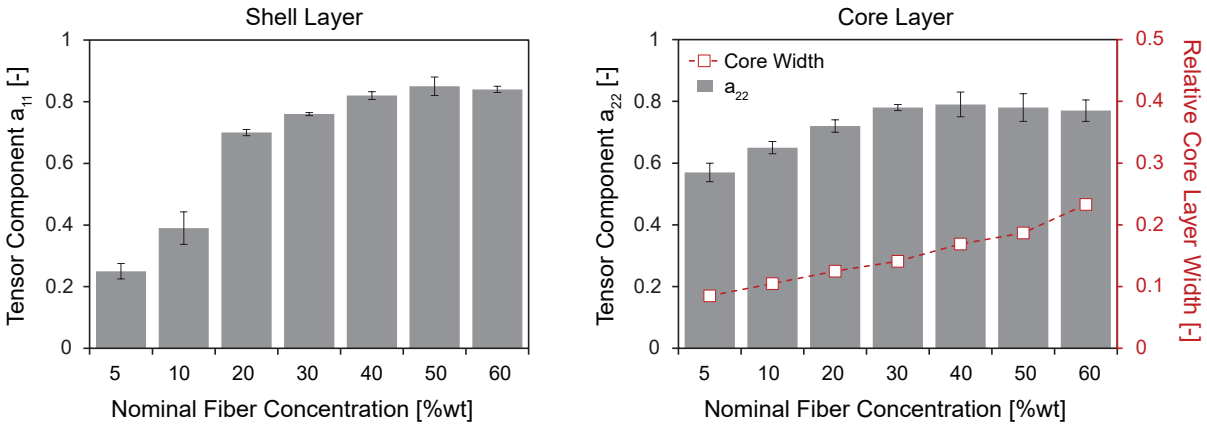

Figure 4.3.: Measured fiber orientation in the shell layer showing degree of in-flow alignment a_{11} (left) and core layer showing cross-flow alignment a_{22} (right) at Location 2 for all trials.

Bay [38] studied the fiber alignment in injection molded strips for varying fiber concentrations of short fiber-reinforced compounds (aspect ratio between 17 and 25). He reports increasing fiber orientation with elevating fiber concentration in the shell layers of his molded strip geometries. Since Bay also reports that the influence of the matrix material is negligible, a comparison with the present work can be done for the fiber alignment in the shell layers. Bay's measurements and the outcome of this work match well, as illustrated in Figure 4.4.

Although Bay's work does not demonstrate as large of a magnitude drop in fiber alignment at low nominal fiber concentration, the overall trend of increased alignment at higher fiber concentration is consistent between the two studies. This finding contradicts the pioneering work done by Folgar and Tucker [35], which found the opposite in their simple shear experiments

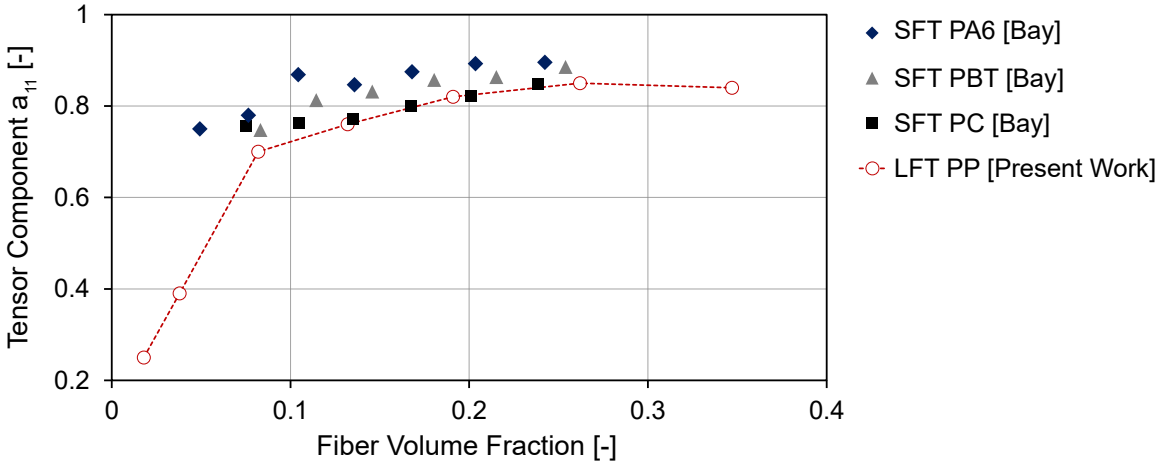

Figure 4.4.: Comparison of experimentally obtained fiber alignment in the shell layers: Results reported by Bay [38] for SFT compounds and measurements of the present work at Location 3.

with decreasing fiber orientation at increasing fiber concentration. The contrasts between this work and that of Folgar and Tucker will be further discussed in the modeling and simulation part of this dissertation (see Chapter 5.2).

4.1.2. Experimental Analysis of Fiber Breakage

The local fiber length was measured in the purged material and at three locations along the centerline of the molded plates. Figure 4.5 summarizes the obtained measurements represented by the number-average fiber length, L_N, and the weight-average fiber length, L_W, for all trials. Overall, the initial fiber length of 15 mm decreases substantially throughout the processing. The results show that increased nominal fiber concentration results in more fiber breakage and reduced fiber length in the molded plates. While additional fiber breakage occurs during mold filling, the majority of the length reduction occurs during plasticating, evident in the measured fiber length in the purged material. The longest weight-average fiber length, L_W, was 4.37 mm for PPGF10 (29.1% of the initial fiber length) and the shortest value for L_W was obtained for PPGF60 at 1.60 mm (10.7% of the initial fiber length). The measurements for PPGF05 and PPGF10 suggest a steady decrease in L_W from the purged material and along the sample locations in the molded plates. In the purged material, L_W was 4.11 mm for PPGF05 and 4.30 mm for PPGF10 and, by location 3, reduced to 3.09 mm (PPGF05) and 2.92 mm (PPGF10). At higher nominal fiber concentrations, the average fiber length increased from location 1 to location 3, suggesting that the last filled portion of the part carries longer fibers compared to the region close to the gate. The increase is most dominant at PPGF40 with a measured L_W value of 1.44 mm at location 1 and 1.75 mm at location 3, or a relative increase of 22%.

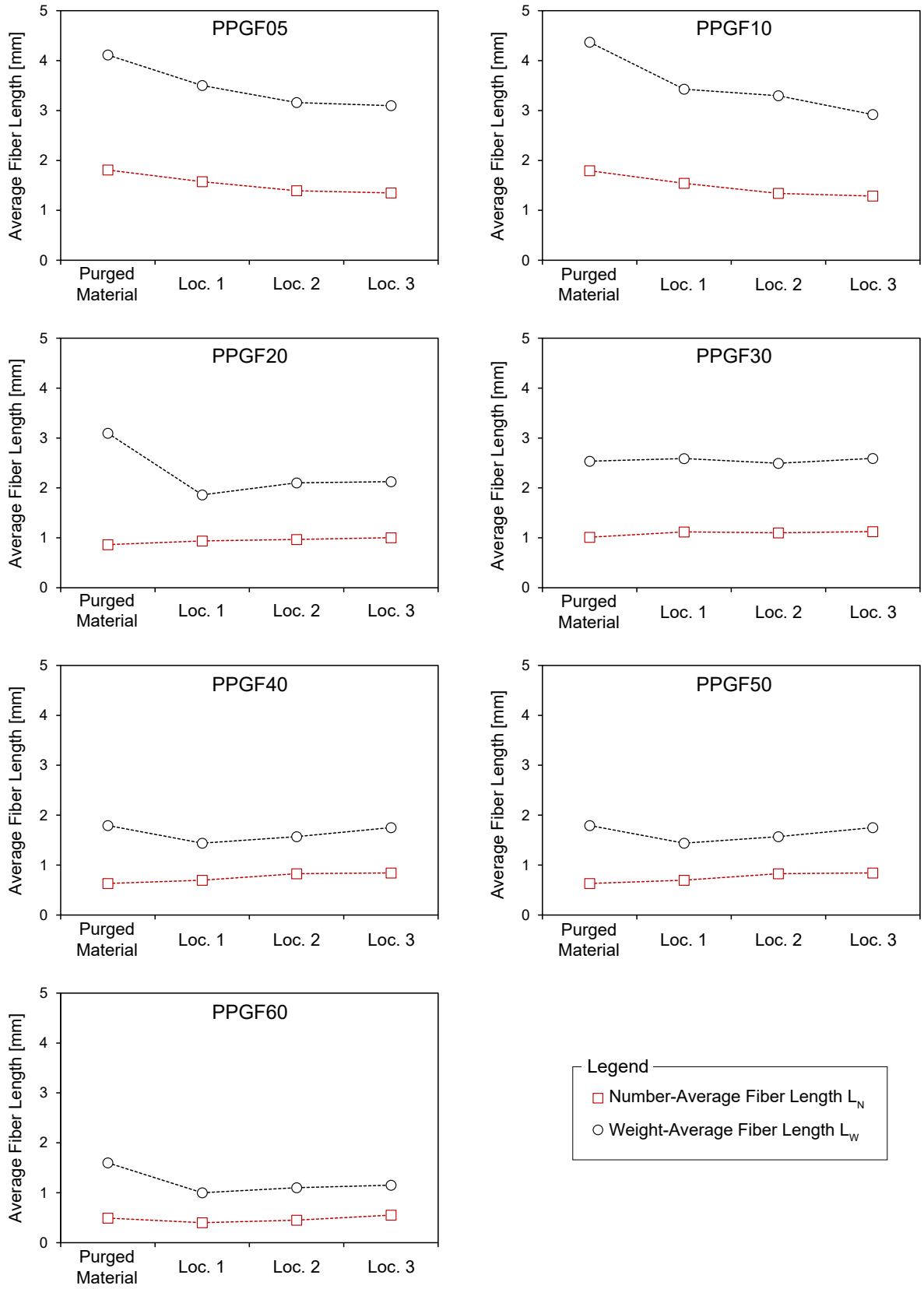

Figure 4.5.: Results of the local fiber length measurements for all trials, showing the number-average fiber length, L_N, and the weight-average fiber length, L_W at four locations: in the purged material, close to the gate (Loc. 1), at the center of the plate (Loc. 2), and at the end of the flow (Loc. 3).

Figure 4.6 shows the fiber length in the plate (averaged for locations 1 through 3) as a function of the nominal fiber volume concentration. Evidently, the fiber concentration has an impact on the residual fiber length. The effect is most distinct for weight-average fiber length, which decreases from 3.25 mm at PPGF05 to 1.08 mm at PPGF60. Overall, the measurements highlight the severe fiber breakage that is present during LFT injection molding. The measured weight-average in the plate is only 21.7% of the initial length (15 mm) for PPGF05 or less than 7.5% for PPGF60.

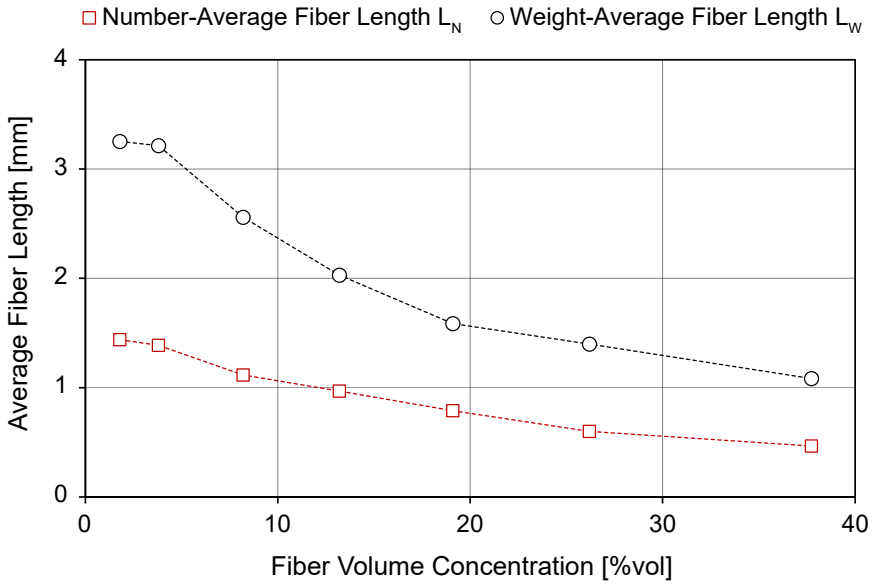

Figure 4.6.: Average fiber length in the molded plate for all trials (averaged for locations 1 through 3).

4.1.3. Experimental Analysis of Fiber Matrix Separation

Global Concentration Gradient Analysis using Pyrolysis

The global fiber concentration variation throughout the molded plates was determined by pyrolysis. The measurements for each trial were repeated three times. The results are depicted as variation relative to the nominal fiber volume concentration. As expected, the uniform filling pattern and the simple part geometry result in symmetric global fiber concentrations as shown in the obtained results for PPGF30 in Figure 4.7.

The average value for each trial is calculated averaging three repeated measurements and by averaging along the symmetry axis for each measured plate (Figure 4.7). The results for all trials are shown in Figure 4.8. The measurements show regions of low and elevated fiber concentration for each trial. PPGF05 has a peak of up to 20% higher fiber concentration along the center of the plate. PPGF10 to PPGF60 show a tendency of depleted fiber concentration close to the

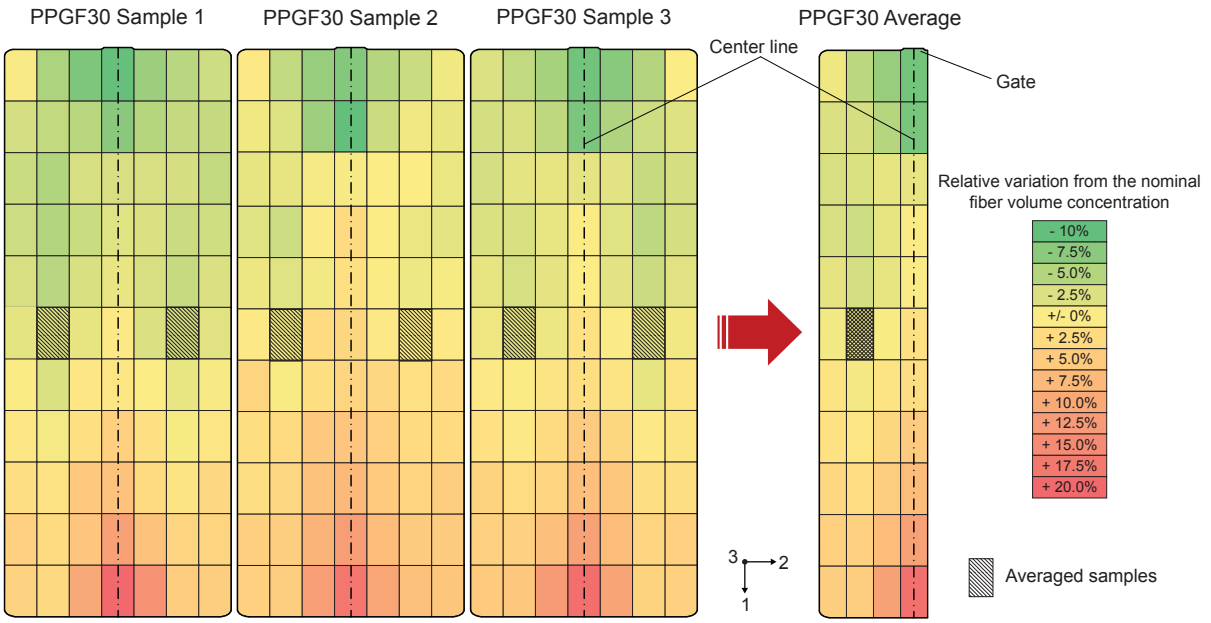

Figure 4.7.: Measured global fiber concentration for PPGF30 by pyrolysis: three repeated measurements and the resulting average.

gate and increased fiber concentration towards the end of the flow.

Figure 4.9 shows the variation of fiber concentration along the centerline of the molded part. The results for PPGF05 show a peak in the center of the plate for a large region (relative flow length of 0.2 to 0.7). The other trials show a common trend of -5.2% fibers close to the gate compared to the nominal fiber concentration and 11% more fibers at the end of the flow.

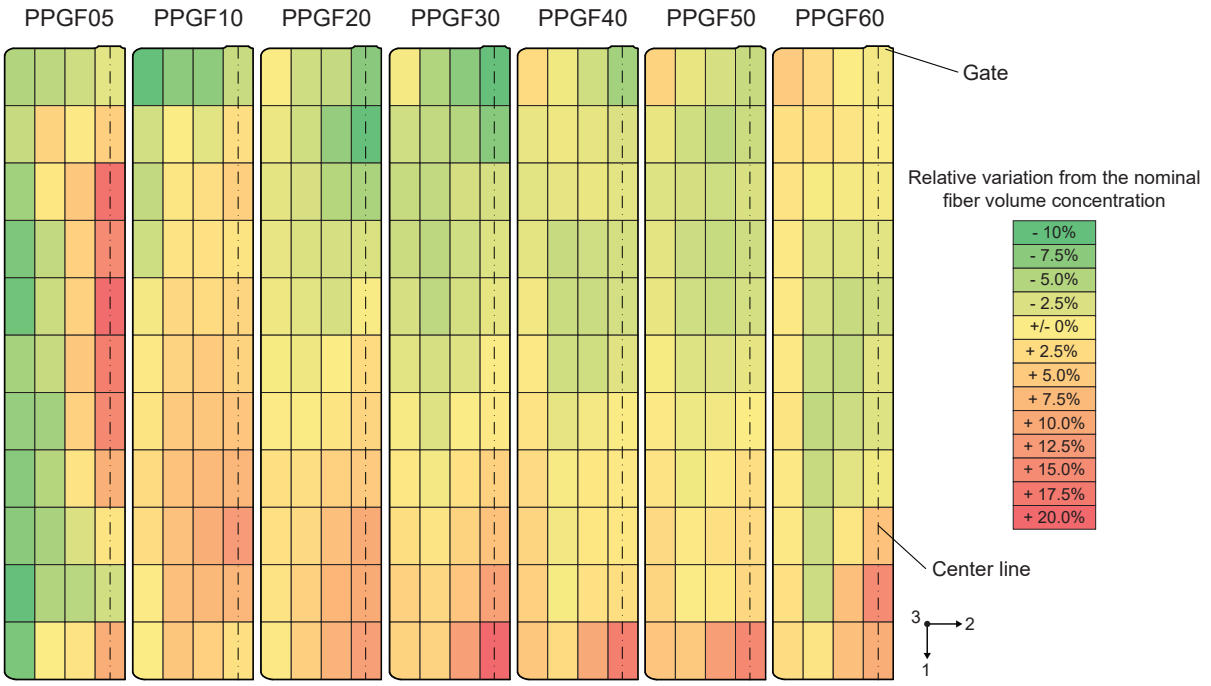

Figure 4.8.: Results of the global concentration gradient analysis for all trials.

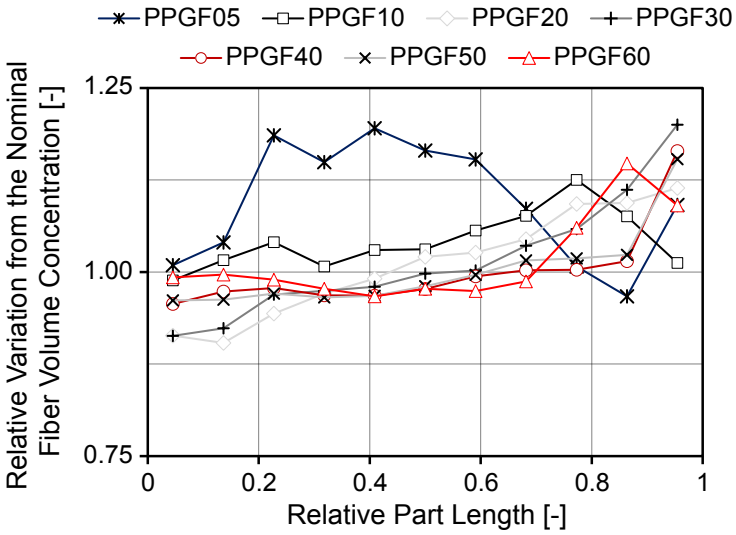

Figure 4.9.: Variation of fiber concentration along the plate length for all trials.

To evaluate the fiber concentration variation in the raw pellets caused by the material production, ten pellets were selected randomly and the weight fraction was determined through pyrolysis. The measurements were repeated ten times for the different pellet types used in this study. Additionally, the fiber concentration in the purged material (air shots) was measured to investigate the homogeneity of the material before the injection stage. Material from five air shots were recovered and 5 g randomly selected samples were measured. While the measured concentration in the pellets and the purged material are slightly below the nominal value, the measurements show that the fiber concentration is homogenous in the raw pellet material as well as after the plasticating phase in the purged material (Table 4.5).

Table 4.5.: Measured fiber concentration in the pellets and in the purged material.

Feed Material	Nominal Concentration	Measured Concentration in the Pellets	Measured Concentration in the Purged Material
PPGF20	20%wt	19.82 ± 0.44%wt	19.99 ± 0.08%wt
PPGF30	30%wt	29.32 ± 0.49%wt	29.45 ± 0.27%wt
PPGF40	40%wt	39.56 ± 0.63%wt	39.72 ± 0.10%wt
PPGF60	60%wt	59.49 ± 0.29%wt	59.30 ± 0.23%wt

Through-thickness Concentration Analysis using µCT

Figure 4.10 shows the measured through-thickness fiber concentrations at Locations 1, 2, and 3 for all trials. The results suggest that the fiber concentration varies substantially in the thickness

direction of all molded plates. The trials at higher concentrations (PPGF20 to PPGF60) show a common pattern in the measured concentration distribution. The measurements indicate a core layer with significantly higher fiber concentrations, which reach values of up to 1.5 times of the nominal concentration for PPGF40 (Location 2). The shell layer and surface region have fewer fibers. For samples close to the gate (Location 1), the width of the core layer is wider than at Locations 2 and 3. There are also secondary concentration peaks close to the sample surfaces (relative thickness of 0.1), reaching values of 1.05 (PPGF20, Location 2) to 1.5 (PPGF40, Location 2). Only PPGF60 shows a fairly constant through-thickness concentration at the end of the flow path (Location 3).

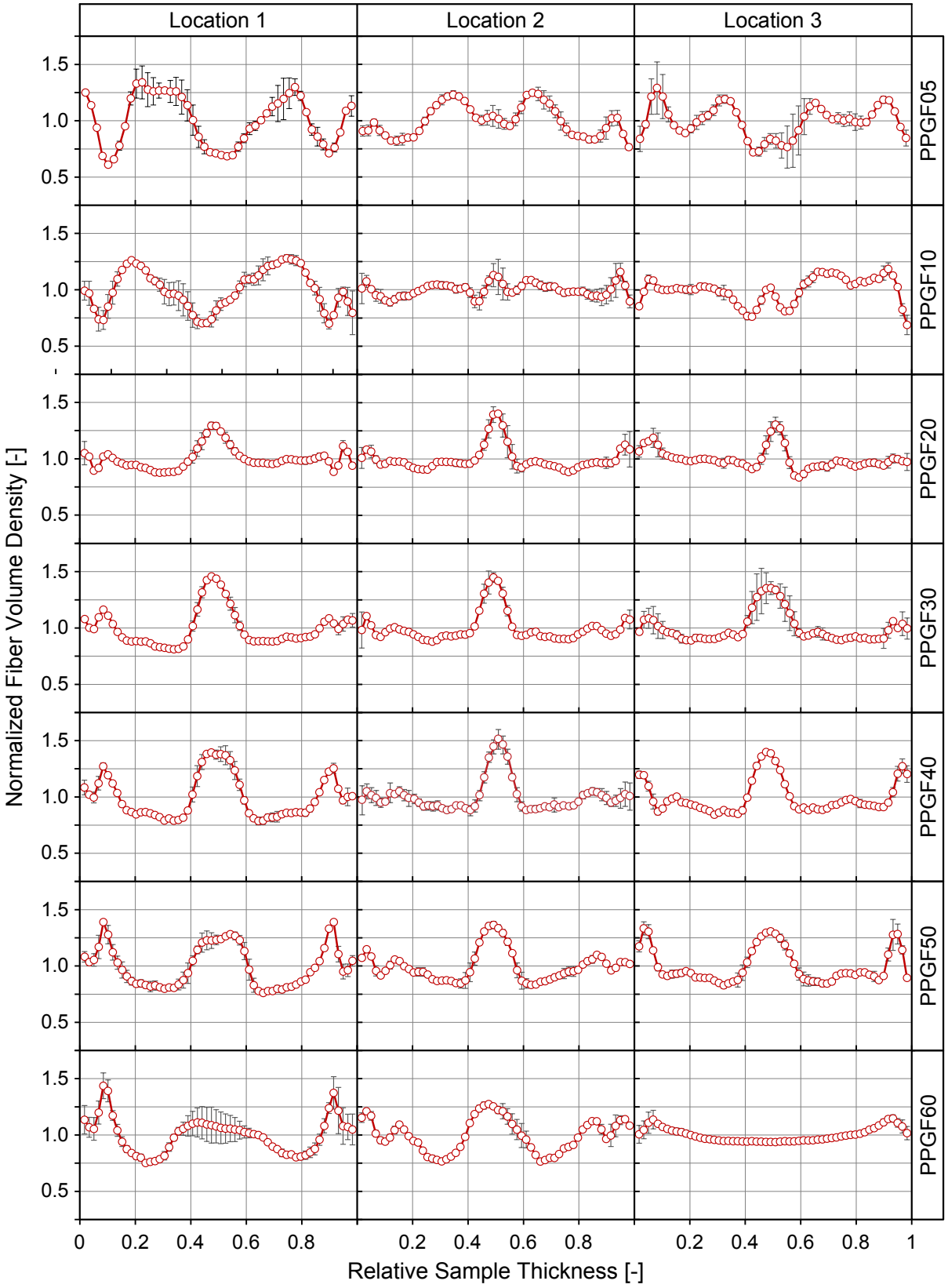

Figure 4.10.: Summary of the through-thickness fiber concentration of Locations 1, 2, and 3 for all trials.

The trials at diluted suspensions (PPGF05 and PPGF10) show a different trend in through-thickness fiber concentration. At Location 1, the core layers for both trials have a fiber depleted core with a normalized fiber concentration of 0.75 and these trials show a maximum of 1.25 in the transition region between shell and core at a relative thickness of approximately 0.3 (0.7). PPGF05 shows a similar pattern of a minimum in the core enclosed by two maxima at Locations 2 and 3 as well. On the other side, the PPGF10 results suggest a minor peak of approximately 1.1 in the core layer, which indicates a through-thickness pattern similar to these found at higher concentrations.

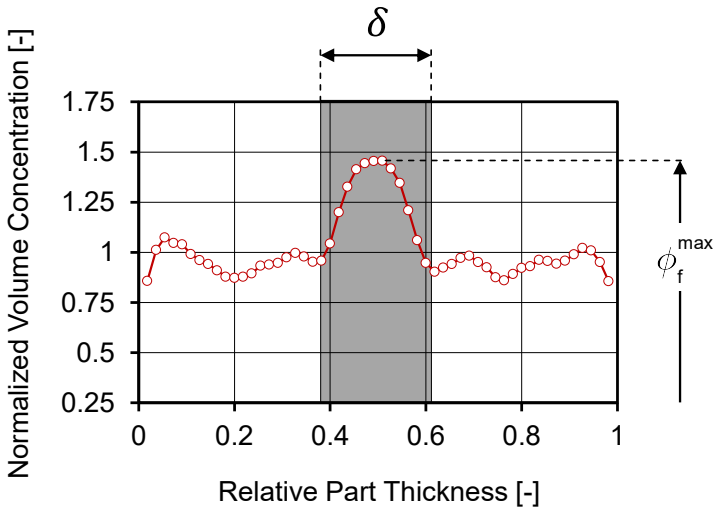

Figure 4.11.: Illustration of core layer thickness δ and fiber concentration maximum ϕ_f^{max}.

For a more concise evaluation, two characteristic values can be defined based on the shape of the normalized fiber volume concentration: the core layer width δ and the maximum fiber concentration in the core layer ϕ_f^{max}, as illustrated in Figure 4.11. The core layer width and maximum concentration measured at Location 2 for all trials is shown in Figure 4.12. The relative core width increases at higher nominal fiber concentrations from 0.10 (PPGF05) to 0.26 (PPGF60). While the maximum fiber concentration in the core layer is 0.97 for PPGF05, it increases to 1.50 for PPGF40, which is the overall highest fiber concentration for all trials. For PPGF50 and PPGF60, it decreases to 1.36 and 1.27, respectively.

Fiber Packing Density Analysis

The average distance between fibers is an important property indicating how densely the fibers are packed in the network and it can be used to further relate the microstructural properties. The average distance between fibers was determined from the µCT scans to obtain a better

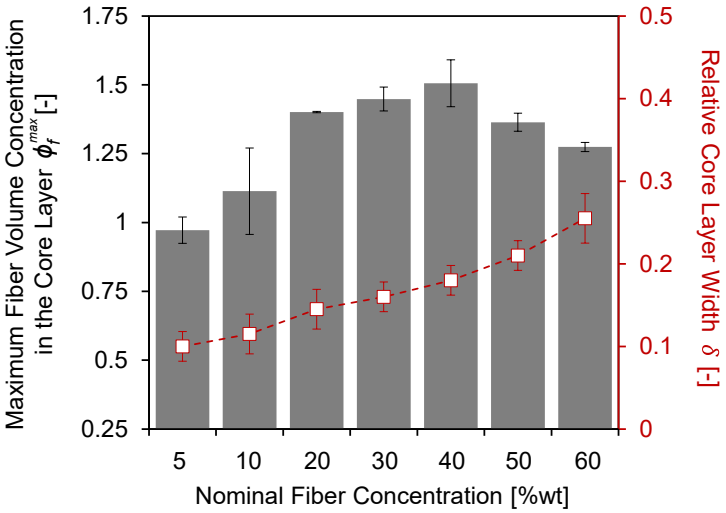

Figure 4.12.: Maximum fiber concentration in the core layer and core layer width at Location 2 for all trials.

understanding of the fiber packing density. For each individual fiber in the 2D slices, the distance of the closest adjacent fiber is determined by performing the nearest neighborhood algorithm in the image processing software Fiji [129], as illustrated in Figure 4.13. The analysis was performed on the center location of all samples. The shell and the core layer were analyzed separately for each sample by processing 2D slices of the in-flow direction and the cross-flow direction separately. Hence, the fibers in the corresponding layer are sliced perpendicularly, leading to a circular shape in the 2D slice, which improves the accuracy of the nearest neighborhood analysis.

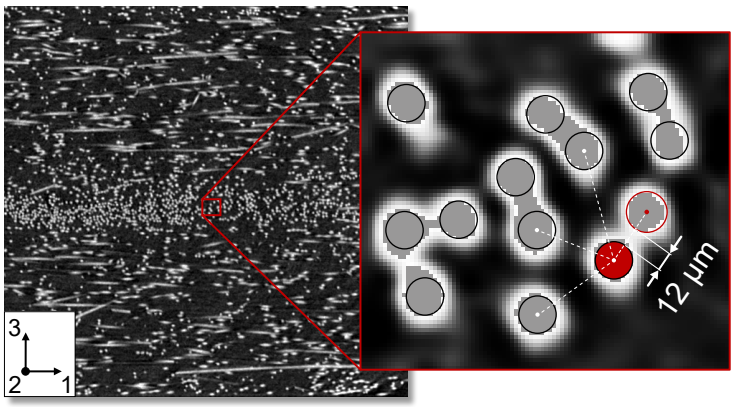

Figure 4.13.: Illustration of the packing density analysis using the nearest neighborhood algorithm.

Figure 4.14 summarizes the obtained average distance between fibers in the core and shell layer for all samples. As expected, the distance decreases from 68.1 µm (PPGF05) to 11.6 µm (PPGF60) with an increase in nominal fiber concentration. The findings at higher nominal fiber concentrations (PPGF20 to PPGF60) suggest that the average distance between fibers in the shell layer is larger than in the core layer. The difference between core and shell is the largest

for PPGF20, PPGF30 and PPGF40, while it is lowest for PPGF60. The PPGF05 measurements show a slightly larger average distance between the fibers in the shell than in the core. For the PPGF10, the measured distance is almost the same for core and shell. Due to the scan resolution of 5.25 µm, the results for higher fiber concentrations (PPGF50 and PPGF60) should be treated cautiously in terms of the absolute distance values obtained in this study.

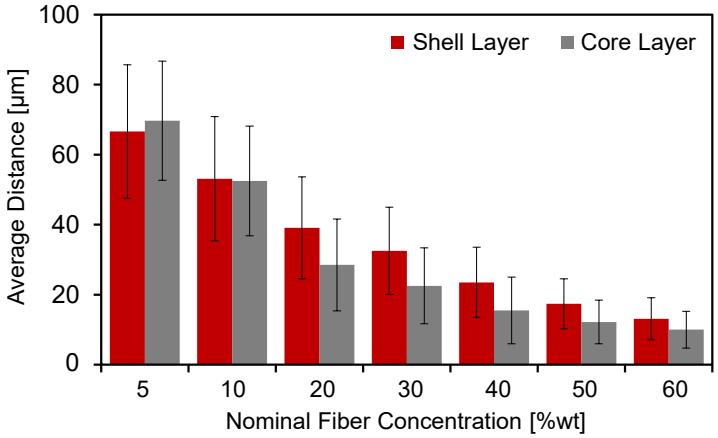

Figure 4.14.: Results of the fiber packing density analysis: Average distance between fibers in the shell and core layer.

Flow Front Analysis

Partial mold fillings were conducted to investigate the transient fiber concentration during mold filling and at the flow front. The partial mold fillings, or short shots, were molded at the same processing conditions without a packing phase for the PP with a nominal fiber concentration of 40%wt (PPGF40). Short shots at 25%, 50%, 75% and 90% fill were done and the fiber concentration was measured using µCT and pyrolysis. Figure 4.15 shows photographs of partially molded parts and the relative sample locations, which are 5 mm, 10 mm and 17 mm from the advancing flow front. Additional measurements of the local fiber concentration through pyrolysis were performed to obtain the fiber concentration gradient along the flow length. Slices between 5 mm and 15 mm were cut from a 20 mm wide strip along the center line of the partial mold fillings.

Figure 4.16 shows the measured through-thickness fiber concentration for the partially filled moldings at a nominal fiber concentration of 40%wt (PPGF40). The results suggest a fairly uniform fiber concentration through the thickness at the flow front without a distinct fiber agglomeration in the core layer for all fillings (Figure 4.16, left), but a decreased fiber concentration towards the surface. At 10 mm from the flow front (Figure 4.16, center), the measurements sug-

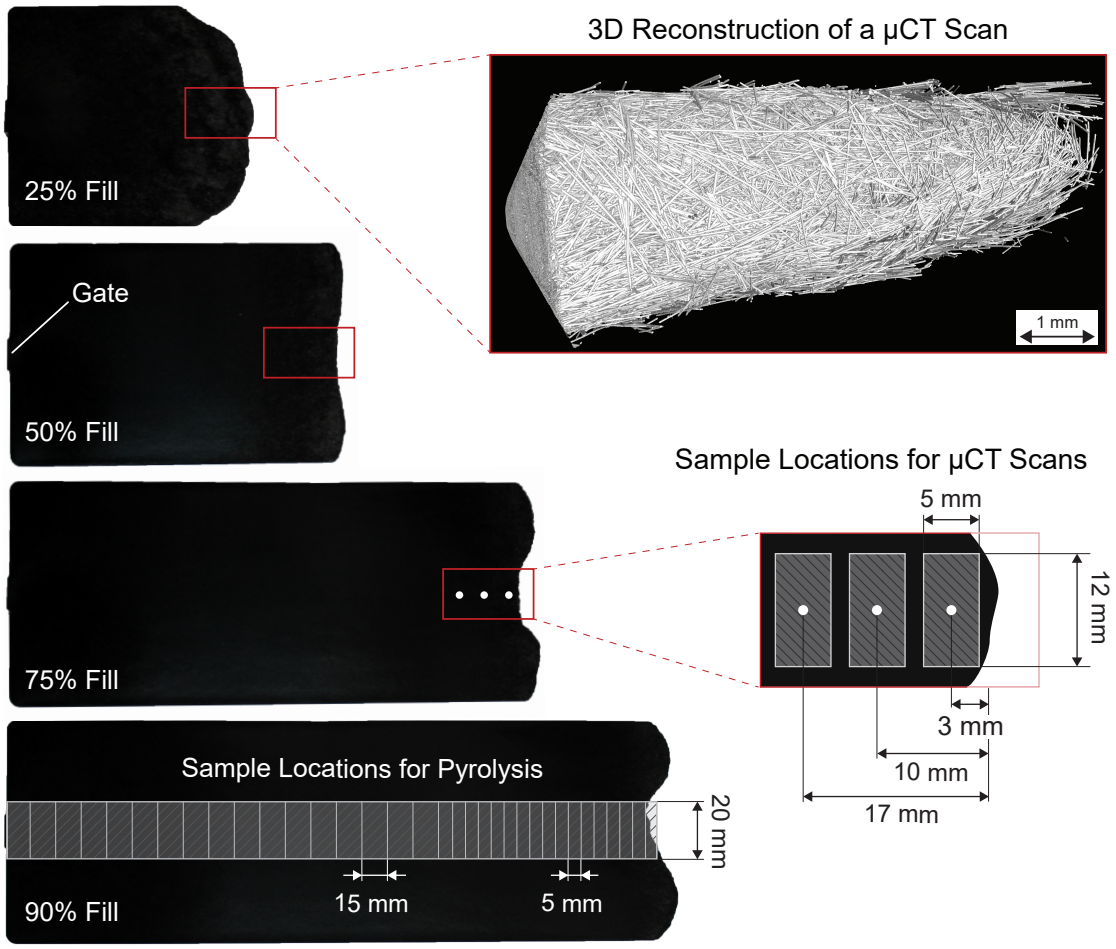

Figure 4.15.: Flow front analysis: PPGF40 short shots (photos) at 25%, 50%, 75% and 90% fill, 3D reconstruction of a µCT scan of the flow front, and sample locations for the measurements.

gest fiber agglomerating in the core. The peak in fiber concentration in the core decreases with increasing mold fill; the peak is 1.5 times the nominal fiber concentration at 25% fill and 1.1 times the nominal fiber concentration for 90% fill. The analysis of samples extracted 17 mm from the flow front show the most distinct core-shell structure. The peak fiber concentration in

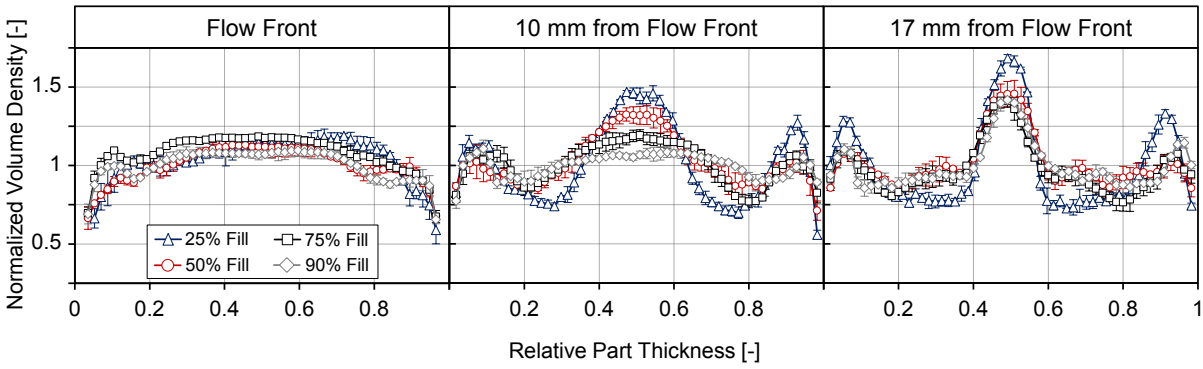

Figure 4.16.: Measured through-thickness fiber concentration at the flow front for partially filled cavity molding (25%, 50%, 75% and 90% fill) at a nominal fiber concentration of 40%wt (PPGF40): At the flow front (left), 10 mm from the flow front (center) and 17 mm from the flow front (right).

the core shows a maximum of approximately 1.4 for 50%, 75% and 90% fill. For the 25% fill, the peak is larger at 1.6 times the nominal fiber concentration.

Figure 4.17 summarizes the measured local fiber concentration with increasing distance from the melt front (three repeated measurements per location). The measurements suggest a substantial peak at the flow front itself can be observed, which reaches between 48%wt for the 75% mold fill and up to 54.7%wt for the 25% mold fill trial. Values above the nominal concentration (40%wt) are measured up to 25 mm from the flow front. At distances above 25 mm, the measured fiber concentration is on average 38.5%wt.

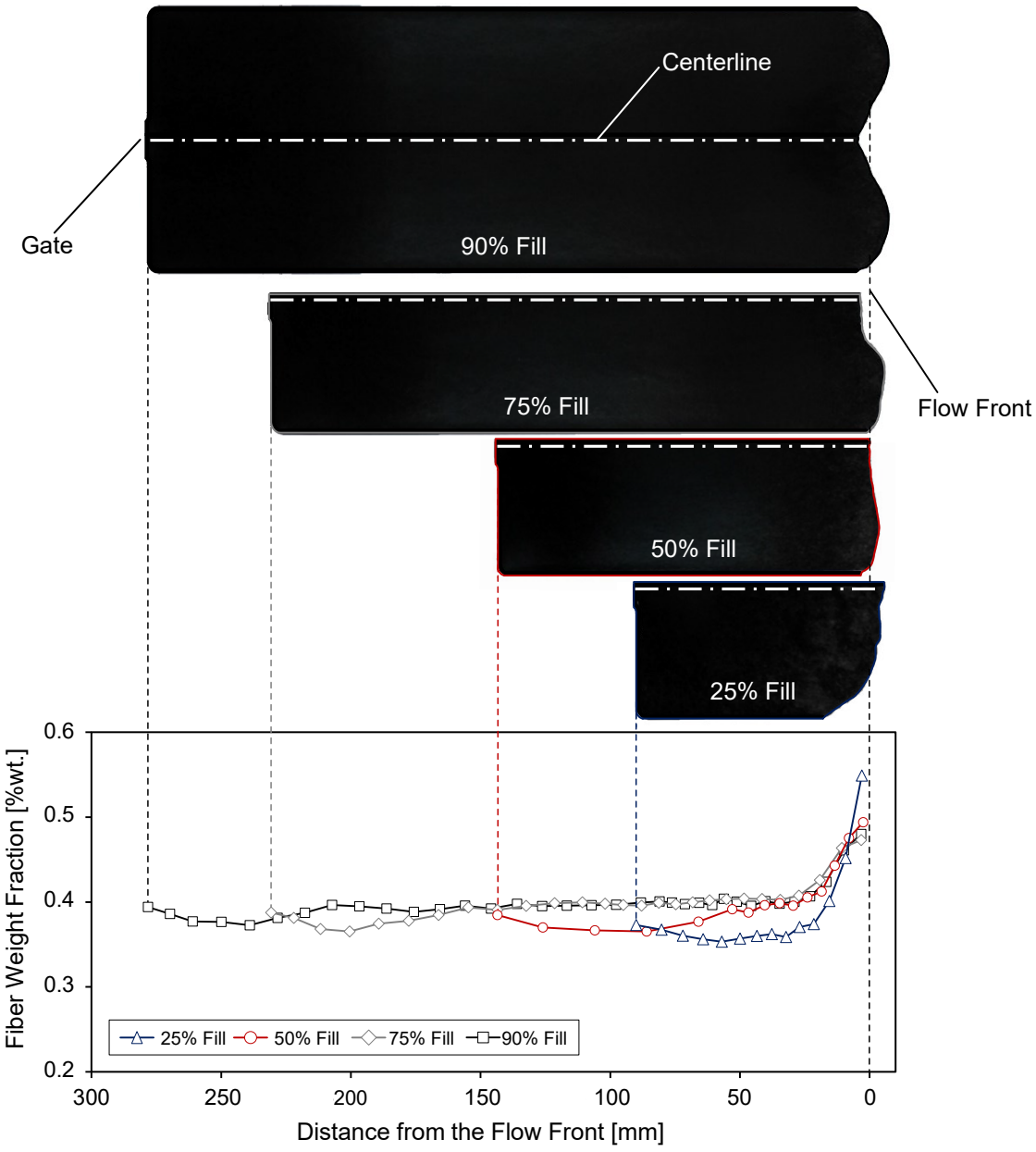

Figure 4.17.: Measured fiber concentration with increasing distance to the flow front for partial mold fillings (25%, 50%, 75% and 90% fill) at a nominal fiber concentration of 40%wt (PPGF40). The illustration of the partial mold fillings for reference (top).

4.1.4. Discussion of Injection Molding Experiments

The results of this experimental study highlight the substantial impact of the process on the microstructure, inducing a heterogeneous fiber configuration along the flow path as well as through the thickness of the injection molded plates.

The through-thickness orientation at higher fiber concentrations (PPGF20 to PPGF60) show the expected core-shell-skin pattern (see Section 2.1). The measurements suggest that the fiber alignment in both the core and shell slightly increases with increasing concentration. Throughout all trials, the core layer width increases steadily from a relative width of 0.09 at PPGF05 to 0.23 at PPGF60. The measurements at lower concentrations (PPGF05 and PPGF10) suggest an additional layer in the through-thickness fiber orientation. This might be related to the packing density of the fibers and the free volume of the fibers in the suspension. In general, a suspension of randomly oriented rods can be divided into three regimes, depending on the volume concentration, ϕ_f, and the aspect ratio, a_r, of the fibers [130]. In the *dilute regime* ($\phi_f < 1/a_r^2$), fibers are sufficiently far apart so that there are no contacts between neighboring fibers. The *semi-concentrated regime* is characterized by some restrictions of fiber movement due to interactions between adjacent fibers. The movement and rotation of fibers in the *concentrated regime* is highly restricted in all direction and the high packing density results in constant interactions between fibers. Evans and Gibson [131] found experimentally that the maximum volume concentration for randomly oriented fibers can be computed by $\phi_{f,max} = 5.3/a_r$. This relationship

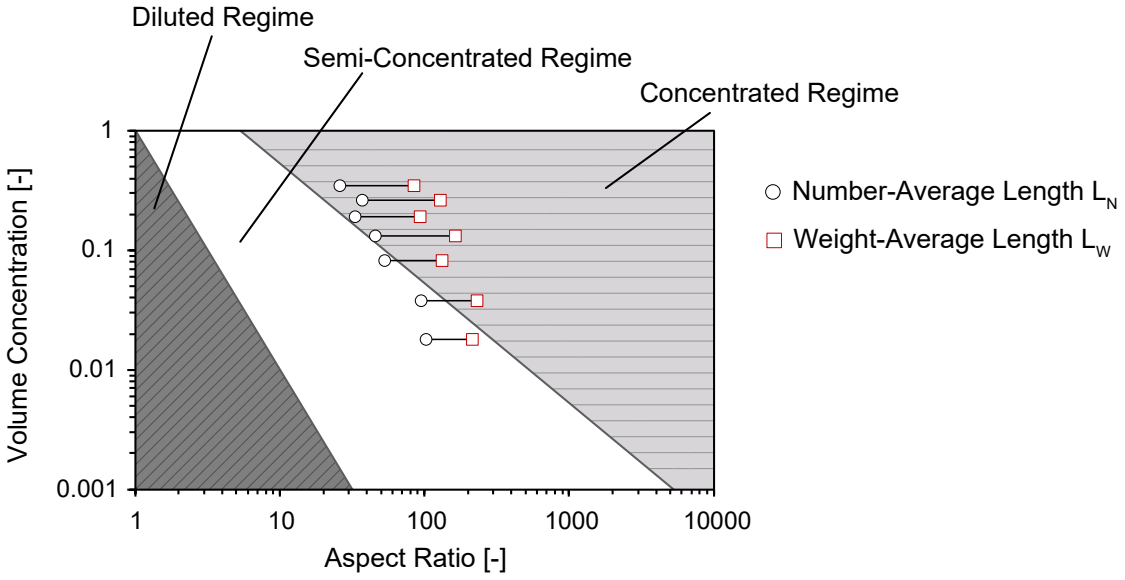

Figure 4.18.: Illustration of the concentration regimes for fiber suspension and measured fiber aspect ratio from all trials in this study.

can be used to estimate the dividing line between semi-concentrated and concentrated regimes [132]. Figure 4.18 illustrates the three regimes and indicates the location of the measured fiber lengths from all trials in this study. The PPGF05 and PPGF10 are within the semi-concentrated regime, suggesting that the fibers have less restriction in movement as opposed to trials with higher concentrations. Hence, this might explain the additional orientation layer for the lower fiber concentrations as the fibers have room and more free volume to move and rotate during mold fill.

The analysis of the through-thickness fiber concentration showed a substantial fiber agglomeration in the core layer and fewer fibers in the shell layers. Figure 4.19 shows a stitched set of low resolution µCT scans of a complete PPGF40 plate (left) and 2D slices of high resolution scans of the core layer and the shell layer respectively (right). This figure highlights qualitatively the fiber concentration gradient induced by injection molding process. At a nominal fiber concentration of 40%wt, the measurements suggest 1.5 times the normal concentration of fibers in the core. The degree of fiber agglomeration can safely be assumed to have an impact on the other microstructural properties.

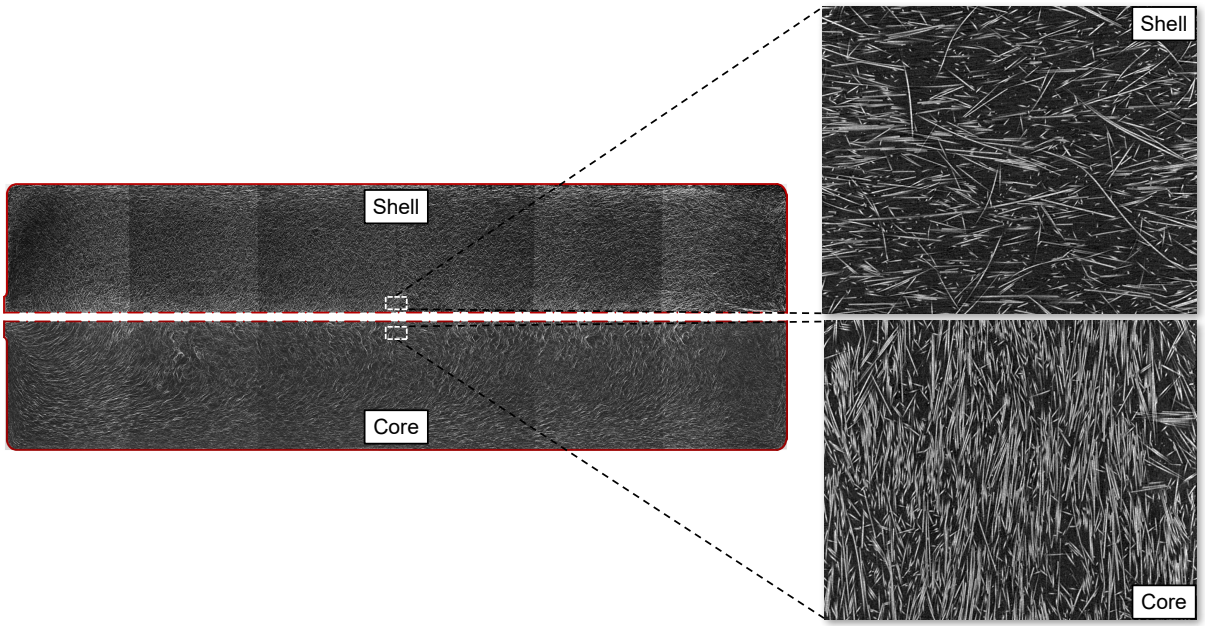

Figure 4.19.: Qualitative illustration of the process-induced fiber matrix separation in LFT injection molding for PPGF40: Stitched set of low resolution µCT scans (left) and 2D slices of high resolution scans of the core layer and the shell layer (right).

The measured through-thickness fiber concentration shows a core-shell pattern similar to that found in the fiber orientation analysis. In fact, the measurements suggest a correlation between the through-thickness orientation and concentration of the fibers. Figure 4.20 shows combined

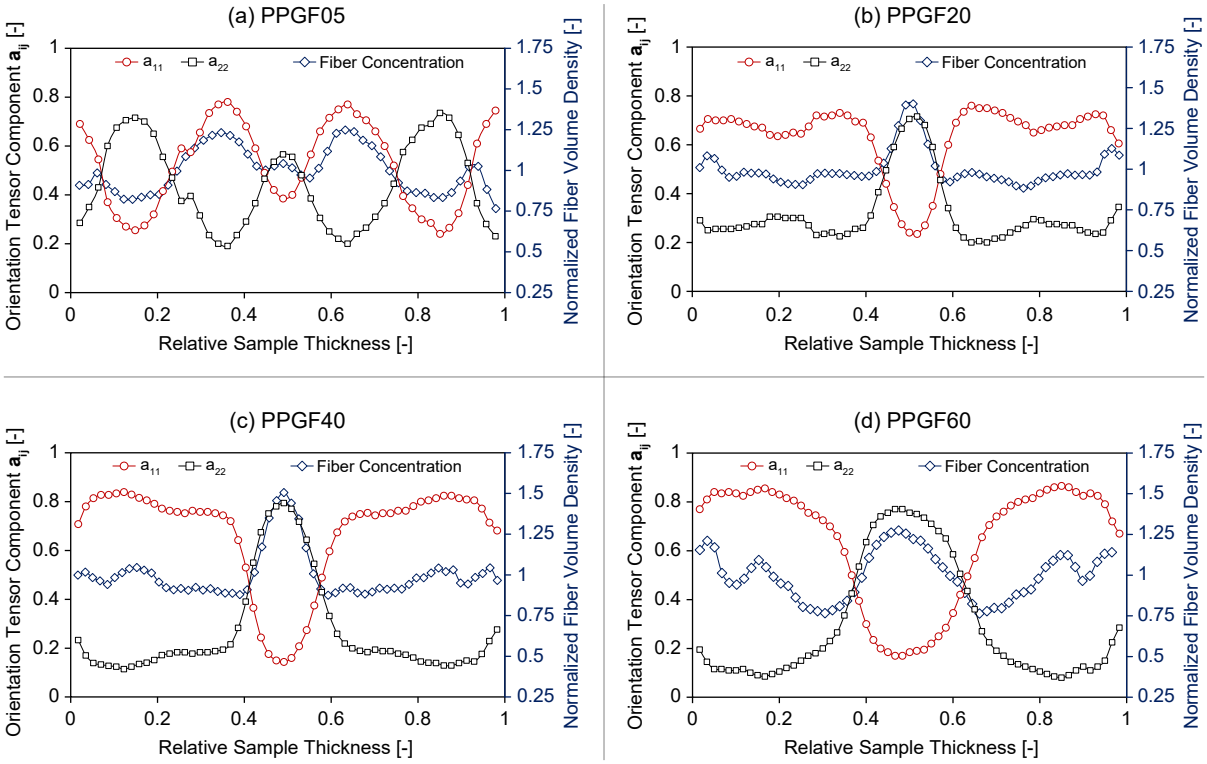

Figure 4.20.: Correlation of the through-thickness fiber concentration and fiber orientation for PPGF05 (a), PPGF20 (b), PPGF40 (c), and PPGF60 (d) at Location 3.

plots of the through-thickness analysis for PPGF05 (a), PPGF20 (b), PPGF40 (c), and PPGF60 (d) at Location 3. The fiber agglomeration in the core aligns with the fiber alignment in the core layer. Noticeably, the width of core layer for both the fiber concentration and the fiber orientation matches well. Particularly interesting is the correlation for PPGF05 with the two layers surrounding the core layer. In these two layers, the maximum fiber concentration coincides with the peak fiber alignment along the direction of flow (a_{11}).

The emerging core-shell-skin pattern for the fiber orientation is attributed to the fountain flow effect [35, 41] (see also Chapter 2.1.1). The observed through-thickness fiber concentration distribution might also be related to the fountain flow phenomenon, as the overall deformation at the advancing flow front causes substantial reorientation of the fibers. The degree of fiber alignment determines how closely the fibers can pack together, or vice versa.

The fiber concentration at any stage during mold filling is not low enough to allow a completely random fiber orientation. In fact, the fiber concentration in most of the trials is in the concentrated regime, as previously shown in Figure 4.18. Hence, the fibers need to be always aligned to some degree. The peak fiber concentration found at the advancing flow front in the PPGF40 partial mold fillings implies strong fiber alignment to accommodate the agglomerating fibers.

This high packing density at the flow front might not be able to carry through the reorientation process at the advancing flow front, at least not for all fibers at the flow front. Hence, the fiber concentration in the shell layers is lower than in the core. Furthermore, Andersson and Toll [40] suggest that the fibers in the core are compressed by the fibers that move through the fountain flow. Furthermore, they argue that stresses emerge acting on the core layer fibers due to the elasticity of the fibers going through the reorientation process, which further compresses the fibers in the core layer and packs them more densely. This hypothesis would also explain why the trials at diluted concentrations (PPGF05 and PPGF10) show different trends in the through-thickness concentration. The low fiber concentration in these trials allows for more random fiber orientation through the part and the alignment-concentration dependence is not as pronounced.

The analysis of fiber concentration through pyrolysis for the entire molded plate shows that there is also a global concentration gradient. The measurements show increasing fiber concentration along the flow path for all trials. While the concentration peak for PPGF05 is in the center of the plate, the measurements of the other trials suggest peaks at the end of the flow. Throughout all trials, the samples close to the gate have the lowest fiber concentration. The findings are aligned with what has been reported in other studies [40, 47–51], which show similar trends.

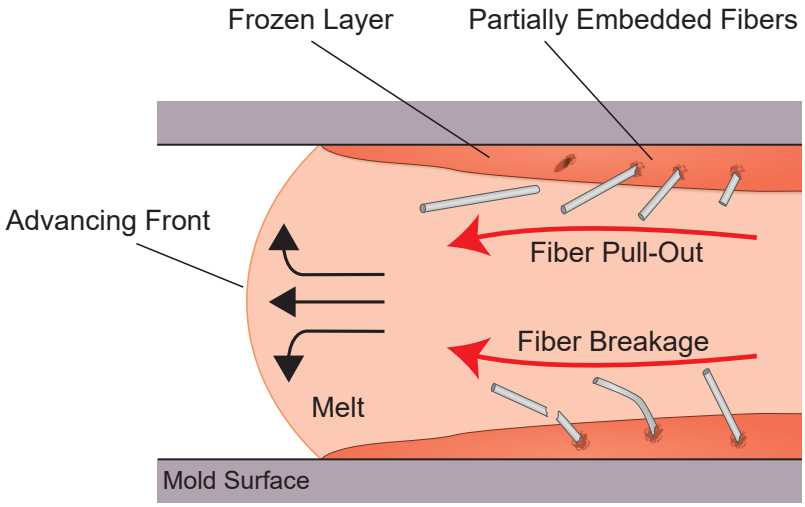

Figure 4.21.: Fiber pull-out and fiber breakage during cavity filling due to partly embedded fibers.

Although no clear explanation for this phenomenon has been established, a reasonable hypothesis for the variation is the interaction between partially embedded fibers and the molten core at the interface of the solidified layer during mold filling. Two mechanisms can cause a change in fiber concentration, as shown in Figure 4.21. Partially embedded fibers in the solidified layers

are exposed to deformation and stresses caused by the advancement of the molten core during cavity filling. Ultimately, the fibers can be either sheared off or pulled out and swept along with the molten core. Either mechanism can result in an increased fiber concentration at the last filled part of the cavity. Analyzing the fiber concentration of the partial mold fillings lends support to the theory because it shows a significant peak in fiber concentration at the melt front for all partial mold fillings. This peak suggests that an elevated concentration of fibers is carried along the flow front. Measurements of the raw pellet material and plasticated material before the injection phase (purged material) confirm that the fiber concentration is constant. Hence, the observed concentration gradients in the molded plates are due to the process-induced fiber matrix separation during cavity fill.

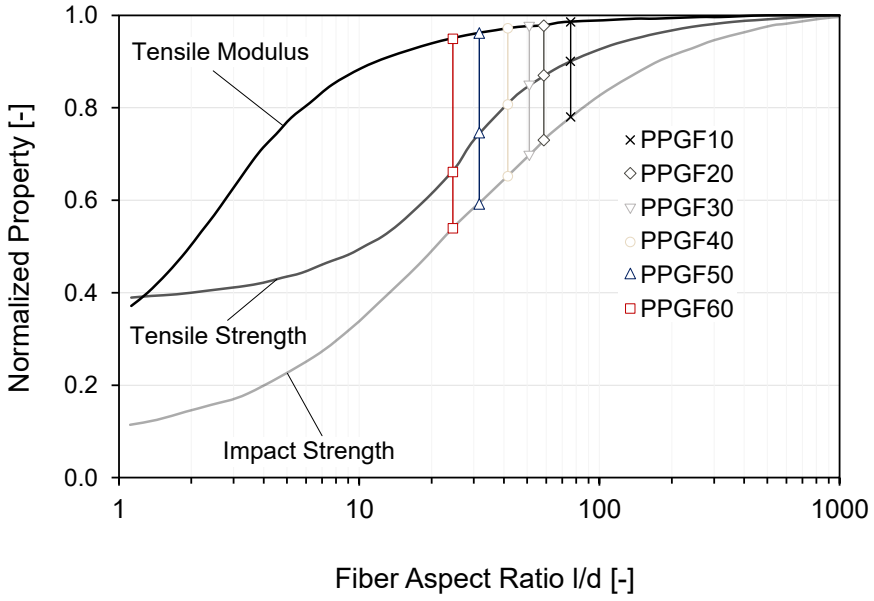

Figure 4.22.: Qualitative illustration of the normalized mechanical properties as function of fiber aspect ratio for tensile modulus, tensile strength, and impact strength, adapted from [71]. The graph shows the measured residual fiber length in the molded plates (L_N), indicating the expected normalized properties.

The fiber length measurements suggest that substantial fiber breakage occurs throughout the entire process. The residual weight-average fiber length, L_W, in the molded plates reduces to approximately 3.25 mm for PPGF05 and 1.08 mm for PPGF60. Figure 4.22 shows a qualitative illustration of the expected effect on the mechanical properties using Schemme's graph [71] (see also Section 2.1.4), highlighting the challenges that process-induced fiber breakage poses for the mechanical performance of the molded part. For all nominal fiber concentrations, Schemme's work suggests that the measured residual lengths are within a range where tensile strength and impact strength are very sensitive to the residual fiber length. Hence, even slight improvements

in preventing fiber breakage could significantly increase the mechanical performance, while small decreases in fiber length could significantly degrade performance.

4.2. Fiber Breakage Study under Controlled Conditions

The results from the previous chapter on fiber breakage in injection molding highlight the severe reduction of fiber length during processing. However, investigating the underlying physics of fiber breakage experimentally in an injection molding process is challenging, because of the complex and changing flow conditions that the fibers are exposed to throughout the various stages of the process. The plasticating stage was identified as the main source of fiber breakage, reducing the fiber length from initially 15 mm to less than 10% of the initial length (PPGF60) before cavity fill. Isolating the mechanisms that cause the fiber breakage during plasticating is limited due to the overlapping effects of fiber-fiber interactions, fiber-mold wall interactions, hydrodynamic effects and, especially, melting effects (see Chapter 2.1.3). At the same time, researchers have expressed the need for basic experimental studies at defined processing conditions to develop a theoretical framework for modeling fiber breakage [5].

Consequently, an experimental setup was developed as part of this work to study fiber breakage under controlled conditions. The device is a scaled Couette rheometer [133], consisting of concentric inner and outer cylinders with a annular gap, as shown in Figure 4.23. While the inner cylinder rotates at a defined speed Ω (or torque $\mathbf{T}$), the outer cylinder is stationary, exposing the material to a simple shear flow within the annular gap. The temperature is controlled through

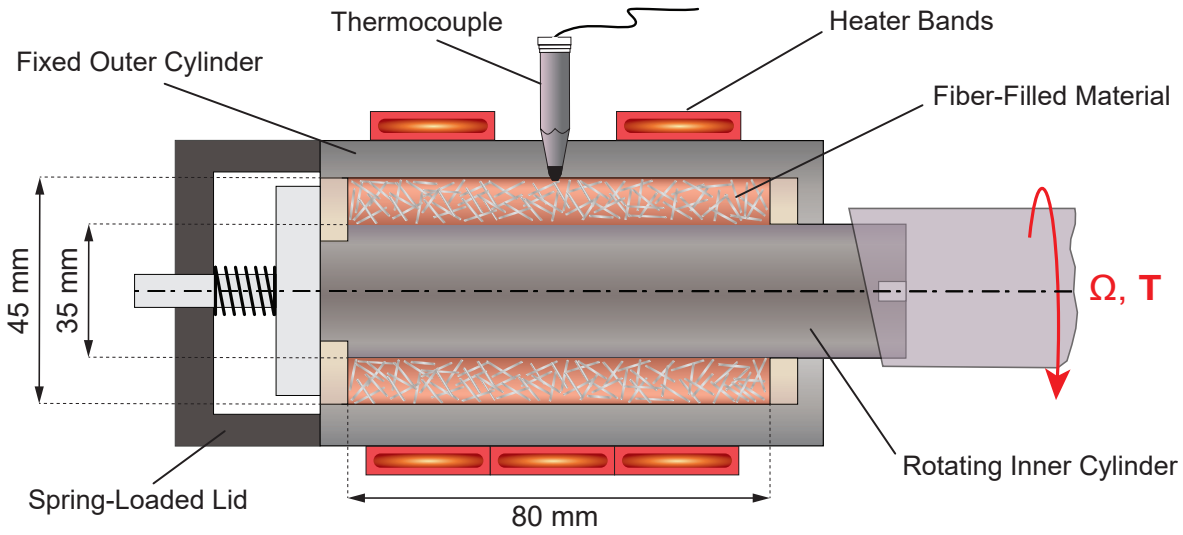

Figure 4.23.: Illustration of the Couette Rheometer set-up for fiber breakage study.

insulated heater bands surrounding the outer cylinder and a thermocouple measuring the melt temperature. The dimensions of the Couette rheometer are designed to be characteristic of the conditions during plasticating in injection molding. The diameter of the inner cylinder is 45 mm, the annular gap is 5 mm, and the length of the annular volume is 80 mm. Ultimately, the characteristic dimensions of the Couette rheometer setup allow a correlation of the findings to regular LFT processes. The Couette rheometer setup is attached to the drive unit of a Plasti Corder^{TM} torque rheometer (C.W. Brabender Instruments Inc., Hackensack, NJ), controlling the rotational speed or torque of the inner cylinder. The individual parts, photos, and technical drawings of the Couette rheometer are shown in Appendix B.

The experimental setup and the experimental plan were conceptualized to isolate and quantify the effects that drive fiber breakage in LFT processing for controlled conditions. The objective of this procedure is to obtain a fundamental and quantitative understanding of the underlying physics of fiber breakage, which can be related to LFT injection molding. The setup allows control of the following processing conditions:

- Melt temperature, T_{Melt}
- The processing speed, Ω, or Torque, $\mathbf{T}$
- The residence time, t_R

Additionally, the influence of the material properties on fiber breakage can be studied by selecting corresponding compounds with defined nominal fiber concentration ϕ_f, initial fiber length $L_{Initial}$, and matrix material. Table 4.6 summarizes the framework for the experimental study and highlights the process characteristics that can be investigated with the developed setup. The experimental procedure and the design of experiments are discussed in the next section.

The degree of fiber breakage can be quantified along the dimensions *processing conditions* and *material properties* using the Couette rheometer setup. To comprehend the impact of these dimensions on fiber breakage and capture it analytically, a mathematical framework is adapted and applied. Shon et al. [134] proposed a basic kinetic model to describe the fiber breakage in continuous and batch mixers. Their model suggests that the rate of fiber length reduction is described by

$$\frac{\mathrm{d}L}{\mathrm{d}t} = -k_f \left(L_0 - L_\infty\right) \tag{4.1}$$

where L_0 is the starting fiber length, L_∞ is the asymptotic value and k_f is the fiber breakage rate

constant. The parameters L_∞ and k_f are fitting parameters, depending on the flow conditions and material properties [134]. The interpretation of L_∞ is that a minimal fiber length exists at which no further breakage occurs for given process conditions. Integrating equation 4.1 yields the exponential decay function

$$L(t) = (L_0 - L_\infty)\, e^{-k_f t} + L_\infty \tag{4.2}$$

Shon et al. did not discuss the implications of the model parameters k_f and $L_{Initial}$ nor propose any physical interpretation for the parameters. However, the model offers a concise way of capturing fiber attrition in the Couette rheometer. Hence, it is applied to fit the experimental data and compare the impact of processing conditions and material properties. The graphical interpretation is illustrated in Figure 4.24, showing arbitrary obtained measurements and the fitted decay function.

A general hypothesis regarding the influence of processing conditions and material properties can be stated as follows

$$L_\infty = f\,(\,\phi_f,\, L_0,\, d,\, \sigma_u,\, \dot{\gamma},\, \eta\,(T, \dot{\gamma}\,)) \tag{4.3}$$

$$k_f = f\,(\,\phi_f,\, d,\, \sigma_u,\, \dot{\gamma},\, \eta\,(T, \dot{\gamma})\,) \tag{4.4}$$

where ϕ_f (fiber concentration), d (fiber diameter), L_0 (initial fiber length) and σ_u (ultimate strength of the fiber) are material properties, while $\dot{\gamma}$ (shear rate) and $\eta\ (T, \dot{\gamma})$ (suspension viscosity) are process conditions.

Table 4.6.: Proposed target values for the experimental fiber attrition study.

Processing Parameters	**Impact on Fiber Breakage**
T_{Melt}	Suspension viscosity and degree of hydrodynamic stress
t_R	Total deformation of the material, rate of fiber breakage and steady state fiber length
$\dot{\gamma}$	Degree of hydrodynamic stress, fiber-fiber interactions and fiber-wall interactions
$(\dot{\gamma}\, t_R)$	Total deformation of the material
Material Property	**Impact on Fiber Breakage**
ϕ_f	Fiber-fiber interactions and suspension viscosity
$L_{Initial}$	Change in the rate of breakage
Matrix Material	Suspension viscosity and degree of hydrodynamic stress

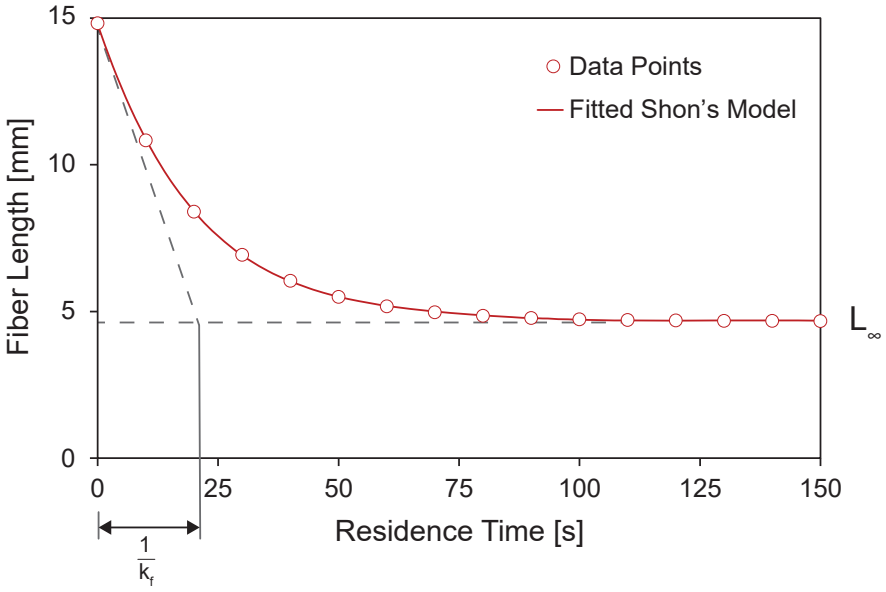

Figure 4.24.: Illustration of an arbitrary fiber length reduction over time in the Couette rheometer fitted by Shon's kinetic model [134].

4.2.1. Experimental Methodology and Design of Experiments

All experiments were conducted under isothermal conditions to exclude any fiber breakage due to melting effects and interactions of fibers with partially molten pellets. Before the beginning of each experiment, the unfilled Couette rheometer is heated up to the defined processing temperature. The material at ambient temperature is filled in the annular gap until completely full. The filling processes takes less than 120 s, using a specially designed funnel system. The processing begins only when the material has reached the defined temperature. Depending on the nominal fiber concentration, the heat-up time takes up to 5 min. To ensure a uniform temperature in the melt, the temperature is measured with an external immersion thermocouple. The Couette rheometer is closed and attached to the Brabender as soon as the desired melt temperature is reached. The lid is spring loaded, forcing the inner cylinder to move out of the fixed outer cylinder, as shown previously in Figure 4.23. This ensures that any air trapped within the material is removed.

The material is processed at a constant rotational speed of the inner cylinder and for a defined period of time. After processing, the still molten sample is removed from the Couette and prepared for fiber length measurements, according to the developed fiber length presented in Chapter 3.3. From each processed specimen at least two samples were extracted for the fiber length analysis. Figure 4.25 shows a typical specimen after being processed in the Couette rheometer and the sample locations for the fiber length measurements.

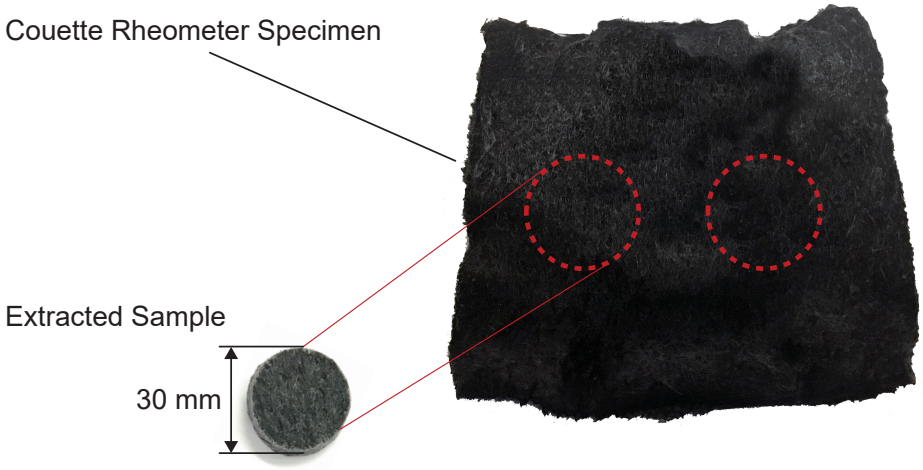

Figure 4.25.: Photo of a molded Couette rheometer specimen and the locations for extracting two samples (Ø=30 mm) for the fiber length analysis.

All Couette rheometer experiments are performed with the same glass fiber-reinforced PP as used in the injection molding trials (SABIC STAMAX^{TM} PPGF) and the material properties are listed in Section 4.1.

The experimental plan is divided into three studies. The first study examines the fiber length reduction over time. While the processing speed is varied, the melt temperature and the fiber weight fraction are kept constant, as summarized in Table 4.7. The experiments were conducted at varying residence times to capture the history of the fiber length reduction. Figure 4.26 illustrates the profile of the processing speed. The residence time is defined as the time after the processing speed has been reached until the drive unit is turned off. The acceleration of the drive unit was measured to be 82±3 RPM per second. Hence, the ramp up time is approximately 0.6 s for 50 RPM, 1.2 s for 100 RPM, and 1.8 s for 150 RPM.

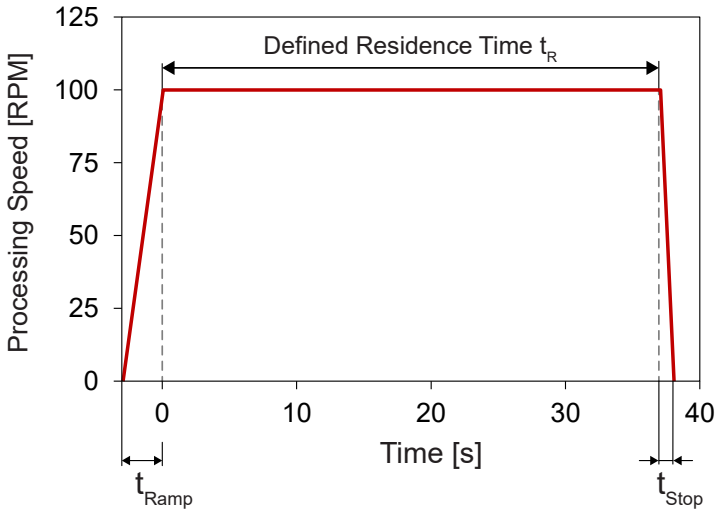

Figure 4.26.: Schematic of the defined processing speed and residence time.

Table 4.7.: Overview of processing conditions for the experimental study on fiber length reduction over time.

	Temperature	Processing Speed	Fiber Concentration
Trial 1	50 RPM	250°C	30%wt
Trial 2	100 RPM	250°C	30%wt
Trial 3	150 RPM	250°C	30%wt

Pre-trial experiments showed that residence times of 20 s, 40 s, 60 s, 120 s and 180 s would sufficiently capture the fiber length reduction over time for studied processing conditions and material. Measurements of the fiber length at lower residence times result in large measurement deviations caused by non-dispersed fiber bundles, as shown in Figure 4.27. The first 20 seconds of processing are characterized by dispersing the coated fiber bundles and substantial fiber reorientation, resulting into a heterogeneous fiber microstructure. While the dispersion and reorientation of the fibers can be studied with the Couette rheometer setup, this work focuses on the fiber breakages when the fibers are fully dispersed (residence time $>$ 20 s).

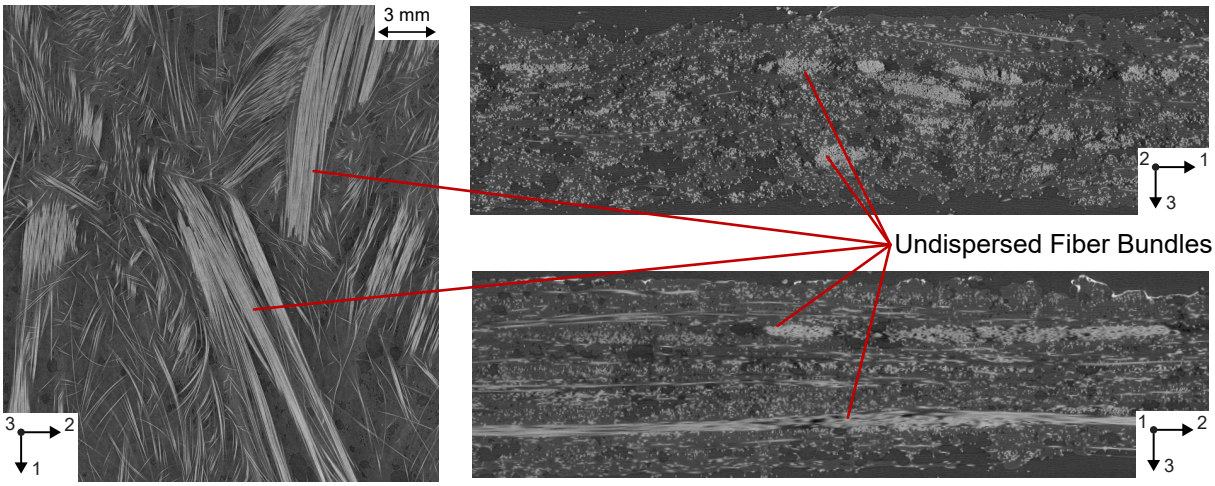

Figure 4.27.: µCT images illustrating undispersed fiber bundles at low residence times: 30%wt., 100 RPM, 250°C and 5 seconds residence time.

The second study focuses on the equilibrium value or unbreakable length, L_∞, at which point no additional fiber breakage occurs for given process conditions. The study aims to quantify the impact of melt temperature, processing speed, and fiber concentration on L_∞. This study was designed as a full factorial DOE with three factors and three levels, as shown in Table 4.8. All experiments in this study are conducted at a residence time of 180 s or 240 s and pre-trial experiments were conducted to ensure that L_∞ was reached.

In the third part of the Couette rheometer study, the initial fiber length of the feed material

Table 4.8.: Summary of the full factorial DOE focusing on the impact of processing conditions and fiber concentration on the unbreakable fiber length, L_∞.

	Processing Speed	Temperature	Fiber Concentration
Low	50 RPM	220°C	20%wt
Medium	100 RPM	250°C	30%wt
High	150 RPM	280°C	40%wt

was varied to investigate how the initial fiber length affects the fiber breakage. The processing speed and the melt temperature were kept constant at 100 RPM and 250°C, respectively. The fiber concentration is 30%wt and the initial fiber lengths of 2.5 mm, 5.0 mm, 10 mm and 15 mm were examined. The experiments at each initial length were conducted at 20 s, 40 s, 60 s, 120 s and 180 s to capture the fiber length reduction over time.

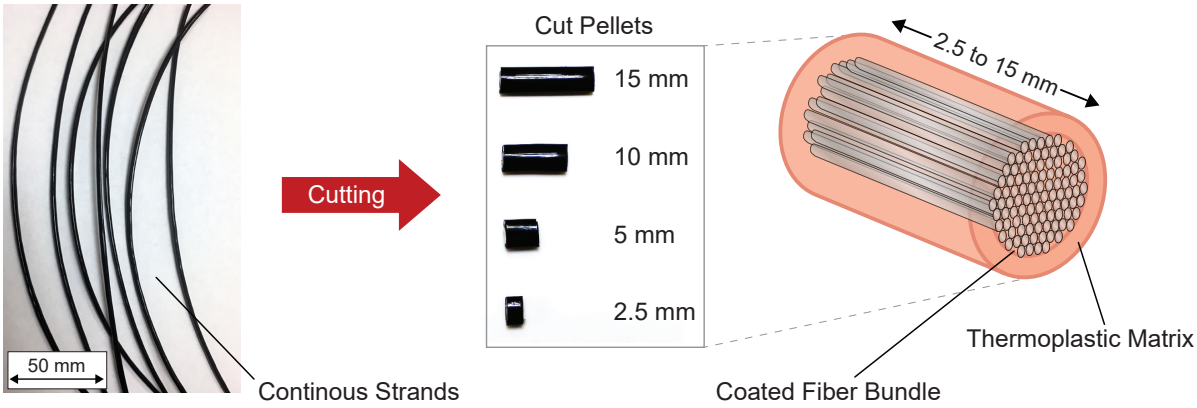

Figure 4.28.: Preparation of feed material with varying initial fiber length by cutting continuous strands of PPGF30 material to defined pellet lengths.

The variation in initial fiber length was reached by producing feed material with varying pellet length. Since the fibers in LFT pellets are aligned along the pellet axis, the fiber length is uniform and equals the length of the pellet. The feed material with different pellet lengths was specially prepared. The material supplier provided un-pelletized, continuous strands of the commercially available STAMAX^{TM} PPGF from a laboratory scale compounding line. The continuous strand was cut into defined length using an automated wire cutter (Artos Model 40-725, Artos Engineering, Brookfield, WI), as illustrated in Figure 4.28. While the glass fiber material and the PP matrix of the continuous strand are identical to the commercially available SABIC STAMAX pellets, slight differences in pellet diameter and fiber concentration are present[1]. Hence, a direct

[1]The diameter of the continuous strand is slightly smaller (3.3 mm compared to 3.5 mm) and less uniform. The fiber concentration is slightly larger than in the commercial pellets (31.62 ± 0.58%wt compared to 29.32 ± 0.49%wt). This can be attributed to the different scale of the laboratory compounding line (e.g, different throughput, pulling speed, and die design).

comparison with results of the commercially available SABIC STAMAX^{TM} pellets needs to be done with caution.

4.2.2. Study of Fiber Length Reduction Over Time

The residual fiber length at varying residence times was measured for three different processing speeds (50 RPM, 100 RPM and 150 RPM) while the isothermal melt temperature (250°C) and fiber concentration (30%wt) were held constant. Figures 4.29 and 4.30 show the obtained measurements for the number-average fiber length, L_N, and weight-average fiber length, L_W, respectively. The markers indicate the measured length average and the standard deviation represented by error bars. The solid lines show the fitted exponential decay model and the obtained fitting parameters ($k_{f,N}$ and L_∞) are summarized in Table 4.9.

Table 4.9.: Summary of fitted model parameters for the measured fiber length reduction over time. Values fitted to L_N and L_W separately. R^2 indicated as a measure of the fitted parameters.

	$\mathbf{L_N}$			$\mathbf{L_W}$		
	$k_{f,N}$	$L_{\infty,N}$	R^2	$k_{f,W}$	$L_{\infty,W}$	R^2
50 RPM	0.027	0.781	0.994	0.025	1.663	0.995
100 RPM	0.053	0.688	0.970	0.042	1.219	0.991
150 RPM	0.053	0.557	0.964	0.062	1.062	0.972

The results show that substantial fiber breakage occurs in the Couette rheometer for all processing speeds with a reduction of fiber length down to less than 11% of the initial fiber length (15 mm). The results confirm the expected exponential decay of fiber length over time until it reaches an asymptotic value, L_∞, at which the average fiber length does not reduce further. The impact of processing speed on fiber breakage is evident on both the rate of fiber attrition and the unbreakable length L_∞. An increase from 50 RPM to 150 RPM results in a reduction in $L_{\infty,W}$ of 36.1%. While L_∞ is reached at approximately 120 s for 150 RPM, it takes approximately 180 s at 50 RPM.

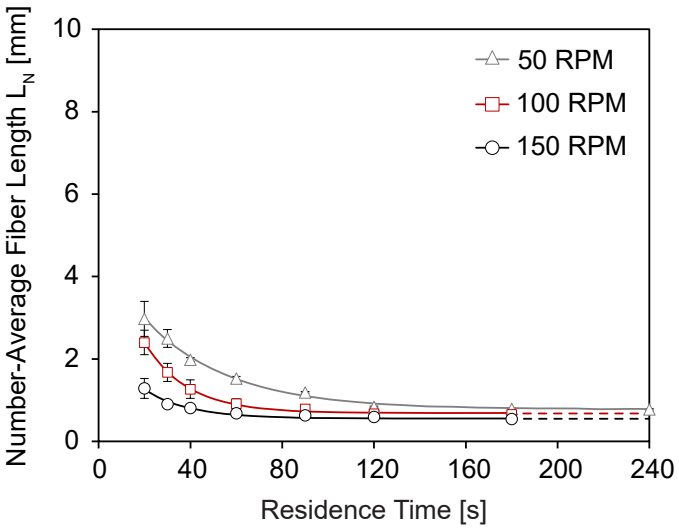

Figure 4.29.: Measurements of the number-average fiber length, L_N, showing the fiber length reduction over time for 250°C, 30%wt and varying processing speeds: 50 RPM, 100 RPM and 150 RPM.

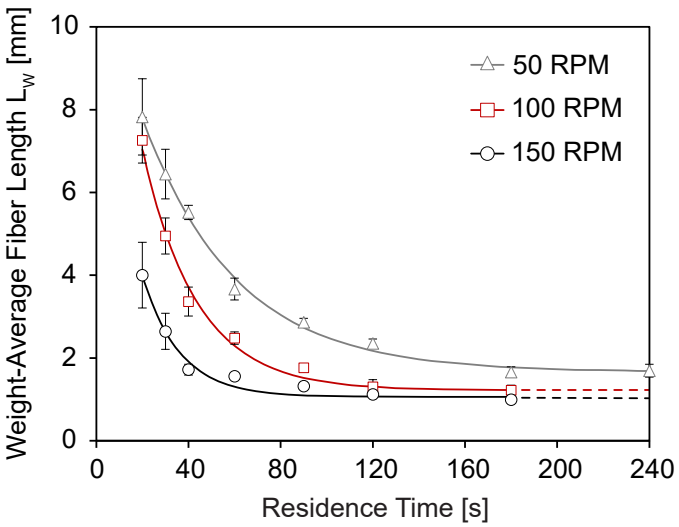

Figure 4.30.: Measurements of the weight-average fiber length, L_W, showing the fiber length reduction over time for 250°C, 30%wt and varying processing speeds: 50 RPM, 100 RPM and 150 RPM.

4.2.3. Study of Unbreakable Length L_∞

The investigation of the impact of processing conditions and fiber concentration on L_∞ allows a concise analysis of the mechanisms that drive fiber attrition, because it excludes fiber breakage and transient attrition at lower residence times. Figures 4.31 (results for L_N) and 4.32 (results for L_W) summarize the results of the three factor, three level DOE.

The isothermal melt temperature was varied between 220°C, 250°C, and 280°C, representing the processing temperature range suggested by the material supplier [124]. The melt temperature affects the suspension viscosity and, consequently, the stresses that the fibers are exposed to

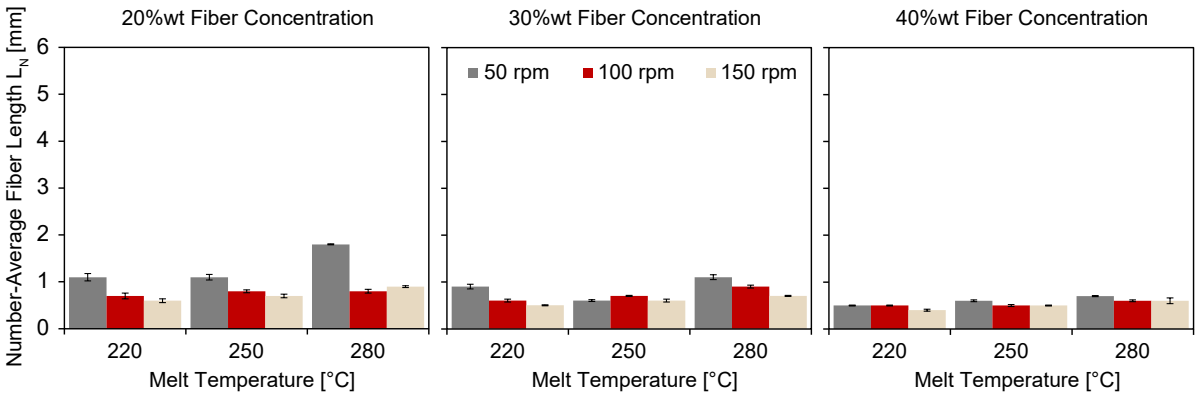

Figure 4.31.: Outcome of DOE on the unbreakable length L_∞ showing the obtained number-average fiber length L_N for 20%wt (left), 30%wt (center), and 40%wt (right).

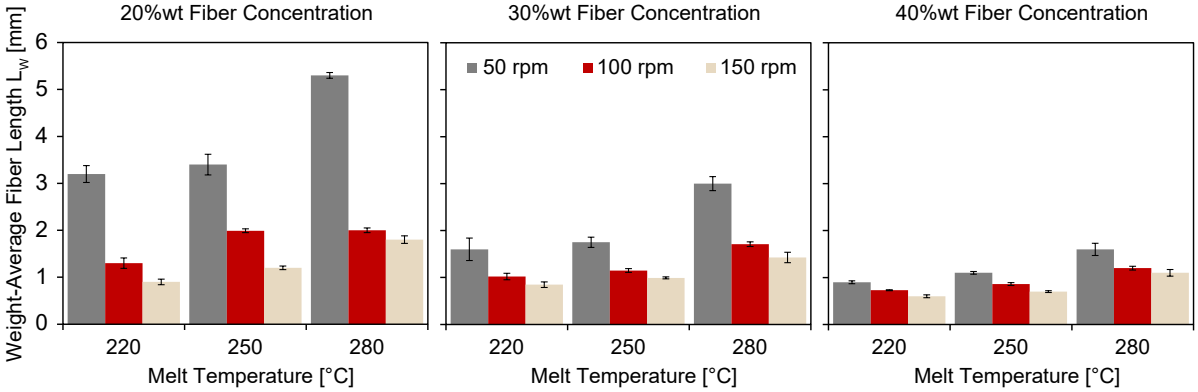

Figure 4.32.: Outcome of DOE on the unbreakable length L_∞ showing the obtained weight-average fiber length L_W for 20%wt (left), 30%wt (center), and 40%wt (right).

during processing. This interdependency is evident in the obtained results. Throughout all conditions in the DOE, an increased temperature results in longer residual fiber lengths. The most substantial impact of melt temperature can be seen for 20%wt fiber concentration at a processing speed of 50 RPM. The measurements suggest a L_W value of 5.32 mm and 3.21 mm for melt temperatures of 280°C and 220°C, respectively. This a relative reduction of 40% due to the change in temperature.

Varying the nominal fiber concentration implies a change in two fiber breakage mechanisms. First, increased fiber concentration results in more fiber-fiber interactions and, second, elevated fiber-mold surface interactions. While the two types of interaction cannot be separated experimentally, the measurements can be used to quantify the effect of fiber interactions as a whole (fiber-fiber and fiber-mold) on the residual fiber length. In all trials, an increased fiber concentration resulted in reduced residual fiber length. At 100 RPM and 220°C, the measured value for L_W is 1.31 mm for a fiber concentration of 20%wt and reduces to 0.73 mm for the 40%wt trial.

Processing speed also had the expected effect on the residual fiber length - an elevated processing speed causes evaluated fiber breakage for all combinations of the DOE, as show previously in Figures 4.31 and 4.32.

The data of the DOE were analyzed statistically to test the relative significance of melt temperature, processing speed and fiber concentration. An analysis of variance (ANOVA) was applied to the measurements to determine differences in means between the factors and the level of the factors of the DOE [135]. Figure 4.33 shows the main effect plots with respect to unbreakable length $L_{\infty,W}$. All three factors influence $L_{\infty,W}$ and have a statistically significant impact on the process-induced fiber breakage.

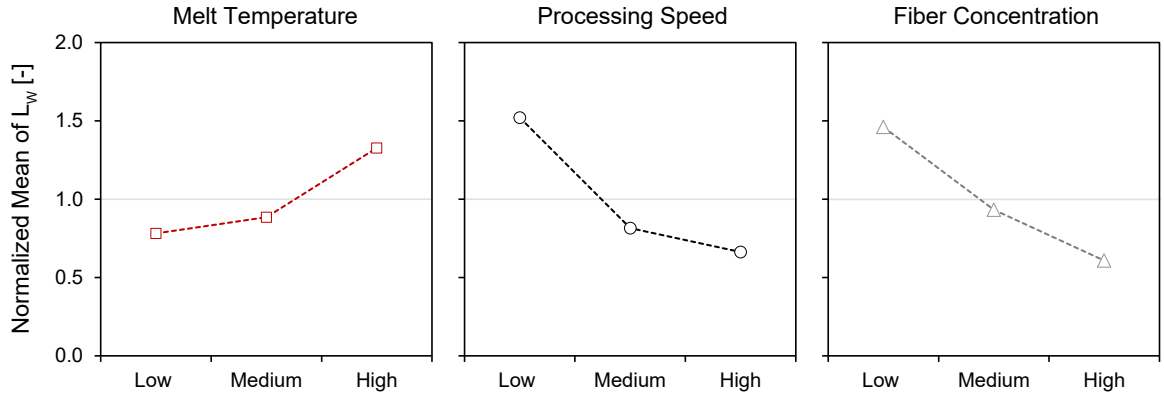

Figure 4.33.: Results of the statistical analysis (ANOVA) showing the main effect plots for $L_{\infty,W}$ for melt temperature (left), processing speed (center), and fiber concentration (right).

Figure 4.34 shows the interaction plots obtained from the ANOVA. The results indicate that processing speed and fiber concentration are statistically independent factors in the DOE. The effect of these two factors on $L_{\infty,W}$ varies over the different levels. Fiber concentration has a larger effect at lower processing speeds than at higher processing speeds. The analysis suggests that melt temperature and fiber concentration affect $L_{\infty,W}$ independently, because their individual effects are constant across the different levels. The results suggest that the interactions between processing speed and temperature are inconsistent. At higher processing speed, the analysis suggests no interactions between the two factors. However, the effect of the processing speed at 50 RPM depends on the level of the factor melt temperature.

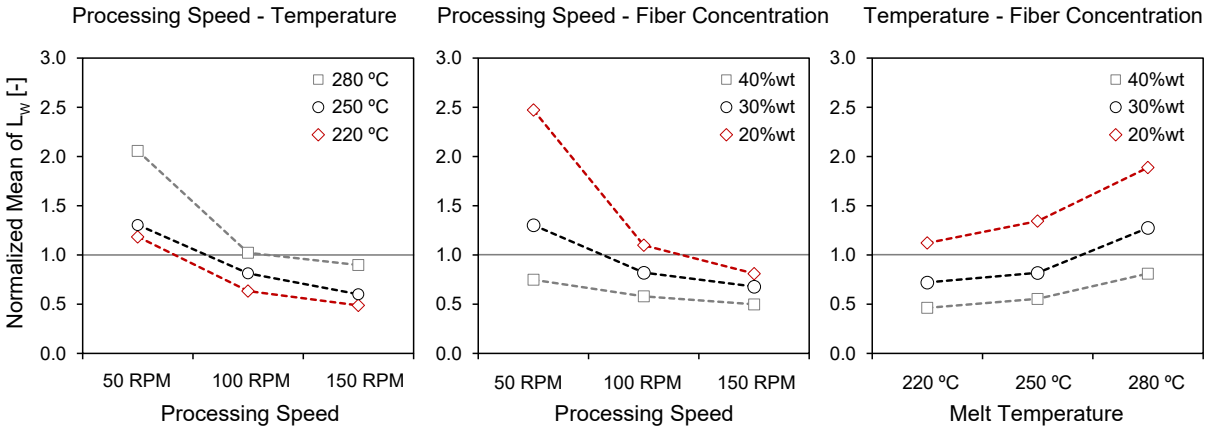

Figure 4.34.: Results of the statistical analysis (ANOVA) showing the interaction plots for $L_{\infty,W}$ for processing speed-temperature (left), processing speed-fiber concentration (center), and temperature-fiber concentration (right).

4.2.4. Impact of Initial Fiber Length

The effect of the initial fiber length on fiber breakage was evaluated for constant processing conditions (250°C) and constant nominal fiber concentration (30%wt). Figures 4.35 and 4.36 show the fiber length reduction for varying initial fiber lengths (2.5 mm, 5 mm, 10 mm, and 15 mm).

The results suggest that the unbreakable fiber length, L_∞, converges to the same value, independent of the initial length of the fibers. For the defined processing conditions, $L_{\infty,W}$ reached a value of 0.782±0.124 mm and $L_{\infty,N}$ reached a value 0.515±0.073 mm. The rate of fiber breakage

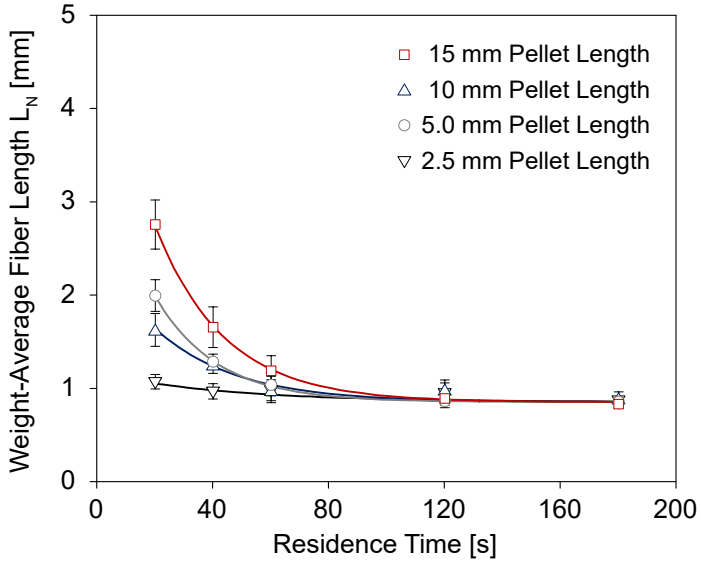

Figure 4.35.: Experimental results, showing the reduction of the number-average fiber length, L_N, over time at 250°, 30%wt, 100 RPM and varying initial fiber length: 2.5 mm, 5 mm, 10 mm, and 15 mm.

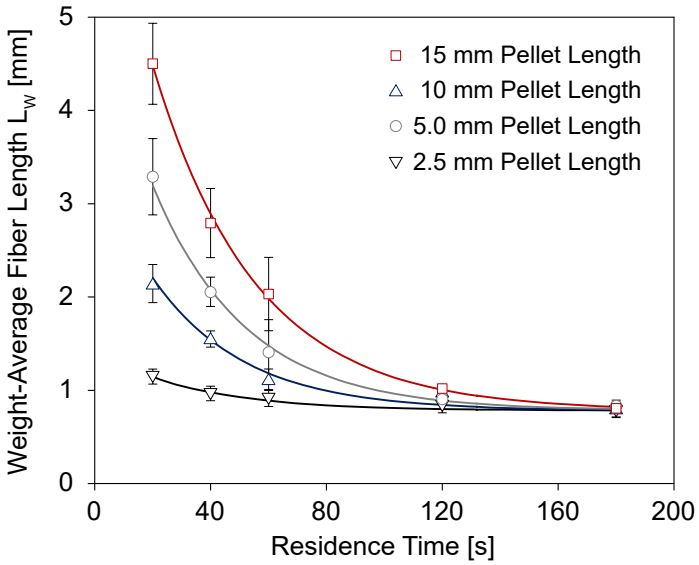

Figure 4.36.: Experimental results, showing the reduction of the weight-average fiber length, L_W, over time at 250°, 30%wt, 100 RPM and varying initial fiber length: 2.5 mm, 5 mm, 10 mm, and 15 mm.

is similar for all initial fiber lengths, which is evident by the obtained values for the fiber breakage rate coefficient, k_f, as shown in Figure 4.37. The average value for $k_{f,N}$ is 0.030±0.002 s^{-1} and 0.042±0.0026 s^{-1} for $k_{f,W}$. Consequently, the rate of fiber breakage and the unbreakable length are independent for constant processing conditions. Furthermore, it can be concluded that any increase in initial fiber length results in longer residence times until the unbreakable length is reached.

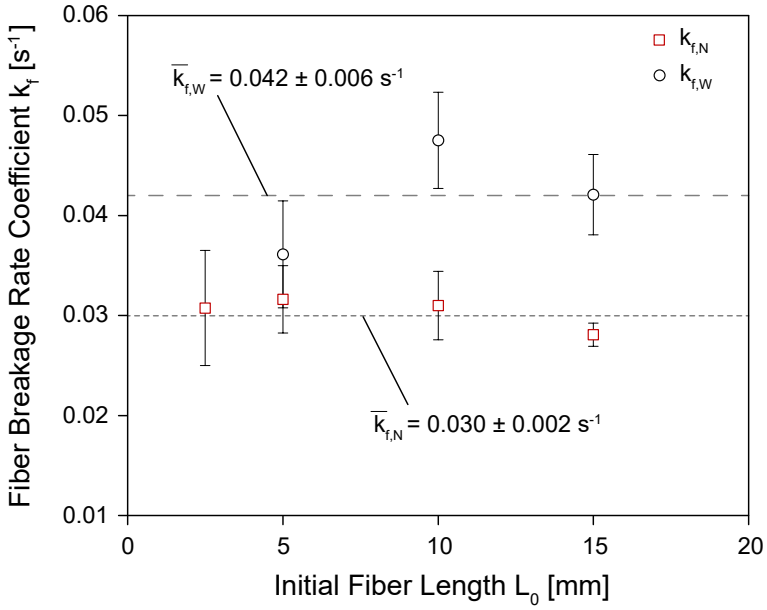

Figure 4.37.: Obtained fiber breakage rate coefficient, k_f, for varying initial fiber length: 2.5 mm, 5 mm, 10 mm, and 15 mm. The horizontal lines indicate the averages values of k_f.

4.2.5. Discussion of the Fiber Breakage Study under Controlled Conditions

The fiber length degradation in a Couette flow under controlled conditions was studied experimentally and the impact of processing conditions (melt temperature, processing speed, fiber concentration and initial fiber length) on fiber attrition was quantified. The developed experimental procedure proved to be a valuable tool to generate quantitative results of fiber breakage for LFT materials. The results highlight the severe fiber length reduction observed in LFT processing, where the harshest processing conditions result in a residual fiber length that is less than 5% of the initial fiber length (40%wt, 150 RPM, 220°C, 180 s). The DOE focusing on L_∞ showed that the effect of fiber concentration, melt temperature and processing speed on the residual length is statistically significant. The initial length of the fibers at constant processing conditions does not affect the rate of fiber breakage nor L_∞, but increases the time at which L_∞ is reached. While the results obtained with the developed Couette rheometer setup might not be transferred directly to the complex flow conditions present in LFT injection molding, it suggests that the benefits of increasing the initial fiber length of the feed material to obtain longer residual fiber lengths is limited without optimizing the processing conditions.
The presented results for the Couette rheometer study are valuable experimental data that serve as a starting point for understanding the underlying physics of fiber breakage and deriving improved processing guidelines for LFT materials. The outcome of the statistical analysis of the DOE focusing on L_∞ suggests a set of important correlations for the processing of LFT:

- All three factors prove to be significant in their effect on the unbreakable length in the Couette rheometer experiments within the tested range.

- The experimental results suggest that the largest effect stems from fiber concentration. As the range of 20%wt to 40%wt represents the most relevant range for industry applications [23], the trade-off between fiber concentration and residual fiber length can be an important consideration in the part design. Depending on the process conditions, an optimal value for the nominal fiber concentration can be found for a desired fiber length.

- The ANOVA analysis suggests that the factor melt temperature is statistically independent of fiber concentration and to some extent independent of processing speed, the control of the temperature profile is an ideal parameter to optimize a process for reduced fiber breakage. However, the outcome of the DOE suggests that the correlation is not linear for

the investigated material. An increase in melt temperature from 250°C to 280°C results in a larger increase in residual fiber length than an increase from 220°C to 250°C.

- The impact of processing speed on fiber breakage appears to be most significant at lower speeds. Although only three speeds were tested, the trend points towards a declining effect at higher processing speeds (or shear rates). Transferring this outcome to the injection molding process, there may be substantial reduction in fiber breakage by lowering the screw speed, which aligns with work by Inoue et al. [21]. The results of this study indicate that the impact of processing speed on fiber breakage is not linear and that that there might be a threshold in shear rate at which a change in screw speeds becomes more significant.

The overall results from the DOE focusing on L_∞ can be summarized to illustrate how the processing conditions and fiber concentration affect the residual fiber length by plotting $L_{\infty,W}$ as the product of the matrix viscosity, η_M, and the average shear rate, $\dot{\gamma}$ (see Figure 4.38). The graph shows the how the residual fiber length reduces with harsher processing conditions (increased processing speed and lower melt temperature). The data provide a starting point and suggest a framework for modeling the unbreakable length $L_{\infty,W}$ as a function of processing conditions, which is shifted by the nominal fiber concentration. The application of the experimental data from the Coeutte rheometer experiments for modeling will be discussed in detail in Chapter 5.3.

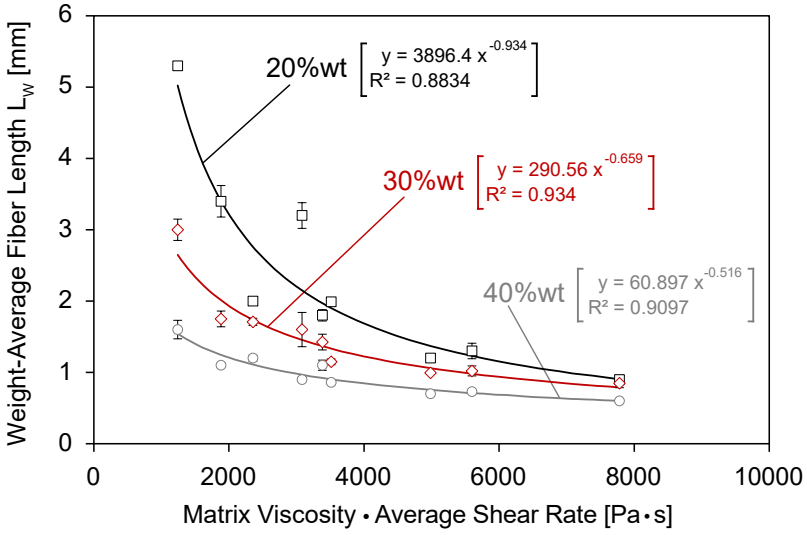

Figure 4.38.: Measurements of $L_{\infty,W}$ from the DOE plotted as function of average shear rate, $\dot{\gamma}$, times the suspension viscosity, η_S.

4.3. Conclusions of Experimental Studies

The outcome of the injection molding experiments demonstrates the significant impact of the process on the fiber microstructure in the molded part. The measurements suggest that the common assumptions of a uniform fiber length and fiber concentration throughout a molded part are not valid. In fact, processing LFT materials results in a fiber microstructure that is significantly heterogeneous. Furthermore, the experiments indicate correlations between fiber alignment, fiber matrix separation, and fiber breakage. Conventionally, the process-induced fiber orientation, fiber length, and fiber concentration are investigated separately and interdependencies are neglected. This work shows that an isolated analysis of the microstructural properties is not well-founded. For example, the measurements of the through-thickness orientation and concentration highlight a correlation that has not been addressed before. Consequently, an extended theoretical framework is required to capture the link between fiber alignment and fiber matrix separation during processing.

The experimental results highlight the challenge that fiber breakage phenomena pose for processing long glass fiber-reinforced thermoplastics. The fiber length in the injection molded parts can reduce to less than 10% of the initial fiber length. Furthermore, the fiber length is not constant along the flow path and can vary up to 25% throughout the part. The developed Couette rheometer setup in combination with the developed measurement technique proved to be a valuable tool to study the fiber breakage of long glass fiber-reinforced thermoplastics under controlled conditions. Using the proposed methodology, a repeatable, accurate and robust set of experimental data can be obtained. The findings from this study are very valuable and can close a gap in available experimental data as it allows the isolation of the impact of process variables on fiber breakage.

5. Evaluation of Modeling Approaches

This chapter presents the results of an evaluative study of numerical models that are used to predict the process-induced fiber microstructure in LFT injection molding. The simulation of the mold filling for fiber-reinforced composites is commonly decoupled on two scales. First, the actual mold filling is solved independently of any change in the fiber microstructure. This simplification assumes that a change of fiber orientation, length or concentration does not affect the flow behavior of the suspension. The second decoupling assumes that the phenomena of fiber alignment, fiber matrix separation, and fiber breakage are independent. All injection molding simulations in this work are performed using Moldex3D^{TM} (Version R15, Service Pack 1), which uses a 3D finite volume method to solve the governing equations. The details of the numerical solver can be found in [136]. The transient, non-Newtonian and non-isothermal flow of the melt during cavity fill can be described by the following governing equations. The conservation of mass is described as

$$0 = \frac{\partial \rho}{\partial t} + \nabla \cdot (\rho \boldsymbol{u}) \tag{5.1}$$

where t is the time, ρ the density, and $\boldsymbol{u}$ the velocity vector.

The conservation of momentum is expressed as

$$\rho \left(\frac{\partial \boldsymbol{u}}{\partial t} + \boldsymbol{u} \cdot \nabla \boldsymbol{u} \right) = -\nabla \cdot \boldsymbol{\sigma} + \rho \boldsymbol{g} \tag{5.2}$$

where $\boldsymbol{\sigma}$ represents the total stress tensor and $\boldsymbol{g}$ is the gravity field.

The total stress tensor, $\boldsymbol{\sigma}$, for Generalized Newtonian Fluid is written as

$$\boldsymbol{\sigma} = -p \boldsymbol{I} + \eta \left(\nabla \boldsymbol{u} + \nabla \boldsymbol{u}^T \right) \tag{5.3}$$

where p is the pressure and η is the viscosity of the fluid, described by an appropriate viscosity model to account for the temperature, pressure and shear rate dependency of polymers.

The conservation of energy is described by

$$\rho C_P \left(\frac{\partial T}{\partial t} + \boldsymbol{u} \cdot \nabla T \right) = \nabla \cdot (k \nabla T) + \eta \dot{\gamma}^2 \tag{5.4}$$

where C_p is the specific heat, k is the thermal conductivity and T is the temperature. The mold filling simulation is highly dependent on the material properties and the rheological and thermal conditions. The viscosity is modeled using the Cross-William-Landel-Ferry (Cross-WLF) model to account for shear thinning and temperature dependency [137, 138]. The pressure-volume-temperature (pvT) is modeled using the modified Tait model [139]. All models and model parameters used for the mold filling simulations in this work are listed in Appendix A.

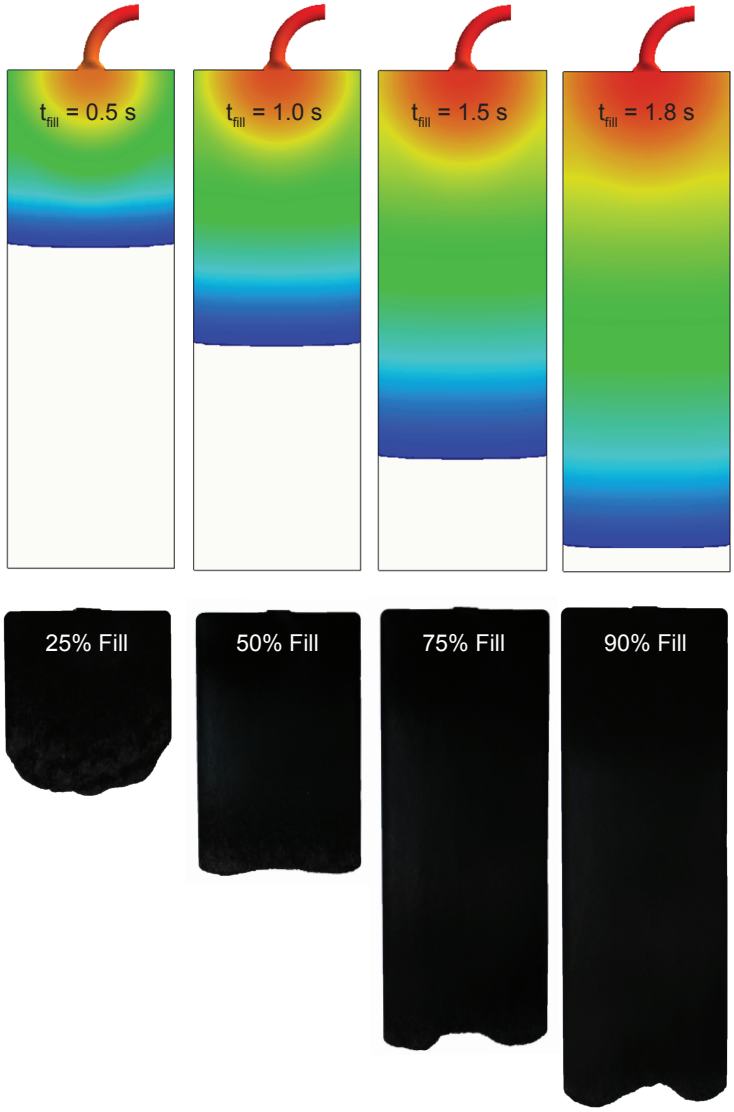

Figure 5.1.: Mold filling study, comparing the simulated mold front advanced with experimental short shots for PPGF40 (see experimental study in Chapter 4.1).

The flow rate as a boundary condition is defined at the mold inlet and no slip is assumed at the mold walls [24]. The plate geometry was discretized into approximately 600,000 elements (hybrid mesh) with at least 16 elements through the thickness to capture the through-thickness variation of fiber orientation and fiber concentration accurately, following a sensitivity study on the impact of meshing on fiber orientation published by Foss et al. [24]. A mold fill study was done to validate the simulation by comparing experimental partial mold fillings (short shots) with the melt front prediction obtained with Moldex3D^{TM}. This mold fill study was done for the PPGF40 injection molding trials (see Section 4.1) and the results are shown in Figure 5.1. Although the mold filling simulations do not fully capture the shape of the melt front, the melt front predictions show strong agreement with the experiments.

In the following sections, the prominent models for fiber alignment (Folgar-Tucker Model [35]), for fiber matrix separation (Suspension Balance Model [116]), and for fiber breakage (Phelps-Tucker Model [5]) are evaluated. All three models are implemented in the commercial version of Moldex3D^{TM}. The simulation results are tested and compared with the experimental results from the previous chapter to evaluate whether the models are capable of predicting the process-induced microstructure.

5.1. Two Phase Suspension Model for Fiber Concentration Prediction

The two phase suspension model proposed by Morris and Boulay [116] was adapted by Tseng et al. for injection molding simulations (see Section 2.3.2) and implemented as a simulation module in Moldex3D^{TM} (Version R15 Service Pack 1). The adapted model requires the input of the particle friction index, n, which is assumed to be a material dependent model parameter and can be obtained from experiments [36]. Although Tseng et al. [36] do not discuss the procedure to obtain n empirically, the boundaries for the model parameter are set to $2 < n < 9$ in Moldex3D^{TM}. A sensitivity study of the particle friction index was performed for the injection molding trial with 20%wt fiber concentration (PPGF20). Figure 5.2 shows the simulation results for varying particle friction indices at location 1 (gate region), location 2 (center of the plate), and location 3 (end of flow region). The results suggest that the effect of the particle friction index, n, on the through-thickness fiber concentration is negligible. Varying the values for n from the lowest value (2) to the highest (9), results in a change of less than 1.5% in the predicted

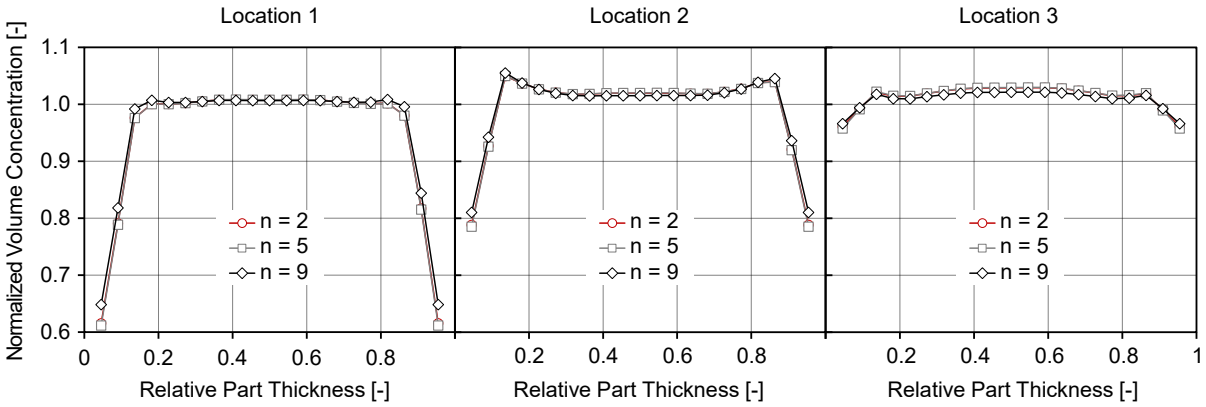

Figure 5.2.: Predicted through-thickness fiber concentration for PPGF20 at locations 1, 2, and 3, for varying particle friction indices: $n = 2$, 5, and 9.

through-thickness results. The same sensitivity of n on the fiber concentration was found for the simulations of PPGF30 and PPGF40. Consequently, the particle friction index was set to $n = 3$ (default value [36]) for the comparison with experimental results.

Figure 5.3 shows the predicted through-thickness fiber concentration for PPGF20, PPGF30, and PPGF40 at locations 1 through 3 using $n = 3$. For all concentrations, the simulation results suggest a layer with depleted fiber concentration close to the surface. The degree of fiber depletion in this layer reduces along the flow path. The effect is most dominant for PPGF20 with a normalized fiber volume concentration of 0.61 in the surface layer at location 1 and 0.95 at location 3. The simulation suggests a constant fiber concentration in the core layer and little difference in concentration from locations 1 to 3. For PPGF20, the normalized volume concentration in the core layer is 1.0 at location 1 and increases to approximately 1.04 at location 3. The predicted change in the concentration in the core layer for PPGF30 and PPGF40 is negligible.

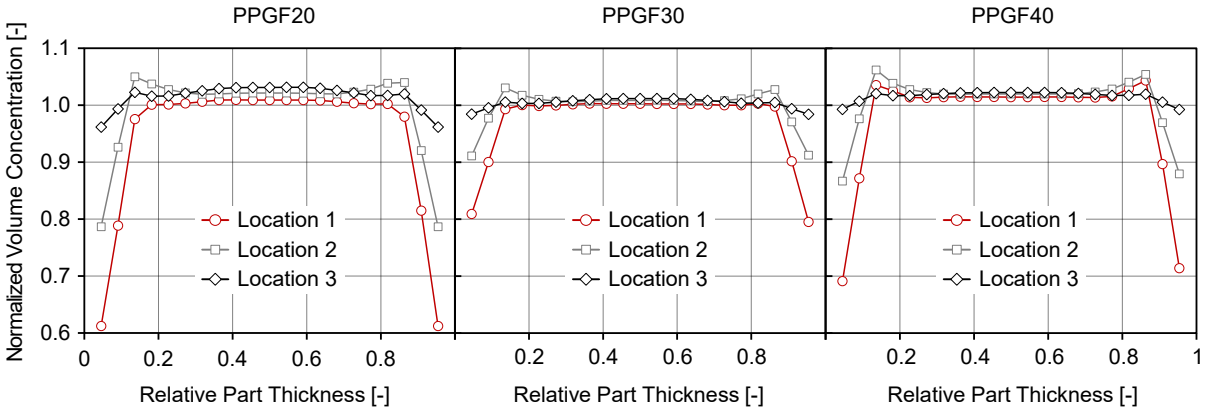

Figure 5.3.: Predicted through-thickness fiber concentration for locations 1, 2, and 3, for PPGF20 (left), PPGF30 (center), and PPGF40 (right), using particle friction indices of $n = 3$ (default value).

In Figure 5.4, the predicted fiber concentration along the flow path for PPGF20, PPGF30,

and PPGF40 suggest an increasing fiber concentration along the flow path. For PPGF20, the normalized fiber volume concentration increases from 0.94 at location 1 to 1.02 at location 3.

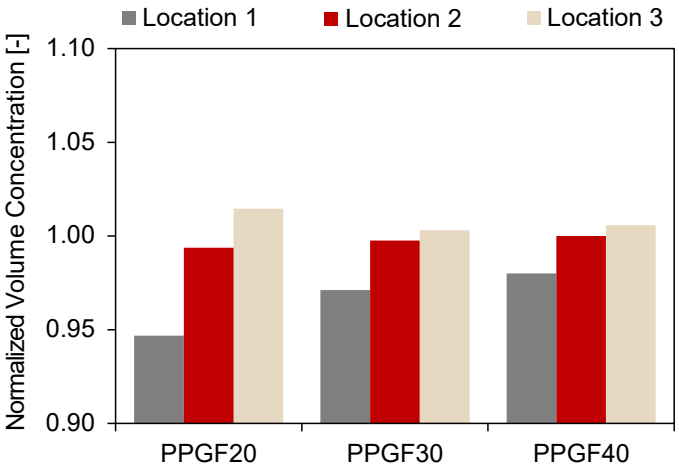

Figure 5.4.: Predicted fiber concentration along the flow path for PPGF20, PPGF30, and PPGF40, using particle friction indices of $n = 3$ (default value).

Figure 5.5 shows the comparison between measurements and simulation results for the fiber concentration along the flow path for PPGF20, PPGF30, and PPGF40. Although the trend of increasing fiber concentration towards the end of the flow path is captured by the simulation, the degree of fiber matrix separation is significantly underestimated.

Comparing the predicted through-thickness fiber concentration with the measurements shows large discrepancies. Figure 5.6 shows the comparison for PPGF20 at location 2. It is seen that the simulation results do not predict the experimentally observed fiber agglomeration in the core. Moreover, the predicted decrease in fiber concentration close to the surfaces do not agree with the measurements, which suggest a slight increase in concentration.

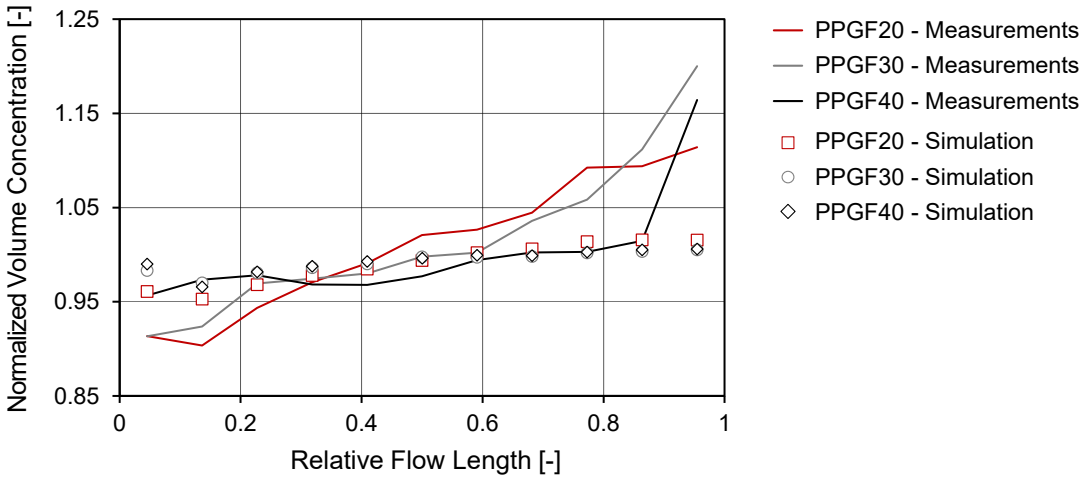

Figure 5.5.: Predicted (markers) and measured (solid lines) fiber concentration along the flow path for PPGF20, PPGF30, and PPGF40.

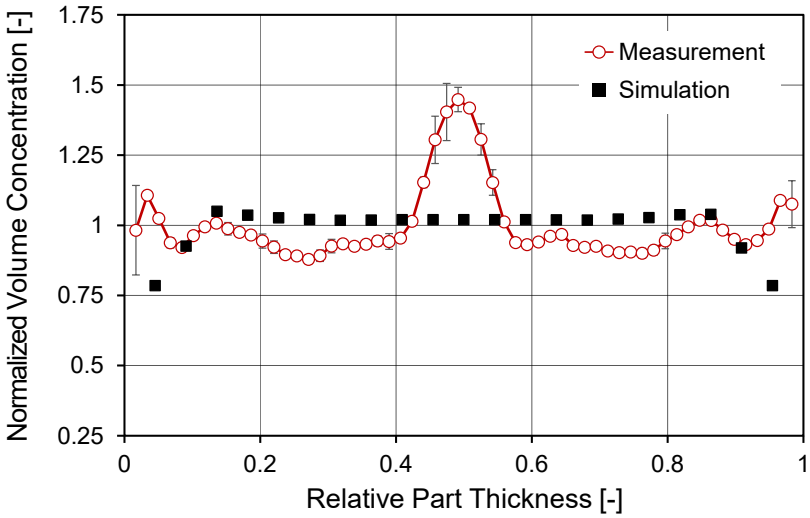

Figure 5.6.: Predicted (markers) and measured (solid lines) through-thickness fiber concentration for at location 2.

5.2. Folgar-Tucker Model for Fiber Orientation Prediction

The Folgar-Tucker model estimates the process-induced fiber alignment from the flow kinematics and is considered a baseline for fiber orientation modeling in the field of discontinuous fiber-reinforced composites [9, 140]. The fiber reorientation is modeled as an isotropic rotary diffusion process and comprises a material dependent fitting parameter, C_I, which accounts for the fiber-fiber interaction of the suspension. Wang and Tucker [114] expanded the original model to the Folgar-Tucker RSC model by adding a second fitting parameter (κ) that slows down the orientation evolution (see also Section 2.3.1). In this work, the Folgar-Tucker RSC model is used to evaluate how well the process-induced fiber orientation can be estimated from process simulations.

Conventionally, the model parameters C_I and κ are assumed to be an intrinsic property of the material, depending on the material (fiber concentration, fiber length, fiber diameter, fiber stiffness) and independent of the process conditions [141]. The parameter is obtained either by fitting simulation results to measured fiber orientation data [24, 35], by relating the fiber orientation evolution to rheological measurements [142] or by particle level simulation [143]. The fitting procedure is time-consuming and costly, leading most researchers and engineers to use default values instead of following a defined procedure of obtaining C_I and κ, resulting in less accurate fiber orientation predictions [24, 35, 141, 144].

To evaluate the Folgar-Tucker RSC model in this work, different parameter sets of C_I and κ are tested for the injection molding simulation of molded plates at 20%wt, 30%wt, and 40%wt

fiber concentration (see Section 4.1). The values for the fitting parameters are obtained in three different ways. First, the C_I and κ values are directly fitted to the measured fiber orientation, representing the baseline of this evaluation as the best fit results. Second, published empirical relationships that claim general transferability for C_I are used to calculate the appropriate values. Lastly, a recently proposed particle level simulation (PLS) approach [145] is applied to find the fiber-fiber interaction coefficients. Finally, the simulation outcome using the different parameter sets are compared with the measured fiber orientation.

For all injection molding simulations, the initial condition of the fiber orientation at the melt entrance point was assumed to be random. As shown by Tseng et al. [146], the initial fiber orientation in the sprue for injection molding does not affect the predicted orientation in the molded part due to large deformations that the material experiences during mold filling. The Invariant Based Optimal Fitting (IBOF) closure was used for all simulations, because it proved to be an accurate and efficient closure approximation for the fourth-order orientation tensor [147]. Fitting C_I and κ to the measured fiber orientation data was done iteratively by first varying C_I until the predicted fiber orientation matches the experimental values in the shell layers. The values for κ were changed to improve the match in the skin and core layers. Figures 5.7, 5.8, and 5.9 show the simulation results using the best fitted parameters compared to the measurements at location 2 for PPGF20, PPGF30, and PPGF40, respectively. The results suggest that the predicted fiber orientation matches very well in the skin and the shell layers. However, the simulation results show large discrepancies in the core layer. For PPGF40, the Folgar-Tucker RSC model predicts a low fiber alignment in cross-flow direction with a value of $a_{22} = 0.31$, while the measurements suggest a value of 0.79 for a_{22}. It was not possible to find a parameter set of C_I and κ that results in an improved fiber orientation prediction in the core layer without substantially overestimating the orientation in the skin and shell layers.

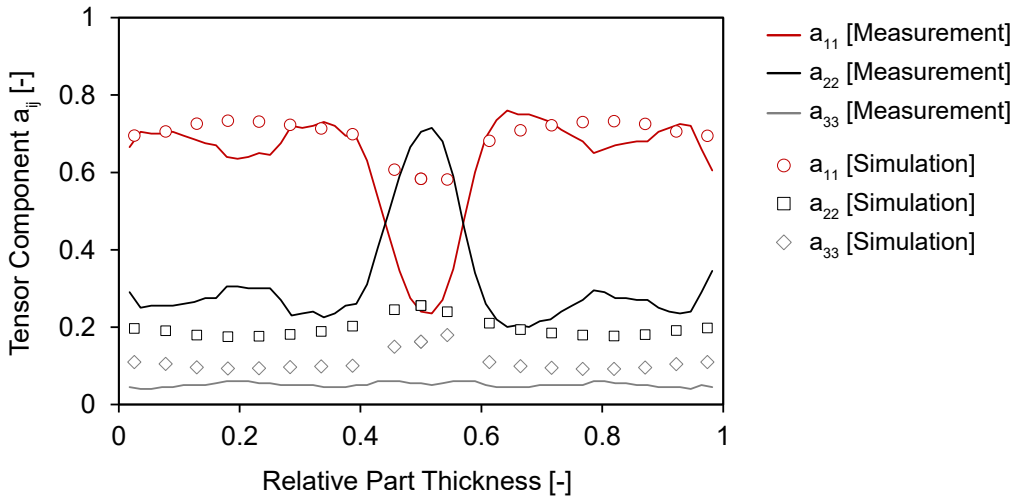

Figure 5.7.: Comparison of the measured through-thickness fiber orientation for PPGF20 at location 2 and the predicted results, using $C_I = 0.020$ and $\kappa = 0.09$

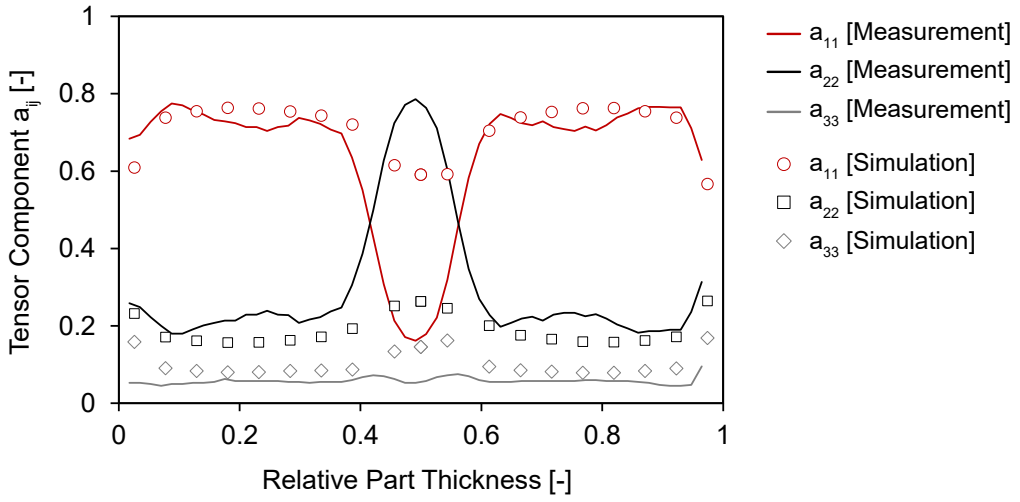

Figure 5.8.: Comparison of the measured through-thickness fiber orientation for PPGF30 at location 2 and the predicted results, using $C_I = 0.015$ and $\kappa = 0.12$

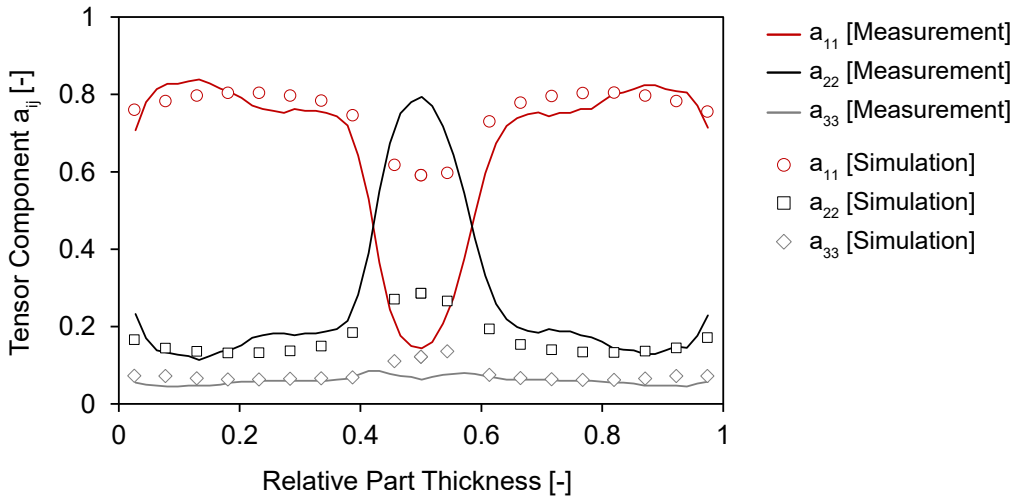

Figure 5.9.: Comparison of the measured through-thickness fiber orientation for PPGF40 at location 2 and the predicted results, using $C_I = 0.0095$ and $\kappa = 0.15$

Recently, a PLS approach was proposed [145], which simulates the motion and interactions of single fibers in simple flow conditions for concentrated fiber suspensions. The PLS is a mechanistic model approach based on the work of Schmid et al. [148]; it was refined first by Londono-Hurtado [25] and later expanded by Ramirez [149] and Perez [34]. The PLS approach simulates the motion of fiber for defined flow conditions and it was utilized in this work as a numerical rheometer to fit the model parameters C_I and κ. The obtained C_I values are used as input value for the Moldex3D^{TM} simulations of the molded plates and compared to the measurements. The work flow is illustrated in Figure 5.10

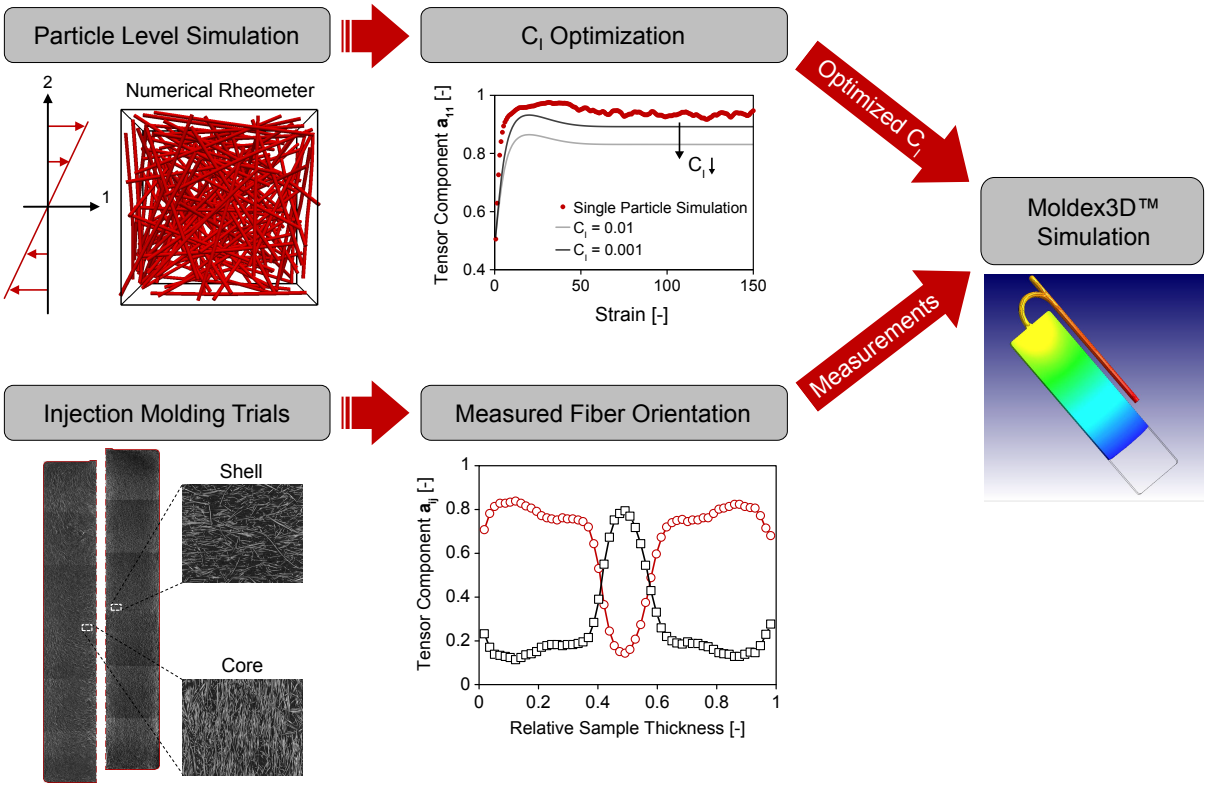

Figure 5.10.: Overview of work flow for evaluating the Folgar-Tucker model: Optimizing the C_I coefficient by using a single particle simulation and numerical rheometer (top); Comparison of Moldex3D simulations (right) with the measured fiber orientation (bottom).

The PLS represents each fiber in the system as a flexible chain of segments or beam elements interconnected by nodes [25, 34, 149]. The PLS models all relevant effects on a micro-level, including hydrodynamic forces, fiber flexibility, and excluded volume forces due to fiber-fiber and fiber-wall contacts. Hence, the individual deformation, alignment, and motion of the fibers in a fluid can be simulated and the orientation can be traced. In particular, the impact of material properties on the fiber alignment at defined processing conditions can be studied numerically. The simulation of the numerical rheometer comprises a designed cell that is exposed to a simple shear flow for defined flow conditions. A fiber cluster with defined properties is placed in a shear

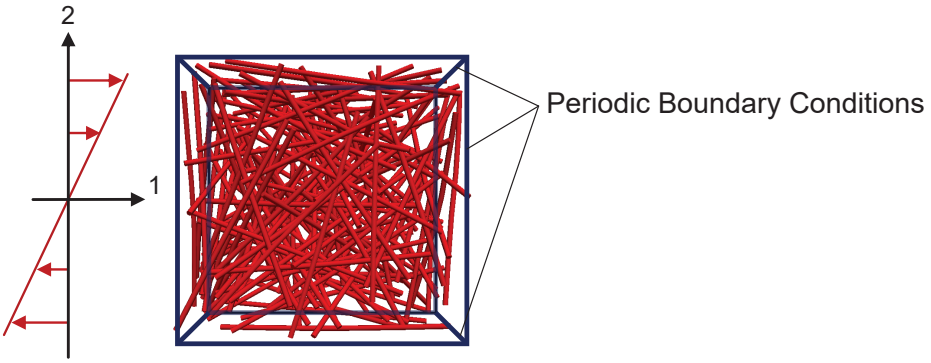

Figure 5.11.: Illustration of the numerical rheometer, defined as a shear cell with periodic boundary conditions.

cell and periodic boundary conditions are defined [145, 149], as illustrated in Figure 5.11. The periodic boundary conditions are adapted from the original work of Lees and Edwards [150] and generate a continuous domain of the suspension, preserving the fiber concentration and the interactions between the fibers at low computational cost [149]. No walls are defined for the numerical rheometer to avoid any fiber-wall interactions. The inputs for the numerical rheometer are summarized in Table 5.1.

Table 5.1.: Input values for the PLS of the numerical rheometer to obtain values for C_I and κ.

	PPGF20	**PPGF30**	**PPGF40**
Fiber Volume Concentration	8.2%vol	13.2%vol	19.1%vol
Fiber Aspect Ratio	60	50	40
Fiber Young's Modulus	73 GPa	73 GPa	73 GPa
Matrix Viscosity	84.3 Pa·s	84.3 Pa·s	84.3 Pa·s
Shear Rate	150 s^{-1}	150 s^{-1}	150 s^{-1}
Residence Time	1 s	1 s	1 s
Number of Fibers	660	480	420
Fiber Element Size	0.095 mm	0.095 mm	0.095 mm

The simulation of the numerical rheometer using the defined fiber aspect ratio and volume concentration results in a unique fiber orientation evolution for PPGF20, PPGF30, and PPGF40. The orientation data is used to fit the Folgar-Tucker RSC model by optimizing the values for C_I and κ. The fitting was done using an optimization procedure based on the Gauss-Newton algorithm for non-linear least square problems [151]. First, the value for C_I was fitted to the steady state orientation, followed by adjusting κ to best match the transient fiber orientation, as illustrated in Figure 5.12.

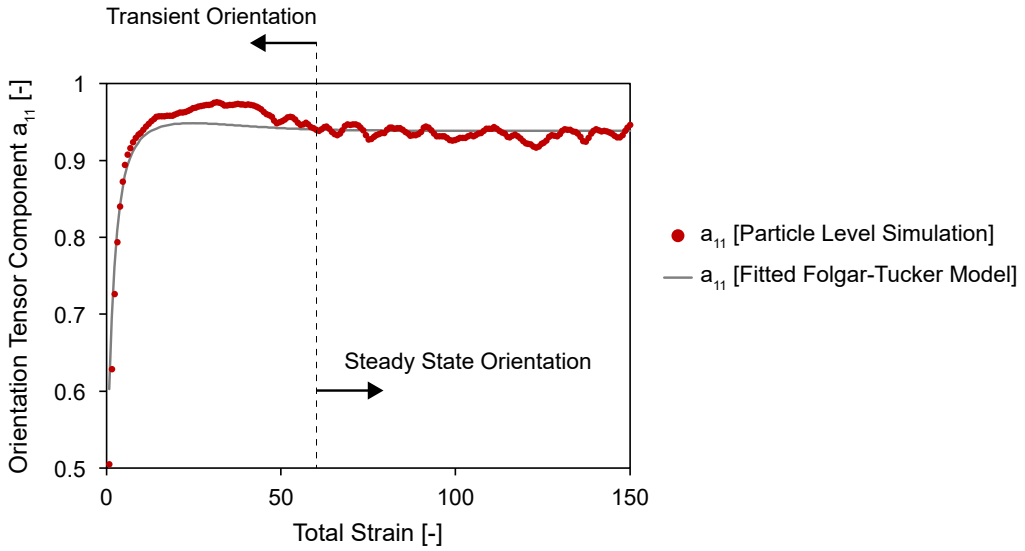

Figure 5.12.: Illustration of the fiber orientation evolution in the shear cell obtained with the PLS for PPGF30 (markers) and the fitted Folgar-Tucker model (solid line).

Next, values for C_I were obtained from empirical relationships reported in literature. Bay et al. [38] derived an empirical relationship for C_I based on their experimental results, given by

$$C_I = 0.00184 \; exp\,(1 - 0.7184 \; \phi_f \; a_r) \tag{5.5}$$

where ϕ_f is the fiber volume fraction and a_r is the fiber aspect ratio. Phan-Thien et al. [143] proposed the following relationship based on their direct fiber simulation approach, given by

$$C_I = 0.03 \; exp\,(0.224 \; \phi_f \; a_r) \tag{5.6}$$

Both relationships suggest that the fiber-fiber interaction coefficient depends on the fiber length and the fiber concentration, but the suggested trends are opposite. While Bay suggests that C_I decreases with increasing fiber volume concentration or fiber aspect ratio, Phan-Thien suggest an increasing C_I. The work by Phan-Thien and Bay do not include an empirical relationship for κ. Hence, κ is set to be 1 for this study, which leads to the original Folgar-Tucker model [152]. Table 5.2 summarizes the obtained parameter sets of C_I and κ. The parameters were used to predict the fiber orientation from the injection molding simulation for PPGF20, PPGF30, and PPGF40. Figures 5.13, 5.14, and 5.15 show the results of the simulation, depicting the values of a_{11} and a_{33} for the different parameter sets. The comparison to the measurements show that the C_I values suggested by Bay et al. substantially overestimate the fiber alignment in the shell layers for all trials. Phan-Thien's empirical relationship suggests values for C_I that lead

Table 5.2.: C_I and κ values for PPGF20, PPGF30, and PPGF40 obtained by four means: i) Phan-Thien et al. [143], ii) Bay et al. [38], iii) the numerical rheometer, and iv) fitted to the measured fiber orientation.

	PPGF20		**PPGF30**		**PPGF40**	
	C_I	κ	C_I	κ	C_I	κ
Phan-Thien et al. [143]	0.02003	-	0.02316	-	0.02460	-
Bay et al. [38]	0.00054	-	0.00016	-	0.00007	-
Numerical Rheometer	0.00350	0.63	0.00510	0.18	0.00557	0.15
Fitted to Measurements	0.02000	0.09	0.01500	0.12	0.00950	0.15

to good agreement with the measurements for PPGF20 and PPGF30, but underestimate the fiber alignment at PPGF40. The parameter set of C_I and κ obtained from numerical rheometer simulation predicted the fiber orientation for PPGF40 well, but overestimated the orientation for the lower fiber concentrations. None of the simulations were able to fully capture the measured through-thickness fiber orientation with the distinct skin-shell-core pattern.

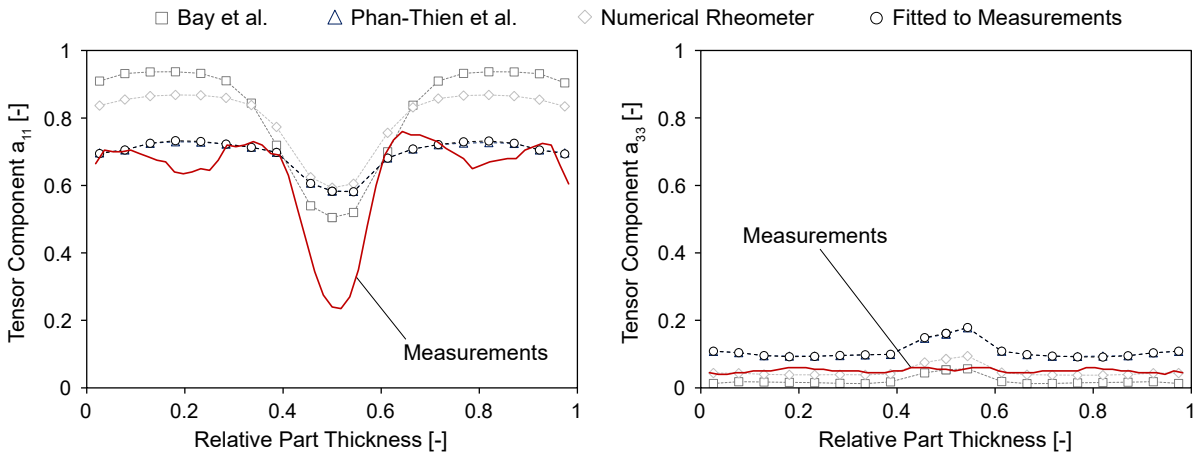

Figure 5.13.: Comparison of predicted and measured fiber orientation at location 2 for PPGF20, showing the tensor components a_{11} (left) and a_{33} (right). The C_I and κ values are obtained from: i) Phan-Thien et al. [143], ii) Bay et al. [38], iii) numerical rheometer, and iv) fitted to measurements.

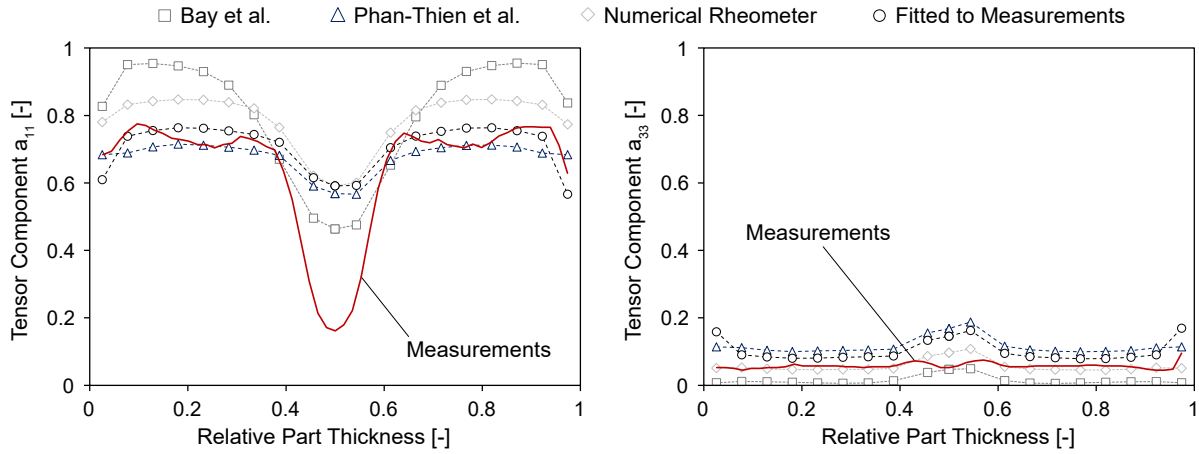

Figure 5.14.: Comparison of predicted and measured fiber orientation at location 2 for PPGF30, showing the tensor components a_{11} (left) and a_{33} (right). The C_I and κ values are obtained from: i) Phan-Thien et al. [143], ii) Bay et al. [38], iii) numerical rheometer, and iv) fitted to measurements.

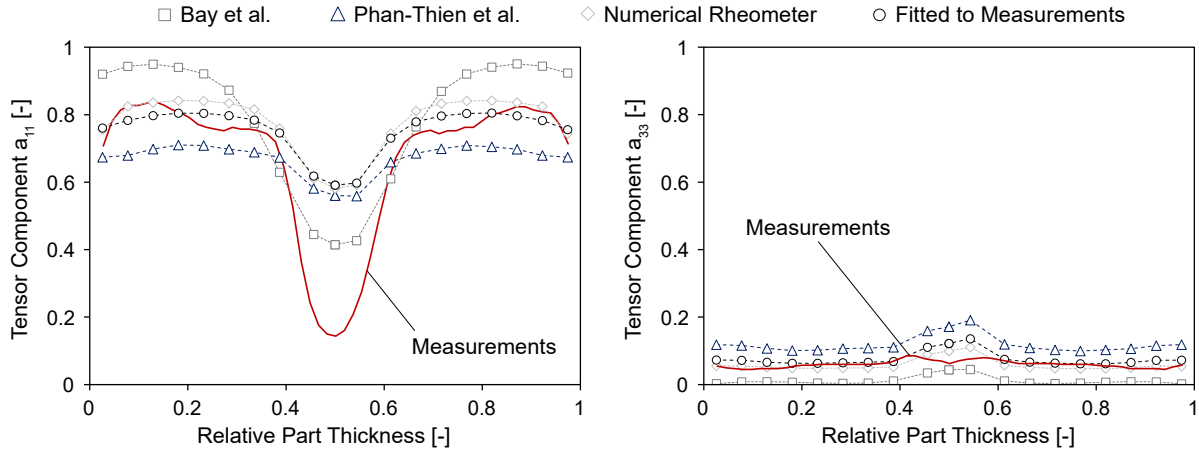

Figure 5.15.: Comparison of predicted and measured fiber orientation at location 2 for PPGF40, showing the tensor components a_{11} (left) and a_{33} (right). The C_I and κ values are obtained from: i) Phan-Thien et al. [143], ii) Bay et al. [38], iii) numerical rheometer, and iv) fitted to measurements.

5.3. Phelps-Tucker Model for Fiber Breakage Prediction

The experimental data obtained from the Couette rheometer study (Section 4.2.3) allow a fundamental evaluation of fiber breakage models. The Phelps-Tucker model [5] for fiber attrition is based on buckling failure as the driving mechanism for fiber breakage during processing (see also Section 2.3.3). In their work, Phelps et al. derive an unbreakable length, L_∞ (or L_{ub}):

$$L_\infty = \left[\frac{\pi^3 E_f d_f^4}{4 \zeta \eta_m \dot{\gamma}} \right]^{1/4} \tag{5.7}$$

where ζ is the dimensionless drag coefficient, η_m the viscosity of the polymer matrix and $\dot{\gamma}$ is the magnitude of the rate-of-deformation tensor. E_f is the elastic modulus of the fiber and d_f is the diameter of the fiber. Hence, the unbreakable fiber length predicted by the Phelps-Tucker model is dependent on the flow conditions ($\dot{\gamma}$), the material properties (η_m, d_f, and E_f) and the fitting parameter (ζ). The dimensionless drag coefficient ζ is assumed to be a material dependent parameter and must be fitted to experimental data [5]. As the first step of evaluating the model, values for ζ are calculated from the experimental data of the Couette rheometer study, because the unbreakable length was obtained for varying processing conditions in this study (see Section 4.23). By rearranging Equation 5.7, the values for ζ can be computed by

$$\zeta = \frac{\pi^3 E_f d_f^4}{4 L_\infty^4 \eta_m \dot{\gamma}} \tag{5.8}$$

Although Phelps et al. [5] did not explicitly state that ζ is dependent on the fiber concentration, it was shown from the Couette rheometer experiments that L_∞ depends on the fiber concentration. Because the other parameters in Equation 5.8 are independent of the fiber concentration, the fitting parameter ζ must reflect the dependency on fiber concentration and separate ζ values are obtained for each fiber concentration (20%wt, 30%wt, and 40%wt). Table 5.3 summarizes the average values calculated for the dimensionless drag coefficient, $\overline{\zeta}$.

Table 5.3.: Obtained values for ζ from the Couette rheometer experiments (see Chapter 4.2.3) .

	Average Value for ζ	**Standard Error of Obtained ζ Values**
20%wt	3.67	1.51
30%wt	8.63	2.00
40%wt	36.73	7.08

Although ζ should not be dependent on the processing conditions, the calculated values show a large range when the processing conditions are changed at constant nominal fiber concentration, reflected in the large standard errors. In fact, the calculated values for ζ vary from 18.96 (150 RPM, 220°C, 30%wt) to 0.754 (50 RPM, 280°C, 30%wt). Figure 5.16 shows the predicted values for L_∞ based on Equation 5.7 and the calculated average value for the dimensionless drag coefficient, $\overline{\zeta}$. The figure shows the measurements and the Phelps-Tucker model prediction for the varying processing conditions ($\eta_m \cdot \dot{\gamma}$). At more gentle processing conditions (high temperature and low processing speed) the model predictions show substantial discrepancies, especially for the 20%wt and 30%wt Couette rheometer experiments.

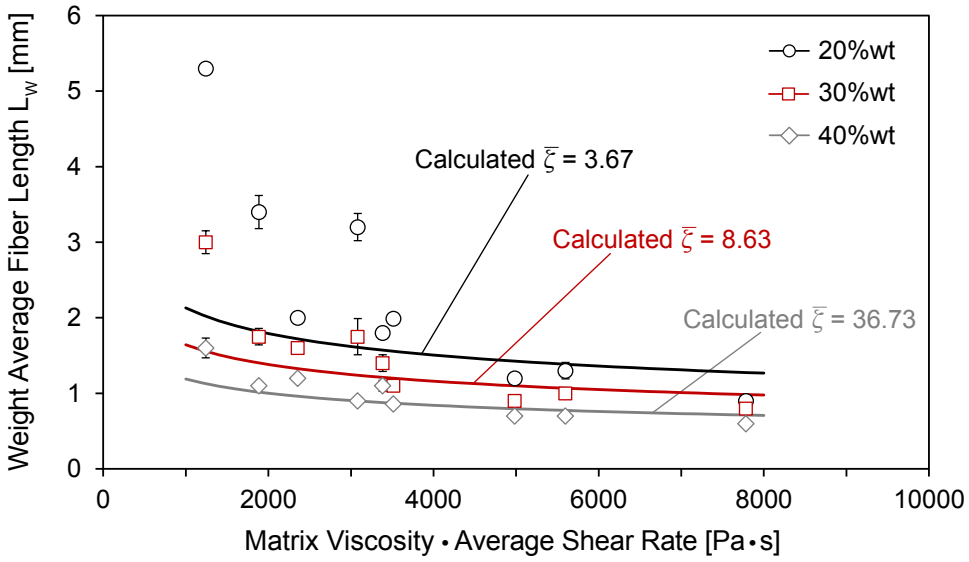

Figure 5.16.: Phelps-Tucker model prediction for L_∞ (solid line) and comparison to experimental data (markers) for 20%wt, 30%wt, and 40%wt fiber concentration.

The Phelps-Tucker model was further evaluated by implementing the model into MATLAB and fitting the fiber breakage coefficient C_B and the dimensionless parameter S to the measured data. The fitting was done using an optimization procedure based on the Gauss-Newton algorithm for non-linear least square problems [151]. The inputs for the fitting procedure are listed in Table 5.4. The shear rate was solved analytically as a simple Couette flow, using the measured viscosity data of the matrix material and assuming a constant temperature (see Appendix A). The values for ζ are calculated from Equation 5.8 and the experimental data for L_∞. The model parameters C_B and S are fitted within the bounds of $0.0001 < C_B < 0.1$ and $0.1 < S < 2$, following the suggestions of Phelps et al. [5, 112].

From this optimization procedure, distinct combinations of the three model parameters (ζ, C_B, and S) are obtained for each of the process conditions and fiber concentrations. To evaluate the

capability of the model to predict fiber breakage, each parameter set obtained from one condition was used to predict the fiber length for the remaining process conditions. The performance of the model prediction is evaluated by calculating the relative error between the predicted weight-average fiber length, L_W, and the measurements. This evaluative study was done separately for the three fiber concentrations (20%wt, 30%wt, and 40%wt).

Table 5.4.: Summary of input values for Phelps-Tucker model parameter fitting scheme.

Input Property	Value
Elastic modulus	73 GPa
Fiber diameter	19 µm
Average shear rate	Analytical solution for a Couette flow (see Appendix B)
Melt viscosity	Obtained from a material card (see Appendix A)
Drag coefficient, ζ	Calculated from experimental data (see Section 4.2.3)
Breakage coefficient, C_B	Range of 0.0001 to 0.1 (according to [5, 112])
Distribution shape factor, S	Range of 0.1 to 2 (according to [5, 112])
Fiber length measurements	Couette rheometer experiments (see Section 4.2.3)

Figures 5.17, 5.18, and 5.19 summarize the results of the evaluative study for 20%wt, 30%wt, and 40%wt, respectively. Each figure shows the obtained model parameters for the defined process condition (top) and the relative error between the predicted and the measured value for L_W is illustrated in a color map (bottom). It was possible to fit a model set of parameters (ζ, C_B, and S) for each condition that predicts the fiber length with less than 5% relative error, as shown by the diagonal components of the color map. However, the results suggest that the performance of predicting the fiber length for changing processing conditions is limited and large relative errors are obtained. In fact, there is set of model parameters that estimates L_W with less than 50% relative error for all processing conditions and the majority of the predictions result in more than 75% relative error.

Melt Temperature		220°C			250°C			280°C		
Processing Speed		50 RPM	100 RPM	150 RPM	50 RPM	100 RPM	150 RPM	50 RPM	100 RPM	150 RPM
Model Fitting	Calculated ζ	0.234	2.010	14.840	0.301	1.375	7.330	0.077	2.010	2.133
	Fitted C_B	0.0015	0.0011	0.0007	0.0016	0.0010	0.0007	0.0011	0.0009	0.0006
	Fitted S	0.385	0.050	0.172	0.568	0.233	0.176	2.000	0.243	0.233
Label		**Run 1**	**Run 2**	**Run 3**	**Run 4**	**Run 5**	**Run 6**	**Run 7**	**Run 8**	**Run 9**
Simulation Results	**Parameters Run 1**									
	Parameters Run 2									
	Parameters Run 3									
	Parameters Run 4									
	Parameters Run 5									
	Parameters Run 6									
	Parameters Run 7									
	Parameters Run 8									
	Parameters Run 9									

Relative Error between Predicted L_W and Measurements

0%	25%	50%	75%	100%	125%	>150%

Figure 5.17.: Results of emulating the fiber breakage in Couette rheometer experiments with the Phelps-Tucker model for 20%wt fiber concentration at varying processing conditions. A set of model parameters (ζ, C_B, and S) is obtained for each processing condition (top) and used to simulate the remaining trials. The relative error between predicted and measured weight-average fiber length, L_W, is shown as a color map (bottom).

Melt Temperature		220°C			250°C			280°C		
Processing Speed		50 RPM	100 RPM	150 RPM	50 RPM	100 RPM	150 RPM	50 RPM	100 RPM	150 RPM
Model Fitting	Calculated ζ	3.751	12.512	18.984	4.292	12.418	15.744	0.751	3.784	5.428
	Fitted C_B	0.0018	0.0010	0.0008	0.0019	0.0010	0.0007	0.0017	0.0011	0.0006
	Fitted S	0.051	0.102	0.180	0.217	0.187	0.050	0.382	0.503	0.051
Label		**Run 1**	**Run 2**	**Run 3**	**Run 4**	**Run 5**	**Run 6**	**Run 7**	**Run 8**	**Run 9**
Simulation Results	**Parameters Run 1**									
	Parameters Run 2									
	Parameters Run 3									
	Parameters Run 4									
	Parameters Run 5									
	Parameters Run 6									
	Parameters Run 7									
	Parameters Run 8									
	Parameters Run 9									

Relative Error between Predicted L_W and Measurements

0%	25%	50%	75%	100%	125%	>150%

Figure 5.18.: Results of emulating the fiber breakage in Couette rheometer experiments with the Phelps-Tucker model for 30%wt fiber concentration at varying processing conditions. A set of model parameters (ζ, C_B, and S) is obtained for each processing condition (top) and used to simulate the remaining trials. The relative error between predicted and measured weight-average fiber length, L_W, is shown as a color map (bottom).

Melt Temperature		220°C			250°C			280°C		
Processing Speed		50 RPM	100 RPM	150 RPM	50 RPM	100 RPM	150 RPM	50 RPM	100 RPM	150 RPM
Model Fitting	Calculated ζ	37.47	47.65	75.11	27.47	39.41	63.32	9.31	15.51	15.29
	Fitted C_B	0.0020	0.0010	0.0009	0.0020	0.0011	0.0008	0.0020	0.0013	0.0006
	Fitted S	0.176	0.105	0.405	0.180	0.175	0.154	0.202	0.180	0.176
Label		**Run 1**	**Run 2**	**Run 3**	**Run 4**	**Run 5**	**Run 6**	**Run 7**	**Run 8**	**Run 9**
Simulation Results	**Parameters Run 1**									
	Parameters Run 2									
	Parameters Run 3									
	Parameters Run 4									
	Parameters Run 5									
	Parameters Run 6									
	Parameters Run 7									
	Parameters Run 8									
	Parameters Run 9									

Relative Error between Predicted L_W and Measurements

0%	25%	50%	75%	100%	125%	>150%

Figure 5.19.: Results of emulating the fiber breakage in Couette rheometer experiments with the Phelps-Tucker model for 40%wt fiber concentration at varying processing conditions. A set of model parameters (ζ, C_B, and S) is obtained for each processing condition (top) and used to simulate the remaining trials. The relative error between predicted and measured weight-average fiber length, L_W, is shown as a color map (bottom).

Next, the model evaluation was extended to the fiber breakage history observed experimentally in the Coeutte rheometer study at 30%wt, 100 RPM and 250°C. The optimization of the fitting parameters was done for seven residence times (20 s, 30 s, 40 s, 60 s, 90 s, 120 s, and 180 s). The best fit for the parameter set (C_B, S, ζ) for the given experimental data was found to be C_B = 0.002, S = 0.1, and ζ = 12.42 (calculated from L_∞). Figure 5.20 shows the predicted fiber length reduction over time for the fitted model parameters and the measurements. The results suggests that the Phelps-Tucker model captures the fiber breakage with a 20.8% relative error for L_W and 45.12% relative error for L_N within the investigated residence times.

In a last step to evaluate the Phelps-Tucker model, injection molding simulations of the simple plate geometry were performed for the PPGF30 trial and the outcome was compared the measurements (see Chapter 4.1). Two sets of model parameters (C_B, S, ζ) were defined for the simulations. First, the default values according to Tseng et al. [36] and Huang et al. [153] were used (C_B = 0.02, S = 0.25, ζ = 3). The second set of parameters consists of the fitted values

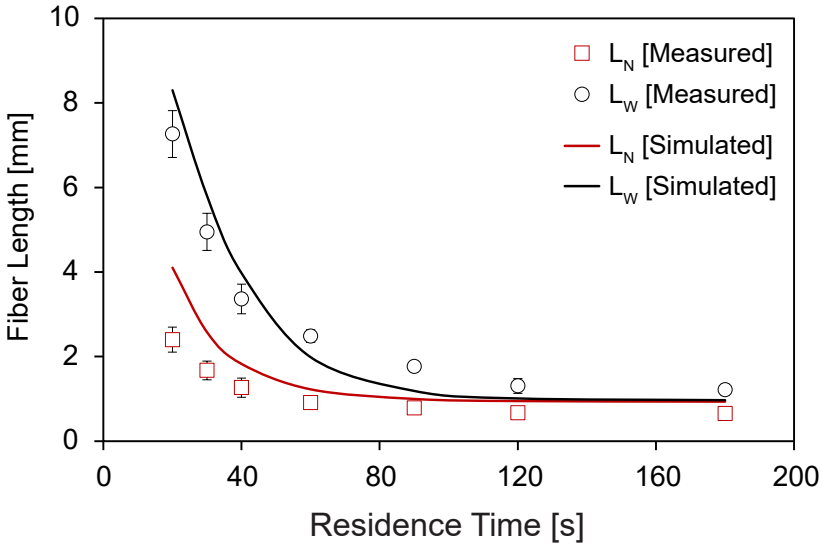

Figure 5.20.: Fiber length reduction over time for 250°C, 30%wt, and 100 RPM: L_N and L_W predicted using the Phelps-Tucker model for the optimized model parameters compared to measurements.

obtained from the Couette rheometer study for PPGF30 (C_B = 0.002, S = 0.1, ζ = 12.42). The initial fiber length in the injection molding simulation was set to the measured fiber length for the purged material (L_W = 3.10 mm). The initial fiber length was defined at the melt entrance of the sprue.

Figure 5.21 shows the comparison of the simulation results and the measurements for location 1, location 2, and location 3. The simulation with the default parameter set substantially underestimates the residual fiber length and shows a relative error -85.6%. The parameter set fitted to the Couette rheometer experiments overestimates the residual fiber length with a relative error of 25.2%. The experiments suggest a slight increase along the flow path from 1.86 mm at location 1 to 2.13 mm at location 3. This tendency is not captured by the simulation, which. in

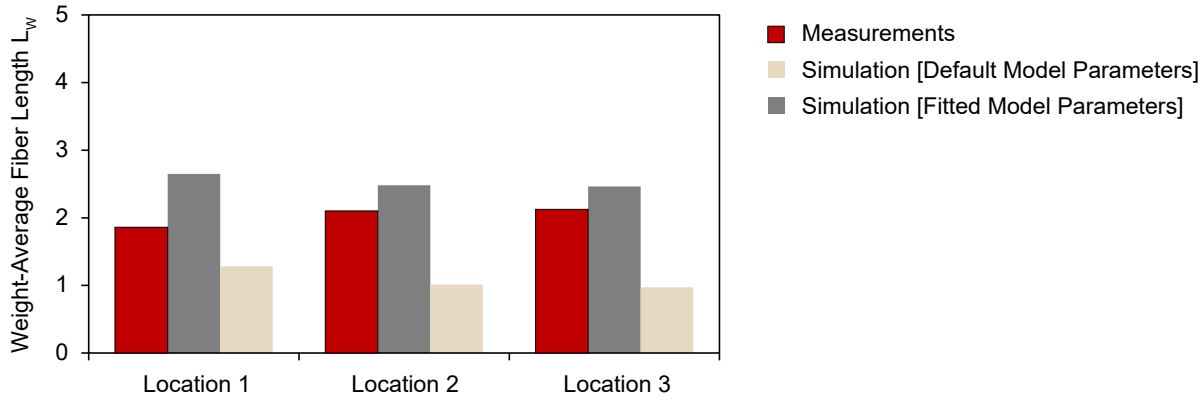

Figure 5.21.: Measured and predicted weight-average fiber length, L_W, for injection molded plate and the PPGF30 trial. The default parameters for the Phelps-Tucker Model are C_B = 0.02, S = 0.25, ζ = 3 and for the fitted parameters from the Couette rheometer are C_B = 0.002, S = 0.1, ζ = 12.42.

fact, suggests a decreasing residual fiber length along the flow path.

A potential reason for the discrepancies in predicting fiber length using the Phelps-Tucker model might be the assumption of buckling as the sole failure mechanism. While Forgacs and Mason [154] reported buckling deformation of a threadlike particle in a diluted suspension for shear deformation, it is not proven that buckling is the primary cause of fiber breakage while processing concentrated fiber-reinforced thermoplastics. In fact, qualitative observations of LFT samples suggest that fibers frequently show large bending deformation, as illustrated in Figure 5.22. Hence, the assumption that buckling is the sole failure mechanism, as the fundamental assumption of the Phelps-Tucker model [5], might not be appropriate in all cases.

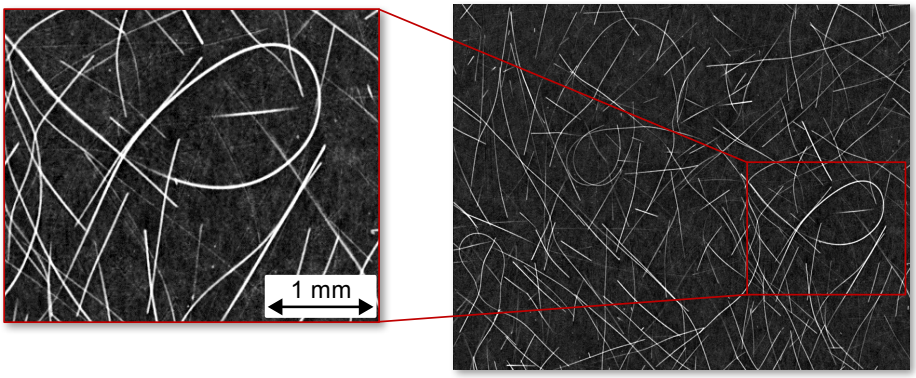

Figure 5.22.: Illustration of fibers experiencing bending deformation in LFT injection, showing a 2D slice from a µCT scan of an injection molded sample (20%wt nominal fiber concentration).

A first model based on bending failure was suggested by Osswald [155]. This modeling approach was tested with the experimental data from the Couette rheometer. The Osswald model assumes that a single fiber can undergo bending deformation caused by the hydrodynamic drag of the moving melt, as shown in Figure 5.23. The hydrodynamic drag acting on the fiber due to the melt moving at speed U_0 can be approximated as a chain of spheres [149]. The Stokes' drag exerted on a single sphere in a viscous fluid is then given by

$$F_{Sphere} = 6\,\eta_m\,U_0 \tag{5.9}$$

where η_m is the viscosity of the matrix. Representing the fiber as a chain of spheres with the same diameter as the fiber, the hydrodynamic force exerted on the fiber is the distributed load, w, calculated by

$$w = \frac{6\,\eta_m\,U_0}{d_f} \tag{5.10}$$

where d_f is the diameter of the fiber.

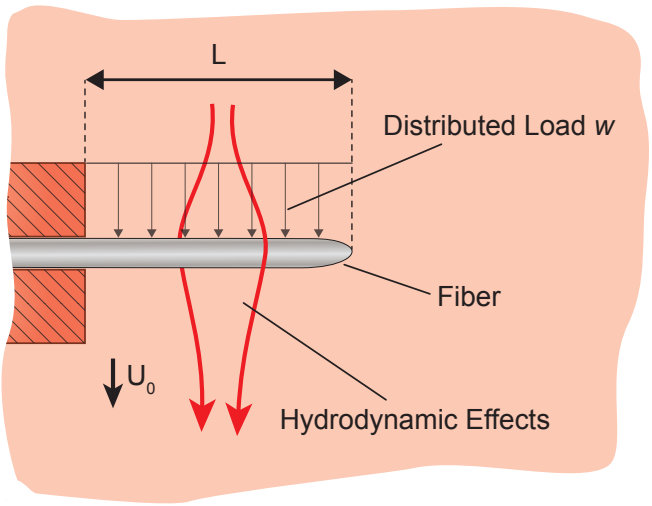

Figure 5.23.: Illustration of a fiber experiencing bending deformation. Adapted from [155].

The largest bending moment is exerted at the fixed end of the fiber. Assuming Euler-Bernoulli beam theory, the maximum stresses at the fiber surfaces can be computed by

$$\sigma_{max} = \pm \frac{96\,\eta_m\,U_0\,L^2}{\pi\,d_f^3} \tag{5.11}$$

Failure due to bending occurs if the stress exceeds the ultimate strength of the fiber, σ_u. Consequently, the unbreakable length, L_∞, can be defined as the maximum length at which no more failure occurs for given flow conditions:

$$L_\infty = \left(\frac{\pi\,\sigma_u\,d_f^3}{96\,\eta_m\,U_0}\right)^{1/2} \tag{5.12}$$

Dividing both sides by the fiber diameter d_f results in

$$\frac{L_\infty}{d_f} = \left(\frac{\pi\,\sigma_u\,d_f}{96\,\eta_m\,U_0}\right)^{1/2} \tag{5.13}$$

The parameter, h, is introduced to describe a characteristic distance, such as channel depth, runner size or cavity thickness [155]. Adding h to the numerator and denominator of the right-hand term gives

$$\frac{L_\infty}{d_f} = \left(\frac{\pi\,\sigma_u\,d_f\,h}{96\,\eta_m\,U_0\,h}\right)^{1/2} \tag{5.14}$$

The characteristic shear rate can be defined as $\dot{\gamma}{=}U_0/h$, so that

$$\frac{L_\infty}{d_f} = \left(\frac{\pi\,\sigma_u\,d_f}{96\,\eta_m\,\dot{\gamma}\,h}\right)^{1/2} \tag{5.15}$$

It is assumed that h is proportional to d_f, $h \propto d_f$, so that

$$\frac{L_\infty}{d_f} \propto \left(\frac{\pi \, \sigma_u \, d_f}{96 \, \eta_m \, \dot{\gamma} \, d_f} \right)^{1/2} \tag{5.16}$$

The proportionality can be resolved by introducing a dimensionless constant, λ, which gives

$$\frac{L_\infty}{d_f} = \lambda \left(\frac{\sigma_u}{\eta_m \, \dot{\gamma}} \right)^{1/2} \tag{5.17}$$

The parameter λ, or attrition number [155], is a material dependent property and a measure of fiber interactions that cause fiber attrition during processing. The parameter is assumed to capture the effects of fiber concentration (fiber-fiber interactions) and fiber-wall interactions. Values for λ can be obtained from the measured L_∞ values of the Couette rheometer experiments and by rearranging Equation 5.18, such that

$$\lambda = \frac{L_\infty}{d_f} \left(\frac{\eta_m \, \dot{\gamma}}{\sigma_u} \right)^{1/2} \tag{5.18}$$

Table 5.5 summarizes the average values calculated for the attrition number, $\overline{\lambda}$. While each fiber concentration (20%wt, 30%wt, and 40%wt) should result in a different value for the attrition number, the processing conditions should not cause a change of λ, such that λ is independent of any change in melt temperature and processing speed. Although the calculated λ values vary with respect to the processing conditions, the overall range in obtained values is significantly smaller compared to the calculated values for ζ of the Phelps-Tucker model.

Table 5.5.: Obtained values for λ from the Couette rheometer experiments (see Chapter 4.2.3).

	Average Value for λ	**Standard Error of Obtained λ Values**
20%wt	0.125	0.013
30%wt	0.083	0.004
40%wt	0.055	0.002

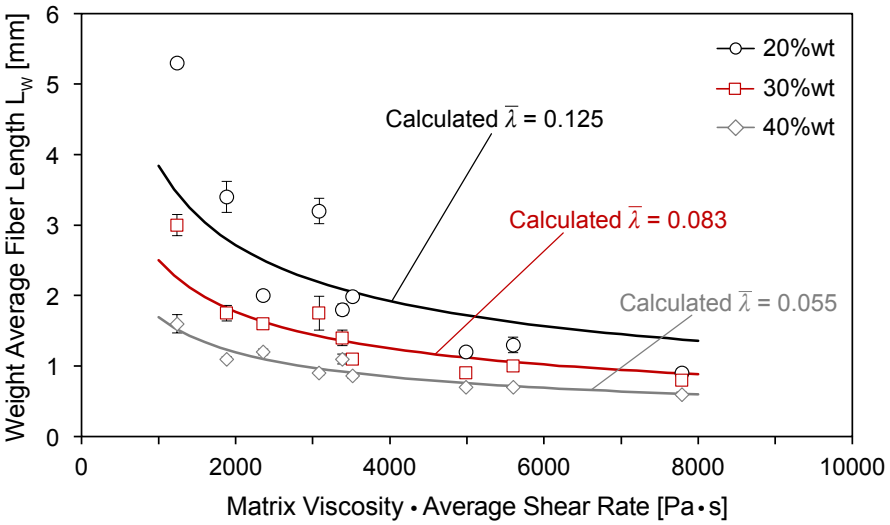

Figure 5.24.: Osswald model prediction for L_∞ (solid line) and comparison to experimental data (markers) for 20%wt, 30%wt, and 40%wt fiber concentration.

Figure 5.24 shows the prediction of the Osswald model for L_∞ and the measurements for the varying processing conditions, represented by $(\boldsymbol{\eta_m} \cdot \dot{\boldsymbol{\gamma}})$. The model predictions are based on Equation 5.18, using the calculated average value for the dimensionless drag coefficient, $\bar{\lambda}$. The results show good agreement for the 30%wt and 40%wt experiments, but the predictions for 20%wt show large discrepancies at gentle processing conditions (high temperature and low processing speed) as well as harsh processing conditions (low temperature and high processing speed). Figure 5.25 shows a comparison of the previous results obtained with the Phelps-Tucker model and the outcome of the new model based on bending failure. For the investigated processing conditions, the Osswald model captures the fiber attrition much better throughout

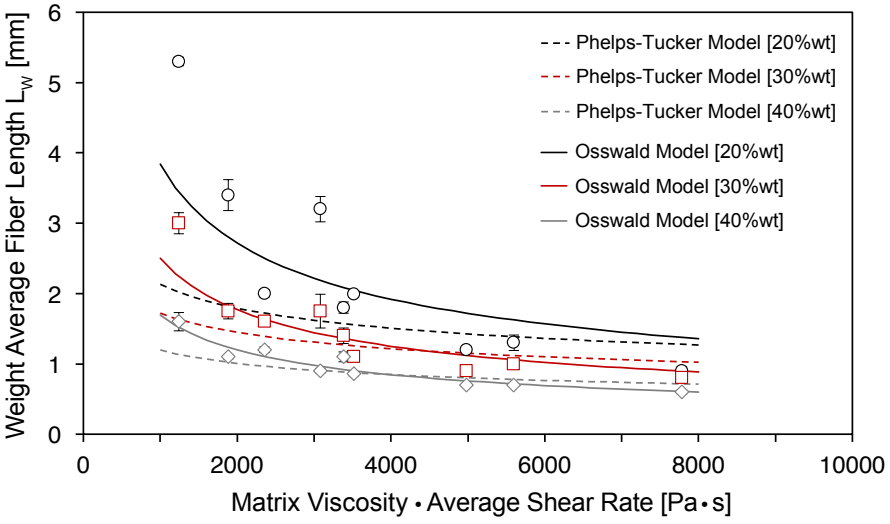

Figure 5.25.: Osswald model prediction for L_∞ (solid line) and comparison to experimental data (markers) for 20%wt, 30%wt, and 40%wt fiber concentration.

the entire range of processing conditions. In particular, the results show that the Osswald model is able to predict the residual fiber length for gentle processing conditions better than the Phelps-Tucker model.

5.4. Discussion and Conclusions

The evaluation of models used to predict the process-induced fiber microstructure of discontinuous fiber-reinforced composites revealed shortcomings in the models' capability to estimate the state of the fibers in the molded part. A research project administered by the Pacific Northwest National Laboratory (PNNL) [156] focused on evaluating the performance of numerical tools for carbon fiber-reinforced thermoplastics, including process-simulation and the structural analysis. In their study, the researchers defined a relative error of 15% as the threshold for the prediction of fiber orientation. Applying the PNNL criterion for the evaluative study of the simulation tools used in this work, most of the simulation results fail to meet the threshold. Overall, it can be concluded that the models are limited in their applications without being able to accurately account for process-induced microstructure and the simulation results would always require experimental validation.

The two phase suspension model adapted for Moldex3D^{TM} was not able to capture the fiber matrix separation that was observed experimentally. The variation in thickness direction showed substantial discrepancies. In particular, the fiber agglomeration in the core layer was not captured by the model. Although an increase in fiber concentration along the flow path was predicted, the extent of increase was significantly underestimated when compared to the measurements. The outcome of the evaluation suggests that the model is not suitable to estimate fiber matrix separation in LFT injection molding at this point. Morris and Boulay [116] originally derived the two phase suspension model for spherical particles and tested it for simple flow conditions under isothermal conditions. Tseng et al. [36] adapted the model for concentrated fiber suspension by incorporating an effective particle radius. The discrepancies found in this work might be rooted in the simplification of adapting the original suspension model for spherical particles to concentrated fiber suspensions. This approach neglects the fiber-fiber interactions present in LFT injection molding and does not address the potential correlation between fiber alignment and fiber matrix separation. Furthermore, the highly dynamic flow conditions in injection molding might require further adaptation from the original Morris and Boulay model

that incorporates the isothermal characteristics of the process and the melt solidification. In conclusion, the evaluative study suggests that the adapted two phase suspension model requires an extended framework that specifically addresses the material behavior of concentrated fiber suspensions before it can be used to predict the fiber matrix separation in LFT injection molding. The Folgar-Tucker model has found widespread industrial acceptance to predict fiber orientation to account for the process-induced anisotropy in molded parts. The model requires a set of material-dependent model parameters that are conventionally fit to experiments. In this work, a PLS approach was used to substitute the experimental fitting procedure by defining a numerical rheometer simulation. The obtained model parameters were applied for predicting the fiber orientation of injection molded plates at varying nominal fiber concentration. While the simulation results show good agreement for the 40%wt moldings, the results at lower concentration overestimate the fiber orientation in the shell layer substantially. More severe discrepancies between simulation and measurements were found using the empirical relationship for C_I suggested by Bay et al. [38], which overestimated the fiber alignment in the shell substantially for all trials. The empirical relationship proposed by Phan-Thien resulted in acceptable fiber orientation predictions for PPGF20 and PPGF30, but underestimated the fiber orientation at PPGF40. The overall results for the obtained fiber-fiber interaction coefficients obtained by the different methods are shown in Figure 5.26. The outcome underlines the challenges of obtaining correct model parameters, because the simulation results are highly dependent on the correct choice of the parameters.

Interestingly, the predicted fiber orientation in the core layer shows substantial discrepancies for the parameter sets tested in this work. In fact, it was not possible to match the predicted fiber orientation in the core without causing severe discrepancies in the skin and shell layers. Similar errors in the prediction of fiber orientation using the Folgar-Tucker model were reported by Kleindel et al. [157]. Their results showed that the Folgar-Tucker model estimated the fiber orientation correctly in the shell layers, but the fiber alignment in the core layer and the width of the core was significantly underestimated. Recently, Tseng et al. [146] addressed the challenges in simulating the fiber orientation in the core layer for injection molding of discontinuous fiber-reinforced thermoplastics. The authors propose an adapted viscosity model, introducing a yield-stress viscosity at low shear rates. They expanded the existing Cross-WLF model by adding the yield stress term represented by the Arrhenius-Eyring equation [146]. This approach led to improved fiber orientation predictions in the core layer. More research is necessary to determine

if the root cause of the discrepancies between simulation and experiment is in fact caused by the modeling of the suspension viscosity. Another reason for the discrepancies might be the simplifying assumption of a constant fiber concentration during processing. The experimental study in this work showed substantial variation of the fiber concentration along the flow path and through the thickness of the molded plates. Furthermore, it was established in this work and in past studies [9, 35, 38, 141, 143] that the process-induced fiber orientation depends on fiber concentration. Hence, any local change in fiber concentration throughout the process affects the fiber orientation behavior. This relationship cannot be captured with a constant C_I value, but would require a model for C_I that includes the effect of fiber matrix separation.

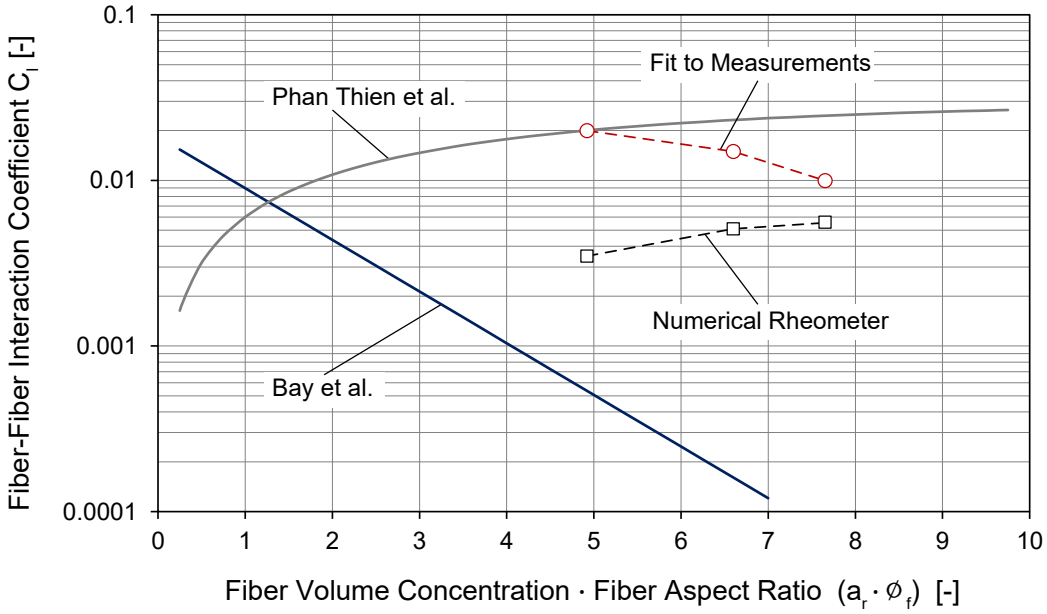

Figure 5.26.: Comparison of the C_I values for PPGF20, PPGF30, and PPGF40, obtained from published empirical relationship (Phan-Thien et al. [143] and Bay et al. [38]), from the numerical rheometer simulations, and by fitting C_I to measurements.

The Phelps-Tucker model for fiber breakage prediction was evaluated using the experimental data from the Couette rheometer study. The simulation results showed that three model parameters can always be adapted to match experimental results. However, it was not possible to show that the model parameters are material-dependent and intrinsic properties. The evaluative study suggests that changing only processing conditions and keeping the model parameters constant results in large errors in the predicted residual lengths for the Couette rheometer experiments. Additionally, the Phelps-Tucker model was tested for the injection molding trials by using default model parameters and a fitted parameter set obtained from the Couette rheometer experiments. For all cases, the simulation results showed a relative error of more than 25%, highlighting

the limitation of using the Phelps-Tucker model for predicting fiber breakage in LFT injection molding. A potential cause for the discrepancies can be related to the fundamental assumption in the Phelps-Tucker model that fibers solely break due to buckling. A preliminary model proposed by Osswald, which assumes bending failure as the driving mechanism for breakage, was tested with the experimental data from Couette rheometer and compared to the Phelps-Tucker model. The results show that the Osswald model captures the measured residual fiber length at long residence times much better than the Phelps-Tucker model. While this is not yet a full validation of the Osswald model, it is a starting point for developing improved fiber breakage models.

6. Summary

This dissertation presented a fundamental analysis of the process-induced fiber configuration in LFT processing. The work focused on three tasks: i) to develop characterization methodologies for quantifying the microstructural properties, ii) to perform experimental studies analyzing the process phenomena, and iii) to evaluate available predictive models. Along these three dimensions, this work outlined the profound complexity that is embedded in the process-microstructure relationship for LFT materials and contributes to a better understanding of the underlying physics of the mechanisms that cause fiber alignment, fiber breakage, and fiber matrix separation.

Chapter 3 summarized the characterization techniques developed as part of this dissertation. The developed methodologies apply µCT and optical measurement systems, combined with image processing algorithms to accurately and efficiently quantify the fiber properties. Furthermore, comparative studies with conventional methodologies were performed, highlighting the challenges in quantifying the microstructural properties in molded samples. The findings can serve as a first step to a standardized approach in characterizing the process-induced fiber configuration, enabling the comparability across experimental research studies.

The experimental studies presented in Chapter 4 resulted in a comprehensive analysis of the process-induced fiber microstructure. The measurements of injection molded samples suggested substantial fiber matrix separation, contradicting the common assumption of a uniform fiber concentration throughout molded parts. The results showed correlation between the microstructural properties, in particular between the measured through-thickness fiber orientation and fiber concentration. The design and development of an experimental procedure to study fiber breakage under controlled conditions using a Couette rheoemeter setup proved to be a novel and valuable tool. This work generated experimental data for a systematic analysis of the underlying physics of fiber breakage. The findings revealed the severe challenges posed by fiber breakage in LFT processing. In fact, the outcome of this work shows that the process-induced fiber break-

age might be the most promising process parameter to be optimized in order to expand the application of LFT materials.

In Chapter 5, modeling approaches in LFT processing were evaluated by applying the findings of the experimental work. The outcome showed that current attempts at modeling the process-induced change in fiber configuration have room for improvement. Even for the simple plate geometry of the injection molding trials or the controlled process conditions of the Couette rheometer experiments, the models failed to provide acceptable results. All predictive tools depend on empirical fitting parameters, without a defined procedure on how to obtain these parameters or a constitutive relationship. However, the outcome of the simulations can depend substantially on the correct choice of parameters. This work showed that default values for the model parameters cannot be assumed to result in accurate simulation outcomes. Nevertheless, a truly predictive tool used in industrial product development processes requires that fitting parameters must be characterizable *a priori*, with little experimental input and ideally through constitutive relationships. The state-of-the-art models tested in this work do not meet these requirements. The findings in this work suggest that the shortcomings of predictive tools might stem from the decoupled approach, where fiber breakage, fiber alignment and fiber matrix separation are each modeled separately.

6.1. Contributions

The work presented in this dissertation contributes the following new elements to the characterization of the process-induced fiber configuration in LFT molding:

- Development of Characterization Techniques
  - Developed methodologies to accurately quantify the fiber microstructure, including the development of i) a new methodology for fiber length measurements using a novel sample preparation technique and image processing algorithm, ii) an image processing algorithm based on simple geometric projections to quantify the fiber orientation from µCT scans, and iii) a novel analysis technique to measure the through-thickness fiber concentration using µCT.
  - Validated the developed characterization procedures for long glass fiber-reinforced PP samples and compared to conventional techniques.

  - Contributed to the attempt of standardization of the characterization of the fiber microstructure for discontinuous fiber-reinforced thermoplastics to provide comparability of experimental studies.

- Experimental Studies
  - Comprehensively characterized the process-induced fiber microstructure for injection molded plates at nominal fiber concentrations varying from 5%wt to 60%wt, including fiber length, fiber orientation, and fiber concentration measurements.
  - Discovered substantial fiber matrix separation in LFT injection that occurs during mold filling. The findings refute the common assumption of a uniform fiber concentration in molded parts, which is assumed to have a significant impact on material modeling and structural analyses of injection molded LFT parts.
  - Analyzed the correlation between the fiber length, fiber orientation, and fiber concentration. The findings suggest that a holistic analysis is required to fully capture the process-induced fiber microstructure, as opposed to the conventional approaches of characterizing the microstructural properties individually.
  - Developed a novel experimental setup to study fiber breakage under controlled conditions, enabling a fundamental study of the underlying physics of fiber breakage.
  - Completed experimental studies that quantify the effect of processing conditions and material properties on fiber breakage under controlled conditions.

- Evaluation of Modeling Approaches
  - Completed a comprehensive assessment of predictive models using the experimental results of this work, indicating that the phenomena of fiber breakage, fiber alignment, and fiber matrix separation cannot be estimated accurately.
  - Showed that the adapted two phase suspension model was not suitable for estimating the fiber matrix separation in LFT injection molding. The findings suggest that the framework of the model needs to be reevaluated fundamentally to make it suitable for concentrated fiber suspensions.
  - Demonstrated that the Folgar-Tucker model provided acceptable results for the fiber orientation in the skin and shell layers, but was inaccurate for the fiber orientation prediction in the core layer. However, the simulation outcome strongly depends on the

correct choice of the fiber-fiber interaction coefficient. The outcome of the evaluative study suggested that accounting for fiber matrix separation is necessary to obtain correct prediction for the fiber orientation in the core layer.

- Tested the Phelps-Tucker model and found that the model could not accurately predict fiber breakage for either the Couette rheometer experiments or the injection molding trials. The analysis showed that the choice of correct model parameters is crucial, but also that it was not possible to find intrinsic parameters, rejecting the model as a truly predictive model.
- Applied the Osswald model for fiber breakage and showed improved predictions of fiber breakage, suggesting that bending failure might be the driving mechanism for fiber breakage during processing.

6.2. Recommendations for Future Work

More work is required to obtain a complete understanding of the process-induced fiber configuration and further exploration may target the following avenues:

- Fiber Breakage
  - Similar to through-thickness variation of fiber concentration and fiber orientation, it is excepted that the fiber length varies along the thickness direction of molded samples. Hence, an adapted fiber length measurement procedure to accurately obtain the through-thickness fiber length distribution would allow further correlation of the relationship between the microstructural properties.
  - A fundamental analysis of the driving mechanism causing fiber breakage in concentrated suspensions is necessary, especially for LFT materials. While the bending failure model proposed by Osswald shows better predictive capability than the Phelps-Tucker model, further work is required to clearly identify how fibers break during LFT processing.
  - The Couette rheometer setup proved to be a valuable tool and enables a wide range further studies along different materials and process parameters. In particular, a study with diluted suspensions would be an important avenue to explore. Testing highly diluted suspensions and comparing them to concentrated suspension would

allow a study of the influence of fiber-fiber interactions and hydrodynamic effects.

- Fiber Matrix Separation
  - The substantial fiber agglomeration in the core layer found in this work may depend on the processing conditions. Hence, an experimental investigation into the effect of process parameters on the through-thickness fiber concentration would be important. Furthermore, the impact of the gate design on fiber migration needs to be identified.
  - Modeling the fiber matrix separation is an important task to be able to predict the fiber concentration in molded parts. As shown in this dissertation, more work is necessary to reliably estimate the migration of fibers during processing. While it is possible to adapt the two phase suspension model, it might be necessary to define a completely new framework for modeling the fiber matrix separation in LFT injection molding, incorporating the dependency of fiber-fiber interactions and fiber orientation.
  - The substantial fiber matrix separation observed in this work can be assumed to have a profound impact on the mechanical performance of a molded part. It is necessary to examine the effect on material modeling and structural analysis by comparing the common assumption of a uniform fiber concentration and the measured fiber concentration distribution.

- Fiber Alignment
  - An important next step is to expand the Folgar-Tucker model with a fiber-fiber interaction coefficient that depends on the local fiber concentration to account for the fiber matrix separation observed in this work. This might be able to overcome the discrepancies in predicting the fiber orientation in the core layers. However, this requires a suitable model for fiber migration (see above). A first step might be to define an empirical function for C_I that accounts for the spatial change in fiber concentration, such as $C_I = f(\phi_f, x, y, z)$, where ϕ_f is the local fiber concentration and x, y, and z are the coordinates of the cavity.
  - The simulation of a numerical rheometer using the PLS approach provides important insights into fiber motion and fiber alignment for defined flow conditions and material properties. Of particular interest would be a study on how the fiber flexibility affects

the fiber orientation. While the Folgar-Tucker model assumes rigid fibers, the flexibility observed for longer fibers might require an adjustment of the model. Tracking single fibers and performing numerical experiments using the PLS approach would help estimate the impact of flexibility.

6.3. Publications

Several articles have been submitted for publication as a result of the research detailed in this dissertation:

- Peer-Reviewed Journal Publications
  - **Goris, S.**, Simon, S., Werner, S., Jäger, S., Angel, Y., Dave, B., Osswald, T.A.: *Fundamental Study on Fiber Breakage under Controlled Conditions for Long Glass Fiber-Reinforced Thermoplastics*, Composites Science and Technology, 2017 [under preparation]
  - Mulholland, T., **Goris, S.**, Boxleitner, J., Osswald, T.A., Rudolph, N.: *Fiber Orientation Effects in Fused Filament Fabrication of Air-Cooled Heat Exchanger*, The Journal of The Minerals, Metals & Materials Society, 2017 [accepted]
  - **Goris, S.** and Osswald, T.A.: *Process-Induced Fiber Matrix Separation in Long Fiber-Reinforced Thermoplastics*, Composites Part A: Applied Science and Manufacturing, DOI:10.1016/j.compositesa.2017.11.024, 2017
  - **Goris, S.**, Back, T., Brands, D., Angel, Y., Drummer, D., Osswald, T.: *A novel fiber length measurement technique for discontinuous fiber-reinforced composites: A comparative study with existing methods*, Polymer Composites, DOI:10.1002/pc.24466, 2017
- Peer-Reviewed Conference Papers
  - **Goris, S.**, Simon, S., Montoya, C., Bechara, A., Brands, D., Angel, Y., Candal, M.V., Osswald, T.A.: *Experimental Study on Fiber Attrition of Long Glass Fiber-Reinforced Thermoplastics under Controlled Conditions in a Couette Flow.* Proceedings of the SPE Annual Technical Conference, Anaheim, CA, 2017
  - Walter, I., **Goris, S.**, Teuwsen, J., Tapia, A., Perez, C., Osswald, T.A.: *A Direct Particle Level Simulation Coupled with The Folgar-Tucker RSC Model to Predict*

Fiber Orientation in Injection Molding of Long Glass Fiber Reinforced Thermoplastics. Proceedings of the SPE Annual Technical Conference, Anaheim, CA, 2017

- Teuwsen, J., **Goris, S.**, Osswald, T.A.: *Impact of the Process-Induced Microstructure on the Mechanical Performance of Injection Molded Long Glass Fiber-Reinforced PP.* Proceedings of the SPE Annual Technical Conference, Anaheim, CA, 2017
- **Goris, S.** and Osswald, T.A.: *Progress on the Characterization of the Process-Induced Fiber Microstructure of Long Fiber-Reinforced Materials.* Proceedings of the 16th SPE Automotive Composites Conference & Exhibition (ACCE), Novi, MI, 2016
- **Goris, S.**, Gandhi, U., Song, Y.Y., Osswald, T.A.: *Analysis of the Process-Induced Microstructure in Injection Molding of Long Glass Fiber-Reinforced Thermoplastics.* Proceedings of the SPE Annual Technical Conference, Indianapolis, IN, 2016
- **Goris, S.**, Fontana, C., Osswald, T.A.: *Fiber Orientation Measurements Using a Novel Image Processing Algorithm for Micro-Computed Tomography Scans.* Proceedings of the SPE Annual Technical Conference, Orlando, FL, 2015
- Perez, C., **Goris, S.**, Ramirez, D., Osswald, T.A.: *The Use of a Direct Particle Simulation to Predict Fiber Motion in Processing of Fiber-Reinforced Thermoplastics.* Proceedings of the international PPS Conference, Graz, Switzerland, 2015
- **Goris, S.**, Perez, C., Gandhi, U., Osswald, T.A.: *Impact of Fiber Orientation Distribution within a D-LFT Strand on Warpage of a Compression Molded Part.* Proceedings of the SPE Annual Technical Conference, Las Vegas, NV, 2014
- Baur, E., **Goris, S.**, Ramirez, D., Schmidtke, P., Osswald, T.A.: *Mechanistic Model to Determine Fiber Orientation Simulation Material Properties.* Proceedings of the SPE Annual Technical Conference, Las Vegas, NV, 2014
- Perez, C., **Goris, S.**, Osswald, T.A.: *Study on the Fiber Properties of a LFT Strand.* Proceedings of the 13th SPE Automotive Composites Conference & Exhibition (ACCE), Novi, MI, 2013

- Books, Book Chapters, and Online Articles
  - Osswald, T.A., Gandhi, U., **Goris, S.**: *Understanding Discontinuous Fiber Reinforced Composites - Automotive Applications.* Hanser Publisher, 2018 [under preparation]

– **Goris, S.**, Back, T., Brands, D., Angel, Y., Drummer, D., Osswald, T.: *Accurate, repeatable, and efficient fiber-length measurements.* SPE Plastics Research Online, 10.2417/spepro.006973, 2017

– **Goris, S.**, Puentes, J., Osswald, T.A.: *Chapter 34. Composites Manufacturing Processes, Manufacturing Engineering Handbook*, 2nd Edition, McGraw-Hill, USA, 2015

References

[1] S. Goris, P. John, and T. A. Osswald: "Chapter 33: Polymer Composites Manufacturing Processes", in: *Manufacturing Engineering Handbook*, 2nd Edition, McGraw-Hill Education, Oct. 2015 (cit. on pp. 1, 2, 11).

[2] S.-Y. Fu, Y.-W. Mai, and B. Lauke: *Science and Engineering of Short Fibre Reinforced Polymer Composites*, First, Woodhead Publishing Limited, 2009 (cit. on p. 1).

[3] M. Rohde, A. Ebel, F. Wolff-Fabris, and V. Altstädt: "Influence of Processing Parameters on the Fiber Length and Impact Properties of Injection Molded Long Glass Fiber Reinforced Polypropylene", *International Polymer Processing*, 26 (3), pp. 292–303, July 2011 (cit. on pp. 1, 16, 17, 19, 29–31).

[4] R. Bailey and H. Kraft: "A Study of Fibre Attrition in the Processing of Long Fibre Reinforced Thermoplastics", *International Polymer Processing*, 2 (2), pp. 94–101, Nov. 1987 (cit. on p. 1).

[5] J. Phelps, A. Abd El-Rahman, V. Kunc, and C. Tucker: "A model for fiber length attrition in injection-molded long-fiber composites", *Composites Part A: Applied Science and Manufacturing*, 51, pp. 11–21, 2013 (cit. on pp. 1–4, 6, 7, 16, 24, 37, 38, 90, 108, 119–121, 126).

[6] M. Priebe and R. Schledjewski: "Processing and properties of glass/polypropylene in long fibre compounding extrusion", *Plastics, Rubber and Composites*, 40 (6-7), pp. 374–379, 2011 (cit. on pp. 1, 30).

[7] H. Friedrich: *Leichtbau in der Fahrzeugtechnik*, ed. by ATZ/MTZ-Fachbuch, Heidelberg: Springer-Verlag GmbH, 2013 (cit. on p. 1).

[8] T. A. Osswald and G. Menges: *Materials Science of Polymers for Engineers*, 3rd editon, Munich: Hanser Publisher, 2012 (cit. on pp. 1, 8, 9, 16, 17, 163).

[9] J. H. Phelps and C. Tucker: "An anisotropic rotary diffusion model for fiber orientation in short- and long-fiber thermoplastics", *Journal of Non-Newtonian Fluid Mechanics*, 156 (3), pp. 165–176, 2009 (cit. on pp. 1, 11, 33–35, 111, 132).

[10] J. L. Thomason and M. A. Vlug: "Influence of fibre length and concentration on the properties of glass fibre-reinforced polypropylene: 4. Impact properties", *Composites Part A: Applied Science and Manufacturing*, 28 (3), pp. 277–288, 1997 (cit. on pp. 1, 22, 23).

[11] C. T. Herakovich: *Mechanics of Fibrous Composites*, First Edition, John Wiley and Sons, Inc., 1998 (cit. on p. 1).

[12] A. Durin, P. De Micheli, J. Ville, F. Inceoglu, R. Valette, and B. Vergnes: "A matricial approach of fibre breakage in twin-screw extrusion of glass fibres reinforced thermoplastics", *Composites Part A: Applied Science and Manufacturing*, 48, pp. 47–56, 2013 (cit. on p. 2).

[13] T. Osswald and J. Hernández-Ortiz: *Polymer Processing - Modeling and Simulation*, ed. by T. Osswald, Munich: Hanser Publishers, 2006 (cit. on pp. 2, 4).

[14] M. Schemme: "Sicherung der Produktqualität bei der Herstellung und Verarbeitung von SMC-Werkstoffen", PhD thesis, University of Erlangen-Nuremberg, 1996 (cit. on p. 2).

[15] K. S. Kumar, V. Patel, A. Tyagi, N. Bhatnagar, and A. K. Ghosh: "Injection Molding of Long Fiber Reinforced Thermoplastic Composites", *International Polymer Processing*, 24 (1), pp. 17–22, Mar. 2009 (cit. on pp. 2, 3).

[16] I. V. K. AVK: *Handbuch Faserverbundkunststoffe - Grundlagen, Verarbeitung, Anwendungen*, ed. by A. .-. I. V. K. e.V., Wiesbaden: Vieweg+Teubner Verlag, 2010 (cit. on p. 2).

[17] T. Kraus and E. Witten: *Composites-Marktbericht 2014*, tech. rep., 2014 (cit. on p. 2).

[18] S. Goris and T. A. Osswald: "Fiber Orientation Measurements Using a Novel Image Processing Algorithm for Micro-Computed Tomography Scans", *Proceedings of the 15th Automotive Composites Conference and Exhibition* 2015 (cit. on p. 2).

[19] K. Brast: "Verarbeitung von langfaserverstärkten Thermoplasten im direkten Plastifizier-Pressverfahren", PhD thesis, 2001 (cit. on p. 3).

[20] R. Hafellner, M. Pichler, G. Wörndle, G. Steinbichler, and P. Egger: "Lange Fasern spritzgiessen", *Kunststoffe*, 90 (3) 2000 (cit. on p. 3).

[21] A. Inoue, M. Kazuya, T. Tanaka, Y. Arao, and Y. Sawada: "Effect of screw design on fiber breakage and dispersion in injection-molded long glass-fiber-reinforced polypropylene", *Journal of Composite Materials*, 49 (1) 2015 (cit. on pp. 3, 17, 19, 30, 31, 104).

[22] M. Metten and M. Cremer: "Langfaserverstaerkte Thermoplaste spritzgiessen - Verfahrensparameter beeinflussen die Faserlaenge", *Kunststoffe*, 90 (1) 2000 (cit. on pp. 3, 20, 21).

[23] V. Vaidya: *Composites for Automotive, Truck and Mass Transit - Materials, Design, Manufacturing*, first edition, Pennsylvania, US: DEStech Publications, Inc., 2011 (cit. on pp. 3, 4, 103).

[24] P. Foss, H.-C. Tseng, J. Snawerdt, Y.-J. Chang, W.-H. Yang, and C.-H. Hsu: "Prediction of fiber orientation distribution in injection molded parts using Moldex3D simulation", en, *Polymer Composites*, 35 (4), pp. 671–680, Apr. 2014 (cit. on pp. 4, 108, 111).

[25] A. Londoño-Hurtado, J. Hernandez-Ortiz, and T. Osswald: "Mechanism of fiber-matrix separation in ribbed compression molded parts", *Polymer Composites*, 28 (4), pp. 451–457, 2007 (cit. on pp. 4, 13, 114).

[26] B. Pipes: "Accelerating the certification process for aerospace composites: Columnist Byron Pipes foresees the certification of simulation software in place of physical testing", *CompositesWorld* Mar. 2014 (cit. on p. 4).

[27] K. Balaji Thattaiparthasarathy, S. Pillay, H. Ning, and U. K. Vaidya: "Process simulation, design and manufacturing of a long fiber thermoplastic composite for mass transit application", *Composites Part A: Applied Science and Manufacturing*, 39 (9), pp. 1512–1521, 2008 (cit. on p. 4).

[28] S. D. Bartus, U. K. Vaidya, and C. A. Ulven: "Design and Development of a Long Fiber Thermoplastic Bus Seat", *Journal of Thermoplastic Composite Materials*, 19 (2), pp. 131–154, 2006 (cit. on p. 4).

[29] U. K. Vaidya, J. C. Serrano, A. Villalobos, J. Sands, and J. Garner: "Design and analysis of a long fiber thermoplastic composite tailcone for a tank gun training round", *Materials & Design*, 29 (2), pp. 305–318, Jan. 2008 (cit. on p. 4).

[30] C. Kuhn, I. Walter, O. Taeger, and T. Osswald: "Experimental and Numerical Analysis of Fiber Matrix Separation during Compression Molding of Long Fiber Reinforced Thermoplastics", *Journal of Composites Science*, 1 (2) 2017 (cit. on pp. 4, 13).

[31] D. C. Guell and T. D. Papathanasiou: *Flow-induced alignment in composite materials*, English, Cambridge: Woodhead, 1997 (cit. on p. 4).

[32] H. Tseng, R.-Y. Chang, and C. Hsu: "An objective tensor to predict anisotropic fiber orientation in concentrated suspensions", *Journal of Rheology*, 60 (2), pp. 215–224, 2016 (cit. on pp. 6, 11, 34, 35).

[33] J. Morris: "A review of microstructure in concentrated suspensions and its implications for rheology and bulk flow", *Rheologica Acta*, 48 (8), pp. 909–923, 2009 (cit. on pp. 6, 7, 35).

[34] C. Perez: "The Use of a Direct Particle Simulation to Predict Fiber Motion in Polymer Processing", Ph.D. Thesis, USA: University of Wisconsin-Madison, 2016 (cit. on pp. 6, 114).

[35] F. Folgar and C. L. Tucker: "Orientation Behavior of Fibers in Concentrated Suspensions", *Journal of Reinforced Plastics and Composites*, 3 (2), pp. 98–119, Apr. 1984 (cit. on pp. 7, 8, 10, 33, 34, 43, 72, 87, 108, 111, 132).

[36] H.-C. Tseng, Y.-J. Chang, and C.-H. Hsu: "Prediction of Fiber Microstructure for Injection Molding: Orientation, Degradation, and Concentration", *Proceedings of the SPE Automotive Composites Conference & Exhibition (ACCE)* 2014 (cit. on pp. 7, 36, 108, 109, 124, 130).

[37] G. B. Jeffery: "The Motion of Ellipsoidal Particles Immersed in a Viscous Fluid", *Proceedings of the Royal Society of London. Series A*, 102 (715), pp. 161–179, Nov. 1922 (cit. on pp. 8, 33).

[38] R. Bay: "Fiber orientation in injection-molded composites: A comparison of theory and experiment", English, Ph.D. University of Illinois at Urbana-Champaign, 1991 (cit. on pp. 8, 25, 72, 116–118, 131, 132).

[39] T. B. Nguyen Thi, A. Yokoyama, K. Ota, K. Kodama, K. Yamashita, Y. Isogai, K. Furuichi, and C. Nonomura: "Numerical approach of the injection molding process

of fiber-reinforced composite with considering fiber orientation", pp. 571–577, 2014 (cit. on p. 8).

[40] S. Toll and P.-O. Andersson: "Microstructure of long- and short-fiber reinforced injection molded polyamide", *Polymer Composites*, 14 (2), pp. 116–125, 1993 (cit. on pp. 8, 12, 13, 15, 88).

[41] Z. Tadmor: "Molecular orientation in injection molding", *Journal of Applied Polymer Science*, 18 (6), pp. 1753–1772, 1974 (cit. on pp. 8, 87).

[42] S. Advani and C. Tucker: "The Use of Tensors to Describe and Predict Fiber Orientation in Short Fiber Composites", *Journal of Rheology (1978-present)*, 31 (8), pp. 751–784, 1987 (cit. on pp. 10, 11, 33, 43).

[43] R. Bailey and B. Rzepka: "Fibre Orientation Mechanisms for Injection Molding of Long Fibre Composites", *International Polymer Processing*, 6 (1), pp. 35–41, Mar. 1991 (cit. on p. 12).

[44] M. Vincent, T. Giroud, A. Clarke, and C. Eberhardt: "Description and modeling of fiber orientation in injection molding of fiber reinforced thermoplastics", *Polymer Blends, Composites and Hybrid Polymeric MaterialsIUPAC MACRO 2004*, 46 (17), pp. 6719–6725, Aug. 2005 (cit. on p. 13).

[45] C. Kuhn, W. Kucinski, O. Taeger, and T. Osswald: "Lightweight Design with Long Fiber Reinforced Polymers - Technological Challenges due to Effect of Fiber Matrix Separation.", *Proceedings of the 16th Automotive Composites Conference and Exhibition* 2016 (cit. on p. 13).

[46] T. A. Osswald: "Numerical Methods for Compression Mold Filling Simulation", PhD thesis, University of Illinois at Urbana - Champaign, 1987 (cit. on p. 13).

[47] D. O'Regan and M. Akay: "The distribution of fibre lengths in injection moulded polyamide composite components", *Journal of Materials Processing Technology*, 56 (14), International Conference on Advances in Material and Processing Technologies, pp. 282–291, 1996 (cit. on pp. 14, 88).

[48] E. Lafranche, P. Krawczak, J.-P. Ciolczyk, and J. Maugey: "Injection moulding of long glass fiber reinforced polyamide 66: Processing conditions/microstructure/flexural

properties relationship", *Advances in Polymer Technology*, 24 (2), pp. 114–131, 2005 (cit. on pp. 14, 19–21, 29, 30, 88).

[49] J. Kubat and A. Syalanczi: "Polymer-Glass Separation in the Spiral Mold Test", *Polymer Science and Engineering*, 14 (12) 1974 (cit. on pp. 14, 88).

[50] R. P. Hegler and G. Mennig: "Phase separation effects in processing of glass-bead- and glass-fiber-filled thermoplastics by injection molding", *Polymer Engineering & Science*, 25 (7), pp. 395–405, 1985 (cit. on pp. 14, 88).

[51] S. Ogadhoh and T. Papathanasiou: "Particle rearrangement during processing of glass-reinforced polystyrene by injection moulding", *Composites Part A: Applied Science and Manufacturing*, 27 (1), pp. 57–63, Jan. 1996 (cit. on pp. 14, 88).

[52] J. Kovács: "Shrinkage alteration induced by segregation of glass beads in injection molded PA6: Experimental analysis and modeling", *Polymer Engineering & Science*, 51 (12), pp. 2517–2525, 2011 (cit. on pp. 14, 15).

[53] L. A. Mondy, H. Brenner, S. A. Altobelli, J. R. Abbott, and A. L. Graham: "Shear-induced particle migration in suspensions of rods", *Journal of Rheology*, 38 (2), pp. 444–452, 1994 (cit. on pp. 14, 16).

[54] A. Ramzy, A. El-Sabbagh, L. Steuernagel, G. Ziegmann, and D. Meiners: "Rheology of natural fibers thermoplastic compounds: Flow length and fiber distribution", *Journal of Applied Polymer Science*, 131 (3), n/a–n/a, 2014 (cit. on p. 15).

[55] G. M. Vélez-García, P. Wapperom, D. G. Baird, A. O. Aning, and V. Kunc: "Unambiguous orientation in short fiber composites over small sampling area in a center-gated disk", *Composites Part A: Applied Science and Manufacturing*, 43 (1), pp. 104–113, 2012 (cit. on pp. 16, 25, 46).

[56] X. Sun, J. Lasecki, D. Zeng, Y. Gan, X. Su, and J. Tao: "Measurement and quantitative analysis of fiber orientation distribution in long fiber reinforced part by injection molding", *Polymer Testing*, 42, pp. 168–174, Apr. 2015 (cit. on pp. 16, 28, 29).

[57] E. Guazzelli and J. Morris: *A Physical Introduction to Suspension Dynamics*, 1st, Cambridge University Press, 2012 (cit. on pp. 16, 35).

[58] P. R. Nott and J. F. Brady: "Pressure-driven flow of suspensions: simulation and theory", *Journal of Fluid Mechanics*, 275, pp. 157–199, 1994 (cit. on pp. 16, 35).

[59] D. Zeng, C. Xia, J. Webb, L. Lu, Y. Gan, X. Sun, and J. Lasecki: "Effect of Fiber Orientation on the Mechanical Properties of Long Glass Fiber Reinforced (LGFR) Composites", *Proceedings of the SAE 2014 World Congress & Exhibition* 2014 (cit. on p. 16).

[60] J. Thomason: "The influence of fibre length and concentration on the properties of glass fibre reinforced polypropylene: 7. Interface strength and fibre strain in injection moulded long fibre PP at high fibre content", *Composites Part A: Applied Science and Manufacturing*, 38 (1), pp. 210–216, Jan. 2007 (cit. on pp. 16, 22, 23).

[61] B. N. Nguyen, S. K. Bapanapalli, J. D. Holbery, M. T. Smith, V. Kunc, B. J. Frame, J. H. Phelps, and C. L. Tucker: "Fiber Length and Orientation in Long-Fiber Injection-Molded Thermoplastics Part I: Modeling of Microstructure and Elastic Properties", *Journal of Composite Materials*, 42 (10), pp. 1003–1029, May 2008 (cit. on pp. 17, 30–33, 54, 55, 58, 62).

[62] Y. Masubuchi, M. Terada, A. Yamanaka, T. Yamamoto, and T. Ishikawa: "Distribution function of fiber length in thermoplastic composites", *Composites Science and Technology*, 134, pp. 43–48, 2016 (cit. on p. 18).

[63] I. W. Burr: "Cumulative Frequency Functions", *Ann. Math. Statist.* (2), pp. 215–232, June 1942 (cit. on p. 18).

[64] W. Weibull: "A Statistical Distribution Function of Wide Applicability", *Journal of Applied Mechanics*, 18, pp. 293–297, 1951 (cit. on p. 18).

[65] R. Turkovich v. and L. Erwin: "Fiber fracture in reinforced thermoplastic processing", *Polymer Engineering & Science*, 23 (13), pp. 743–749, 1983 (cit. on p. 19).

[66] J. Thomason and M. Vlug: "Influence of fibre length and concentration on the properties of glass fibre-reinforced polypropylene: 1. Tensile and flexural modulus", *Composites Part A: Applied Science and Manufacturing*, 27 (6), pp. 477–484, Jan. 1996 (cit. on pp. 21–23).

[67] J. Thomason: "The influence of fibre length, diameter and concentration on the impact performance of long glass-fibre reinforced polyamide 6,6", *Composites Part A: Applied Science and Manufacturing*, 40 (2), pp. 114–124, Feb. 2009 (cit. on pp. 21, 22).

[68] J. Thomason, M. Vlug, G. Schipper, and H. Krikor: "Influence of fibre length and concentration on the properties of glass fibre-reinforced polypropylene: Part 3. Strength

and strain at failure", *Composites Part A: Applied Science and Manufacturing*, 27 (11), pp. 1075–1084, Jan. 1996 (cit. on pp. 22, 23).

[69] J. Thomason: "The influence of fibre length and concentration on the properties of glass fibre reinforced polypropylene: 5. Injection moulded long and short fibre PP", *Composites Part A: Applied Science and Manufacturing*, 33 (12), pp. 1641–1652, Dec. 2002 (cit. on p. 22).

[70] J. Thomason: "The influence of fibre length and concentration on the properties of glass fibre reinforced polypropylene. 6. The properties of injection moulded long fibre PP at high fibre content", *Composites Part A: Applied Science and Manufacturing*, 36 (7), pp. 995–1003, July 2005 (cit. on pp. 22, 30).

[71] M. Schemme: "Langfaserverstaerkte Thermoplaste", *Kunststoffe*, 93, pp. 106–109, 2003 (cit. on pp. 23, 24, 89).

[72] G. Velez-Garcia: "Experimental Evaluation and Simulations of Fiber Orientation in Injection Molding of Polymers Containing Short Glass Fibers", PhD thesis, Virginia Polytechnic Institute and State University, 2012 (cit. on p. 25).

[73] P. Hine, N. Davidson, R. Duckett, and I. Ward: "Measuring the fibre orientation and modelling the elastic properties of injection-moulded long-glass-fibre-reinforced nylon", *Composites Science and Technology*, 53 (2), pp. 125–131, Jan. 1995 (cit. on p. 25).

[74] S. Stock: *MicroComputed Tomography: Methodology and Applications*, English, Boca Raton: CRC Press, 2009 (cit. on pp. 26, 27).

[75] T. B. Nguyen Thi, M. Morioka, A. Yokoyama, S. Hamanaka, K. Yamashita, and C. Nonomura: "Measurement of fiber orientation distribution in injection-molded short-glass-fiber composites using X-ray computed tomography", *Journal of Materials Processing Technology*, 219, pp. 1–9, May 2015 (cit. on pp. 26, 28).

[76] H. Altendorf: "3D Morphological Analysis and Modeling of Random Fiber Networks", PhD thesis, Technische Universität Kaiserslautern, 2011 (cit. on p. 26).

[77] U. Gandhi, S. De Boodt, V. Kunc, and Y. Y. Song: "Method to measure orientation of discontinuous fiber embedded in the polymer matrix from computerized tomography scan data", *Journal of Thermoplastic Composite Materials* 2015 (cit. on pp. 27, 28, 39, 43).

[78] M. Krause, J. M. Hausherr, B. Burgeth, C. Herrmann, and W. Krenkel: "Determination of the fibre orientation in composites using the structure tensor and local X-ray transform", *Journal of Materials Science*, 45 (4), p. 888, Nov. 2009 (cit. on pp. 27, 45).

[79] D. Salaberger, K. A. Kannappan, J. Kastner, J. Reussner, and T. Auinger: "Evaluation of Computed Tomography Data from Fibre Reinforced Polymers to Determine Fibre Length Distribution", *International Polymer Processing*, 2011/03, pp. 283–291, 2011 (cit. on p. 27).

[80] A. Bernasconi, F. Cosmi, and P. Hine: "Analysis of fibre orientation distribution in short fibre reinforced polymers: A comparison between optical and tomographic methods", *Composites Science and Technology*, 72 (16), pp. 2002–2008, 2012 (cit. on p. 28).

[81] F. Buck, B. Brylka, V. Müller, T. Müller, K. A. Weidenmann, A. N. Hrymak, F. Henning, and T. Böhlke: "Two-scale structural mechanical modeling of long fiber reinforced thermoplastics", *Composites Science and Technology*, 117, pp. 159–167, 2015 (cit. on p. 28).

[82] C. Perez, S. Goris, and T. A. Osswald: "Study on the Fiber Properties of a LFT Strand", *SPE Automotive Composites Conference & Exhibition (ACCE)*, 13th Annual 2013 (cit. on pp. 28, 56).

[83] S. Fliegener, M. Luke, and P. Gumbsch: "3D microstructure modeling of long fiber reinforced thermoplastics", *Composites Science and Technology*, 104, pp. 136–145, 2014 (cit. on p. 28).

[84] A. Ayadi, H. Nouri, S. Guessasma, and F. Roger: "Determination of orthotropic properties of glass fibre reinforced thermoplastics using X-ray tomography and multiscale finite element computation", *Composite Structures*, 136, pp. 635–649, 2016 (cit. on p. 28).

[85] C. Hannesschläger, V. Revol, B. Plank, D. Salaberger, and J. Kastner: "Fibre structure characterisation of injection moulded short fibre-reinforced polymers by X-ray scatter dark field tomography", *Case Studies in Nondestructive Testing and Evaluation*, 3, pp. 34–41, Apr. 2015 (cit. on p. 28).

[86] A. Bernasconi, F. Cosmi, and D. Dreossi: "Local anisotropy analysis of injection moulded fibre reinforced polymer composites", *Deformation and Fracture of Compos-*

ites: Analytical, Numerical and Experimental Techniques, with regular papers, 68 (12), pp. 2574–2581, Sept. 2008 (cit. on p. 28).

[87] N. Graupner, F. Beckmann, F. Wilde, and J. Müssig: "Using synchroton radiation-based micro-computer tomography (SR μ-CT) for the measurement of fibre orientations in cellulose fibre-reinforced polylactide (PLA) composites", *Journal of Materials Science*, 49 (1), pp. 450–460, Jan. 2014 (cit. on p. 28).

[88] T. Köpplmayr, I. Milosavljevic, M. Aigner, R. Hasslacher, B. Plank, D. Salaberger, and J. Miethlinger: "Influence of fiber orientation and length distribution on the rheological characterization of glass-fiber-filled polypropylene", *Polymer Testing*, 32 (3), pp. 535–544, 2013 (cit. on p. 28).

[89] M. De Monte, E. Moosbrugger, and M. Quaresimin: "Influence of temperature and thickness on the off-axis behaviour of short glass fibre reinforced polyamide 6.6 Quasi-static loading", *Composites Part A: Applied Science and Manufacturing*, 41 (7), pp. 859–871, July 2010 (cit. on p. 28).

[90] S. Moennich, R. Gloeckner, and F. Becker: "Analysis of Fibre Orientation using CT Data" 2011 (cit. on p. 28).

[91] H. Rolland, N. Saintier, C. Mareau, and G. Robert: "Fatigue Mechanisms in Short Glass Fibre Reinforced Thermoplastic: In Situ X-Ray Microtomography Observations and Microstructure Modelling", *Proceedings of the 7th European Conference on Composite Materials* 2016 (cit. on p. 28).

[92] M. J. Cieslinski, D. G. Baird, and P. Wapperom: "Obtaining repeatable initial fiber orientation for the transient rheology of fiber suspensions in simple shear flow", *Journal of Rheology*, 60 (1), pp. 161–174, 2016 (cit. on p. 28).

[93] K. J. Meyer, J. T. Hofmann, and D. G. Baird: "Initial conditions for simulating glass fiber orientation in the filling of center-gated disks", *Composites Part A: Applied Science and Manufacturing*, 49, pp. 192–202, 2013 (cit. on p. 28).

[94] F. Inceoglu, J. Ville, N. Gharmri, J. L. Pradel, A. Durin, R. Valette, and B. Vergnes: "Correlation Between Processing Conditions and Fiber Breakage During Compounding of Glass Fiber-Reinforced Polyamide", *Polymer Composites*, 32 (11), pp. 1842–1850, 2011 (cit. on pp. 29–31).

[95] D. E. Spahr, K. Friedrich, J. M. Schultz, and R. S. Bailey: "Microstructure and fracture behaviour of short and long fibre-reinforced polypropylene composites", *Journal of Materials Science*, 25 (10), pp. 4427–4439, 1990 (cit. on p. 29).

[96] International Organization for Standardization: *ISO 22314: Plastics - Glass-fibre-reinforced products - Determination of fibre length*, 2006 (cit. on p. 30).

[97] R. M. Bajracharya, A. C. Manalo, W. Karunasena, and K. Lau: "Experimental and theoretical studies on the properties of injection moulded glass fibre reinforced mixed plastics composites", *Composites Part A: Applied Science and Manufacturing*, 84, pp. 393–405, 2016 (cit. on p. 30).

[98] S. H. Bumm, J. L. White, and A. I. Isayev: "Glass fiber breakup in corotating twin screw extruder: Simulation and experiment", *Polymer Composites*, 33 (12), pp. 2147–2158, 2012 (cit. on p. 30).

[99] J. Wang, C. Geng, F. Luo, Y. Liu, K. Wang, Q. Fu, and B. He: "Shear induced fiber orientation, fiber breakage and matrix molecular orientation in long glass fiber reinforced polypropylene composites", *Materials Science and Engineering: A*, 528 (78), pp. 3169–3176, 2011 (cit. on p. 30).

[100] G. Jin, X. Lin, G. Tian, S. Zhang, M. Wang, and X. Wang: "Entrance flow of long glass fiber reinforced polypropylene through contraction die", *Journal of Reinforced Plastics and Composites*, 35 (2), pp. 111–123, Jan. 2016 (cit. on p. 30).

[101] V. Kunc, C. L. Tucker, G. Velez-Garcia, B. Frame, and B. N. Nguyen: "Fiber length distribution measurement for long glass and carbon fiber reinforced injection molded thermoplastics", *Proceedings of the 7th Annual Automotive Composites Conference and Exhibition* 2007 (cit. on pp. 30–32, 54–56, 58, 62).

[102] U. Yilmazer and M. Cansever: "Effects of processing conditions on the fiber length distribution and mechanical properties of glass fiber reinforced nylon-6", *Polymer Composites*, 23 (1), pp. 61–71, 2002 (cit. on p. 30).

[103] A. Huq and J. Azaiez: "Effects of length distribution on the steady shear viscosity of semiconcentrated polymer-fiber suspensions", *Polymer Engineering & Science*, 45 (10), pp. 1357–1368, 2005 (cit. on p. 30).

[104] H. Zhuang, P. Ren, Y. Zong, and G. Dai: "Relationship between fiber degradation and residence time distribution in the processing of long fiber reinforced thermoplastics", *eXPRESS Polymer Letters*, 2 (8), pp. 560–568, 2008 (cit. on p. 30).

[105] D. Teixeira, M. Giovanela, L. B. Gonella, and J. S. Crespo: "Influence of injection molding on the flexural strength and surface quality of long glass fiber-reinforced polyamide 6.6 composites", *Materials & Design*, 85, pp. 695–706, 2015 (cit. on p. 30).

[106] P. Ren and G. Dai: "Fiber dispersion and breakage in deep screw channel during processing of long fiber-reinforced polypropylene", *Fibers and Polymers*, 15 (7), pp. 1507–1516, July 2014 (cit. on p. 30).

[107] M. R. Hartwich, H. Mayr, and R. Stengler: "FASEP ULTRA - Automated Analysis of fibre length distribution in glass-fibre-reinforced products", *Proceedings of Optical Measurement Systems for Industrial Inspection* 2009 (cit. on pp. 30–32).

[108] R. Giusti, G. Lucchetta, and I. Dubrovich: "Effect of Screwgeometry on Long Glass Fiber Breakage During Injection", *Proceedings of the Annual Technical Conference SPE* 2015 (cit. on pp. 30, 31).

[109] S. Kleindel, D. Salaberger, R. Eder, H. Schretter, and C. Hochenauer: "Measurement and Numerical Simulation of Void and Warpage in Glass Fiber Reinforced Molded Chunky Parts", *International Polymer Processing*, 30 (1), pp. 100–112, Mar. 2015 (cit. on p. 31).

[110] P. Hine, B. Parveen, D. Brands, and F. Caton-Rose: "Validation of the modified rule of mixtures using a combination of fibre orientation and fibre length measurements", *Composites Part A: Applied Science and Manufacturing*, 64, pp. 70–78, Sept. 2014 (cit. on pp. 31, 56).

[111] W. Schijve: *Eigenschaftsermittlung und Pruefung von langfaserverstaerkten Thermoplasten*, tech. rep., EATC, 2008 (cit. on pp. 32, 59).

[112] J. H. Phelps: "Processing-Microstructue Models for Short- and Long-Fiber Thermoplastic Composites", PhD thesis, University of Illinois at Urbana-Champaign, 2009 (cit. on pp. 33, 120, 121).

[113] C. Hopmann, M. Weber, J. van Haag, and M. Schöngart: "A validation of the fibre orientation and fibre length attrition prediction for long fibre-reinforced thermoplastics", *AIP Conference Proceedings* 2015 (cit. on p. 33).

[114] J. Wang, J. O'Gara, C. L. Tucker, and III: "An objective model for slow orientation kinetics in concentrated fiber suspensions: Theory and rheological evidence", *Journal of Rheology*, 52 (5), pp. 1179–1200, 2008 (cit. on pp. 34, 111).

[115] D. Leighton and A. Acrivos: "The shear-induced migration of particles in concentrated suspensions", *Journal of Fluid Mechanics*, 181, pp. 415–439, 1987 (cit. on p. 35).

[116] J. F. Morris and F. Boulay: "Curvilinear flows of noncolloidal suspensions: The role of normal stresses", *Journal of Rheology*, 43 (5), pp. 1213–1237, 1999 (cit. on pp. 35, 36, 108, 130).

[117] J. Richardson and W. Zaki: "Sedimentation and fluidisation: Part I", *Chemical Engineering Research and Design*, 75 (Supplement), S82–S100, Dec. 1997 (cit. on p. 36).

[118] X. J. Fan, N. Phan-Thien, and R. Zheng: "Simulation of fibre suspension flow with shear-induced migration", 90, pp. 47–63, 2000 (cit. on p. 36).

[119] Moldex3D, CoreTech System Co. Ltd: "Predicting Fiber Breakage with Moldex3D: http://www.moldex3d.com/en/newsletter/predicting-fiber-breakage-with-moldex3d" 2017 (cit. on p. 38).

[120] T. A. Osswald, J. P. Hernández, K. Tschohl, and H. Wagner: "A Novel Fiber Orientation Evaluation Using a Directional Imagine Processing Technique", *Proceedings of the Anuual Technical Conference of the Society of Plastics Engineers* 2003 (cit. on pp. 39, 40).

[121] V. Kunc, S. Case, H. Santos-Villalobos, and S. Simunovic: "The stiffness tensor for composites with curved discontinuous fibers", *Composites Part A: Applied Science and Manufacturing*, 72, pp. 239–248, May 2015 (cit. on p. 44).

[122] V. Kunc: "Structure-Property Relationships in Flow Formed Discontinuous Fiber Reinforced Composites", PhD Thesis, Virginia Polytechnic Institute, 2013 (cit. on p. 55).

[123] H. Wang: "Fiber Property Characterization by Image Processing", Master Thesis, Lubbock, TX: Texas Tech University, 2007 (cit. on p. 56).

[124] SABIC: *Processing Guides: SABIC Stamax*, 2016 (cit. on pp. 57, 67, 98).

[125] D. L. Krasteva: "Integrated Prediction of Processing and Thermomechanical Behavior of Long Fiber Thermoplastic Composites", PhD Thesis, Portugal: University of Minho, 2009 (cit. on p. 59).

[126] D. Salaberger, J. Kastner, and T. Auinger: "Evaluation of Computed Tomography Data from Fibre Reinforced Polymers to Determine Fibre Length Distribtion" 2013 (cit. on p. 64).

[127] W. Grellmann and S. Seidler: *Polymer Testing*, Second Edition, DOI: 10.3139/9781569905494, Hanser Publisher, 2013 (cit. on p. 65).

[128] SABIC: *SABIC STAMAX Material Datasheet*, 2017 (cit. on p. 66).

[129] J. Schindelin, I. Arganda-Carreras, E. Frise, V. Kaynig, M. Longair, T. Pietzsch, S. Preibisch, C. Rueden, S. Saalfeld, B. Schmid, J.-Y. Tinevez, D. J. White, V. Hartenstein, K. Eliceiri, P. Tomancak, and A. Cardona: "Fiji: an open-source platform for biological-image analysis", *Nat Meth*, 9 (7), pp. 676–682, July 2012 (cit. on p. 81).

[130] C. L. Tucker: "Flow regimes for fiber suspensions in narrow gaps", *Journal of Non-Newtonian Fluid Mechanics*, 39 (3), pp. 239–268, Jan. 1991 (cit. on p. 85).

[131] K. Evans and A. Gibson: "Prediction of the maximum packing fraction achievable in randomly oriented short-fibre composites", *Composites Science and Technology*, 25 (2), pp. 149–162, Jan. 1986 (cit. on p. 85).

[132] A. I. A. El-Rahman and C. L. T. III: "Mechanics of random discontinuous long-fiber thermoplastics. Part II: Direct simulation of uniaxial compression", *Journal of Rheology*, 57 (5), pp. 1463–1489, 2013 (cit. on p. 86).

[133] M. F. A. Couette: "Etudes sur le Frottement des Liquides", *Annales de Chimie et de Physique*, 21, pp. 433–510, 1890 (cit. on p. 90).

[134] K. Shon, D. Liu, and J. L. White: "Experimental Studies and Modeling of Development of Dispersion and Fiber Damage in Continuous Compounding", *International Polymer Processing*, 20 (3), pp. 322–331, Sept. 2005 (cit. on pp. 91–93).

[135] S. F. Sawyer: "Analysis of Variance: The Fundamental Concepts", *Journal of Manual & Manipulative Therapy*, 17 (2), 27E–38E, Apr. 2009 (cit. on p. 100).

[136] R.-y. Chang and W.-h. Yang: "Numerical simulation of mold filling in injection molding using a three-dimensional finite volume approach", *International Journal for Numerical Methods in Fluids*, 37 (2), pp. 125–148, 2001 (cit. on p. 106).

[137] M. M. Cross: "Rheology of non-Newtonian fluids: A new flow equation for pseudoplastic systems", *Journal of Colloid Science*, 20 (5), pp. 417–437, June 1965 (cit. on p. 107).

[138] M. L. Williams, R. F. Landel, and J. D. Ferry: "The Temperature Dependence of Relaxation Mechanisms in Amorphous Polymers and Other Glass-forming Liquids", *Journal of the American Chemical Society*, 77 (14), pp. 3701–3707, July 1955 (cit. on p. 107).

[139] R.-Y. Chang and S.-Y. Chiou: "A unified K-BKZ model for residual stress analysis of injection molded three-dimensional thin shapes", *Polymer Engineering & Science*, 35 (22), pp. 1733–1747, 1995 (cit. on p. 107).

[140] H.-C. Tseng, R.-Y. Chang, and C.-H. Hsu: "Numerical prediction of fiber orientation and mechanical performance for short/long glass and carbon fiber-reinforced composites", *Composites Science and Technology*, 144, pp. 51–56, May 2017 (cit. on p. 111).

[141] R. Zheng, R. I. Tanner, and X. J. Fan: *Injection Molding - Integration of Theory and Moldeing Methods*, Springer, 2011 (cit. on pp. 111, 132).

[142] M. J. Cieslinski: "Using a Sliding Plate Rheometer to Obtain Material Parameters for Simulating Long Fiber Orientation in Injection Molded Composites", Ph.D. Thesis, Blacksburg, Virginia: Virginia Polytechnic Institute and State University, 2015 (cit. on p. 111).

[143] N. Phan-Thien, X. J. Fan, R. I. Tanner, and R. Zheng: "Folgar-Tucker constant for a fibre suspension in a Newtonian fluid", *Journal of Non-Newtonian Fluid Mechanics*, 103 (23), pp. 251–260, 2002 (cit. on pp. 111, 116–118, 132).

[144] R. S. Bay and C. L. Tucker: "Fiber orientation in simple injection moldings. Part II: Experimental results", *Polymer Composites*, 13 (4), pp. 332–341, 1992 (cit. on p. 111).

[145] I. Walter, S. Goris, J. Teuwsen, A. Tapia, C. Perez, and T. Osswald: "A Direct Particle Level Simulation Coupled with The Folgar-Tucker RSC Model to Predict Fiber Orientation in Injection Molding of Long Glass Fiber-Reinforced Thermoplastics", *Proceedings of the SPE Annual Technical Conference* 2017 (cit. on pp. 112, 114, 115).

[146] H.-C. Tseng, R.-Y. Chang, and C.-H. Hsu: "Improved fiber orientation predictions for injection molded fiber composites", *Composites Part A: Applied Science and Manufacturing*, 99, pp. 65–75, Aug. 2017 (cit. on pp. 112, 131).

[147] D. H. Chung and T. H. Kwon: "Invariant-based optimal fitting closure approximation for the numerical prediction of flow-induced fiber orientation", *Journal of Rheology*, 46 (1), pp. 169–194, Jan. 2002 (cit. on p. 112).

[148] C. Schmid: "Simulations of Flocculation in flowing Fiber Suspensions", PhD thesis, University of Wisconsin-Madison, 1999 (cit. on p. 114).

[149] D. Ramirez: "Study of Fiber Motion in Molding Processes by Means of a Mechanistic Model", Ph.D. Thesis, Madison, WI: University of Wisconsin-Madison, 2014 (cit. on pp. 114, 115, 126).

[150] A. Lees and S. Edwards: "The computer study of transport processes under extreme conditions", *Journal of Physics C: Solid State Physics*, 5 (15), p. 1921, 1972 (cit. on p. 115).

[151] J. Nocedal and S. Wright: *Numerical Optimization*, 2nd, New York: Springer-Publisher, 2006 (cit. on pp. 115, 120).

[152] J. Wang: "Improved Fiber Orientation Predictions for Injection Molded Composites", *Dissertation*, University of Illinois at Urbana-Champaign 2007 (cit. on p. 116).

[153] C.-T. Huang and H.-C. Tseng: "Simulation prediction of the fiber breakage history in regular and barrier structure screws in injection molding", *Polymer Engineering & Science*, DOI: 10.1002/pen.24660, 2017 (cit. on p. 124).

[154] O. Forgacs and S. Mason: "Particle Motions in Sheared Suspensions - Orbits of Flexible Threadlike Particles", *Journal of Colloid Science*, 14 1959 (cit. on p. 126).

[155] T. Osswald: "Personal correspondence and discussion", *Train from Wolfsburg, Germany, to Aachen, Germany* June 2016 (cit. on pp. 126–128).

[156] N. Nguyen, X. Jin, V. Kunc, and C. Tucker: *Validation of New Process Models for Large Injection-molded Long-fiber Thermoplastic Composite Structures*, PNNL Report under Contract DEAC05e76RL01830, The US Department of Energy, 2012 (cit. on p. 130).

[157] S. Kleindel, D. Salaberger, R. Eder, H. Schretter, and C. Hochenauer: "Prediction and Validation of Short Fiber Orientation in a Complex Injection Molded Part with Chunky Geometry", *International Polymer Processing*, 30 (3), pp. 366–380, June 2015 (cit. on p. 131).

A. Viscosity Data

The viscosity is modeled using the Cross-William-Landel-Ferry (Cross-WLF) equation, given by

$$\eta\left(T,\dot{\gamma},p\right) = \frac{\eta_0}{1+\left(\frac{\eta_0\,\dot{\gamma}}{\tau^*}\right)^{1-n}} \tag{A.1}$$

where η_0 is the zero shear viscosity, τ^* is the critical shear stress, p the pressure and n is the power law index. The zero shear viscosity is calculated by

$$\eta_0\left(T,p\right) = D_1 \exp\left[\frac{-A_1\left(T-T^*\right)}{A_2+\left(T-T^*\right)}\right] \tag{A.2}$$

where D_1 and A_1 are fitting parameters, T is the temperature and the reference temperature, T^*, is obtained by

$$T^* = D_2 + D_3\,p \tag{A.3}$$

where D_2 is the glass transition temperature at low pressure and D_3 is a fitting parameter accounting for the pressure dependency. The pressure dependency term, A_2, is given by

$$A_2 = \tilde{A}_2 + D_3\,p \tag{A.4}$$

where $\tilde{A}_2$ is a fitting parameter.

The model parameters for the materials used in this dissertation are obtained from the Moldex3D$^{\text{TM}}$ Databank (Version R15, Service Pack 1) and summarized in Table A.1 (PP 579S), Table A.2 (PPGF20), Table A.3 (PPGF30), and Table A.4 (PPGF40).

Table A.1.: Summary of parameter values of the Cross-WLF model values for SABIC® PP 579S, obtained from the Moldex3D™ Material Databank (Version R15, Service Pack 1)

Coefficient	Value	Units
n	0.28593	[-]
τ^*	38278	Pa
D_1	1.747E+13	Pa·s
D_2	263.15	K
D_3	0	$\mathrm{K\,Pa^{-1}}$
A_1	30.85	[-]
$\tilde{A}_2$	51.6	K

Table A.2.: Summary of parameter values of the Cross-WLF model values for SABIC® STAMAX™ 20YM240, obtained from the Moldex3D™ Material Databank (Version R15, Service Pack 1)

Coefficient	Value	Units
n	0.296	[-]
τ^*	27990	Pa
D_1	4.113E+15	Pa·s
D_2	263.15	K
D_3	0	$\mathrm{K\,Pa^{-1}}$
A_1	36.424	[-]
$\tilde{A}_2$	51.6	K

Table A.3.: Summary of parameter values of the Cross-WLF model values for SABIC® STAMAX™ 30YM240, obtained from the Moldex3D™ Material Databank (Version R15, Service Pack 1)

Coefficient	Value	Units
n	0.33	[-]
τ^*	20670	Pa
D_1	4.9E+17	Pa·s
D_2	263.15	K
D_3	0	$\mathrm{K\,Pa^{-1}}$
A_1	40.48	[-]
$\tilde{A}_2$	51.6	K

Table A.4.: Summary of parameter values of the Cross-WLF model values for SABIC® STAMAX™ 40YM240, obtained from the Moldex3D™ Material Databank (Version R15, Service Pack 1)

Coefficient	Value	Units
n	0.3395	[-]
τ^*	17500	Pa
D_1	7.06E+17	Pa·s
D_2	263.15	K
D_3	0	$\mathrm{K\,Pa^{-1}}$
A_1	41.562	[-]
$\tilde{A}_2$	51.6	K

B. Couette Rheometer

B.1. Couette Rheometer Design

The individual parts of the Couette rheometer are displayed in Figure B.1, showing: (1) the inner cylinder, (2) the fixture and base, (3) the heater band, (4) the fixed outer cylinder, (5) the spring-loaded aluminum socket with a compression spring (Music Compression Wire 720x080x250 from LEE Spring Company, Brooklyn, NY), (6) the outer cap, (7) the inner cap, (8) the large brass bearing, (9) the small brass bearing, and (10) the thermocouple (type SEFE-J-1 from OMEGA Engineering Inc., Stamford, CT). A technical drawing of the Couette rheometer setup is depicted in Figure B.2.

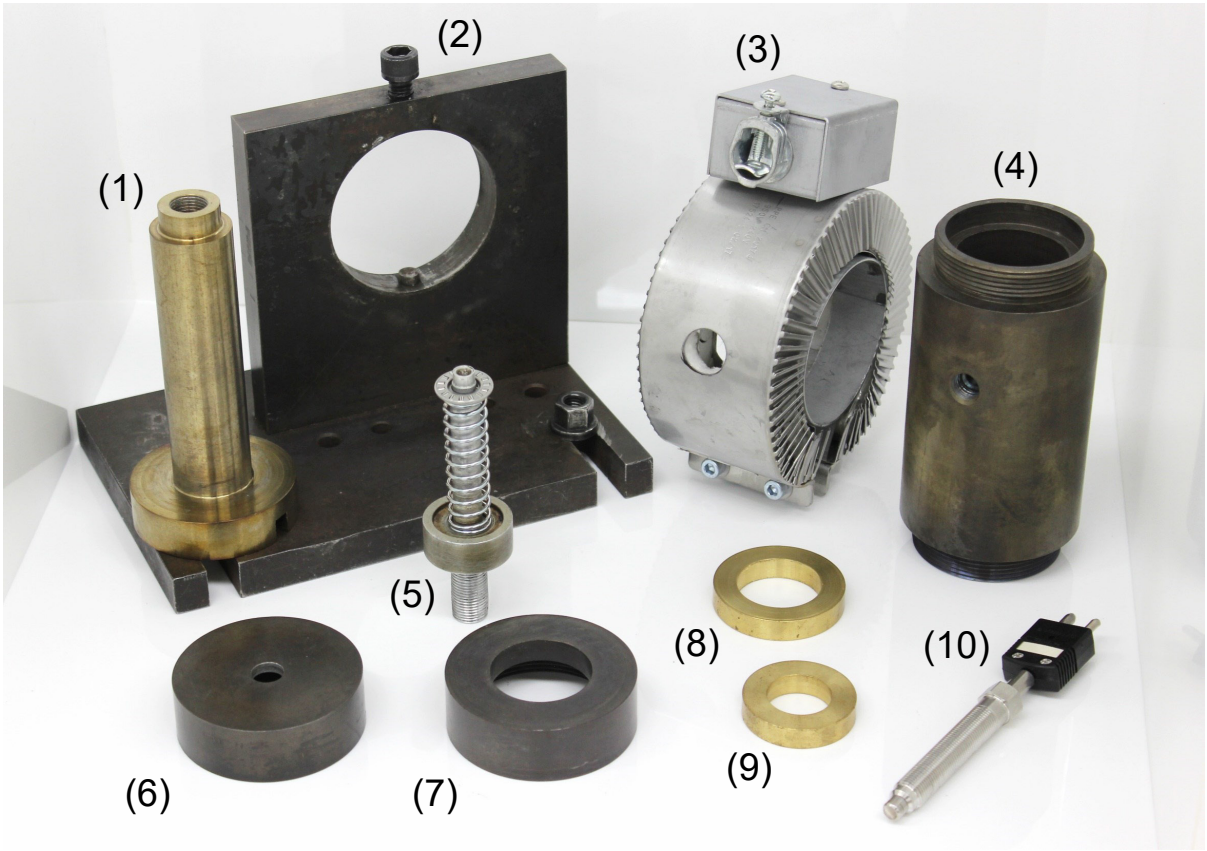

Figure B.1.: Photo of the individual parts of the Couette rheometer setup.

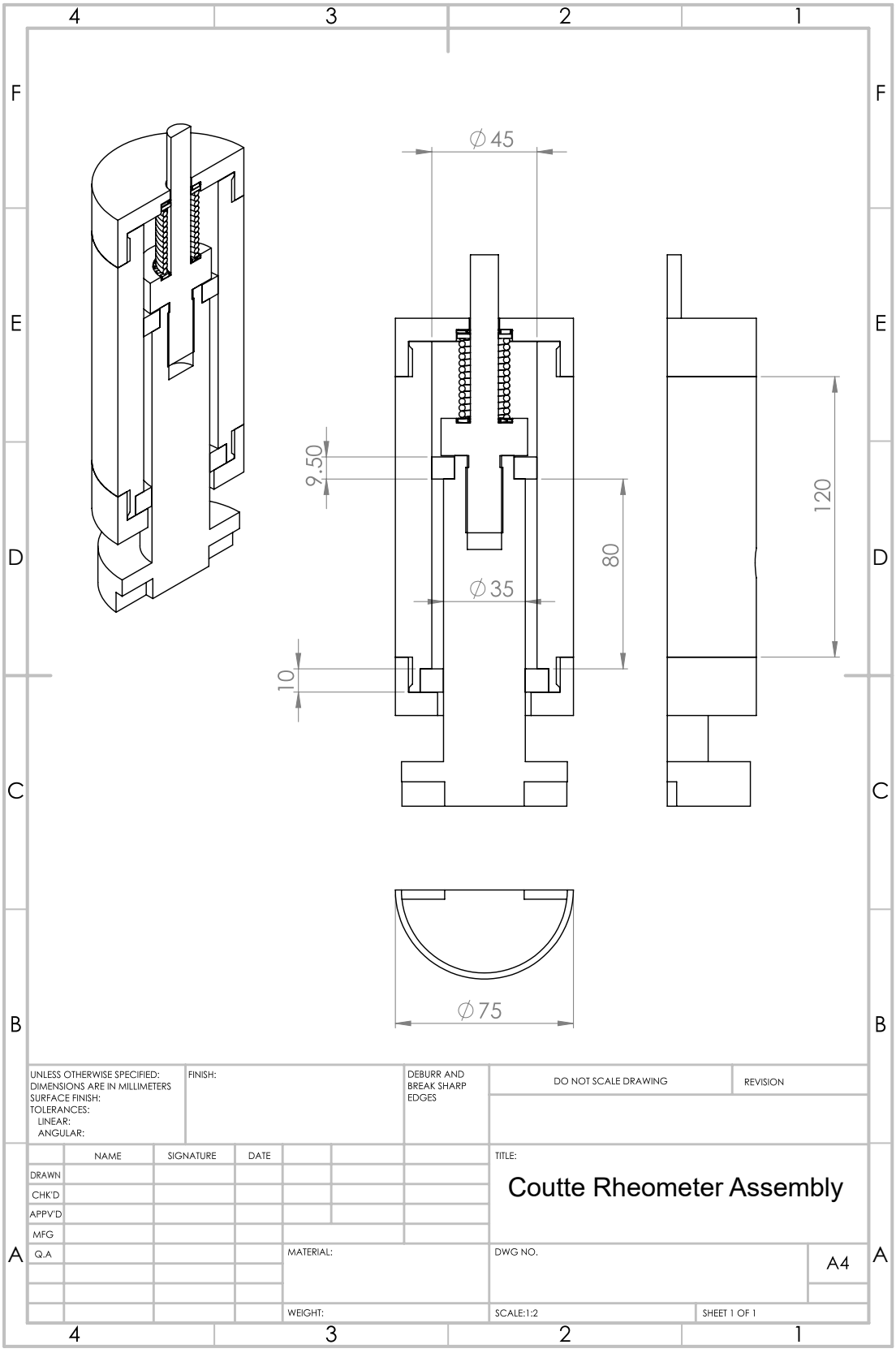

Figure B.2.: Technical drawing of the Couette Rheometer setup. Measurements shown in millimeter (mm).

B.2. Couette Rheometer flow

The Couette flow in the annular gap is a drag flow induced by the stationary outer cylinder and the rotating inner cylinder as schematically depicted in Figure B.3.

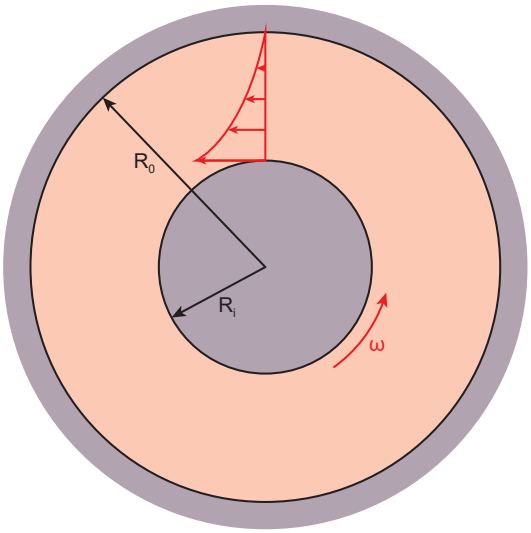

Figure B.3.: Schematic illustration of the Couette flow. Figure directly taken from [8].

The average shear rate can be calculated by

$$\dot{\gamma} = \frac{R_i\,\Omega}{h} \tag{B.1}$$

where R_i is the radius of the inner cylinder, Ω is the angular velocity of the rotating inner cylinder and h is the annular gap between the inner cylinder and outer cylinder.